University of Reading

Department of Meteorology

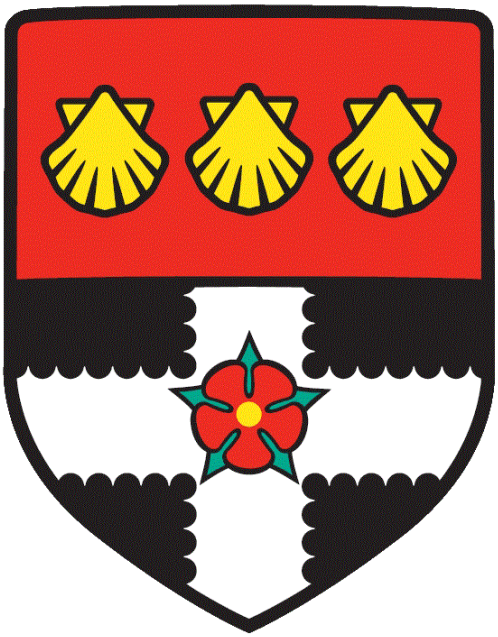

The Atlantic/Pacific atmospheric moisture budget asymmetry: the role of atmospheric moisture transport

Philip Macleod Craig

A thesis submitted for the
degree of Doctor of Philosophy

July 2018

Declaration

I confirm that this is my own work and the use of all material from other sources has been properly and fully acknowledged.

- Philip Macleod Craig

Publications

The work in chapter 3 of this thesis has appeared in the following publication:

Craig, P.M., Ferreira,D. and Methven,J. (2017) The contrast between Atlantic and Pacific surface water fluxes. *Tellus A*, **69**(1330454).

All computations in this publication were carried out by Philip Craig except for the fresh-water transports from ECCOv4 which were calculated by David Ferreira. PC lead the analysis of the results and the writing of the article with feedback from both co-authors.

Abstract

The contrast between basin-integrated precipitation minus evaporation ($P - E$) of the Atlantic and Pacific Oceans is about 0.4 Sv (1 Sv $\equiv 10^9$ kg s^{-1}). The Atlantic is net evaporative and the Pacific near neutral - a result consistent across datasets. This asymmetry has been linked to the higher sea surface salinity (SSS) in the Atlantic than in the Pacific (at all latitudes) and the absence of deep-water formation in the Pacific. This thesis focuses on the interbasin $P - E$ contrast and the atmospheric moisture transports associated with it.

Here, it is shown that the $P-E$ asymmetry is primarily a result of greater Pacific precipitation per unit area south of 30°N, with greater Atlantic evaporation per unit area north of 30°N making a smaller contribution.

Comparing the atmospheric moisture fluxes across the catchment boundaries of the ocean drainage basins (the integral of which is equal to basin-integrated $P-E$) shows that anomalous eastward fluxes across South-East Asia, in contrast to westward fluxes across other boundaries, dominate the annual mean $P - E$ asymmetry, rather than the flux across Central America as is often stated.

Using an airmass trajectory model it is shown that the moisture fluxes across catchment boundaries are dominated by contributions from the neighbouring basins. This also reveals that the atmosphere imports moisture to the Pacific more efficiently than to the Atlantic/Indian basins. Backward trajectories with Indian Ocean origin are associated with net precipitation of 0.43 Sv across the Pacific.

The Somali low-level jet and Asian Summer Monsoon dominate the $P - E$ asymmetry by diverting trajectories away from Africa into westerly flow across India towards the Pacific. This causes the anomalous eastward fluxes across South-East Asia and therefore the strong Pacific precipitation south of 30°N. These results highlight the importance of continental geometry and steady large-scale circulation features in the mean state of the $P - E$ asymmetry.

Acknowledgements

I would like to take the opportunity to thank various people who have helped with the process of this research and the writing of this thesis. Firstly, I am very grateful to my supervisors, David Ferreira and John Methven, for giving me the opportunity to attempt this research project and for all their assistance along the way. Thanks also go to my monitoring committee, Rémi Tailleux and Richard Allan, for their additional advice every six months and keeping me on track. This research would have been all the more difficult were it not for the help of Hans de Leeuw in using the trajectory model, even after he had left the department.

I would also like to thank the PhD students and post-docs on Lyle 5 for the help and advice over the last couple of years, and the support during the last few months of writing. Also thanks to the people of Lyle 5 for the long lunch breaks, coffee & cake on Thursdays and trips to the Harris Garden during summer. I would also like to give a big thanks to the wider PhD community both past and present for making these last three-and-a-half years enjoyable and helping me to unwind with Friday evenings at the SCR/Cotton Club, pub crawls etc.

I would also like to extend my gratitude to the Natural Environment Research Council and the SCENARIO Doctoral Training Partnership for the funding to come to Reading for this project and for the financial support for travel and conferences.

Finally, I would like to thank my mother for the free accommodation and taxi service during the two months I spent at home while I finished writing my thesis.

"Water, water everywhere, Nor any drop to drink."

—Samuel Taylor Coleridge, The Rime of the Ancient Mariner

Abbreviations

ACC	Antarctic Circumpolar Current
ALOS	Advanced Land Observation System
AMOC	Atlantic Meridional Overturning Circulation
ASAR	Advanced Synthetic-Aperture Radar
AWP	Atlantic Warm Pool
CMIP5	Coupled Model Intercomparison Project Phase 5
COARE	Coupled Ocean-Atmosphere Response Experiment
CFSR	Climate Forecast System Reanalysis
DJF	December January February
ECCO	Estimating the Circulation and Climate of the Ocean
ECMWF	European Centre For Medium Range Weather Forecasts
ENSO	El Niño Southern Oscillation
FLEXPART	Flexible Particle Dispersion Model
GCM	General Circulation Model
Geofabric	Australian Hydrological Geospatial Fabric
GPCP	Global Precipitation Climatology Project
HydroSHEDS	Hydrological data and maps based on Shuttle Elevation Derivatives at multiple Scales
HYSPLIT	Hybrid Single Particle Langrangian Integrated Trajectory Model
IFS	Integrated Forecasting System

IMBIE	Ice Sheet Mass Balance Inter-Comparison Exercise
IOD	Indian Ocean Dipole
ITCZ	Intertropical Convergence Zone
ITF	Indonesian Throughflow
JJA	June July August
LLJ	Low-Level Jet
MAM	March April May
MIT	Massachusetts Institute of Technology
MOC	Merdional Overturning Circulation
NAO	North Atlantic Oscillation
NCAR	National Center for Atmospheric Research
NCEP	National Centers for Environmental Prediction
NIMA	United States National Imagery and Mapping Agency
NPIW	North Pacific Intermediate Water
NWP	Numerical Weather Prediction
OAFlux	Objectively Analyzed air-sea Fluxes
OLR	Outgoing Longwave Radiation
OPI	OLR Precipitation Index
PALSAR	Phase-Array L-band Synthetic-Aperture Radar
PDW	Pacific Deep Water
PSS	Practical Salinity Scale
ROTRAJ	Reading Offline Trajectory Model
RTM	River Transport Model

SODA	Simple Ocean Data Assimilation
SON	September October November
SPCZ	South Pacific Convergence Zone
SRTM	Shuttle Radar Topography Mission
SSM/I	Special Satellite Microwave Imager
SSS	Sea Surface Salinity
SST	Sea Surface Temperature
TIROS	Television and Infrared Satellite
TOVS	TIROS Operation Vertical Sounder
USGS	United States Geological Survey
WOA	World Ocean Atlas
WOCE	World Ocean Circulation Experiment

Contents

Chapter 1

Introduction

Patterns of evaporation (E) and precipitation (P) are a major factor in the sea surface salinity (SSS) of the global ocean. Evaporation removes freshwater from the surface of the oceans which increases SSS and precipitation adds freshwater and freshens the ocean. Differences between E and P therefore set the SSS. It is well established that there a is contrast between SSS across the Atlantic and Pacific Oceans where Atlantic SSS is greater across the Atlantic (Broecker, 1991). High subpolar Atlantic SSS leads to sinking of dense water through a process called deep convection, but the fresher subpolar Pacific does not permit such sinking to occur (Warren, 1983).

Most current theories behind the existence of the Atlantic Meridional Overturning Circulation (AMOC) and MOC asymmetry take the SSS and moisture budget asymmetries into account. However, the current understanding of the atmospheric moisture budget asymmetry is somewhat limited as it is restricted to focusing on asymmetries in evaporation or atmospheric moisture transport across Central America. This thesis will provide a more complete understanding of the Atlantic/Pacific moisture budget asymmetry by investigating evaporation and precipitation patterns in more detail and determining the most important atmospheric moisture transports between ocean drainage basins. A more complete understanding of the atmospheric moisture budgets of the oceans can hopefully be included in theories regarding the Atlantic/Pacific MOC asymmetry which often attribute the SSS contrast to higher Atlantic sea surface temperatures (SSTs) caused by the AMOC's heat transport resulting in stronger Atlantic E with the excess moisture transported in the trade winds across Central America and freshening the Pacific.

1.1 The sea surface salinity and moisture budget asymmetries

1.1.1 Sea surface salinity

Higher sea surface salinities (SSS) are generally found in the subtropical oceans with lower salinities found at higher latitudes (Figure 1.1). The greatest SSS (40.1 psu; practical salinity units) is found in the Red Sea where surface salinities are in excess of 37 psu throughout the basin. The Mediterranean Sea also has high surface salinities, particularly towards the eastern end of the basin where SSS reaches 39.1 psu. The Gulf of Persia also has high salinities in excess of 37 psu. However, the greatest open-ocean SSS is found in the North Atlantic subtropical gyre (D'Addezio and Bingham, 2014) where salinities reach approximately 37.4 psu. The lowest SSS (5.0 psu) is found in the Gulf of Bothnia between Sweden and Finland (Håkansson *et al.*, 1996).

The most remarkable feature of large-scale SSS patterns is the contrast between the Atlantic and Pacific Oceans (Figure 1.1) which exists at all latitudes (Figure 1.2). In the southern hemisphere the difference is about 1 psu in the subtropical gyre but in the nothern hemisphere subtropical gyre the difference is up to 2 psu (Gordon *et al.*, 2015). The difference in salinity is particularly remarkable in the subpolar gyres (Warren, 1983; Wills and Schneider, 2015) where,

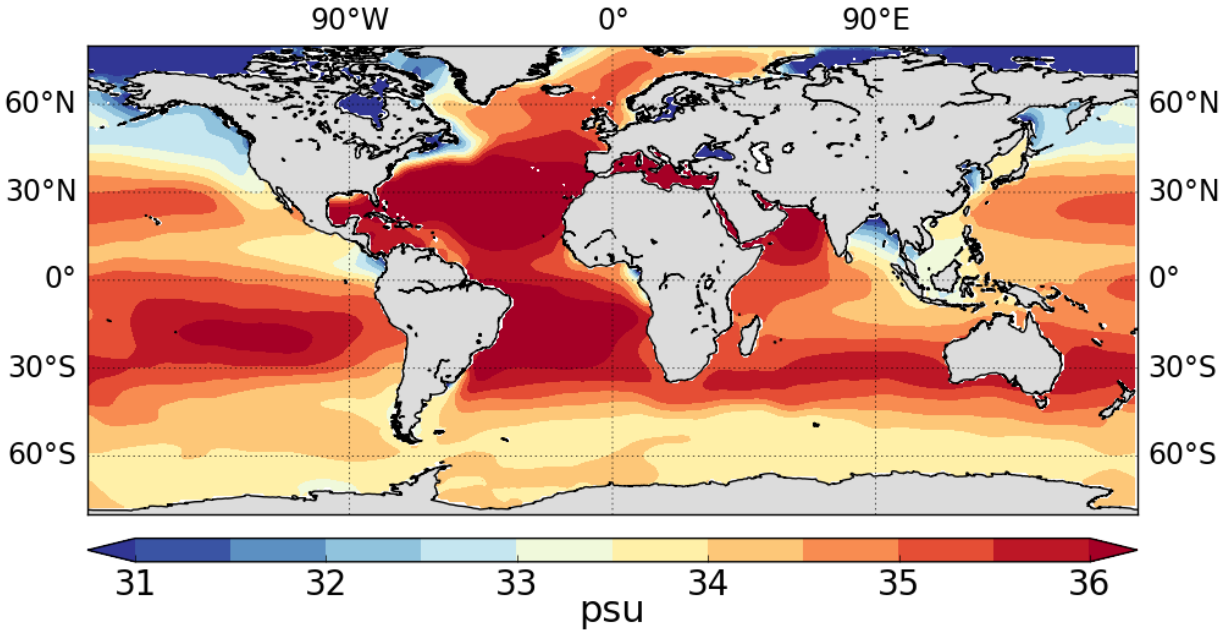

Figure 1.1: Annual mean (1955-2013) SSS from the World Ocean Atlas (Zweng *et al.*, 2013) in practical salinity units (psu) with the contours spaced evenly every 0.5 psu. These units are from the practical salinity scale (PSS-78). The practical salinity, S, of seawater is the ratio of electrical conductivity of seawater at 15°C and with the pressure at one standard atmosphere (1013.25 hPa) to the electrical conductivity of a potassium chloride solution at the same temperature and pressure (Millero *et al.*, 2008).

north of 40°N, zonal mean Atlantic SSS is approximately 34.5 psu where as zonal mean Pacific SSS decreases from approximately 33.5 psu to 32 psu (Figure 1.2). This region of SSS $>$ 34 psu in the subpolar Atlantic extends poleward of 60°N into the Norwegian Sea and around the north coast of Scandinavia (Figure 1.1). The Pacific is bounded in the north by the Bering Strait but the Arctic Ocean is much fresher near the Bering Strait than it is between Greenland and Scandinavia. The Indian Ocean also has higher salinities than much of the Pacific, most notably in the Arabian Sea, but SSS decreases from west to east across the Indian Ocean (Figure 1.1).

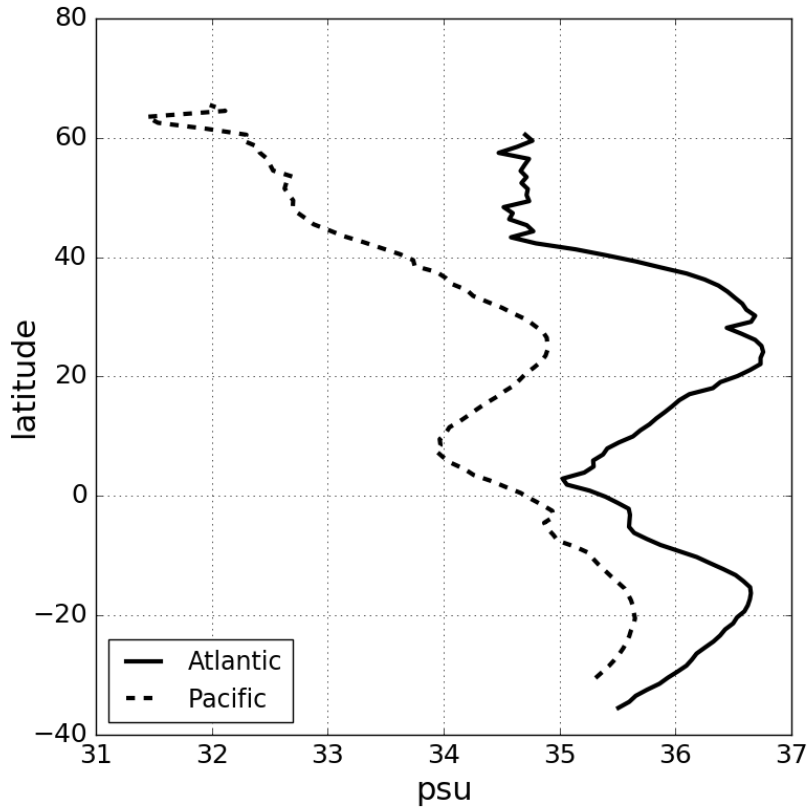

Figure 1.2: Annual mean (1955-2013) zonally averaged SSS for the Atlantic (solid line) and Pacific (dashed line) Oceans from the 2013 World Ocean Atlas (Zweng *et al.*, 2013). These zonal means are calculated between 60°N and 35°S for the Atlantic and the Bering Strait and 30°S for the Pacific, matching the extents used in chapter 3. The Mediterranean and Baltic Seas are not included in the Atlantic zonal mean.

The salinity contrast between the Atlantic and Pacific Oceans also exists below the surface, at least as deep as 2000 m (Figure 1.3). At 2000 m depth the salinity difference between the two oceans is reduced to less than 0.5 psu but still present at all latitudes. In the eastern subtropical North Atlantic a salinity maximum is present slightly poleward of 30°N off the coasts of Africa and the Iberian Peninsula (Figure 1.3(d)). This is a result of the outflow of high salinity water from the Mediterranean Sea which spreads around the Atlantic Ocean after overflowing across the Camarinal Sill (Candela, 2001).

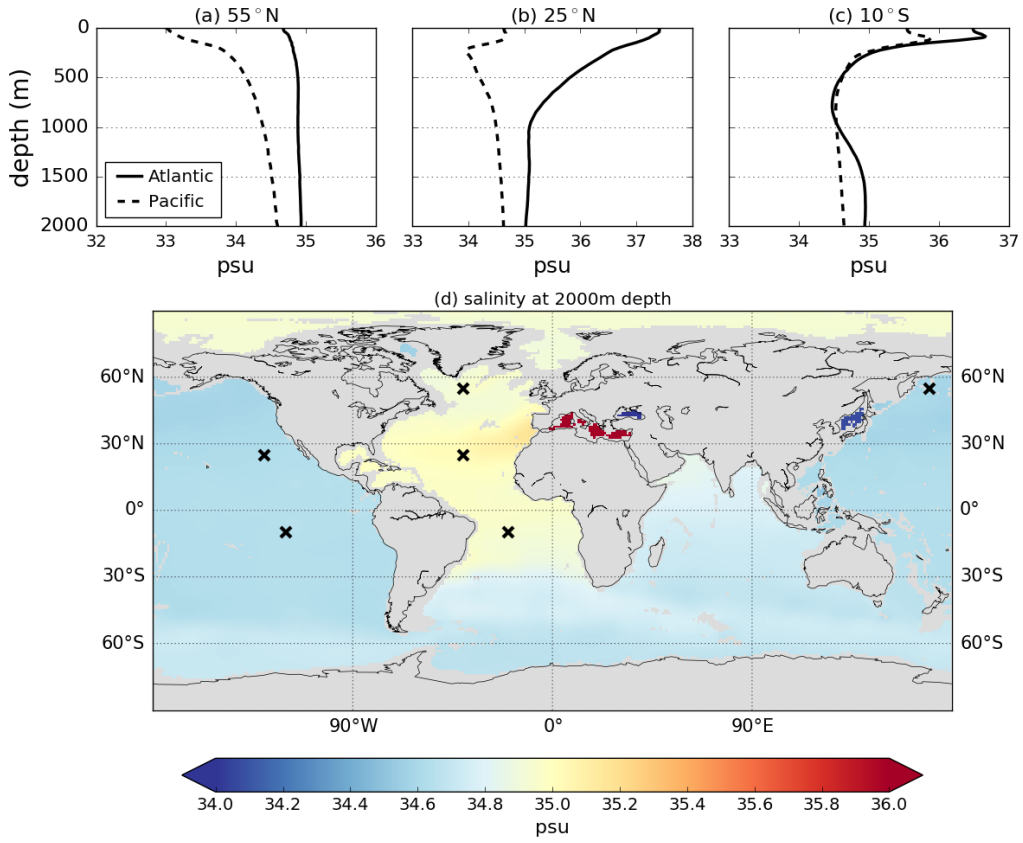

Figure 1.3: Annual mean (1955-2013) vertical profiles of salinity for the upper 2000 m for points in the Atlantic and Pacific Oceans at (a) 55°N, (b) 25°N and (c) 10°S, and (d) global salinity and 2000 m. The locations of the vertical profiles in panels (a)-(c) are shown by the black crosses in panel (d). All data is from the World Ocean Atlas (Zweng *et al.*, 2013).

1.1.2 Atmospheric moisture budget

Across the oceans the subtropics are occupied by regions of net evaporation ($E > P$) where the descending branch of the Hadley Cell brings dry air into the atmospheric boundary layer. Over the continents this results in the existence of deserts where evaporation minus precipitation ($E - P$) is approximately zero as there is little moisture to evaporate and fall as precipitation. In the tropics a band of strong net precipitation ($E < P$) stretches across the oceans in the Intertropical Convergence Zone (ITCZ) where the easterly trade winds (Figure 1.5) converge at the surface and latent heat release causes air parcels to be more buoyant leading to vertical motion in the ascending branch of the Hadley Cell. The ITCZ also causes the existence of major rainforests such as the Amazon and Congo where there are major regions of net precipitation on the tropical continents (Figure 1.4). Poleward of the midlatitudes (about 45°) in both hemispheres the oceans and continents are dominated by precipitation from extratropical cyclones in the storm tracks (*e.g.* Hawcroft *et al.*, 2012). In extratropical cyclones, bands of ascending air

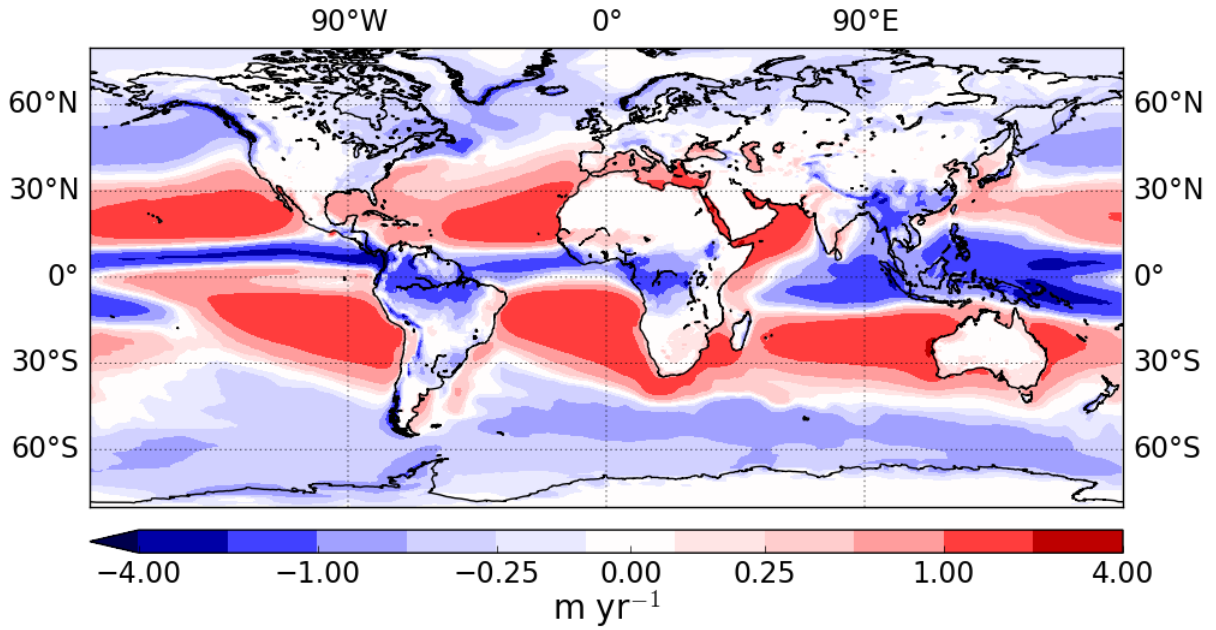

Figure 1.4: Annual mean (1979-2014) global evaporation minus precipitation ($E-P$) from ERA-Interim (see section 2.1.1). Red contours indicate regions of net evaporation ($E - P > 0$) and blue contours indicate regions of net precipitation ($E - P < 0$). The value of $E - P$ doubles as the contours increase.

known as warm conveyor belts can transport large amounts of moisture which leads to precipitation (Eckhardt *et al.*, 2004). The poleward sector of an extratropical cyclone carries more moisture than the equatorward sector due to the difference in humidity between high and low latitudes (Pfahl *et al.*, 2015), therefore the net moisture transport from extratropical cyclones is poleward.

Other key mechanisms of moisture transport are monsoon systems (seasonal reversals of wind direction) which are important in South Asia (Baker *et al.*, 2015), west Africa (Lèlè *et al.*, 2015) and North America (Berbery, 2001). Low-level jets (LLJs)[1] play an important role in regional extreme precipitation events (Gimeno *et al.*, 2016). There are many well-studied LLJs, for example the Caribbean (Whyte *et al.*, 2008), South American (Marengo *et al.*, 2004) and Great Plains (Higgins *et al.*, 1997). LLJs generally occur in the warm season (Gimeno *et al.*, 2016) although some are prevelant all year round (*e.g.* Turkana LLJ, Nicholson, 2016).

Integrating $E-P$ across ocean basins and including the contribution from rivers (runoff, R) gives the net freshwater flux for the oceans: $E - P - R$ (evaporation minus precipitation minus runoff), which can be calculated from both atmospheric and oceanographic data (see chapter 3). Runoff can be calculated either directly from observations of river streamflow (Baumgart-

[1]defined by Bonner (1968) as maximum wind speed exceeding 12 m/s and decreasing by at least 6 m/s within the bottom 3 km of the atmosphere

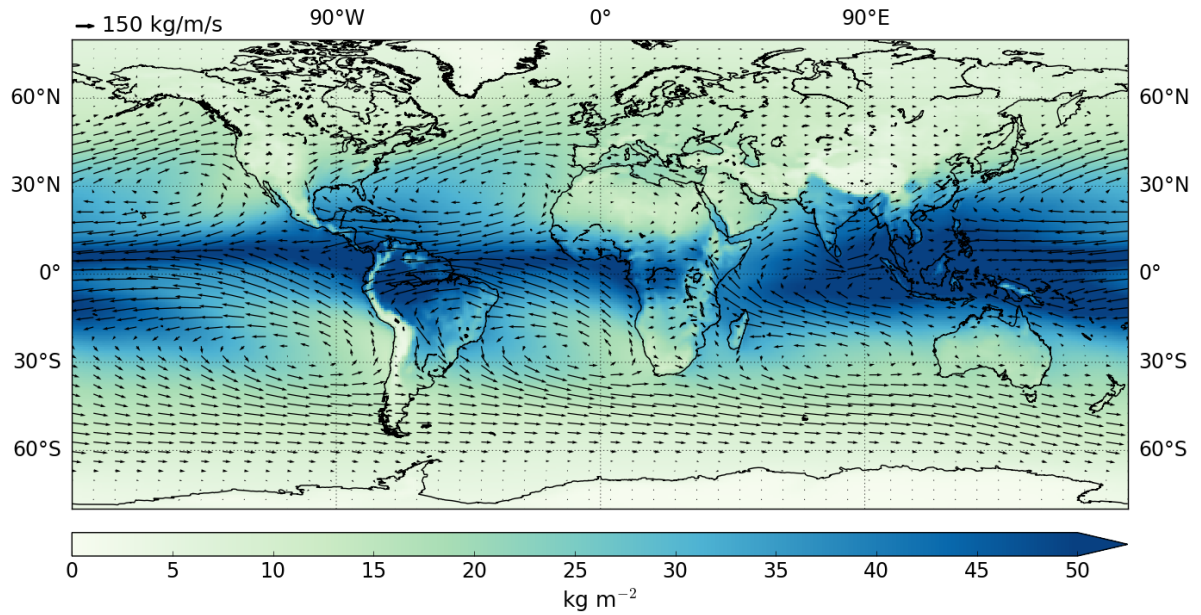

Figure 1.5: Annual mean (1979-2014) ERA-Interim total column water vapour (colours) and vertically-integrated moisture fluxes (arrows - see top left for scale).

ner and Reichel, 1975; Clark *et al.*, 2015) or inferred from net precipitation over land (Dai and Trenberth, 2002). Across the global ocean there is approximately 13 Sv (1 Sv $\equiv 10^9$ kg s^{-1} $\equiv 10^6$ m^3 s^{-1}) evaporation and 12 Sv precipitation (Trenberth *et al.*, 2007) with runoff making up the 1 Sv imbalance between oceanic E and P. The existence of an asymmetry in the basin-scale $E - P - R$ between the Atlantic and Pacific Oceans has been discussed in previous studies (Broecker, 1991; Rahmstorf, 1996) where the Atlantic is a net evaporative basin and the Pacific has been estimated to have $E - P - R$ closer to zero or have a weak surplus of precipitation and runoff (Talley, 2008). The Indian Ocean has net evaporation of similar value to the Atlantic Ocean (Ganachaud and Wunsch, 2003).

The most studied regions of the atmospheric moisture budget asymmetry are the subpolar oceans (Warren, 1983; Emile-Geay *et al.*, 2003; Czaja, 2009; Wills and Schneider, 2015) as this is relevant for the asymmetry in MOC and deep water formation (see section 1.2). Both subpolar regions have an excess of P over E but this is stronger for the subpolar Pacific (Emile-Geay *et al.*, 2003). This was initally shown by Warren (1983) (estimated from maps but later confirmed using gridded datasets by Emile-Geay *et al.*, 2003) to be due to greater area-averaged Atlantic evaporation and similar area-averaged precipitation rates in the two basins. The inter-basin contrast in evaporation rates is a direct consequence of enhanced northward heat transport from the AMOC increasing subpolar Atlantic sea surface temperatures (SSTs) (Warren, 1983). It is currently unclear whether this holds at basin scale for the Atlantic and Pacific. Some authors (*e.g.* Weijer *et al.*, 1999) suggest that basin-scale Atlantic evaporation is greater due to the

AMOC thus resulting in the contrast in $E - P$, and therefore SSS, between the Atlantic and Pacific. In chapter 3 (Craig *et al.*, 2017) the main component (E, P or R) of the moisture budget asymmetry at basin-scale will be determined.

The moisture budget asymmetry is often explained (at basin scale) by atmospheric moisture transport as the atmosphere exports more moisture from the Atlantic to the Pacific in the trade winds across Central America (Figure 1.5) than is imported to the Atlantic across Africa (Weyl, 1968; Broecker, 1991; Zaucker and Broecker, 1992; Schmittner *et al.*, 2011; Singh *et al.*, 2016). This is considered to be a result of lower orography along Central America than Africa and gaps in the Central American mountain range which facilitate strong moisture transport (Xu *et al.*, 2005). The Isthmus of Panama is often stated as the primary location for Atlantic to Pacific moisture transport (Dietrich, 1963; Zaucker and Broecker, 1992; Leduc *et al.*, 2007), despite being only a narrow gap in the mountains. This interpretation, however, ignores all the other moisture fluxes surrounding the drainage basins of the Atlantic and Pacific Oceans and also assumes that the moisture crossing Central America only has origin from the Atlantic Ocean, ignoring any remote sources. Atmospheric moisture transport will be the primary focus of this thesis with these issues addressed in chapter 4 and 5 respectively.

1.1.3 Link between salinity and moisture fluxes

Sea surface salinity is known to be strongly affected by the hydrological cycle and this has been the subject of much study (*e.g.* Bingham *et al.*, 2012; Ren *et al.*, 2014; Yu *et al.*, 2017). Salinity in the mixed layer evolves subject to the following equation (*e.g.* Delcroix *et al.*, 1996):

$$\frac{\partial S}{\partial t} = \frac{S_0(E-P)}{h} - \mathbf{u} \cdot \nabla S - w\frac{\partial S}{\partial z} - \Gamma(w_e)(S - S_b) \tag{1.1}$$

where h is the mixed layer thickness, $\mathbf{u}$ is the horizontal velocity vector, w is the vertical velocity, Γ is the Heaviside function[2], w_e is the entrainment velocity, S_b is salinity just below the base of the mixed layer and z is the vertical co-ordinate. The first term on the right-hand side represents the surface forcing, the second term represents horizontal advection, the third term represents vertical advection and the fourth term represents entrainment. Only the surface forcing term is linked to the hydrological cycle. The link between the hydrological cycle and SSS is evident when comparing Figures 1.1 and 1.4. Areas of high salinity (the subtropics) cor-

[2]The Heaviside function is a step function such that entrainment is only considered when the mixed layer deepens Kraus and Turner (????).

respond to areas of net evaporation ($E - P > 0$) and areas with lower salinities (beneath the ITCZ and subpolar regions) correspond to areas with net precipitation ($E - P < 0$). Equivalently, in equation (1.1) the surface forcing term in equation (1.1), a net loss of water from the surface of the ocean causes an increase in salinity ($\frac{\partial S}{\partial t} > 0$) and a net gain of water at the surface results in a decrease in salinity ($\frac{\partial S}{\partial t} < 0$). Note that salinity minima do not correspond exactly to minima in $E - P$. Tchilibou *et al.* (2015) showed that Ekman transport of salt causes the SSS minima to be located north of the ITCZ in both the Atlantic and Pacific, with the SSS minimum caused by the South Pacific Convergence Zone offset to the south. This is represented by horizontal advection of salt, the second term in equation (1.1).

Due to the close relation between SSS and $E - P$ some authors have attempted to use SSS as a 'rain gauge' for the ocean (e.g. Ren *et al.*, 2014) due to problems with remotely observing precipitation and evaporation. Yu (2011) used the rain gauge concept to show that $E - P$ dominates the seasonal cycle of mixed layer salinity in regions where heavy precipitation occurs (*e.g.* Atlantic/Pacific ITCZ). In other regions Ekman transport of salt or entrainment dominate the seasonal cycle of mixed layer salinity. The signature of $E - P$ on large scale SSS patterns is only identifiable in long term climatologies (see chapter 4) *e.g.* Durack and Wijffels (2010) showed that changes to basin-averaged Atlantic and Pacific SSS are consistent with observed changes in the hydrological cycle.

1.2 Atlantic Meridional Overturning Circulation

Another important difference between the Atlantic and Pacific Oceans is the existence of a deep meridional overturning circulation (MOC) in the Atlantic but not in the Pacific. Figure 1.6 shows a simplified illustration of the global overturning circulation from Talley (2013). In the Atlantic mass is transported northward in the upper ocean before sinking in the high latitude North Atlantic and returning south in a deep western boundary current before upwelling in the Southern Ocean. The circulation in the North Pacific, however, is more isolated from the rest of the global circulation with only a weaker connection to upper ocean transport in the rest of the Pacific. The Atlantic, Pacific and Indian Oceans are all connected through the Antarctic Circumpolar Current (ACC) which receives deep water from all three oceans and provides them with Antarctic Bottom Water and intermediate water.

The asymmetry in MOC is linked to the SSS asymmetry as the subpolar Atlantic has high enough SSS to permit deep convection but subpolar Pacific SSS is too fresh (Warren, 1983).

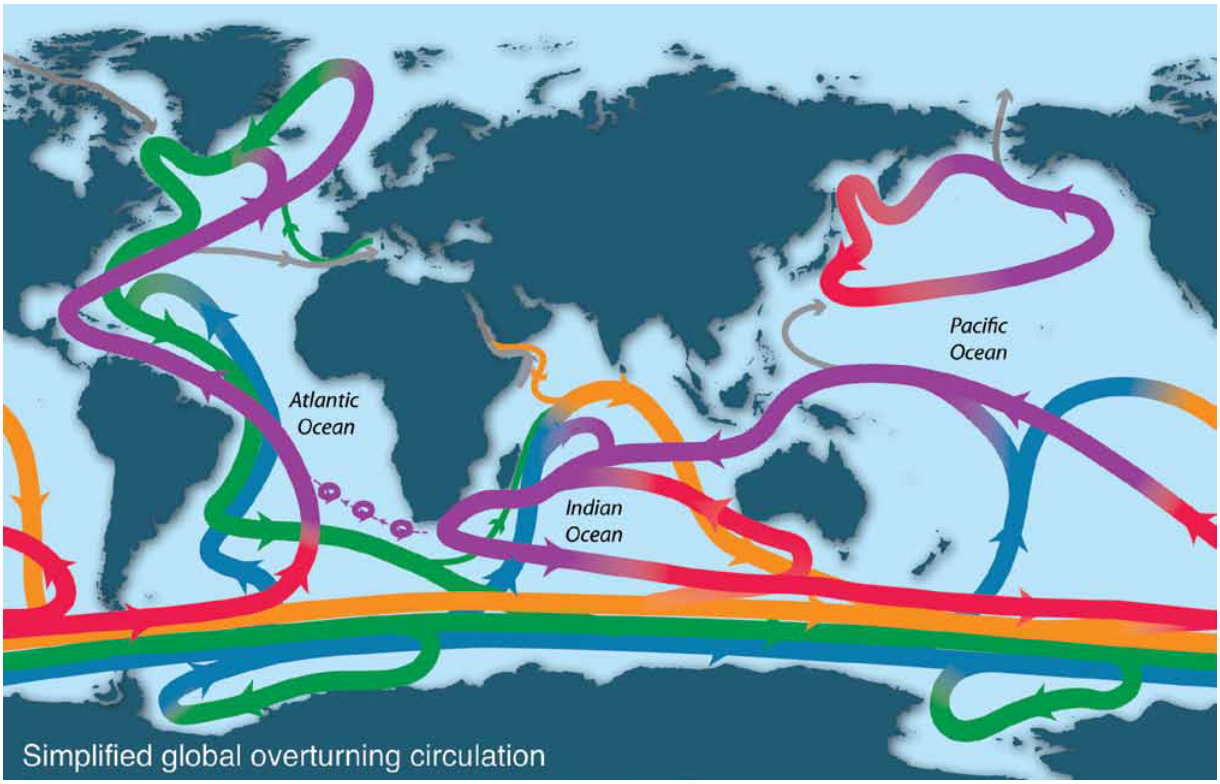

Figure 1.6: Simplified schematic of the overturning circulation from a Southern Ocean perspective from Talley (2013). Purple = upper ocean and thermocline. Red = denser thermocline and intermediate water. Orange = Indian Deep Water and Pacific Deep Water. Green = North Atlantic Deep Water. Blue = Antarctic Bottom Water. Grey = Bering Strait components and Mediterranean and Red Sea inflow.

Deep convection is the process by which surface water comes into contact with water from far below the surface. It occurs only during winter in very specific locations: the Labrador Sea, Greenland Sea and the Gulf of Lions in the northwestern Mediterranean Sea (Marshall and Schott, 1999). The cold wintertime air temperatures are required to generate sufficient surface buoyancy loss to increase water density enough for convection to occur.

Deep convection does not occur anywhere in the Pacific Ocean or its marginal seas. This is because the surface water is too fresh and its salinity cannot be increased enough sink to great depths (Warren, 1983) and the sub-surface water in the North Pacific is strongly stratifed (Talley, 2013). North Pacific Intermediate Water (NPIW) is formed in the Okhotsk Sea through brine rejection (Talley, 1991) and enters the North Pacific in the Oyashio-Kuroshio confluence region (Talley, 1993). NPIW is the only water mass formed through surface ventilation in the Pacific Ocean. Deep water can form in the Pacific Ocean, but not through surface ventilation. Instead, Pacific Deep Water (PDW) is formed through diapycnal mixing (Talley, 2013) and upwelling of bottom waters from the Southern Ocean. In the abscence of deep convection, the

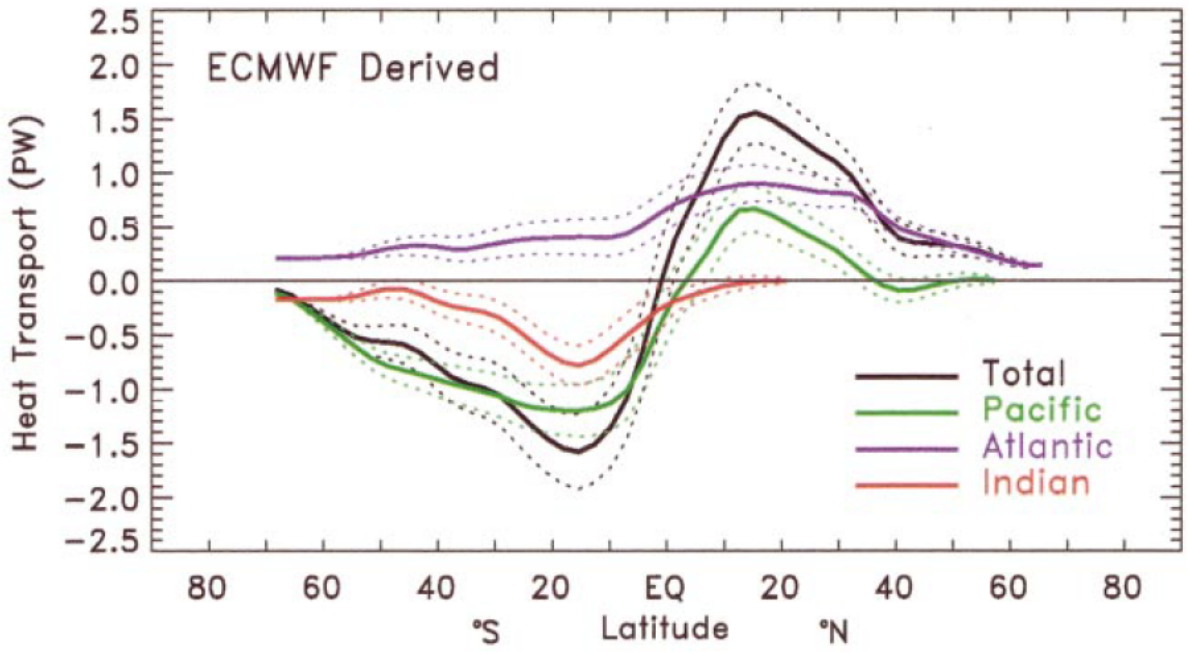

Figure 1.7: Zonal mean ocean heat transports in the global (black), Atlantic (purple), Pacific (green) and Indian (red) Oceans from Trenberth and Caron (2001). These are "implied" ocean transports from residually derived surface fluxes from the European Centre for Medium Range Weather Forecasts (ECMWF) reanalysis data for February 1985 to April 1989. The dashed lines represent error bars of 1 standard deviation. Units are petawatts (1 PW $\equiv 10^{15}$ W). ©American Meteorological Society. Used with permission.

circulation in the North Pacific is primarily wind-driven Ekman transport in a shallow overturning cell and gyre circulation with a western boundary current (Talley, 2003).

Another key difference between the Atlantic and Pacific Oceans which is an important part of the Atlantic MOC (AMOC) is the ocean heat transport. The ocean is expected to transport heat from regions where heat in gained (tropics) to regions where heat is lost (midlatitudes) at the surface. This is indeed the case for the Pacific and Indian Oceans but not for the southern Atlantic. Trenberth and Caron (2001) showed, using surface fluxes from a reanalysis product, that heat transport in the Atlantic Ocean is northwards at all latitudes but poleward in both hemispheres in the Pacific (Figure 1.7). In the North Atlantic, substantially more heat is lost to the atmosphere than in the North Pacific (Talley, 2003) resulting in northward heat transport in the Atlantic as part of the AMOC. In the South Atlantic, heat is transported up a large scale temperature gradient (SSTs increase towards equator) and is converged into the North Atlantic with a cross-equatorial transport of 0.5 PW (1 PW $\equiv 10^{15}$ J s^{-1}) (Buckley and Marshall, 2016).

The AMOC has also been referred to as the Thermohaline Circulation which suggests it is purely driven by fluxes of heat and salt, but this has been the subject of some debate. Wunsch (2002) argued that the mass flux of the ocean is primarily wind-driven and that surface buoy-

ancy fluxes are neccessary but are not the primary drivers of the ocean's circulation. However, Saenko *et al.* (2002) found, using a coupled atmosphere-ocean climate model, that thermal forcing is the dominant driving force of the AMOC and that the Thermohaline Circulation compensates for net Atlantic evaporation.

The existence of the AMOC and its enhanced northward ocean heat transport has often been linked to the milder wintertime temperatures across western Europe compared to north-eastern North America (Broecker, 1997; Latif *et al.*, 2000). However, Seager *et al.* (2002) showed that this temperature contrast is expected as north-westerly winds advect cold, continental air towards north-eastern North America and south-westerly winds advect warm, maritime air towards western Europe. Seager *et al.* (2002) also showed that a dynamic ocean is not required for this temperature contrast to exist as the interaction between the atmospheric circulation with the ocean's mixed layer results in seasonal release of heat stored in the ocean.

Nevertheless, the AMOC is a very important feature of the northern hemisphere's climate. Climate models show that the AMOC will weaken in the 21st century, but disagree on the strength of the decline (Cheng *et al.*, 2013). Further into the future, the AMOC may continue to weaken if global temperatures continue to rise and anthropogenic emissions are not decreased (Bakker *et al.*, 2016). Jackson *et al.* (2015) showed that a weaker AMOC has several impacts, including a widespread cooling of the northern hemisphere and a stronger North Atlantic storm track.

A warming climate is also expected to affect the hydrological cycle *i.e.* "wet-get-wetter, dry-get-drier" (Held and Soden, 2006). The asymmetry between the Atlantic and Pacific atmospheric moisture budgets is therefore expected to increase and, as a result, the SSS asymmetry would do the same (Levang and Schmitt, 2015). Atmospheric moisture transport across Central America is projected to increase with warming (Levang and Schmitt, 2015; Singh *et al.*, 2016) which Singh *et al.* (2016) found to be a result of increased transport distances rather than changes to evaporation. It should be noted that in the "wet-get-wetter, dry-get-drier" scenario increased precipitation does not follow Clausius-Clapeyron scaling ($\sim 7\%\,\mathrm{K}^{-1}$) and instead models show increases of $1-2\%\,\mathrm{K}^{-1}$ (Stephens and Ellis, 2008). The Clausius-Clapeyron relation,

$$\frac{\mathrm{d}\ln e_s}{\mathrm{d}T} = \frac{L}{RT^2}, \tag{1.2}$$

describes how saturation vapour pressure, e_s, changes with temperature, T, where L is the latent heat of vapourization and R is the gas constant. This is due to the "energetic constraint"

where the intensity of the hydrological cycle is controlled by capability of the troposphere to radiate away latent heat released by precipitation rather than the availability of moisture (Allen and Ingram, 2002).

There is observational evidence for an increased SSS asymmetry consistent with an intensified hydrological cycle (Durack and Wijffels, 2010; Skliris *et al.*, 2014). Both these studies show that the SSS asymetry also amplifies between the subpolar Atlantic and Pacific, but model projections by Levang and Schmitt (2015) suggest that subpolar Atlantic SSS will decrease. Increased subpolar Atlantic SSS would suggest increased deep convection and a stronger AMOC, but the opposite for decreased subpolar Atlantic SSS. The intensified hydrological cycle would also leads to increased tropical Atlantic SSS (Levang and Schmitt, 2015) which have been associated with increased moisture transport across Central America (Wang *et al.*, 2013). Northward advection of positive SSS anomalies may then offset lower subpolar SSS and act to restore the strength of the AMOC (Wang *et al.*, 2013).

Atmospheric moisture transport across Central America has also been linked to the SSS and MOC asymmetries in Paleoclimate studies. For example, Leduc *et al.* (2007) used various proxies to link Dansgaard-Oeschger events (spells of rapid warming in the last glacial period) and Heinrich events (large collapses of the North American ice sheet into the Atlantic) to millenial-scale fluctuations in sea surface salinity of 2-4 psu in the equatorial East Pacific. Leduc *et al.* (2007) suggested that the Atlantic ITCZ shifted southward thus reducing atmospheric moisture transport to the Pacific which increased Pacific SSS and decreased Atlantic SSS, resulting in a weaker AMOC. However, it should be noted that these findings are based on proxy data which have large uncertainties associated with them.

This thesis will not specifically focus on the AMOC and the MOC asymmetry, but the link between the MOC asymmetries and the moisture budget and SSS asymmetries cannot be overlooked. Ultimately the moisture budget asymmetry and the associated atmospheric moisture transports will be linked to the current understanding of the MOC asymmetry but a detailed study of the MOC asymmetry will not be provided here. For more indepth discussion of the AMOC see the review by Buckley and Marshall (2016) and for the MOC asymmetry see Ferreira *et al.* (2018).

1.3 Reasons for the Atlantic/Pacific asymmetries

1.3.1 Basin Geometries

The relative shapes and sizes of the Atlantic and Pacific Oceans has been suggested by several authors as the reason for the asymmetry in salinity, moisture budget and MOC (Schmitt *et al.*, 1989; Ferreira *et al.*, 2010; Nilsson *et al.*, 2013). The Atlantic Ocean is approximately half the size of the Pacific Ocean with the Atlantic comprising of approximately 23% of the global ocean and the Pacific 46% (Talley *et al.*, 2011) where the global ocean covers approximately 71% of the surface of the Earth. The Atlantic, however, extends further north and has more important marginal seas than the Pacific which is bounded in the north by the Bering Strait.

The differing widths of the two basins is thought to affect the hydrological cycle via the stationary wave patterns (Wills and Schneider, 2015) and the fetch of the storm tracks (Ferreira *et al.*, 2010). Schmitt *et al.* (1989) suggested that the narrower North Atlantic contributes to the overall net evaporative nature of the Atlantic because a greater fraction of the surface area is crossed by dry air from the neighbouring continents.

Ferreira *et al.* (2010) showed that the relative widths of the basins play a role in the Pacific/Atlantic asymmetries. When the zonal mean temperature and salinity properties of a narrow ocean basin are swapped with the zonal mean properties of a wider, fresher basin, deep water will form in the northern region of the wider basin. However, atmospheric moisture export from the narrow basin is still stronger than from the wide basin. The narrow basin therefore eventually becomes more saline again and deep water formation returns to its northern regions, highlighting the role of atmospheric moisture transport in the Atlantic/Pacific SSS/MOC asymmetries.

By altering the extent of continents in an aquaplanet, Nilsson *et al.* (2013) showed the effect of the wind field on the Atlantic/Pacific asymmetries. When an Africa-like continent terminates close to the zero-wind line in the Southern Hemisphere, deep water formation is localized to a narrow Atlantic-like basin due to westward Sverdrup transport of salt into the narrow basin. When the Africa-like continent extends further south, salinification of the narrow basin is controlled by atmospheric moisture transport.

1.3.2 Land features

Another potential factor in setting asymmetries between the Atlantic and Pacific Oceans is the features of the continents surrounding each basin, specifically the orography and ice sheets. The drainage basins of the two basins are separated by the Rocky Mountains and the Andes which are confined to the west of the North and South American continents. The peaks of the Rockies are consistently at least 2000 m above sea level and the Andes are often in excess of 4000 m above sea level (Figure 2.12).

The Rocky Mountains are known to deflect the westerly flow in the midlatitudes causing the tilt in the North Atlantic storm track (Brayshaw *et al.*, 2009) and the Andes act as a barrier to prevent moisture transport from Atlantic to Pacific in the tropics when the ITCZ shifts south (Leduc *et al.*, 2007). On the Asian continent the major orographic features are the Himalayas and the Tibetan plateau which play a role in the Asian monsoon through land-sea temperature contrasts (Hahn and Manabe, 1975) and in shaping the North Pacific storm track (Saulière *et al.*, 2012). However, the Mongolian mountains to the north, despite their lesser altitudes, have been found to have a greater impact on the North Pacific storm track (White *et al.*, 2017).

In the Southern Hemisphere, Antarctica is almost completely covered by two ice sheets (East and West). Schmittner *et al.* (2011) showed that the atmosphere above is at least 20°C cooler when the ice sheet is present compared to a model set-up where it is removed. In the absence of the Antarctic ice sheets the meridional temperature gradient is reduced, weakening the southern hemisphere westerlies which also shift equatorward by about 10° latitude. This results in a similar shift of the upwelling of Antarctic Bottom Water in the Southern Ocean which decreases AMOC strength as Agulhas leakage of salty Indian Ocean water around Africa is restricted (Schmittner *et al.*, 2011).

Using coupled ocean-atmosphere models, Schmittner *et al.* (2011) and Sinha *et al.* (2012) investigated changing the height of the orography to find any impacts on the global ocean circulation. They found that the strength of the AMOC increases with higher orography but in a completely flat world deep water forms in the North Pacific instead of the North Atlantic. This is due to changes in the salinity of each basin where the North Atlantic is approximately 4 psu less saline with flat continents and the North Pacific is 2-3 psu more saline (Sinha *et al.*, 2012). With higher orography, atmospheric moisture transport from Pacific to Atlantic is reduced in the midlatitudes but the trade winds still transport moisture from the Atlantic to Pacific across Central America. The total moisture transport across Central America is not affected much by

changing the orography as increased flow across higher orography is compensated by broader and deeper flow across smoothed orography (Xu *et al.*, 2005).

1.3.3 Multiple Equilibria

It is possible to find different stable states of the overturning circulation, known as multiple equilibria, using a hierarchy of models from a simple box model (Stommel, 1961) to a general circulation model (GCM) with idealized geometry (Marotzke and Willebrand, 1991) to a GCM with realistic geometry (Huisman *et al.*, 2012). Changing the salinities or temperatures of two connected oceans in these models alters the strength of the overturning circulation such that the system will jump into different equilibrium states, a phenomena known as hysteresis.

Marotzke and Willebrand (1991) found four different stable states of operation: "northern sinking" where deep water forms in the northen hemisphere in both basins; "southern sinking" where deep water forms in the southern hemisphere in both basins; "conveyor" which is most similar to the observed present-day circulation; and "inverse-conveyor" where deep water forms in the north of a large, Pacific-like basin but not in a narrower, Atlantic-like basin. Therefore each hemisphere can operate in two states, either with high latitude deep water formation or without any at all. If all combinations of these two states are possible in each basin hemisphere then there should be 16 different steady states. However, Marotzke and Willebrand (1991) only found the 4 steady states referred to above.

Huisman *et al.* (2009) and Kamphuis *et al.* (2011) argue that the existence of a present-day conveyor is likely due to interbasin asymmetries determining a preference for a particular state. Reversing external asymmetries can still result in a conveyor state similar to the present-day AMOC (Kamphuis *et al.*, 2011; Huisman *et al.*, 2012). For example, reversing the SSS asymmetry can still result in two stable states (inverse conveyor and weak conveyor) as shown by Huisman *et al.* (2012). It is further suggested by Huisman *et al.* (2012) that continental asymmetries, rather than the freshwater flux asymmetry, play a role in the preference for North Atlantic sinking. However, the continental asymmetries described in section 1.3.1 influence the atmospheric branch of the hydrological cycle and therefore the atmospheric moisture budgets of the ocean basins (Ferreira *et al.*, 2010; Wills and Schneider, 2015). This hints at a strong coupling between the various Pacific/Atlantic asymmetries.

1.3.4 Ocean Transport and Dynamics

Ocean transports of heat, freshwater and salt have also been noted to play an important role in the asymmetries between the Atlantic and Pacific. In particular, the subpolar asymmetries have been studied in some detail. Warren (1983) found that the tilted zero wind stress curl line in the North Atlantic, separating the subtropical and subpolar gyres, permits stronger salt advection from the high salinity subtropics into the subpolar North Atlantic than in the Pacific. Emile-Geay *et al.* (2003) drew similar conclusions with updated datasets. Czaja (2009) investigated the temporal behaviour of the North Atlantic and North Pacific jet streams finding the North Atlantic jet to be more variable than its Pacific counterpart which means that salt is transported more efficiently across the intergyre boundary in the North Atlantic. Additionally, Czaja (2009) showed that the intergyre boundary coincides with the $E - P = 0$ line in the North Atlantic but is poleward of the North Pacific $E - P = 0$ line. Therefore, water parcels in the North Pacific experience freshening due to net precipitation before crossing the intergyre boundary and water parcels of low salinity compared to the North Atlantic are advected into the North Pacific subpolar gyre.

The Agulhas current, a western boundary current in the southern Indian Ocean, is thought to affect Atlantic salinity and AMOC strength (Weijer *et al.*, 1999; Beal *et al.*, 2011) through "Agulhas leakage" where warm and salty thermocline waters enter the South Atlantic around the Cape of Good Hope. Weijer *et al.* (1999) demonstrated that heat and salt fluxes act to strengthen the AMOC and that the wind-driven circulation across 30°S is very important for the heat and salt budgets of the Atlantic.

Although precipitation is largely driven by evaporation Shoshiro *et al.* (2008) showed how ocean dynamics can influence precipitation. Sharp SST gradients in the Gulf Stream cause atmospheric pressure adjustments in the marine boundary layer which leads to surface wind convergence. Resulting ascending motion leads to a narrow band of precipitation which is anchored to the Gulf Stream by the surface wind convergence. Shoshiro *et al.* (2008) also speculated on how this phenomena is linked to the AMOC, of which the Gulf Stream is the upper limb, suggesting that future changes to the AMOC strength would affect precipitation patterns and tropospheric circulation due to the Gulf Stream's influence on the troposphere.

1.4 Research questions

As a clear asymmetry between the atmospheric moisture budgets of the Atlantic and Pacific Oceans exists and this must be balanced by differences in the atmospheric moisture fluxes entering and leaving the ocean drainage basins. It is therefore important to understand which of these fluxes have the strongest influence on the atmospheric moisture budget asymmetry with regards to moving towards a better understanding of the link between the atmospheric hydrological cycle and the SSS and MOC asymmetries. The main topic of this thesis is:

Why do persistent asymmetries between the atmospheric moisture budgets of the Atlantic, Pacific and Indian Oceans exist?

Overall, this research aims to provide a detailed understanding of the relative contributions of moisture which has 'origin' in each ocean basin to the moisture budgets of each basin with an emphasis on the Atlantic and Pacific SSS asymmetry. The following research questions will be addressed:

1. Can the basin-scale asymmetry in $E-P-R$ be attributed to an asymmetry in evaporation, precipitation or runoff?
2. How are the mean state and interannual variability of the basin-integrated atmospheric moisture budgets related to the time average and variability in moisture fluxes across the boundaries between the basins?
3. Which atmospheric moisture fluxes, partitioned into ocean drainage basins of origin, are dominant in influencing the moisture budget asymmetry?
4. Which dynamical processes are most important in transporting moisture to influence the moisture budget asymmetry?

Questions 1 and 2 will be addressed in chapters 3 and 4 respectively using ERA-Interim data and the final two questions will be addressed in chapter 5 using an airmass trajectory model with supporting information from chapter 4.

1.5 Overview

This thesis consists of seven chapters. In chapter 2 the various datasets and methodology used in this study will be described. In chapter 3 the asymmetry in salinity and moisture budgets between the Atlantic and Pacific Oceans will be discussed with a view to finding the dominant part of the asymmetry: evaporation, precipitation or runoff, thus answering question 1. In chapter 4 the mean state and interannual variability of the inter-basin moisture transports will be discussed along with their link to salinity. Chapter 5 will apply the trajectory model to partition the moisture fluxes on the boundaries between ocean drainage basins into their origin basins with a view to finding the dominant transports in setting the asymmetries in moisture budget and salinity between the Atlantic and Pacific. Conclusions will be drawn in chapter 6 along with suggestions for future work.

Chapter 2

Data and Methods

In this chapter, section 2.1 describes the various datasets used in chapters 3-5, section 2.2 discusses Eulerian and Langrangian perspectives of understanding atmospheric transport and introduces the trajectory model, and section 2.3 describes how the ocean drainage basins were defined.

2.1 Datasets

2.1.1 ERA-Interim

Throughout this thesis, the Interim European Centre for Medium-Range Weather Forecasts (ECMWF) Reanalysis (ERA-Interim) will be used (Dee *et al.*, 2011). ERA-Interim covers the time period from January 1st 1979 to present with the 36-year period spanning 1979-2014 used in this research. This reanalysis product uses the ECMWF forecast model (Integrated Forecasting System; IFS) which has three fully coupled components for the atmosphere, land surface and ocean waves. The atmospheric component of the IFS has a spectral dynamical core with a hybrid η vertical co-ordinate (Simmons and Burridge, 1981). The model has a T255 horizontal resolution on a reduced Gaussian grid ($\sim$79 km grid spacing) and 60 vertical levels. ERA-Interim uses a 4D-VAR data assimilation scheme with 12-hourly analysis cycles which combine observations with prior information from the model.

ERA-Interim data in two different formats is used in this thesis. Spectral data output by the ECMWF model and transformed onto a reduced Gaussian grid and on the 60 hybrid model levels is used by a Lagrangian trajectory model in chapter 5. Data interpolated to an N128 full Gaussian grid ($0.75^\circ \times 0.75^\circ$ horizontal resolution) and 37 unevenly spaced pressure levels

from 1000 hPa to 1 hPa are also used in chapter 5. Vertical integrals on the full Gaussian grid are used in chapters 3 and 4. Accumulated (time-integrated) surface variables are used in chapter 3. Note that pressure level parameters are provided every 6 hours and surface parameters are provided every 3 hours.

2.1.2 Dai and Trenberth runoff

In chapter 3, an estimate of global continental freshwater discharge from rivers into the oceans from Dai and Trenberth (2002) is used. This estimate used streamflow data from several different organizations for the 921 largest rivers in the world. The farthest downstream (closest to the river mouth) gauge stations were used and the streamflow data extrapolated to the river mouth using the ratio betwen the simulated flow at the farthest downstream station and the simulated flow at the river mouth from a river transport model (RTM). The RTM was used to route runoff in 0.5° cells towards the ocean and continental discharge was estimated by summing then simulated river outflows within each 1° latitude zone.

This dataset increased total global continental discharge by 18.7% and the total drainage area covered by 20.4% in comparison to previous estimates. The 921 rivers now cover 68% of drainage areas. Dai and Trenberth (2002) estimated the total discharge to be 37288$\pm$662 km^3 yr^{-1} or 1.18$\pm$0.02 Sv (excluding Antarctica) which is 7% of global precipitation and 35% of terrestrial precipitation (excluding Antarctica and Greenland). This dataset is available online from the National Center for Atmospheric Research's (NCAR) Climate Analysis Section catalogue (http://www.cgd.ucar.edu/cas/catalog/). This dataset has been used in calculating ocean freshwater transport (Dai and Trenberth, 2003; Schanze *et al.*, 2010) and for forcing an ocean model (Valdivieso *et al.*, 2014). In chapter 3 it is used to complete the net freshwater flux ($E - P - R$) with $E - P$ from ERA-Interim and the result is compared to other estimates of $E - P - R$.

2.1.3 GPCP

The Global Precipitation Climatology Project (GPCP, Adler *et al.*, 2003) estimate of precipitation is used in chapter 3. GPCP is a merged dataset using both satellite and rain gauge data which provides rain rates on daily and monthly time frames at 1°$\times$1° and 2.5°$\times$2.5° horizontal resolutions respectively. Various types of satellite data are included in the GPCP estimate, such as the microwave-based Special Satellite Microwave Imager (SSM/I), a geosynchronous infrared (IR)

based technique relating cloud-top area to rain rate, the Television and Infrared Observational Satellite (TIROS) Operational Vertical Sounder (TOVS) instruments which infer precipitation from deep clouds, and low-orbit outgoing longwave radiation (OLR) observations. The TOVS and OLR estimates were added in version 2 (Adler *et al.*, 2003). Different merging techniques were used over different time periods as no microwave estimates were available before 1987 (Adler *et al.*, 2003), but version 2.1 included a longer recalibration of the OLR precipitation index (OPI) to SSM/I-based estimates (Huffman *et al.*, 2009). The introduction of SSM/I data in 1987 caused a discontinuity in the dataset (Adler *et al.*, 2003). In chapter 3, monthly means of version 2.1 of GPCP (Huffman *et al.*, 2015) are used on a $1^\circ \times 1^\circ$ latitude-longitude (interpolated from the $2.5^\circ \times 2.5^\circ$ grid) grid to compare to the interannual variability of ERA-Interim precipitation over the oceans.

2.1.4 ECCOv4

In chapter 3 the Estimating the Circulation and Climate of the Ocean' project version 4 (ECCOv4; Forget *et al.*, 2015) is used to calculate the freshwater divergences in volumes of the ocean. ECCOv4 uses an adjoint method at $\sim 1^\circ$ resolution with the Massachusetts Institute of Technology general circulation model (MITgcm) to fit the time-evolving (1992-2016) ocean state to various observations (Argo, satellites, WOCE etc.). Some variables, such as wind stress, are used from ERA-Interim to calculate air-sea fluxes and adjusted as part of the optimization procedure to fit the modelled trajectory to ocean observations.

2.1.5 SODA 3.4.2

In chapter 4 SSS from the Simple Ocean Data Assimilation (SODA) version 3.4.2 dataset (Carton *et al.*, 2018) is used to assess the statistical relationship between the interannual variability of atmospheric moisture transport between ocean drainage basins and ocean salinity. SODA 3.4.2 is based on the NOAA Geophysical Fluid Dynamics CM2.5 coupled model at 0.25° horizontal resolution with 50 vertical levels and assimilates data from the World Ocean Atlas as well as both in-situ and satellite SST observations. The assimilation procedure involved a linear deterministic sequential filter which constructs the ocean state from the forecast based on the difference between observations and forecast. It is forced by ERA-Interim at the surface with the COARE4 (Coupled Ocean-Atmosphere Response Experiment version 4; Fairall *et al.*, 2003) bulk formula.

2.2 Trajectory modeling

This section describes the Eulerian and Lagrangian approaches to atmospheric modeling, as well as highlighting the difference between trajectory models and Lagrangian models, before describing the ROTRAJ model.

2.2.1 Eulerian perspective

The Eulerian approach to modelling atmospheric transport investigates the atmospheric flow at fixed points in space throughout a time period. An Eulerian model determines how the flow evolves in time across the spatial domain. The 3D velocity field in an Eulerian model is therefore defined as

$$\mathbf{U} = (u(x, y, z, t), v(x, y, z, t), w(x, y, z, t)) \tag{2.1}$$

where u, v and w are the horizontal and vertical velocity components, x, y and z are locations in the horizontal and vertical, and t is time. Eulerian flow is often depicted graphically by streamlines (lines everywhere tangent to the velocity field at time t). From an Eulerian perspective, location and time are independent variables.

2.2.2 Lagrangian perspective

When applying the Lagrangian perspective to study atmospheric transport the atmosphere must be considered as a collection of air parcels. In a Lagrangian model the 3D velocity field is considered as :

$$\mathbf{U} = (u(t) = x'(t), v(t) = y'(t), w(t) = z'(t)), \tag{2.2}$$

i.e. the rate of change of location over time t. Lagrangian flow is depicted graphically as a pathline or trajectory calculated by integrating:

$$\frac{\mathrm{d}\mathbf{x}(t)}{\mathrm{d}t} = \mathbf{U}(\mathbf{x}(t), t), \tag{2.3}$$

with initial condition $\mathbf{x}(t_0) = \mathbf{x}_0$. Note that in Lagrangian flow the location of each air parcel, $\mathbf{x}(t)$, is dependent on time.

The Lagrangian or material derivative is defined as

$$\frac{D\zeta}{Dt} = \frac{\partial\zeta}{\partial t} + \mathbf{U} \cdot \nabla\zeta, \tag{2.4}$$

i.e. the rate of change of some variable ζ. The Lagrangian derivative is a combination of the Eulerian rate of change (first term on right-hand side, equation (2.4)) and advection of ζ by the velocity field (second term on right-hand side, equation (2.4)).

A trajectory model makes a kinematic (velocity and density are prescribed as an external input) calculation by integrating equation (2.3) backwards or forwards in time from gridded model data. This can be done either from model output (*i.e.* "offline") or calculated during the integration of a numerical weather prediction (NWP) model (*i.e.* "online"). Trajectories have many uses in atmospheric science, such as studying the history of atmospheric composition (Fleming *et al.*, 2012), studying Foehn winds (Würsch and Sprenger, 2015) and attributing moisture origins (Sodemann *et al.*, 2008). A Lagrangian model, however, solves the equations following trajectories (*e.g.* Cain *et al.*, 2012). This thesis applies the former approach, which is a Lagrangian diagnostic rather than a Lagrangian model.

2.2.3 ROTRAJ Trajectory model

This study uses the Reading Offline Trajectory (ROTRAJ) model (Methven, 1997). This model can calculate both forward and backward trajectories from atmospheric reanalyses. As the model is "offline" the equations of motion are not integrated in the trajectory calculations, instead the model integrates the trajectory equation,

$$\frac{D\mathbf{x}}{Dt} = \mathbf{U}(\mathbf{x}, t), \tag{2.5}$$

backward or forward in time using the 4th order 4-stage Runge-Kutta method. This method evaluates the velocity field at four points for each time-step n:

$$k_1 = u(t_n, x_n)\Delta t \tag{2.6}$$

$$k_2 = u(t_n + \frac{\Delta t}{2}, x_n + \frac{k_1}{2})\Delta t \tag{2.7}$$

$$k_3 = u(t_n + \frac{\Delta t}{2}, x_n + \frac{k_2}{2})\Delta t \tag{2.8}$$

$$k_4 = u(t_n + \Delta t, x_n + k_3)\Delta t \tag{2.9}$$

$$x_{n+1} = x_n + \frac{k_1}{6} + \frac{k_2}{3} + \frac{k_3}{3} + \frac{k_4}{6}, \tag{2.10}$$

after Press *et al.* (2003). This method is more stable and more accurate than other methods (Press *et al.*, 2003; Griffiths and Higham, 2010) such as the forward Euler method used in some popular trajectory models (*e.g.* FLEXPART (Flexible Particle dispersion model; Stohl, 1998) and HYSPLIT (Hybrid Single Particle Lagrangian Integrated Trajectory Model; Stein *et al.*, 2015).

Since the model calculates trajectories offline, various atmospheric variables (*e.g.* specific humidity, potential vorticity) can be interpolated to the trajectory location at each 6 hour time-step using bilinear interpolation in the horizontal direction, cubic vertical interpolation and linear time interpolation (Methven, 1997). The model uses ERA-Interim spectral data on model levels on the full Gaussian grid (Dee *et al.*, 2011) but can be initialized on pressure, isentropic or model levels and data can be output on pressure or model levels.

The ROTRAJ model can be used for many different applications. Examples include pollutant transport (Newell and Evans, 2000); detecting stratospheric water vapour accumulations from aircraft (Wilcox *et al.*, 2012); identifying airmasses in cyclones (Martínez-Alvarado *et al.*, 2014); detecting gas flares in Nigeria (Fawole *et al.*, 2016); and identifying the origins of England and Wales precipitation variability (de Leeuw *et al.*, 2017).

2.3 Defining Ocean Drainage Basins

This section describes the data and method used to construct the boundaries between the drainage basins of each ocean basin. These will be used primarily as the release points for trajectories in chapter 5 and also to evaluate moisture fluxes in chapter 4. Figure 2.1 shows the drainage basins for the major oceans and seas. The aim is to use topographic datasets (section 2.3.3) to approximate the catchment boundaries and the ocean drainage basins they surround. These will not precisely match Figure 2.1 as they are approximated and also because different extents of the ocean drainage basins will be used to suit this study.

2.3.1 Terminology

Some key terminology which will be used throughout this thesis is defined here.

- **Drainage basin/catchment area**: area of land in which the precipitation gathers and flows towards a common outlet;
- **Catchment boundary**: a physical line which seperates drainage basins;
- **Continental divide**: a boundary between the drainage basins of different oceans.

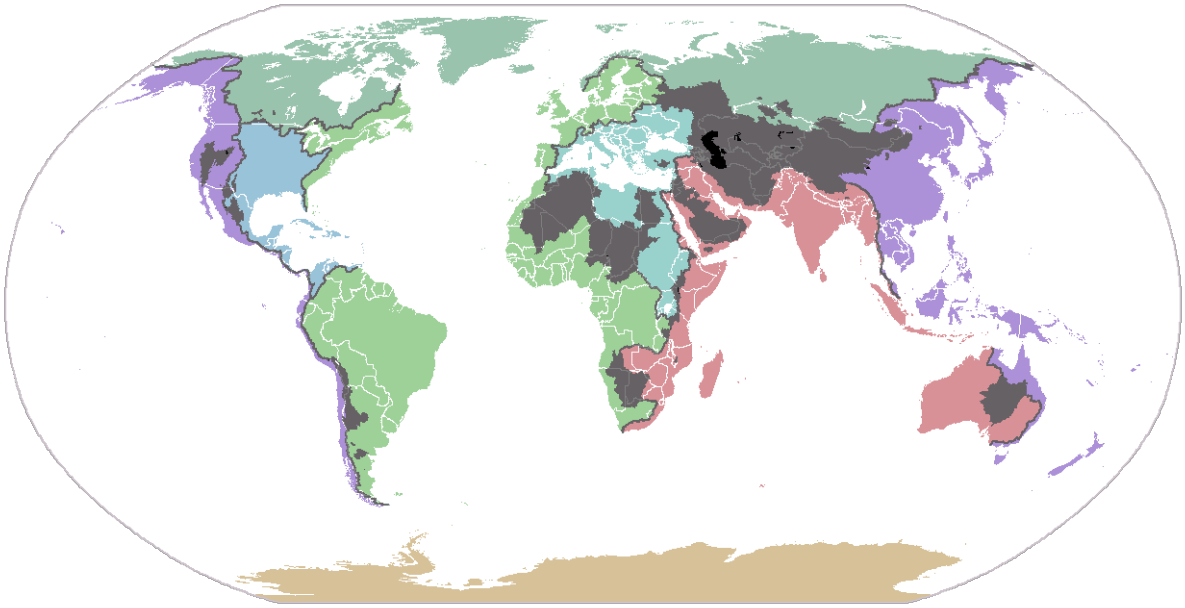

Figure 2.1: Depiction of the major ocean drainage basins from radicalcartography.net. Light green regions drain into the Atlantic Ocean, dark green into the Arctic Ocean, purple into the Pacific Ocean, red into the Indian Ocean, brown into the Southern Ocean, blue into the Caribbean Sea and turquoise into the Mediterranean Sea. Grey regions are endorheic basins which do not drain into the global ocean. The catchment boundaries in this map were identified using USGS Hydro1k data.

2.3.2 Method

Using Figure 2.1 as a template, the various datasets delineating drainage basins (section 2.3.3) were overlain on a map of the ETOPO5 topography and segments of the boundaries were approximated by manually selecting points along the boundaries to create segments as a suitable dataset defining the catchment boundaries does not exist. To obtain points between the end points of the segments, linear interpolation was used to find points spaced approximately 75 km apart which is approximately within the resolution of the ECMWF model (Dee *et al.*, 2011). Some studies which present ocean drainage basins have used river-routing datasets (e.g. Rodriguez *et al.*, 2011; Wills and Schneider, 2015) and others have used maximum topography (Levang and Schmitt, 2015; Singh *et al.*, 2016). However, the accuracy available from this method is sufficient enough not to require a river-routing dataset as it is within the horizontal resolution of the ECMWF model (Dee *et al.*, 2011). Using maximum topograpy is also problematic as catchment boundaries do not neccessarily follow maximum topography. This problem can be seen in Singh *et al.* (2016) where the catchment boundaries leave the land and cross over seas and rivers.

2.3.3 Datasets

This section describes the datasets used to construct the ocean catchment boundaries which will be used in chapters 4 and 5 of this thesis.

2.3.3.1 HydroSHEDS

The Hydrological data and maps based on Shuttle Elevation Derivatives at multiple Scales (HydroSHEDS; Lehner *et al.*, 2008) dataset from the United States Geological Survey (USGS) uses high resolution satellite data from the Shuttle Radar Topography Mission (SRTM) to determine the boundaries of river catchment areas. Currently at version 1.2 (Lehner *et al.*, 2013), HydroSHEDS covers most of the globe at resolutions of 3 arc-seconds, 15 arc-seconds and 30 arc-seconds. HydroSHEDS is available from www.hydrosheds.org. Note that the previous version (1.1) was used in this work and is restricted between 60°N and 60°S (Figure 2.2) although this has been extended beyond these limits in version 1.2 (Lehner *et al.*, 2013). HydroSHEDS was used to define the American, African and South-East Asian catchment boundaries (Figure 2.6-2.8), as well as the Arctic catchment boundary along Eurasia (Figure 2.9) and the boundary of the River Plate drainage basin which forms part of the Southern Ocean catchment boundary (Figure 2.10).

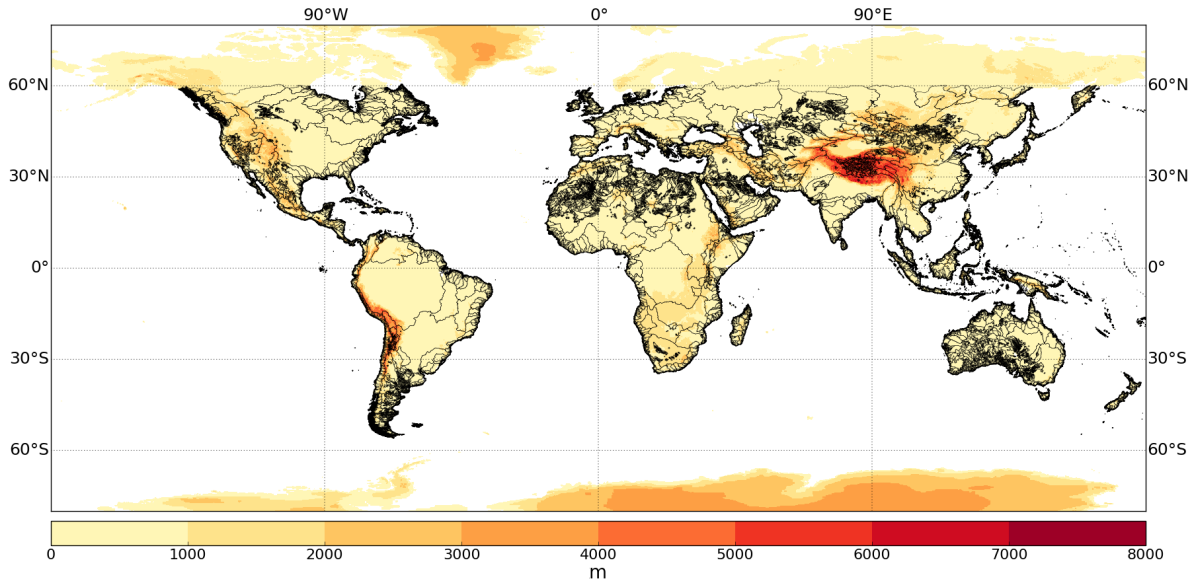

Figure 2.2: Continental topography from the ETOP05 dataset (contours) and river catchment boundaries from the HydroSHEDS dataset (Lehner *et al.*, 2008) (black lines).

2.3.3.2 ETOPO05

ETOPO5 is a global dataset of topography (contours, Figure 2.2) and bathymetry provided by the National Oceanic and Atmospheric Administration on a 5-minute latitude/longitude grid (National Geophysical Data Center, 1993) with 12 points per degree. When defining the catchment boundaries, the ETOP05 dataset shows which topographic features the catchment boundaries are located along and when no catchment boundary data were available (Scandinavia, western Russia, Alaska) the topography acted as a guide based on Figure 2.1.

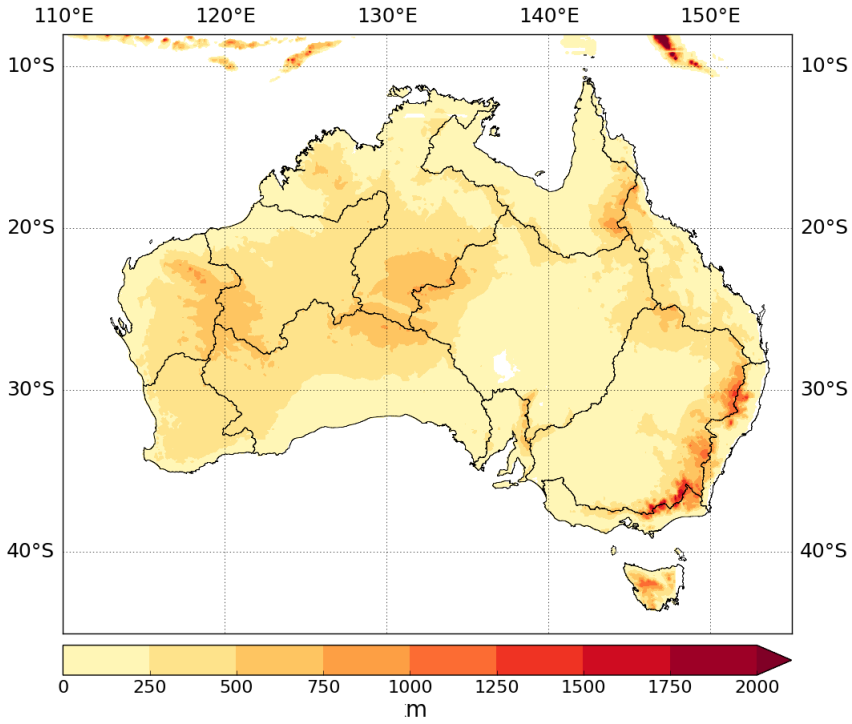

Figure 2.3: The catchment boundaries for Australia's major drainage basins (Bureau of Meteorology, 2015) (black lines) overlain on topography from the ETOP05 dataset (contours).

2.3.3.3 Geofabric

The Australian Hydrological Geospatial Fabric (Geofabric) is a digital database constructed by the Bureau of Meteorology of surface and groundwater features which records the spatial relationships between important hydrological features. Input data for Geofabric includes a 9 second digital elevation model which is used to construct hydrology reporting regions (Bureau of Meteorology, 2015). The topographic drainage divisions of Geofabric are shown in Figure 2.3. Geofabric is used for the Australian parts of the South-East Asian and Southern Ocean catchment boundaries (Figures 2.8 and 2.10 respectively) instead of HyroSHEDS as it provides only the eleven major hydrological regions for Australia rather than every single river

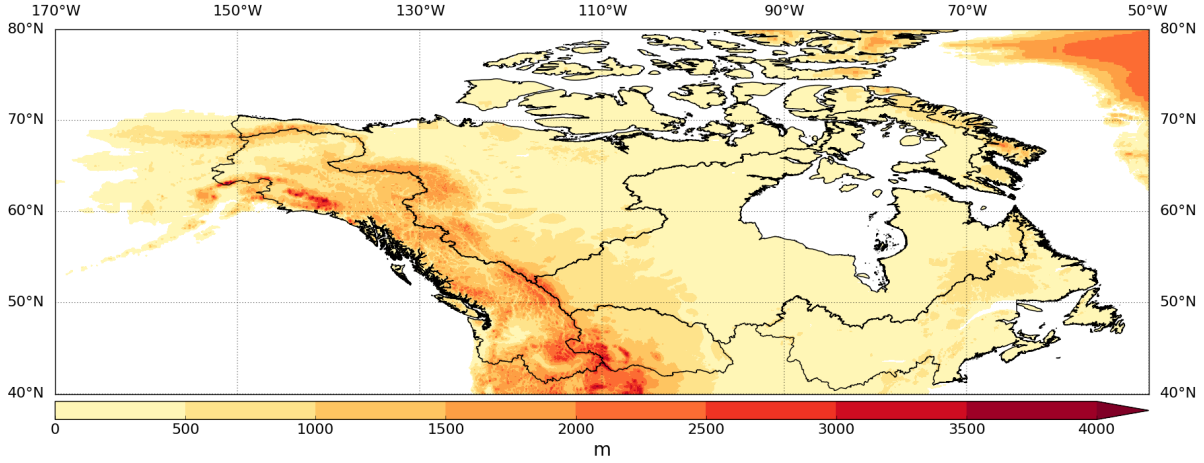

Figure 2.4: Canadian drainage basins from Natural Resources Canada (black lines) overlain on ETOT05 topography (contours).

drainage basin in HydroSHEDS (Figure 2.2). The data is available from the Geofabric webpage: http://www.bom.gov.au/water/geofabric/.

2.3.3.4 Natural Resources Canada

Figure 2.4 shows the Canadian boundaries of the drainage basins for the Atlantic Ocean, Arctic Ocean, Hudson Bay and Pacific Ocean. This data is part of the Atlas of Canada and was obtained from Natural Resources Canada. The ocean drainage basin dataset (Natural Resources Canada, 2009) was developed from the hydrographic layers of a global digital dataset produced by the United States National Imagery and Mapping Agency (NIMA). Similar to Geofabric, Figure 2.4 provides only the major hydrological regions for Canada and also extends further north than version 1.1 of HydroSHEDS (Figure 2.2). This dataset is used to define the Canadian part of the Arctic catchment boundary (Figure 2.9).

2.3.3.5 Ice Sheet Mass Balance Inter-Comparison Exercise (IMBIE)

Figure 2.5 shows the drainage basins of Greenland from the ice sheet mass balance intercomparison exercise (IMBIE). The drainage divides in Figure 2.5 are actually ice motion divides (Rignot and Mouginot, 2012) which are based on changes in direction of ice flow. Rignot and Mouginot (2012) estimated these divides using various satellite data: Envisat Advanced Synthetic-Aperture Radar (ASAR), Advanced Land Observation System (ALOS)'s Phase-Array L-band SAR (PALSAR) and the RADARSAT-1 SAR. The data for the Rignot and Mouginot (2012) divides are available at http://imbie.org/ and used to define the Arctic catchment boundary across Greenland (Figure 2.9).

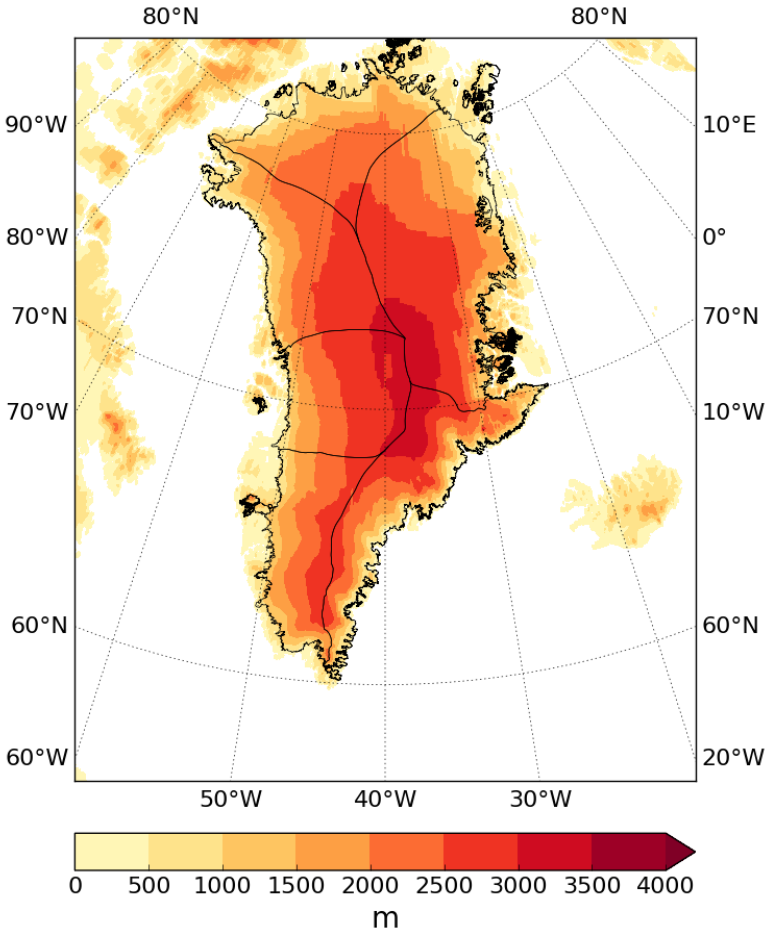

Figure 2.5: Rignot and Mouginot (2012) Greenland ice sheet boundaries (black lines) overlain on ETOP05 topography (contours).

2.3.4 Catchment boundaries

Each catchment boundary is described below. Overall there are nine catchment boundaries as the boundaries surrounding the Arctic and Southern Ocean drainage basins are split into three sectors (Atlantic, Indian and Pacific). Table 2.1 shows the longitude-latitude co-ordinates of the start and end points as well as the number of points of each boundary. The catchment boundaries are shown individually in Figures 2.6-2.10 and all together in Figure 2.11.

2.3.4.1 Americas

The continental divide between the Atlantic and Pacific drainage basins follows the spine of the Rocky Mountains (Figure 2.6) starting at the Snow Dome at 52°N in Canada. The Snow Dome is a "triple divide" or "hydrological apex" *i.e.* a point where three drainage basins meet. Although the Snow Dome is taken as the hydrological apex of the Atlantic, Arctic and Pacific drainage basins in this study, Triple Divide Peak further South in Montana can also be con-

Table 2.1: Number of points in each catchment boundary and the longitude-latitude coordinates of the start and end points of each boundary. The Arctic and Southern Ocean catchment boundaries are split into three sectors based on the which of the other three oceans it seperates the Arctic or Southern Ocean from.

catchment boundary	number of points	start	end
Americas	155	(117.45°W, 52.03°N)	(71.03°W, 15.32°S)
Africa and Middle East	214	(41.98°E, 40.08°N)	(20.22°E, 35.00°S)
South-East Asia	165	(92.18°E, 32.71°N)	(144.97°E, 20.48°S)
Arctic Atlantic	197	(117.45°W, 52.03°N)	(41.98°E, 40.08°N)
Arctic Indian	103	(41.98°E, 40.08°N)	(92.18°E, 32.71°N)
Arctic Pacific	220	(92.18°E, 31.71°N)	(117.45°W, 52.03°N)
Southern Atlantic	185	(71.03°W, 15.32°S)	(20.22°E, 35.00°S)
Southern Indian	184	(20.22°E, 35.00°S)	(144.97°E, 20.48°S)
Southern Pacific	212	(144.97°E, 20.48°S)	(71.03°W, 15.31°S)

sidered to be the hydrological apex of North America depending on whether Hudson Bay is included in the Atlantic or Arctic basin. Here, Hudson Bay is included in the Atlantic basin.

After the southern end of the Rocky Mountains the boundary follows the mountain ranges in Mexico and Central America, almost following the coastline in Central America. The boundary joins the Andes in Colombia - a section which was troublesome for Levang and Schmitt (2015) and Singh *et al.* (2016) as their use of maximum topography caused the eastern branch to be included in their boundary but the rivers between the eastern and western branches drain into the Atlantic basin. The boundary follows the spine of the Andes until 15°S near the border between Peru and Bolivia.

2.3.4.2 Africa and the Middle-East

This catchment boundary serparates the drainage basins of the Atlantic and Indian Oceans with the Mediterranean Sea included in the Atlantic drainage basin. The boundary shown in Figure 2.7 is the combination of the boundaries from Figure 2.1 that the Indian Ocean basin has with the Atlantic and Mediterranean basins. The boundary between the Atlantic and Indian Ocean drainage basins begins in the mountains of north-west Turkey, follows the mountains in Syria, Lebanon and Israel into the Sinai Peninsula and follows the mountains along the Egyptian Coast before cutting through Ethiopia to Lake Victoria. South of Lake Victoria, the boundary cuts through Tanzania and follows the northern edge of the River Zambezi drainage basin westwards and the western edge of the Okavango basin before cutting south-east along

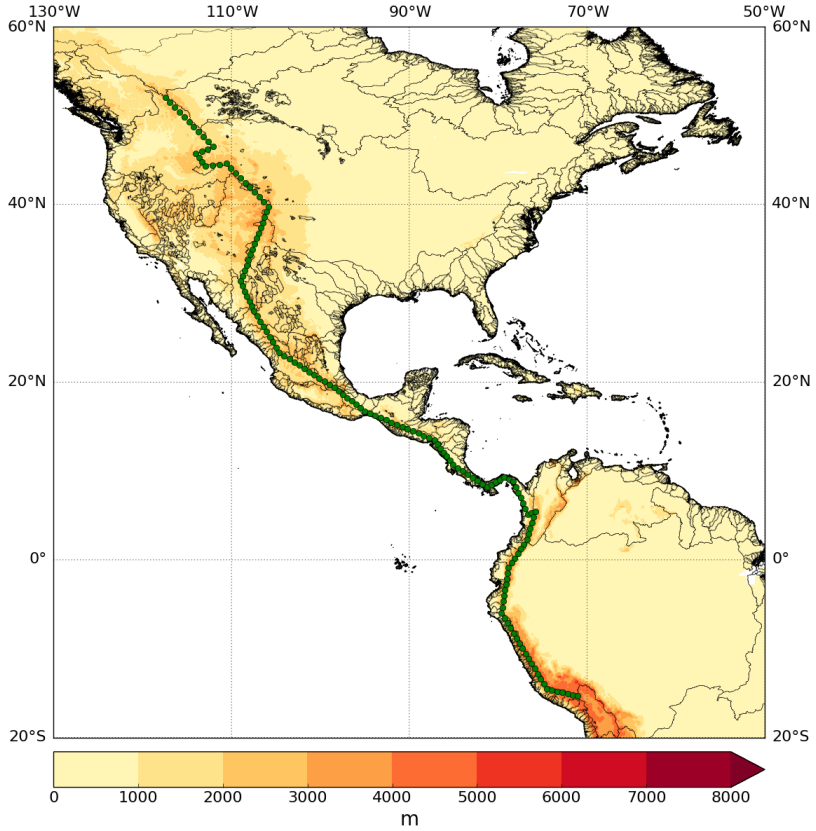

Figure 2.6: Points used for the American catchment boundary (green circles) overlain on HydroSHEDS data (black lines) and ETOP05 topography (contours).

the northern edge of the Orange basin and following the southern edge round to Cape Agulhas.

Figure 2.7 represents an improvement compared to Singh *et al.* (2016) where there are several errors in the location of the catchment boundary. In the north it follows the Zagros mountains before cutting acrosss the Red Sea into the middle of the Sahara Desert, then crossing the Red Sea again before following the maximum topography along a path more similar to Figure 2.7. The Singh *et al.* (2016) catchment boundary errneously suggests that the Tigris and Euphrates rivers drain into the Mediterranean Sea and also cuts across the River Nile and Red Sea in an unphysical manner. The catchment boundary in Figure 2.7 is much more realistic and the HydroSHEDS data clearly shows the large catchment area for the Nile which extends south of the equator to Lake Victoria.

2.3.4.3 South-East Asia

The boundary between the drainage basins of the Indian and Pacific Oceans is depicted in Figure 2.8. Starting at 32°N on the Tibetan Plateau, the boundary extends southwards through Burma, Thailand and Malaysia. It is after leaving Malaysia that the boundary shown in Figure

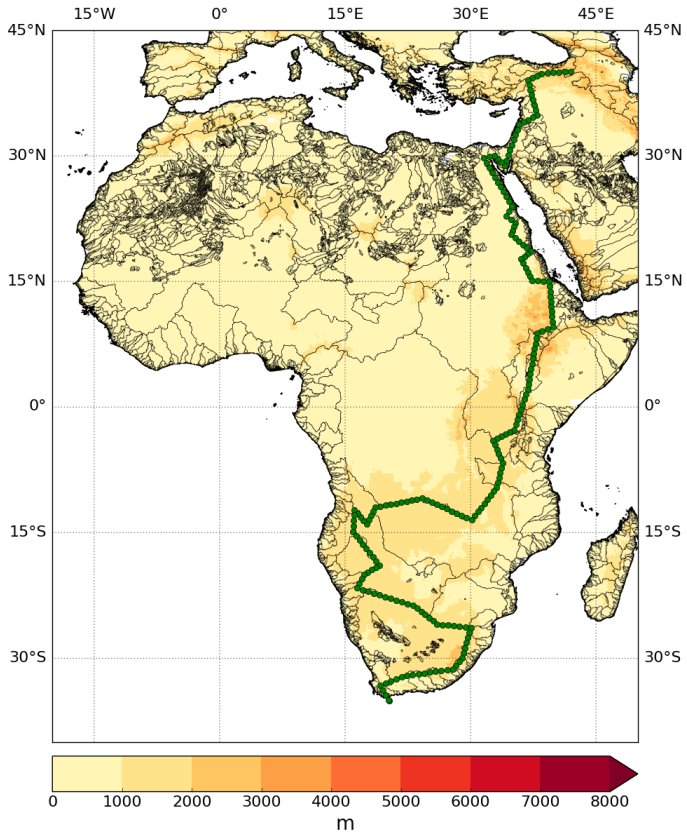

Figure 2.7: Points used for the African and Middle-Eastern catchment boundary (green circles) overlain on HydroSHEDS data (black lines) and ETOP05 topography (contours).

2.8 differs from that shown in Figure 2.1. In Figure 2.1, the boundary cuts straight through the Java and Banda Seas then rejoins the land on Australia east of Darwin. In Figure 2.8 however, the boundary moves onto the west coast of Sumatra which it follows until Java and then cuts straight across to New Guinea and southwards across the Torres Strait before terminating in Queensland at 20°S. The approach used here also differs from the boundaries shown by Wills and Schneider (2015) and Levang and Schmitt (2015). The former also follow the west coast of Sumatra and Java but enter Australia at a similar location to Figure 2.1, while the latter use maximum topography and the boundary cuts across the islands further to the north (Borneo and Sulawesi) and continues further south into Australia, terminating at 30°S. Placing the catchment boundary along 8°S (Figure 2.8) avoids the region of strong moisture flux convergence (Figure 3.1(b)) and means that there is consistency between the western/eastern boundaries of the Pacific/Indian Oceans used in chapters 3 and 4/5.

2.3.4.4 The Arctic

The boundary for the Arctic Ocean drainage basin is shown in Figure 2.9. There are several key differences between the Arctic boundaries shown in Figures 2.9 and 2.1. Firstly, the Atlantic

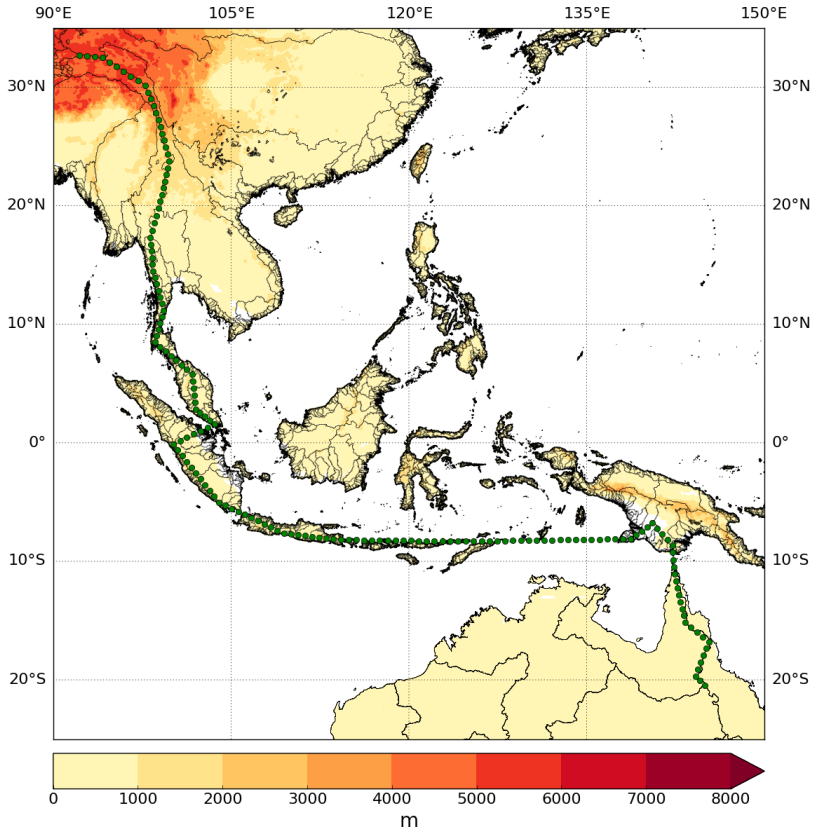

Figure 2.8: Points used for the South-East Asian catchment boundary (green circles) with HydroSHEDS and Geofabric data (black lines) and ETOP05 topography (contours).

sector of the boundary in Figure 2.9 starts at the Snow Dome (red circle on North America, Figure 2.9) instead of Triple Divide Peak (see section 2.3.4.1 and blue triangle in Figure 2.9) and therefore Hudson Bay is not included in the Arctic drainage basin for this estimate. The drainage divide crosses Greenland following the ice sheet drainage boundaries from Rignot and Mouginot (2012) then extends eastwards to Svalbard and turns southwards to Scandinavia. This shape of the boundary includes the Nordic and Labrador Seas in the Atlantic Ocean, where deep convection occurs.

A key feature of the Arctic boundary shown in Figure 2.9 is the southerly extent through Iran and along the Himalayas rather than tracking further north through Russia, Kazakhstan and Mongolia. The purpose of this is to the include the large Central Asian endorheic basin in the Arctic drainage basin. For such regions $E - P \approx 0$ (Stohl and James, 2005) and there is no relationship between the moisture budgets of these regions and SSS so would be unneccessary to consider this basin separately. Including the Central Asian endorheic basin in the Arctic drainage basin means that the Atlantic sector of the Arctic boundary terminates in northern Turkey and the boundary between the Arctic and Indian Ocean catchment areas extends from

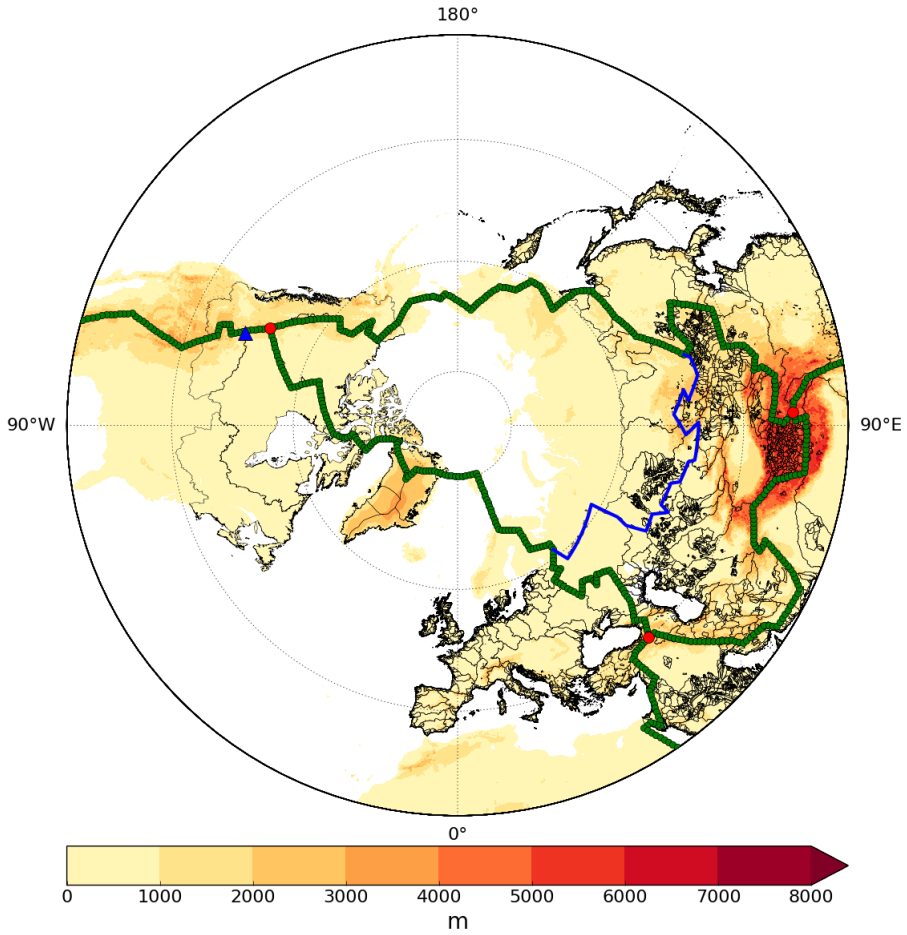

Figure 2.9: Points used for the catchment boundary of the Arctic Ocean drainage basin (green circles) overlain on the catchment boundaries from Natural Resources Canada, Rignot and Mouginot (2012) and the HydroSHEDS dataset and ETOP05 topography. The large red circles indicate the intersections of the Arctic catchment boundary with the American, African and South-East Asian catchment boundaries. The blue triangle indicates the location of Triple Divide Peak on the American catchment boundary and the blue line across northern Eurasia shows the northern boundary of the Central Asian endorheic basin.

northern Turkey to the eastern Tibetan Plateau.

The Pacific sector of the Arctic boundary cuts north-east across China, through Russia and across the Bering Strait at 65°N (the northern limit of the Pacific Ocean). Before completing the boundary and returning to the Snow Dome in Canada, it shifts to the north-east after the Bering Strait to include the drainage basin of the River Yukon which flows into the Bering Sea (part of the Pacific Ocean). Levang and Schmitt (2015) failed to use the correct path of the boundary through Alaska by using maximum topography. Instead, their boundary cuts straight through the middle of Alaska, straight through the Yukon basin which almost reaches the north coast. The boundaries in Figures 2.1 and 2.9 show the correct route of the continental divide.

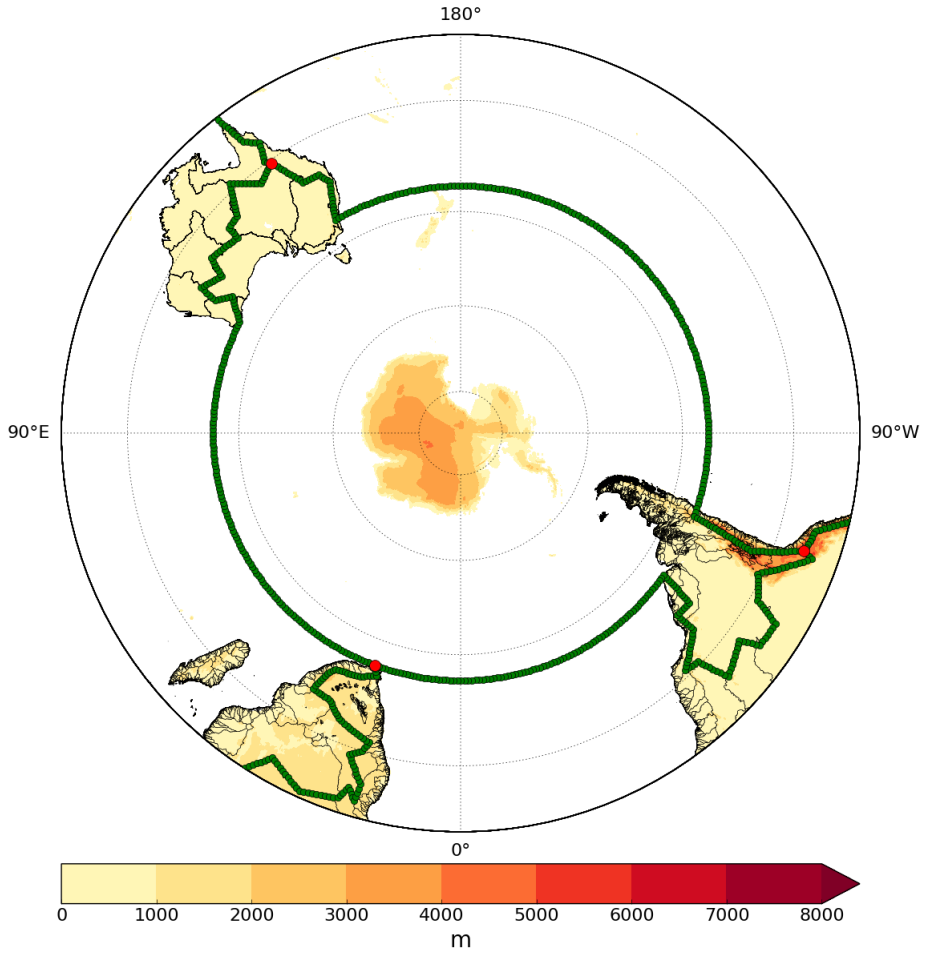

Figure 2.10: Points used for the catchment boundary of the Southern Ocean drainage basin (green circles) overlain on Geofabric catchment boundaries (Figure 2.3) HydroSHEDS data and ETOP05 topography. The large red circles indicate the intersections of the Southern Ocean catchment boundary with the American, African and South-East Asian catchment boundaries.

2.3.4.5 Southern Ocean

The boundary of the Southern Ocean was somewhat simpler to construct (Figure 2.10). A northern extent of the Southern Ocean of 35°S was chosen as this matches the approximate southern limits of Africa and South-West Australia. There are four land areas which drain into the Southern Ocean: Antarctica, Australia, New Zealand and South America. Antarctica is obviously in the centre of the Southern Ocean and the region of the north island of New Zealand which is north of 35°S is too small to contribute any significant amount of runoff to the moisture budget. Australia, however, has rivers which drain into the Southern Ocean, as shown by Figure 2.3, which are included in the Southern Ocean drainage basin (Figure 2.10). In South America the mouth of the River Plate enters the ocean between 35°S and 36°S. The location of this outflow presents a problem as it feeds water into the region of the confluence between the northwards Falklands current and the southwards Brazil current. The surface currents then

travel eastwards as part of the subtropical gyre and are then recirculated northwards. It could therefore be equally valid to include the River Plate basin in either the Atlantic or Southern Ocean drainage basin as the discharge from the River Plate likely contributes to the water budget of both oceans. However, any attempt to determine the destination of River Plate outflow and which ocean's water budget is has most effect on would overcomplicate the matter further so the River Plate basin was simply included in the Southern Ocean drainage basin where it initially enters anyway.

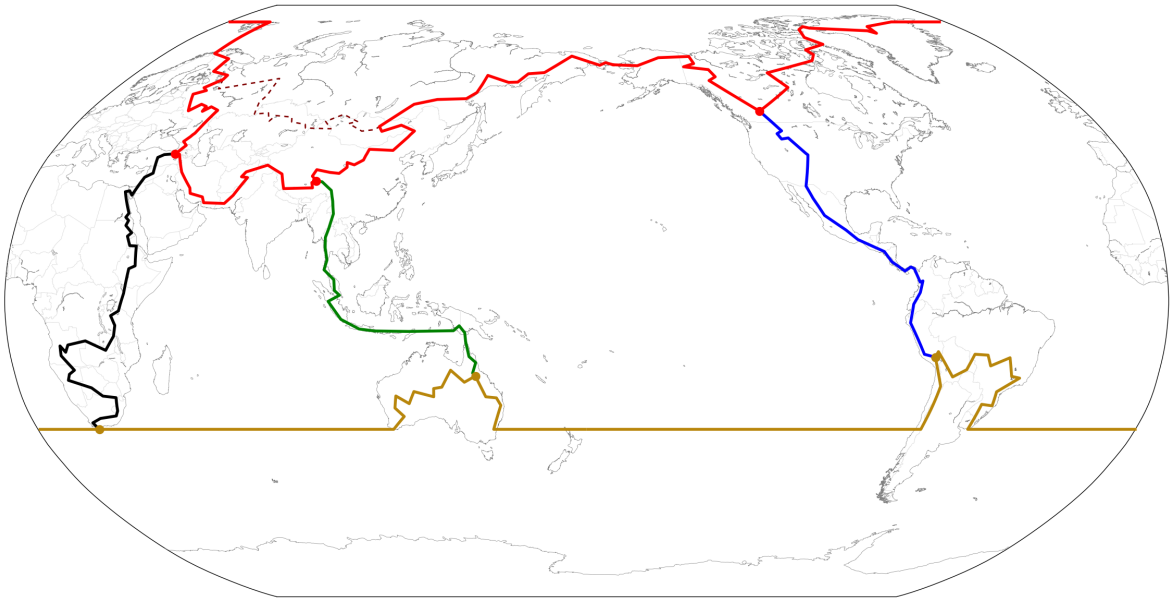

Figure 2.11: All the catchment boundaries: Americas (blue), Africa and Middle East (black), South-East Asia (green), Arctic (red) and Southern (gold). The red/gold dots indicate the end points of the different sectors of the Arctic/Southern catchment boundaries. The dashed maroon line is the northern boundary of the Central Asian endorheic basin.

2.3.5 The Ocean Drainage Basins

The catchment boundaries described in sections 2.3.4.1-2.3.4.5 are shown in Figure 2.11. Together they form the boundaries of the drainage basins for the Atlantic, Pacific, Indian, Arctic and Southern Oceans. From Figure 2.11 it is clear that despite the greater size of the Pacific Ocean the area of land included in the Atlantic drainage basin is much larger than that for the Pacific drainage basin. Most of the North and South American continents drain into the Atlantic Ocean, as do most of Africa and Greenland and all of Europe. Only narrow strips near the western coasts of the Americas drain into the Pacific Ocean, along with part of eastern Asia, the Maritime Continent and a tiny strip of eastern Australia. The Indian Ocean drainage basin includes the Arabian Peninsula and Indian subcontinent, plus a mostly narrow strip of eastern Africa and much of the northern and western regions of Australia. Most of Russia drains into

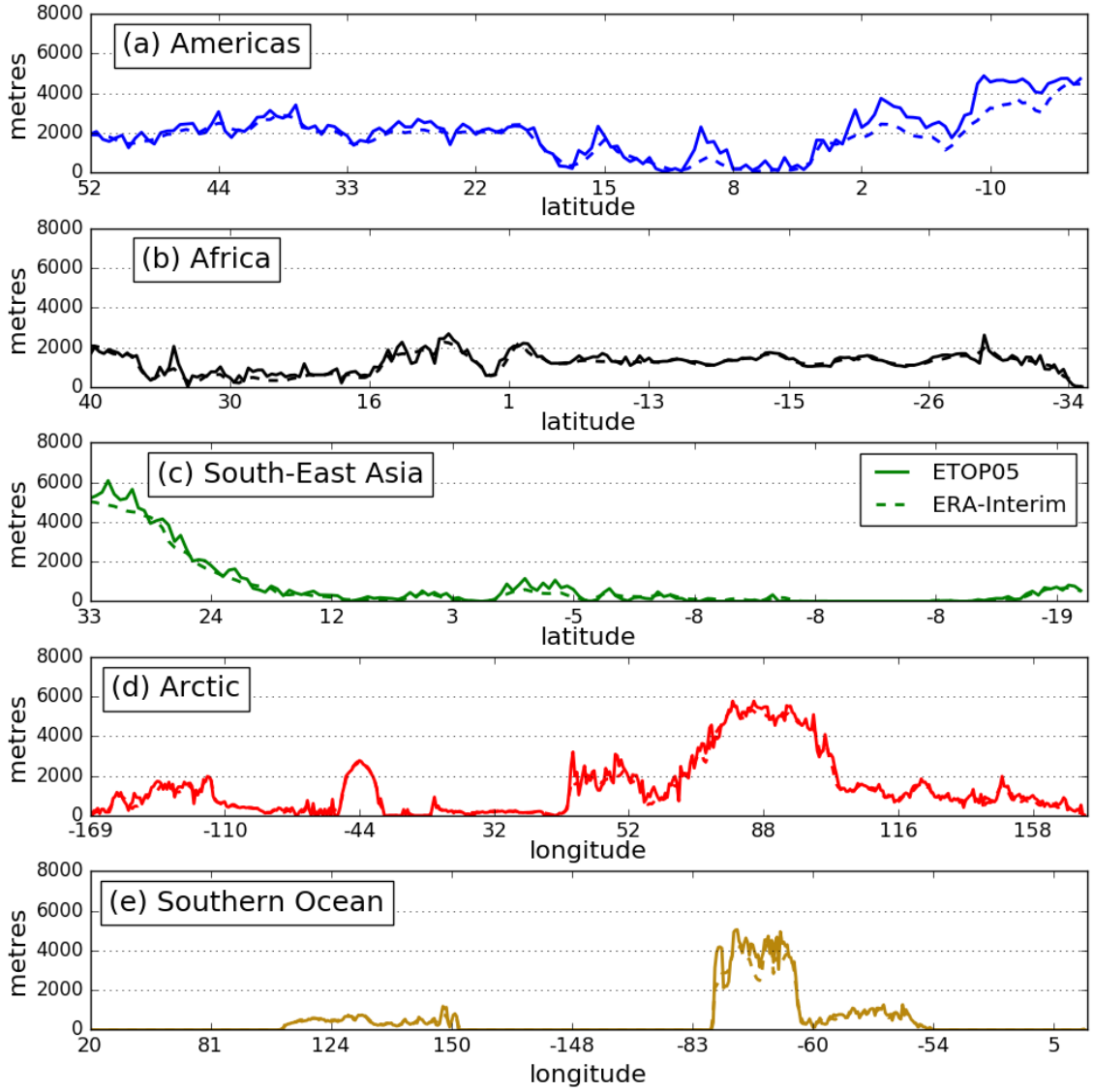

Figure 2.12: Comparison between orography from ETOP05 (solid lines) and ERA-Interim (dashed lines) along each catchment boundary. Note that ERA-Interim does not provide an estimate of orography from the IFS but it can be calculated using the geopotential (Φ) where the orography is Φ/g. The estimates are plotted against distance along the catchment boundaries but labelled by either latitude or longitude.

the Arctic Ocean along with some of Alaska and northern Canada and Greenland. Antarctica is the main land region in the Southern Ocean drainage basin, the other land regions in this drainage basin are New Zealand, much of southern and eastern Australia, and the River Plate basin in South America plus all the land south of 35°S.

Figure 2.12 shows that the orography along the catchment boundaries shown in Figure 2.11 is generally well estimated by ERA-Interim compared to the higher resolution ETOP05 dataset. The ERA-Interim orography (Φ/g, where Φ is the geopotential) performs worst along the Andes in South America along the American and Southern Ocean catchment boundaries

(Figure 2.12(a,e)). As the Andes is quite a narrow mountain range (Figure 2.6) the underestimation of the height of the orography is likely due to the lower resolution of the ECMWF model. However, the shape of the orography along the catchment boundaries is generally captured by ERA-Interim and the underestimation of the height of the orography is not substantial. The catchment boundaries shown in Figure 2.11 are therefore suitable for use in chapters 4 and 5 of this thesis.

Chapter 3

The contrast between Atlantic and Pacific surface water fluxes

This chapter is adapted from the paper published in *Tellus A* (Craig *et al.*, 2017).

3.1 Introduction

The Atlantic Ocean is known to have higher sea surface salinity (SSS) than the Pacific Ocean at all latitudes. In the northern hemisphere, differences of up to 2 psu (practical salinity units) are present in the subtropical gyres (Gordon *et al.*, 2015) and at high latitudes, with the difference reduced to 1 psu in the southern hemisphere subtropical gyres (Figure 3.1(a)). Salinity patterns are linked to the hydrological cycle (Schmitt, 2008) with regions of high SSS corresponding to regions of positive $E-P$ (evaporation minus precipitation) and regions of low SSS corresponding to regions of negative $E-P$ (Figure 3.1(b)). Some authors have attemped to use SSS as a "rain gauge" for the ocean (Ren *et al.*, 2014) and others have investigated how SSS has changed with the intensification of the hydrological cycle in recent decades (Skliris *et al.*, 2014). Durack and Wijffels (2010) found that the contrast in SSS between the Atlantic and Pacific has increased from 1950-2008, consistent with an intensified hydrological cycle expected from global warming conditions (Held and Soden, 2006).

The high salinity in the high latitude North Atlantic is associated with deep water formation through deep convection in the Greenland and Labrador Seas and a deep Atlantic Meridional Overturning Circulation (AMOC) (Marshall and Schott, 1999). There is no such

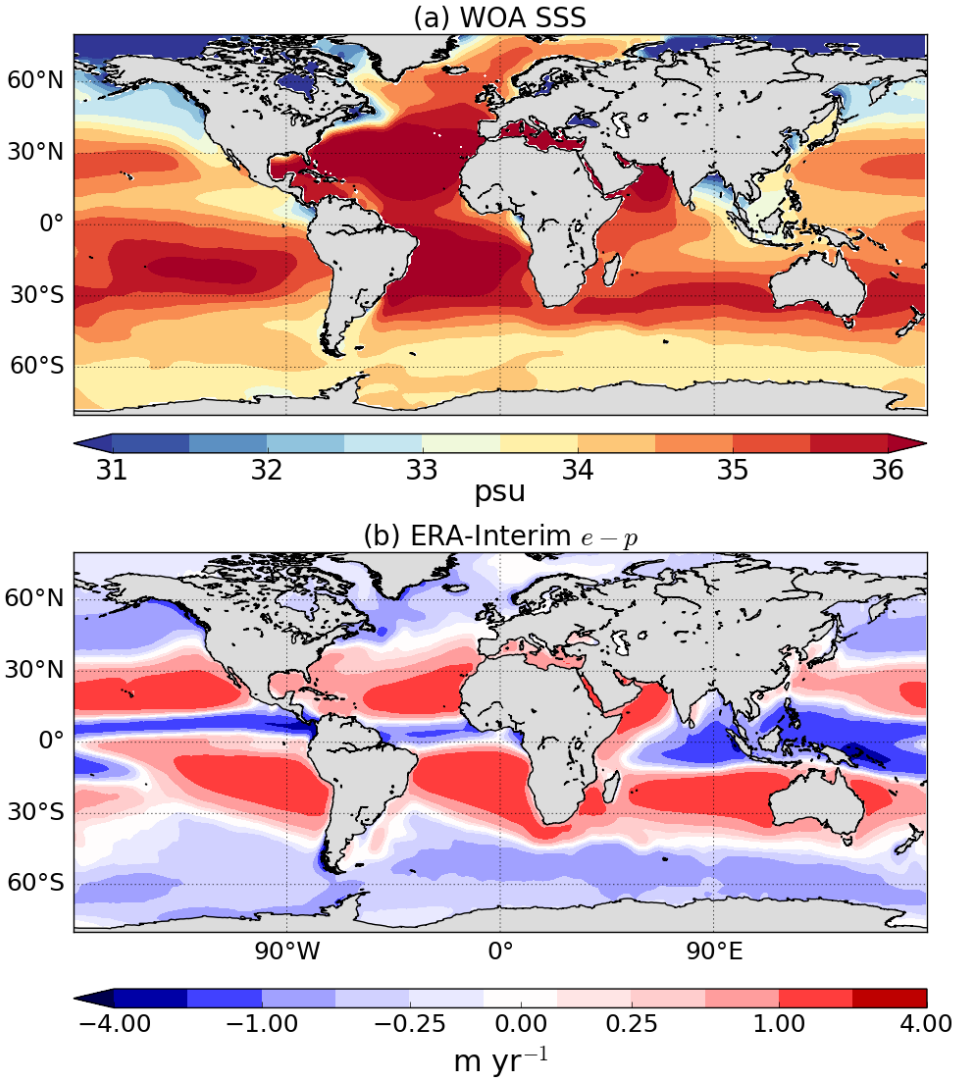

Figure 3.1: (a) Annual mean SSS (1955-2012) from the World Ocean Atlas (Zweng *et al.*, 2013) and (b) Annual mean (1979-2014) $e-p$ from ERA-Interim vertically integrated moisture flux divergence. A Gaussian filter was applied to smooth the data in panel (b).

deep convection in the North Pacific as SSS is too low for sinking to occur (Warren, 1983) and the Meridional Overturning Circulation there is wind-driven and confined to the upper ocean. Various reasons have been put forward to explain the asymmetry in MOC, such as differences in basin geometry (Schmitt *et al.*, 1989; Ferreira *et al.*, 2010; Nilsson *et al.*, 2013), the configuration of mountain ranges (Schmittner *et al.*, 2011; Sinha *et al.*, 2012), interbasin salt fluxes (Weijer *et al.*, 1999) and the existence of multiple equilibria of the MOC (Huisman *et al.*, 2009) – see also the review by Weaver *et al.* (1999). In nearly all published hypotheses not involving multiple equilibria, the net surface water flux (evaporation minus precipitation; $E-P$) is a key element, either as a cause or as a consequence of the MOC asymmetry. Indeed, it seems natural that the larger net evaporation ($E-P>0$) in the Atlantic than in the Pacific (well noted in the litera-

ture, at least for high-latitudes) should be part of any theory for the MOC and SSS asymmetry between basins.

Warren (1983) pointed out that the Pacific has a lower evaporation rate compared to the Atlantic at high latitudes. He also investigated the effect of the line of zero wind stress curl on salt advection into the northern North Atlantic and Pacific, and suggested that the tilted Atlantic zero wind stress curl line allowed for more salt advection than in the Pacific from the high salinity subtropics. Using updated datasets, Emile-Geay *et al.* (2003) drew a similar conclusion. They further suggested that moisture transport associated with the Asian monsoon could contribute to the freshening of the subpolar North Pacific (no such transport exists over the subpolar North Atlantic) although no quantification of this effect was offered. Revisiting the idea of Warren (1983), Czaja (2009) found that the tilted zero wind stress curl line coincides with the line separating net evaporation from net precipitation ($E - P < 0$) in the Atlantic but not the Pacific. Higher subopolar salinity in the Atlantic can therefore be maintained more easily in the Atlantic than in the Pacific. Czaja (2009) also investigated the temporal behaviour of the North Atlantic and North Pacific jet streams, finding the North Atlantic to be more variable, a feature which is efficient at driving salt advection into the subpolar gyre.

The higher subpolar North Atlantic mean evaporation rate noted by Warren (1983), Emile-Geay *et al.* (2003) and Wills and Schneider (2015) was attributed to higher Atlantic sea surface temperatures (SSTs). The colder Pacific SSTs were explained by Warren (1983) to be a result of cold upwelling in the subpolar North Pacific. However, Czaja (2009) argued that the higher subpolar Atlantic evaporation is simply a positive feedback: the higher rate of evaporation is caused by higher SSTs which is a result of the enhanced northward ocean heat transport (Trenberth and Caron, 2001) by the AMOC. Wills and Schneider (2015) found that atmospheric transient eddies and stationary-eddy vertical motion are dominant terms in setting zonal variations in the surface water flux for subpolar North Atlantic and Pacific. Transient eddies freshen the subpolar North Pacific (while salinifying the subpolar North Atlantic) because the Pacific storm track covers a larger area. Stationary-eddy vertical motion freshens the subpolar North Pacific more than the subpolar North Atlantic due to poleward motion and surface stress associated with the Aleutian low and subtropical high. The arguments of Wills and Schneider (2015) are linked to the relative width of the subpolar basins highlighted by Schmitt *et al.* (1989): the Atlantic is narrower so a greater fraction of it is affected by dry air coming off the downstream continent, thus the area-averaged evaporation rate is stronger.

Many previous studies have focused on the $E - P$ asymmetry between the far northern regions of both oceans, although Rahmstorf (1996) focused on the positive Atlantic $E-P$ north of 30°S. It is unclear where $E - P$ is the critical quantity since the SSS asymmetry between the basins exists at all latitudes. In addition, discussion of the $E - P$ asymmetry has often been framed, implicitly or explicitly, as an asymmetry in evaporation, neglecting the possible roles for precipitation and runoff.

In this paper we aim to answer the following questions:

1. How robust is the Pacific/Atlantic $E - P - R$ asymmetry across datasets?
2. Is the Pacific/Atlantic asymmetry present at all latitudes?
3. Is the $E - P - R$ asymmetry mainly due to an asymmetry in evaporation, precipitation or runoff?
4. Can interannual variability of $E-P$ be attributed to interannual variability in evaporation or precipitation?

To address these questions, we will compare various published freshwater flux estimates obtained with a range of methods. Importantly, we will show that $E-P$ from ERA-Interim (estimated using vertically integrated atmospheric moisture flux divergence or the forecast model E and P fields) combined with an independent estimate of R agree well with other estimates from both oceanic and atmospheric data. This step gives us ground to further explore the ERA-Interim E and P fields separately and address questions 3 and 4 above.

The budget calculations (for the atmosphere and ocean) used to compute the net surface water flux ($E-P$) and net freshwater flux ($E-P-R$) are summarized in section 2. A brief description of the selected datasets is given in section 3.3. These estimates are compared in section 3.4. In section 3.5, annual means, seasonal cycles and interannual variability of the evaporation and precipitation from ERA-Interim are discussed in the Atlantic and Pacific Oceans. Conclusions will be drawn in section 3.6. Note that, for completeness, results for the Indian Ocean are also shown but that our discussion largely focuses on the Atlantic and Pacific basins.

3.2 Budget Framework

This section describes the methods used to calculate the surface water flux from atmospheric data (section 3.2.1) and the net freshwater flux from oceanic data (sections 3.2.2 and 3.2.3).

It should be noted that, although similar in spirit, these calculations use completely different inputs (wind and specific humidity on one side, temperature and salinity on the other) and yet, as will be demonstrated in section 3.4, they give remarkably similar results.

3.2.1 Atmospheric moisture budget

In the atmosphere evaporation minus precipitation ($e-p$, where e and p are rates at grid points), can be related to the vertical integral of the mass continuity equation for water vapour (Berrisford *et al.*, 2011):

$$e - p = \frac{\partial\, TCWV}{\partial t} + \nabla \cdot \frac{1}{g} \int_0^1 \mathbf{u} q \frac{\partial \tilde{p}}{\partial \eta} \mathrm{d}\eta \tag{3.1}$$

where $TCWV = \frac{1}{g}\int_0^1 q\frac{\partial \tilde{p}}{\partial \eta}\mathrm{d}\eta$ is the total column water vapour, g is gravitational acceleration, $\mathbf{u}$ is the velocity vector, q is specific humidity and $\tilde{p}$ is pressure. The second term on the right-hand side of equation (3.1) is the vertically integrated moisture flux divergence (denoted div$\mathbf{Q}$ hereafter, here written in terms of η the terrain-following hybrid pressure co-ordinate used in the ERA-Interim reanalysis where $\eta = 1$ represents the surface and $\eta = 0$ represents the top of the atmosphere). Ice and liquid water are neglected as their mass transports are small when compared to those of water vapour (Berrisford *et al.*, 2011).

Integrated over long timescales, div$\mathbf{Q}$ approximately balances $e - p$ (Trenberth *et al.*, 2011) since the tendency term (first term on the right-hand side of equation (3.1)) is orders of magnitude smaller than div$\mathbf{Q}$ and $E - P$. The annual mean ERA-Interim (1979-2014) div$\mathbf{Q}$ over the global oceans is shown in Figure 3.1(b). As expected, moisture flux divergence implying net evaporation is found in the subtropics and convergence implying net precipitation is found in the Intertropical Convergence Zone (ITCZ) and in mid- to high-latitudes. Note the clear correspondence between the $e - p$ and SSS patterns: the regions of positive (negative) $e - p$ in Figure3.1(b) correspond approximately to regions of high (low) salinity in (a). The subtropical gyres occupy regions of high SSS and $e - p$ with the highest open ocean SSS found in the North Atlantic subtropical gyre (D'Addezio and Bingham, 2014). Salinity minima are found slightly to the north of the ITCZ ($e - p$ minima) in both the Atlantic and Pacific due to northwards Ekman transport of salt (Tchilibou *et al.*, 2015). The salinity minimum caused by the South Pacific Convergence Zone (SPCZ) is also offset from the $e - p$ minimum due to Ekman transport.

3.2.2 Mass transport in the ocean

The net freshwater flux ($E - P - R$) can be estimated by completely independent means from oceanographic data alone. Consider the integral of the the mass continuity equation for the ocean over a fixed volume V between latitudes ϕ_N and ϕ_S and from the western to eastern boundaries of an ocean basin:

$$\frac{\mathrm{d}M}{\mathrm{d}t} + \oiint_{\partial V} \rho \mathbf{u} \cdot \mathbf{n} \mathrm{d}A = 0 \tag{3.2}$$

where $M = \iiint_V \rho \mathrm{d}V$, ∂V is the boundary of the volume and $\mathbf{n}$ is the outward-facing normal vector. Assuming steady state, equation (3.2) can be rewritten as:

$$P - E + R = \iint_{\phi_N} \rho \mathbf{u} \cdot \tilde{\mathbf{n}} \, \mathrm{d}x\mathrm{d}z - \iint_{\phi_S} \rho \mathbf{u} \cdot \tilde{\mathbf{n}} \, \mathrm{d}x\mathrm{d}z \tag{3.3}$$

where $\tilde{\mathbf{n}}$ is the northward-pointing normal vector. This simply states that the difference between the flux across two longitude-height sections is equal to the net (integrated) input of water at the ocean's surface between the sections, $P - E = \iint_{\text{surf}} (p - e) \mathrm{d}x\mathrm{d}y$ (e and p as in equation (3.1)), plus runoff R into the ocean basin. The latter is effectively the integrated flux across the western and eastern boundaries.

3.2.3 Oceanographic method to estimate freshwater transport

The mass balance equation (3.3) allows the calculation of $P - E + R$ from the mass fluxes through two sections. This method can be applied precisely in a General Circulation Model where the velocity field is known with high accuracy. On hydrographic sections, however, temperature, salinity and other tracers are measured at a range of depths at locations along a ship's route, but velocities are not. Horizontal velocities are estimated from thermal wind balance and determination of a reference velocity. Uncertainties in this method are so large that a direct estimation of $E - P - R$ from the mass balance equation (3.3) is impractical on hydrographic sections. The uncertainty in estimates of $E-P-R$ can be significantly reduced by combining the mass balance with the salinity balance (Wijffels, 2001; Ganachaud and Wunsch, 2003; Talley, 2008).

Integration of the salt budget over a fixed volume, assuming that any sources of salt are negligible (Wijffels *et al.*, 1992), gives:

$$\frac{\partial M_s}{\partial t} + \oiint_{\partial V} \rho s \mathbf{u} \cdot \mathbf{n} \, \mathrm{d}A = 0 \tag{3.4}$$

where the mass of salt $M_s = \iiint_V \rho s \mathrm{d}V$ with salinity s. In steady state, equation (3.4) becomes

$$\iint_{\phi_N} \rho s \mathbf{u} \cdot \tilde{\mathbf{n}} \, \mathrm{d}x\mathrm{d}z - \iint_{\phi_S} \rho s \mathbf{u} \cdot \tilde{\mathbf{n}} \, \mathrm{d}x\mathrm{d}z = 0. \tag{3.5}$$

The mass and salt balances, eqs. (3.3) and (3.5), can be combined using a reference salinity s_0 to re-scale the salt budget:

$$P - E + R = \iint_{\phi_N} \left(1 - \frac{s}{s_0}\right) \rho \mathbf{u} \cdot \tilde{\mathbf{n}} \, \mathrm{d}x\mathrm{d}z - \iint_{\phi_S} \left(1 - \frac{s}{s_0}\right) \rho \mathbf{u} \cdot \tilde{\mathbf{n}} \, \mathrm{d}x\mathrm{d}z. \tag{3.6}$$

This equation uses two observed properties (temperature and salinity) from hydrographic sections. As pointed out by Ganachaud and Wunsch (2003), uncertainties associated with estimation of $P - E + R$ (equation (3.6)) are about one order of magnitude lower than attempting to estimate the same quantity directly from equation (3.3). Note also that, in practice, the choice of s_0 has little impact on the freshwater transport estimates (Talley, 2008).

When using equation (3.6), the northern section is often set at the Bering Strait and the expression is approximated assuming a uniform salinity s_{BS} across the strait, yielding:

$$P - E + R = T_{\mathrm{BS}} \left(1 - \frac{s_{\mathrm{BS}}}{s_0}\right) - \iint_{\phi_S} \left(1 - \frac{s}{s_0}\right) \rho \mathbf{u} \cdot \tilde{\mathbf{n}} \, \mathrm{d}x\mathrm{d}z \tag{3.7}$$

where T_{BS} is the net (northward) mass transport across the Bering Strait. Note that for a south section ϕ_S in the Pacific, T_{BS} is positive (i.e. northward/outward of the domain defined by the two sections), but is negative for in the Atlantic (i.e. inward flux into the domain). The first term on the right-hand side of equation (3.7) is sometimes referred to as the Bering Strait "leakage".

Variants of equation (3.6) (or equation (3.7)) are found in the literature. Wijffels (2001) sets the reference salinity equal to the mean salinity along each section and works with the salinity anomalies about the mean salinity. Wijffels *et al.* (1992) do not use a reference salinity when combining the mass and salt budgets, but rather express the salinity in kg of salt per kg of water:

$$(P - E + R) = \iint_{\phi_N} (1 - s) \rho \mathbf{u} \cdot \tilde{\mathbf{n}} \, \mathrm{d}x\mathrm{d}z - \iint_{\phi_S} (1 - s) \rho \mathbf{u} \cdot \tilde{\mathbf{n}} \, \mathrm{d}x\mathrm{d}z \tag{3.8}$$

defining a true freshwater transport *i.e.* the part of the ocean transport which is "fresh". However, equation (3.8) is heavily weighted towards the mass balance since $s \sim 0.035 \ll 1$, and so this method has the same limitations as the pure mass balance equation (3.3).

3.3 Datasets

We compare estimates of $E - P - R$ (*i.e.* positive into the atmosphere) from seven different datasets. We do not aim to be exhaustive in our choice, but rather to include a range of methods available for such computations at the global scale. Importantly, these estimates include methods relying nearly exclusively on atmospheric or oceanographic data, while other methods combine measurements from both fluids. Note that Wijffels *et al.* (1992) calculated the first global distribution of freshwater transport using the results of Baumgartner and Reichel (1975) for E, P and R in 5° latitude bands. However, this estimate produced a strongly negative value of $E - P - R$ for the Pacific. This was shown by Wijffels (2001) to be incorrect: it is likely the result of poor or sparse observations from Baumgartner and Reichel (1975). Estimates from Wijffels *et al.* (1992) will therefore not be discussed further.

3.3.1 Atmospheric reanalyses

We use monthly mean data from the ERA-Interim reanalysis dataset from the ECMWF (European Centre for Medium-Range Weather Forecasts) for the years 1979-2014 (Dee *et al.*, 2011). The data are on a full N128 Gaussian grid at $0.75° \times 0.75°$ horizonal resolution and with 60 vertical levels. ERA-Interim uses a 4D-VAR data assimilation scheme with 12-hourly analysis cycles which combine observations with prior information from the model. Pressure level parameters are provided every 6 hours and surface parameters are provided every 3 hours.

ERA-Interim allows for $E-P$ to be calculated in two ways: from div$\mathbf{Q}$ using equation (3.1) and from separate evaporation and precipitation fields which are output as the accumulated (time-integrated) fluxes at the lower boundary over each forecast. In the reanalysis system the forecasts are restarted every 12 hours from the previous analysis. Many studies have used div$\mathbf{Q}$ to calculate $E - P$ (*e.g.* Seager and Henderson, 2013; Brown and Kummerow, 2014) but Berrisford *et al.* (2011) points out that the difference between div$\mathbf{Q}$ and $E - P$ from the forecast model is small when averaged globally so when $E - P$ is integrated over an ocean basin only a small difference should be expected between the div$\mathbf{Q}$ and forecast model calculations. Here, values of $E - P$ (div$\mathbf{Q}$) from ERA-Interim will be combined with run-off estimates R from Dai and Trenberth (2002) (see below).

Dai and Trenberth (2003) estimated freshwater transports using $P-E$ from ECMWF (1979-1993) and NCEP/NCAR (1979-1995) reanalyses along with improved estimates of R from Dai and Trenberth (2002). These improved estimates of R were calculated from streamflow data for

Table 3.1: Table of latitude boundaries for each of the estimates shown in Figures 3.2 and 3.3. The Mediterranean and Baltic Seas are included in the ERA-Interim estimate at the relevant basin scales and in the latitude bands where they join the main Atlantic Ocean. BS refers to the Bering Strait and a star denotes that the latitudes shown are only approximate.

	ERA-Interim & ECCOv4			Dai and Trenberth (2003)		
	Atlantic	Pacific	Indian	Atlantic	Pacific	Indian
Fig. 3.2(b)	35°S-60°N	30°S-BS	>35°S	32°S-60°N	30°S-BS	>32°S
Fig. 3.2(a)	35°S-45°N	30°S-47°N		32°S-45°N	30°S-47°N	
Fig. 3.3	45°N-60°N	47°N-BS		45°N-60°N	47°N-BS	
Fig. 3.3	24°N-45°N	24°N-47°N	>8°S	24°N-45°N	24°N-47°N	>8°S
Fig. 3.3	16°S-24°N	17°S-24°N	20°S-8°S	16°S-24°N	16°S-24°N	20°S-8°S
Fig. 3.3	35°S-16°S	30°S-17°S	35°S-20°S	30°S-16°S	30°S-16°S	32°S-20°S
	Schanze *et al.* (2010)			Ganachaud and Wunsch (2003)		
	Atlantic	Pacific	Indian	Atlantic	Pacific	Indian
Fig. 3.2(b)	35°S-70°N*	35°S-BS	>35°S			>32°S
Fig. 3.2(a)	35°S-45°N	35°S-45°N		30°S-47°N	30°S-47°N	
Fig. 3.3	45°N-60°N	45°N-60°N				
Fig. 3.3	25°N-45°N	25°N-45°N	>5°S	24°N-47°N	24°N-47°N	>8°S
Fig. 3.3	15°S-25°N	15°S-25°N	25°S-5°S	19°S-24°N	17°S-24°N	20°S-8°S
Fig. 3.3	35°S-15°S	35°S-15°S	35°S-25°S	30°S-19°S	30°S-17°S	32°S-20°S
	Talley (2008)			Valdivieso *et al.* (2014)		
	Atlantic	Pacific	Indian	Atlantic	Pacific	Indian
Fig. 3.2(b)	32°S-59°N	30°S-BS	>32°S	32°S-70°N	32°S-BS	>32°S
Fig. 3.2(a)	32°S-45°N	30°S-47°N		32°S-47°N	32°S-47°N	
Fig. 3.3	45°N-59°N	47°N-BS		47°N-70°N	47°N-BS	
Fig. 3.3	24°N-45°N	24°N-47°N	>8°S	26.5°N-47°N	24°N-47°N	
Fig. 3.3	16°S-24°N		20°S-8°S	16°S-26.5°N	17°S-24°N	
Fig. 3.3	32°S-16°S		32°S-20°S	32°S-16°S	32°S-17°S	32°S-20°S

the world's 921 largest rivers at the furthest downstream gauge station which were then extrapolated to the river mouth. By extrapolating to the river mouth total global runoff was increased by 19% compared to previous datasets. By using reanalysis $P-E$ and the new R dataset (along with the same transport of 0.794 Sv (1 Sv $\equiv 10^6\,\mathrm{m^3\,s^{-1}}$) as used by Wijffels *et al.* (1992) at the Bering Strait), Dai and Trenberth (2003) showed that the southward freshwater transport at all latitudes in the Atlantic and northward transport in the South Pacific are stronger than shown by Wijffels *et al.* (1992).

3.3.2 Independent estimates of E and P

The oceanic freshwater budget was quantified by Schanze *et al.* (2010) using atmospheric data from independent sources for surface freshwater fluxes. GPCP (Global Precipitation Climatology Project, Adler *et al.*, 2003) was used for precipitation and OAFlux (Objectively Analyzed air-sea Fluxes; Yu and Weller, 2007) for evaporation for the period 1987-2006, with the Dai and Trenberth (2002) runoff. Freshwater transports were estimated by integrating $e - p - r$ meridionally over each basin. A transport of 0.8 Sv is used at the Bering Strait and iceberg forcings of 0.01 and 0.06 Sv are added near Greenland and Antarctica respectively. This method leaves an imbalance of 0.32 Sv at 55°S which could not be constrained to a particular basin.

3.3.3 Hydrographic sections

Ganachaud and Wunsch (2003) used geostrophic inverse box modeling on hydrographic sections from the World Ocean Circulation Experiment (WOCE) to estimate $E - P - R$ from ocean transports using equation (3.6). The model used determines a high-resolution geostrophic velocity field to ensure that the circulation allows for near-conservation of mass, heat and salt. Four sections were used in both the Atlantic and Pacific and three used in the Indian Ocean. The Indonesian Througflow (ITF) transport was 15 ± 5 Sv from the 1989 JADE section (Ganachaud *et al.*, 2000). Note that using data from hydrographic sections has the effect of aliasing ocean variability as each section was recorded in a different month and/or a different year. For complete details of the routes and dates of each section see Figure 1 in Ganachaud and Wunsch (2003).

Talley (2008) used absolute geostrophic velocity analyses from hydrographic sections by J. Reid, combined with Ekman transports using NCEP reanalysis winds to estimate freshwater transports using equation (3.7). Geostrophic reference velocities were adjusted to ensure mass balance through each section. A reference salinity of $s_o = 34.9$ g/kg was used and the transports through the Bering Strait and the ITF were set to 1 Sv and 10 Sv respectively.

3.3.4 Ocean reanalyses

Valdivieso *et al.* (2014) computed freshwater transports from the University of Reading UR025.4 ocean reanalysis (1993-2010) at $\frac{1}{4}^\circ$ resolution. This reanalysis uses a variational method with the NEMO ocean modelling framework to constrain the ocean state by numerous observations (AVISO, Argo, etc.). The simulation is forced by ERA-Interim atmospheric reanalysis at the

ocean surface and the Dai and Trenberth (2002) runoff at the land mask edge. Note that the e field used to force the model is not taken from the ERA-Interim reanalysis, but recomputed as a function of the modeled SST. In addition, $E - P - R$ estimated from Valdivieso *et al.* (2014) include increments from the data assimilation method, *i.e.* it is assumed that assimilation increments to the ocean state, required by oceanic observations, represent errors in the surface forcing.

The "Estimating the Circulation and Climate of the Ocean" project version 4 (ECCOv4; Forget *et al.*, 2015) uses an adjoint-based method at $\sim 1^\circ$ resolution with the MITgcm to fit the time-evolving (1992-2011) ocean state to numerous observations (WOCE sections, Argo, sea level anomalies, sea ice concentration, satellite SST products, etc). Freshwater transport divergences shown here are computed using equation (3.3). Note that, as for the UR025.4 ocean reanalysis, atmospheric variables from ERA-Interim are used to compute air-sea fluxes (from bulk formulae and the simulated ocean state) and that they are adjusted as part of the optimization procedure to fit the modeled trajectory to ocean observations.

3.4 Comparison of $E - P - R$ estimates

In this section we compare the seven datasets described in section 3.3 and shown in Figures 3.2 and 3.3. To recap, the estimates from ERA-Interim and Dai and Trenberth (2003) (ERA-40) combine atmospheric reanalyses with the Dai and Trenberth (2002) runoff estimate. Schanze *et al.* (2010) also uses atmospheric data, with E and P coming from separate datasets. Valdivieso *et al.* (2014) and ECCOv4 are both based on ocean reanalyses while Ganachaud and Wunsch (2003) and Talley (2008) use oceanographic observations alone.

Figure 3.2 shows $E - P - R$ for the Atlantic, Pacific and Indian basins for each dataset described in section 3.3; panel (a) corresponds approximately to the latitudinal band 35°S-45°N and panel (b) to 35°S-65°N. The exact latitudinal boundaries used in calculating each estimate are shown in Table 3.1. Error bars are shown for most of the estimates although Dai and Trenberth (2003) and Schanze *et al.* (2010) did not provide any estimates of uncertainty. The error bars on the ERA-Interim based estimated are a combination of interannual variability and the $\mathrm{div}\mathbf{Q} - (E - P)$ residual using the error in quadrature method. The uncertainties presented by Ganachaud and Wunsch (2003) include uncertainties in the Ekman transport (set to 50% of the initial value) and model error which is dominated by aliasing of ocean variability (see section 3.3.3). Talley (2008) used a Monte Carlo approach to estimate the errors in the Ekman and

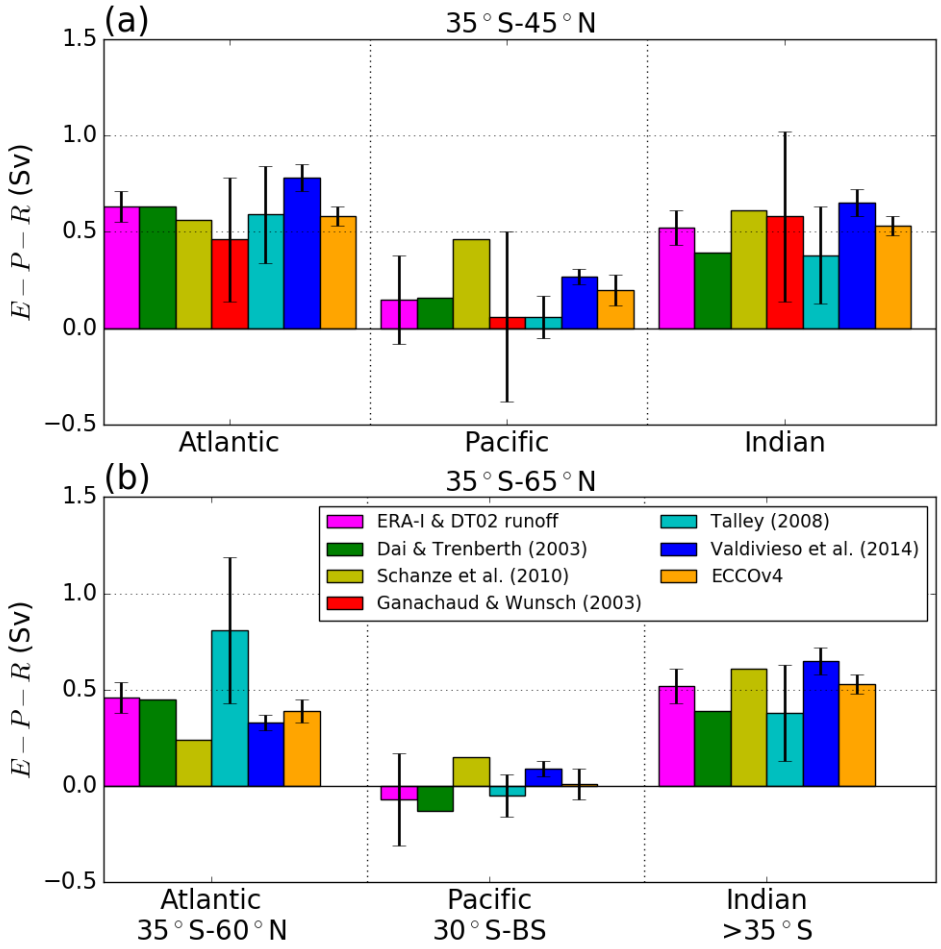

Figure 3.2: Basin-integrated net freshwater flux ($E-P-R$) for each ocean basin over different latitudinal extents: (a) approximately 35°S-45°N and (b) approximately 35°S-65°N. The latitude boundaries shown above each subfigure are approximate and do not apply to each estimate. Exact boundaries used in calculating each estimate are shown in Table 3.1. Estimates based on atmospheric data are shown first followed by the oceanographic estimates.

geostrophic components of freshwater transports. For a full discussion of the error calculations performed, refer to section 2.3 of Talley (2008). The uncertainties presented for the ECCOv4 estimate represent interannual variability of the freshwater divergences. Valdivieso *et al.* (2014) presented uncertainties which represent interannual variability in the eddy and throughflow components of freshwater transport.

All estimates show that the Atlantic has a higher $E-P-R$ than the Pacific at both latitude ranges. Most of the estimates suggest that Indian $E-P-R$ is almost as high as the Atlantic in (a), with two suggesting that the Indian $E-P-R$ is greater. Most studies suggest that the Pacific has a low $E-P-R$ for the latitude range in (a) except for Schanze *et al.* (2010) who find a high $E-P-R$ value for the Pacific that is close to the Atlantic values. ERA-Interim matches ERA-40 (Dai and Trenberth, 2003) in the Atlantic and Pacific and has higher $E-P-R$ in the

Indian Ocean. The error bars are small, indicating that the budget residual and interannual variability of ERA-Interim $E-P$ is low and that the asymmetry between Atlantic and Pacific is steady in time. The larger error bars for the Pacific suggest that interannual variability of $E-P$ is higher or that the budget residual is higher (or a combination of both). The oceanographic estimates of Ganachaud and Wunsch (2003) and Talley (2008) match within their uncertainty estimates in all basins. The ECCOv4 estimate agrees remarkably well with the ERA-Interim estimate in all basins. Valdivieso *et al.* (2014), however, is consistently higher than all other estimates apart from Schanze *et al.* (2010) in the Pacific.

When extending the domain further north (Figure 3.2b), the asymmetry between the Atlantic and Pacific oceans becomes stronger as three of the estimates indicate that the Pacific has negative $E-P-R$ while the Atlantic $E-P-R$ remains positive in all estimates. Talley (2008) actually finds that Atlantic $E-P-R$ *increases* with the northward extension of the domain (see below). Note that Valdivieso *et al.* (2014) gives lower $E-P-R$ than both atmospheric reanalyses and ECCOv4 possibly due to the more northerly extent used (see Table 3.1). Overall, the estimates are consistent in highlighting the differences in $E-P-R$ between ocean basins.

In order to see whether the differences between basins is found (and robust) at smaller scale, $E-P-R$ in latitude bands are shown in Figure 3.3. The size of these bands is limited by the resolution of the Ganachaud and Wunsch (2003) and Talley (2008) estimates which are based on the routes taken by ships collecting the hydrographic sections. In the midlatitude North Atlantic, Talley (2008) produces a band with positive $E-P-R$ whereas the other estimates give negative values. This explains why the basin-integrated $E-P-R$ from Talley (2008) increases when the domain is extended to 60°N in Figure 3.2(b). Inspection of $e-p$ (Figure 3.1) shows net precipitation poleward of 45°N in all basins. This value for the North Atlantic from Talley (2008) is clearly an outlier although there is a large uncertainty for that band. ERA-Interim and Dai and Trenberth (2003) are well matched in the midlatitude North Atlantic but ERA-Interim $E-P-R$ is greater in the northern and southern subtropics with the opposite occurring in the tropics. ECCOv4 agrees well with ERA-Interim throughout the Atlantic but has notably lower $E-P-R$ in the southern hemisphere subtropics. The error bars on the ERA-Interim div$\mathbf{Q}$, however, are somewhat larger in these bands than in the northernmost band due to residuals which are an order of magnitude larger. It is also important to note that these estimates are all taken over different time periods so important events may have been missed out.

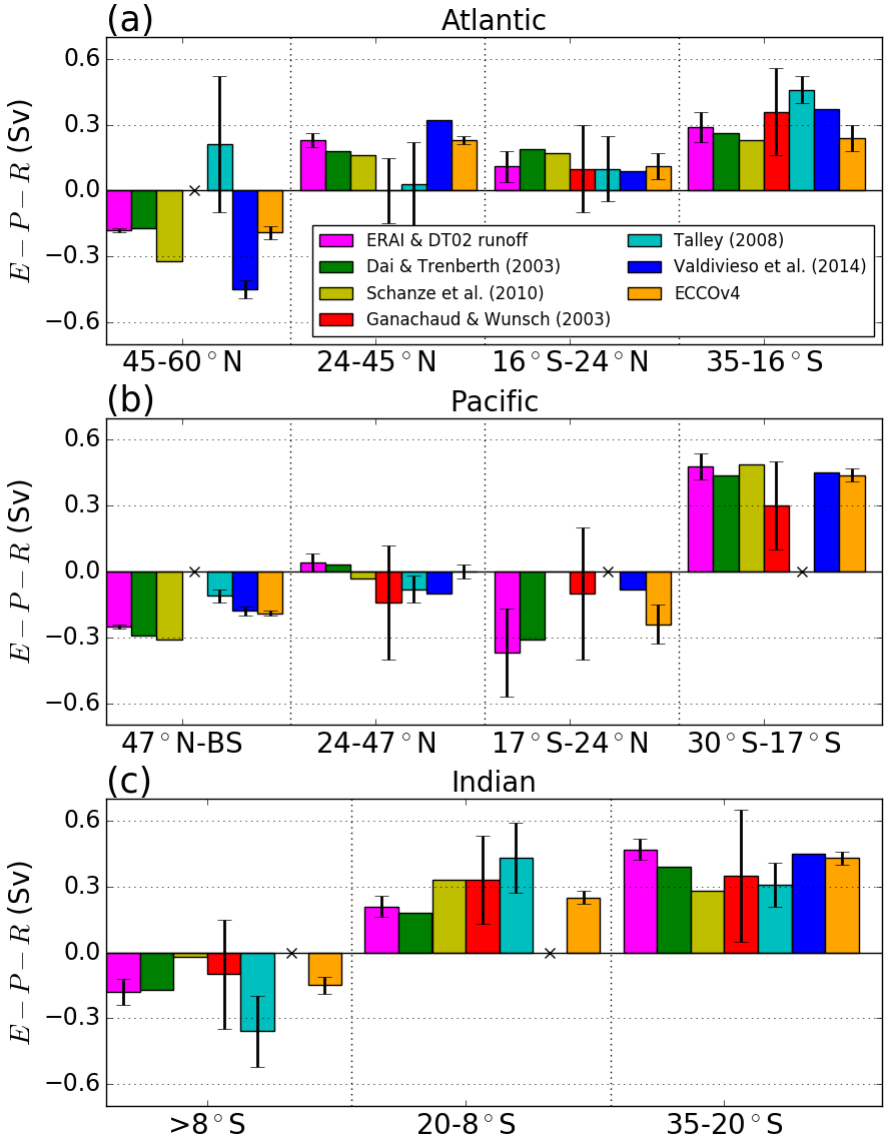

Figure 3.3: $E-P-R$ for latitude bands within the (a) Atlantic, (b) Pacific and (c) Indian oceans for the estimates described in section 3.3. Latitudes below each subfigure refer to those used to break up ERA-Interim. The exact boundaries used in calculating each estimate are shown in Table 3.1. Crosses denote that there is no estimate provided for a band, otherwise $E-P-R=0$.

In the northern hemisphere subtropical Pacific (Figure 3.3b) both atmospheric reanalyses (and NCEP, not shown) show weak positive $E-P-R$ while four of the other estimates are negative (ECCOv4 is indistinguishable from zero). The strongly positive Pacific $E-P-R$ (in comparison to other estimates) from Schanze *et al.* (2010) shown in Figure 3.2 is mainly due to a tropical band which has $E-P-R=0$. The other estimates suggest that the tropical band has negative $E-P-R$ with the atmospheric reanalyses producing stronger negative $E-P-R$ than Ganachaud and Wunsch (2003) and Valdivieso *et al.* (2014). From 47°N to the Bering Strait each estimate agrees that the Pacific has negative $E-P-R$ although it is worth noting that the estimates based on atmospheric data give values of $E-P-R$ which are more

negative than the oceanographic estimates.

In the Indian Ocean (Figure 3.3(c)) the atmospheric reanalyses do not agree as closely as they do over the other ocean basins. This difference appears to occur over the southern part of the ocean and may be a direct result of the different bands used (Table 3.1) which may also contribute towards ERA-Interim having the highest $E - P - R$ overall in that band. The two atmospheric reanalysis products agree much closer in the other two bands but there is more disagreement between the estimates in these bands (despite falling within error bars). One reason for this may be that the oceanographic estimates based on hydrographic sections do not represent climatology and are therefore significantly biased by various factors affecting the freshwater transport such as ITCZ location and wind speed. The different values of the ITF transport used by Ganachaud and Wunsch (2003) and Talley (2008) may also be a factor in the large differences between these estimates. All estimates are in good agreement in the subtropics with a range of approximately $E - P - R = 0.15$ Sv.

A key outcome of the above analysis is that the net freshwater flux $E - P - R$ from ERA-Interim div$\mathbf{Q}$ combined with Dai and Trenberth (2002) runoff agrees well with other estimates, both at basin scale and in latitude bands. We use this as a basis for further analyzing the ERA-Interim fields.

Table 3.2: Annual mean (1979-2014) area-averaged moisture budget residuals for the Atlantic and Pacific Oceans with $\bar{e}$, $\bar{p}$ and $\bar{e} - \bar{p}$ in mm/day.

	residual	$\bar{e}$	$\bar{p}$	$\bar{e} - \bar{p}$
Atlantic	0.08	4.01	2.69	1.32
Pacific	0.08	4.14	4.07	0.07

3.5 ERA-Interim E and P

As shown in section 3.4, the globally averaged residual between div$\mathbf{Q}$ and $E - P$ from time-average surface accumulated forecasts is small in ERA-Interim. The 1979-2014 annual mean globally-averaged residual is 0.06 ± 0.3 mm/day which is an order of magnitude higher than the residual of 0.003 ± 0.3 mm/day calculated by Berrisford *et al.* (2011) for a shorter time period (1989-2008). Residuals at the scale of ocean basins (Table 3.2) are also small and on the same order of magnitude as the global average. Additionally, basin-averaged residuals for both oceans are only small percentages of basin-averaged E and P (less than 3%). In the Atlantic the residual does not affect the sign of $E - P - R$ estimates (cf error bars in Figure 3.2) but since the

Pacific basin-averaged $E-P$ is close to zero, the sign of the net $E-P-R$ is therefore rendered uncertain (Figure 3.2).

Estimates of the partition of $E-P$ into separate evaporation and precipitation estimates over the global oceans are known to be 8-9% too large in ERA-interim (Berrisford *et al.*, 2011) and they are also overestimated in other reanalyses (Trenberth *et al.*, 2011). Brown and Kummerow (2014) point out that this problem is particularly marked in tropical regions although this has improved from ERA-40 (Dee *et al.*, 2011). They suggest that observations of near-surface specific humidity from ships and buoys have a dry bias which results in an overestimation of evaporation and therefore precipitation. In the extratropics, however, precipitation tends to be underestimated. For example, England and Wales precipitation in ERA-Interim is only 72% of the observed rainfall (de Leeuw *et al.*, 2015), with similar results found for other countries at the end of the North Atlantic storm track.

We will now use the separate E and P fields (instead of div$\mathbf{Q}$) to further analyze the Atlantic/Pacific asymmetry.

3.5.1 Annual mean latitude bands

Figure 3.4 shows the net freshwater flux and its constituent parts split into 10° latitude bands from 30°S to 60°N. Here, the fluxes are area-weighted averaged in each band to allow for a more meaningful comparison between ocean basins (e.g. a band in the tropical Pacific has much larger area than a band in the tropical Atlantic). Area-averaged evaporation, precipitation and runoff are denoted by $\bar{e}$, $\bar{p}$ and $\bar{r}$ respectively.

From Figure 3.4 it is clear that, within each basin, $\bar{p}$ is more variable than $\bar{e}$ across latitudinal bands, with peaks in the deep tropics showing the location of the ITCZ. Evaporation decreases with latitude in the northern hemisphere, reflecting the influence of SST on evaporation (D'Addezio and Bingham, 2014) as well as the lower relative humidity characteristic of the subtropical atmosphere (due to air coming from neighbouring continents and descending into the boundary layer in the subtropical highs). In the Atlantic (Figure 3.4(a)), runoff has a particularly large impact on the net surface flux: despite $\bar{e}$ exceeding $\bar{p}$ in the 0°-10°S band, the net flux is negative because of large runoff ($\bar{r}$) from rivers such as the Amazon and Congo.

To further localize the asymmetries seen at large scale (Figures 3.2 and 3.3), the differences (Pacific minus Atlantic) are shown in Figure 3.5. The most noticeable asymmetry is that Pacific $\bar{p}$ exceeds Atlantic $\bar{p}$ in almost all latitudes with the difference peaking slightly above 100

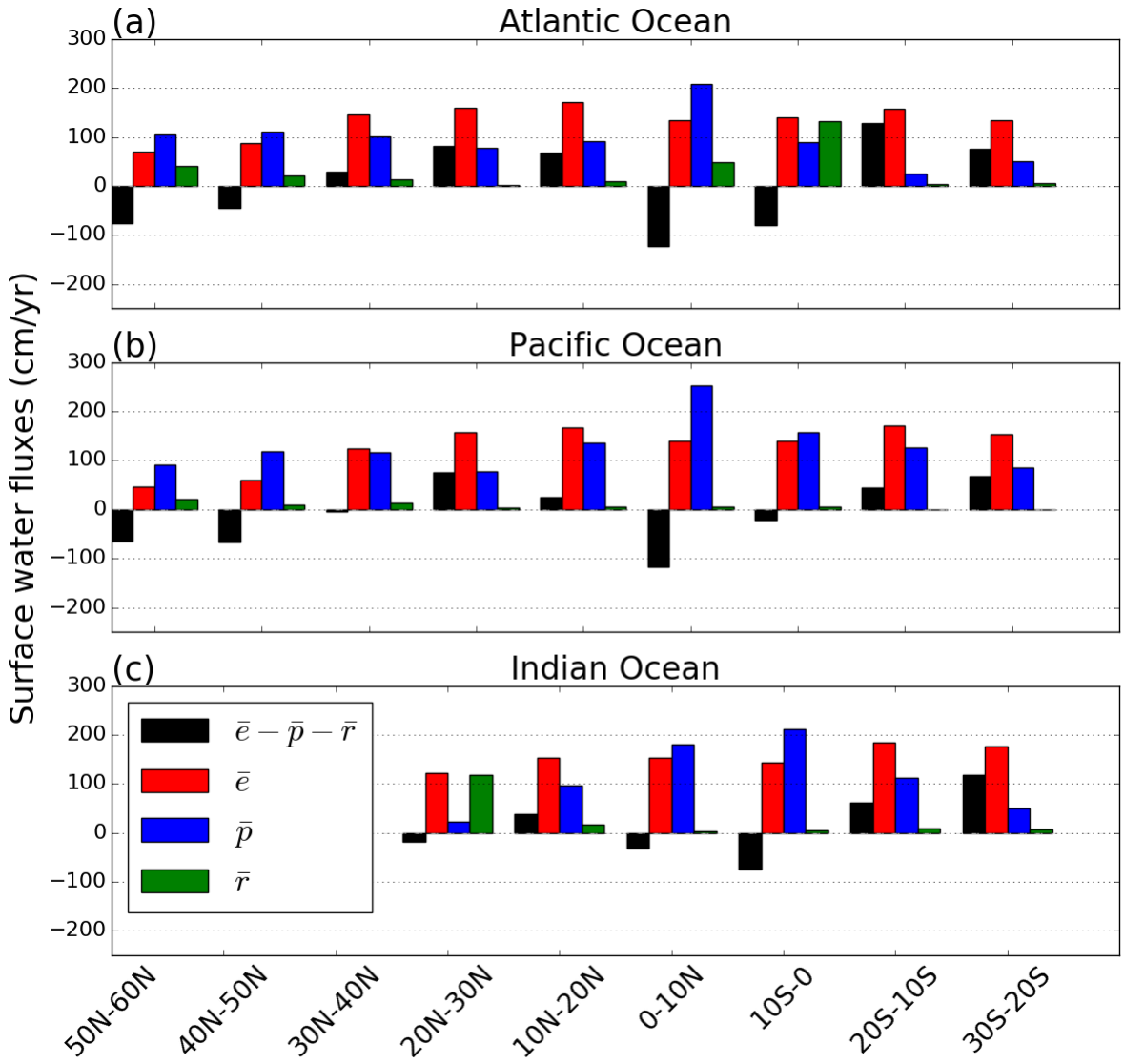

Figure 3.4: Annual mean area-averaged ERA-Interim (1979-2014) surface water fluxes in 10° latitude bands for the (a) Atlantic, (b) Pacific and (c) Indian oceans with Dai and Trenberth (2002) runoff divided into the same 10° latitude bands.

cm/yr in the 20-10°S band, likely due to the presence of the SPCZ. Note that south of 30°N $\bar{e}$ is remarkably similar in both ocean basins.

In the 50°N-60°N band, Atlantic $\bar{p}$ is 15 cm/yr greater than in the Pacific. Note that this result is sensitive to the choice of the latitudinal extents: for slightly larger bands (Emile-Geay *et al.*, 2003; Wills and Schneider, 2015), $\bar{p}$ is similar across basins and $\bar{e}$ is greater in the Atlantic than the Pacific. Polewards of 40°N the Atlantic $\bar{e}$ exceeds the Pacific $\bar{e}$ by about 20 cm/yr: this is likely related to higher SSTs in the North Atlantic than the North Pacific (Warren, 1983) and the greater fraction of the North Atlantic affected by the advection of cold, dry air from the continents (Schmitt *et al.*, 1989). Wills and Schneider (2015) argued that the asymmetry in the subpolar regions is primarily due to moisture fluxes from transient eddies which cause

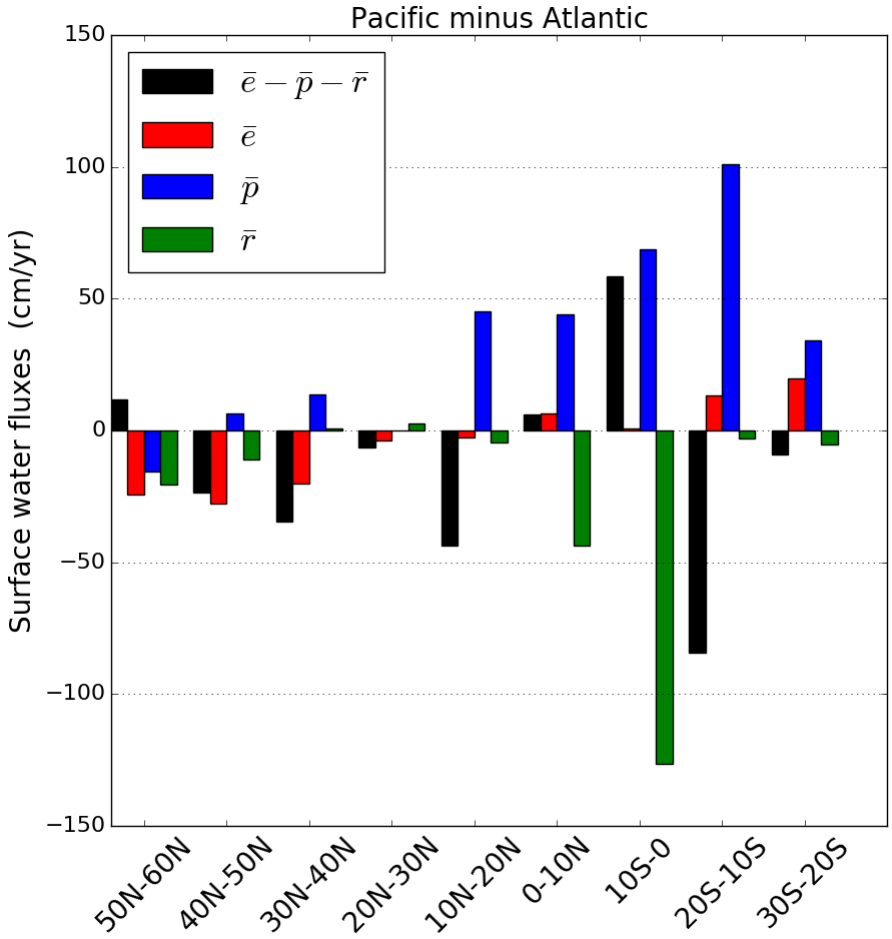

Figure 3.5: Differences between area-averaged annual mean ERA-Interim (1979-2014) Pacific and Atlantic surface water fluxes in 10° latitude bands scaled by area with Dai and Trenberth (2002) runoff divided into the same 10° latitude bands.

negative $E - P$ over the subpolar North Pacific and positive $E - P$ over the subpolar North Atlantic. The total runoff into the Atlantic is greater than into the Pacific with most of the difference between the two basins occurring in the 0°-10°N and 10°S-0° bands where some of the world's largest rivers can be found. The mouths of the two largest (Amazon and Congo) plus three of the top twenty are in the band to the south of the equator (Dai and Trenberth, 2002). The Orinoco (third largest) and three more of the top forty discharge into the Atlantic band immediately north of the equator.

Although a larger $\bar{e}$ is found in the North Atlantic than in the North Pacific, the asymmetry in the net freshwater flux across the basins is mostly caused by an asymmetry in $\bar{p}$, *i.e.* relatively strong precipitation in the Pacific. There are only three 10° bands where Pacific $\bar{e} - \bar{p} - \bar{r}$ is greater. Two of which (10°S-0° and 0°-10°N) are a result of the strong asymmetry in $\bar{r}$ (masking a large precipitation excess in the Pacific) and the other is the narrow northern most band in the Pacific which contributes very little to the basin-averaged net flux. Note that despite the fact

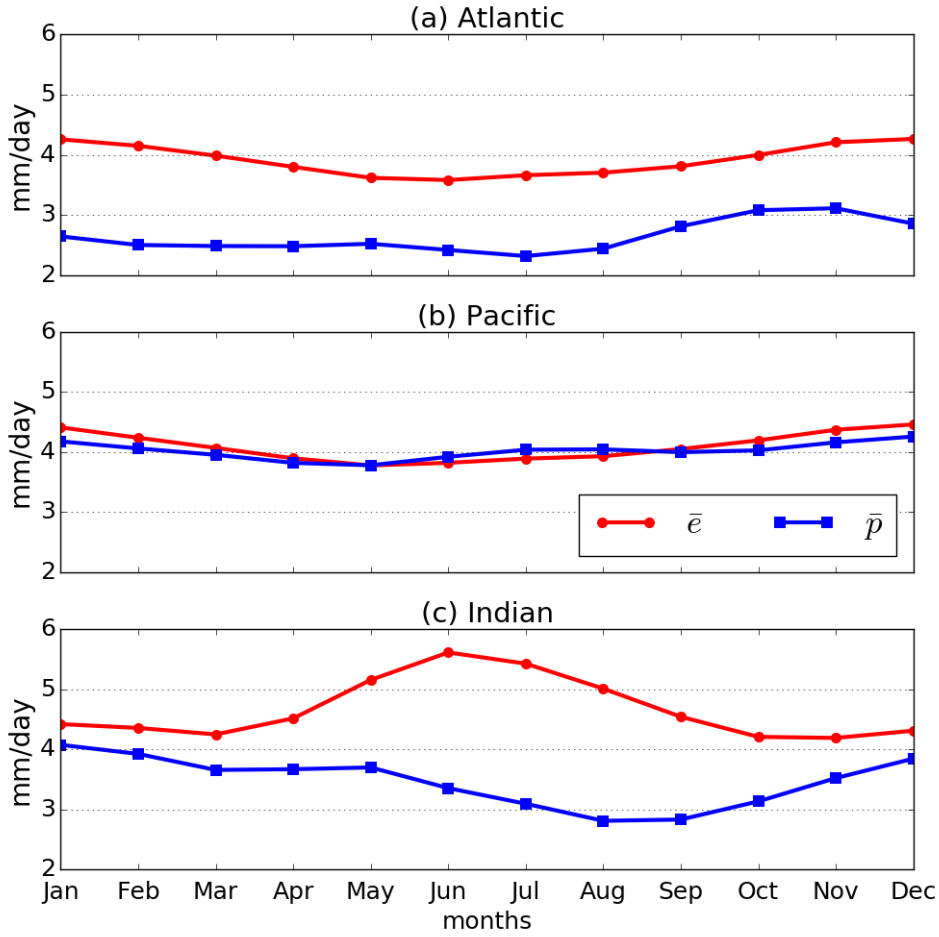

Figure 3.6: Climatological monthly means (1979-2014) of ERA-Interim $\bar{e}$ and $\bar{p}$ for the (a) Atlantic (35°S-60°N), (b) Pacific (30°S-Bering Strait) and (c) Indian (>35°S) Oceans at basin scale (first row of ERA-Interim columns in Table 3.1).

that these bands have less negative $\bar{e} - \bar{p} - \bar{r}$ in the Pacific, the salinity asymmetry still holds at all latitudes.

3.5.2 Seasonal variation

Figure 3.6 shows the seasonal cycle of $\bar{e}$ and $\bar{p}$ for each ocean basin; the maps of the climatological seasonal means of $e - p$, e and p are shown in Figures 3.7-3.9. Atlantic and Pacific mean evaporation rates are very similar (and quite constant at $\sim$4 mm/day). There is however a substantially lower precipitation rate in the Atlantic than in the Pacific, with Atlantic $\bar{p}$ near 2.5 mm/day compared to 4 mm/day in the Pacific. These features are present throughout the year, with the $\bar{e} - \bar{p}$ always positive over the Atlantic and always close to zero over the Pacific. In the Pacific, $\bar{e}$ and $\bar{p}$ have similar annual cycles with a decrease from January to May followed by an increase during the rest of the year. The annual cycle of $\bar{e}$ has a similar amplitude (~ 0.7 mm/day) in both basins but the amplitude of $\bar{p}$ is weaker in the Pacific (~ 0.5 mm/day com-

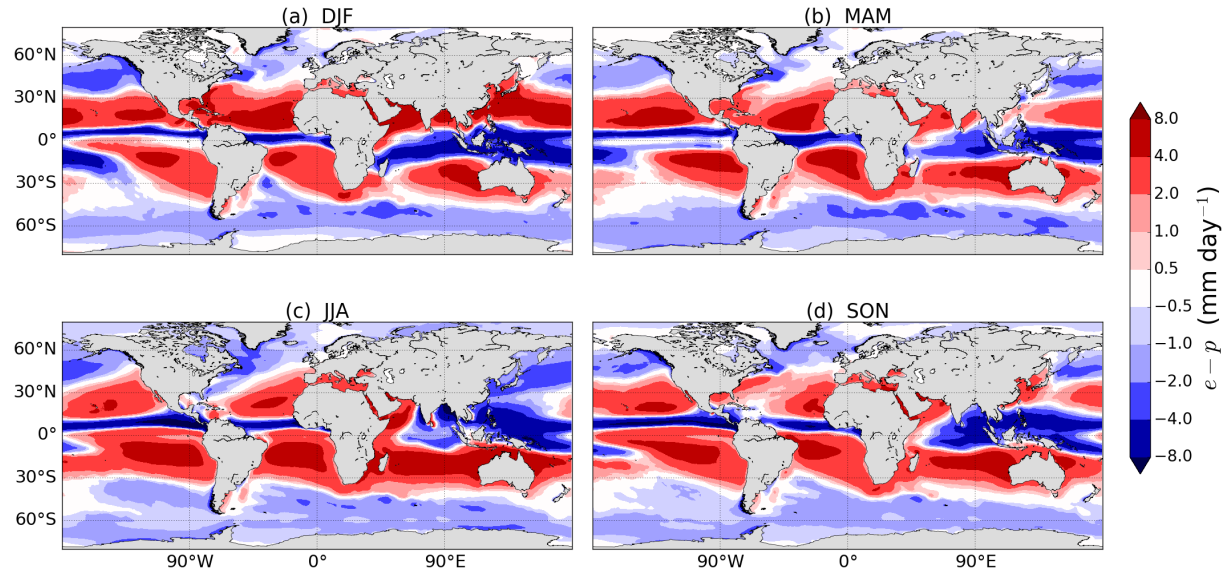

Figure 3.7: Climatological seasonal mean ERA-Interim $e-p$ from accumulated surface forecasts 1980-2014 for (a) December-January-February (DJF), (b) March-April-May (MAM), (c) June-July-August (JJA) and (d) September-October-November (SON).

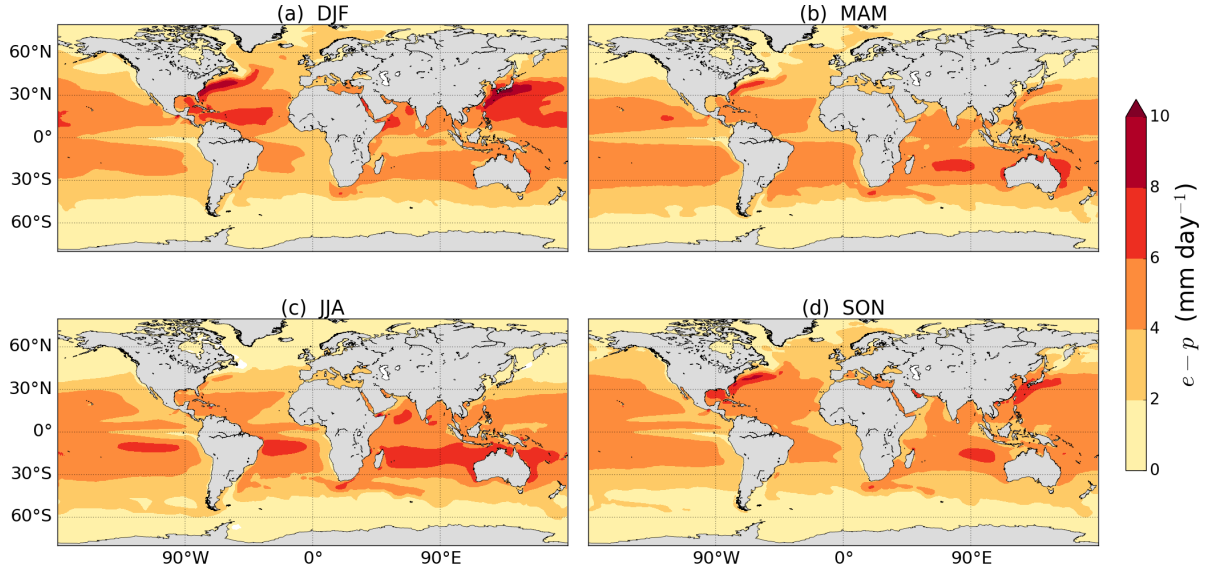

Figure 3.8: Climatological seasonal mean ERA-Interim evaporation 1980-2014 for (a) DJF, (b) MAM, (c) JJA and (d) SON.

pared to ~ 0.8 mm/day).

These effects are also reflected in the spatial pattern of seasonal $e-p$ which largely follows the spatial pattern of precipitation (Figures 3.7-3.9). The subtropical regions (where $e-p>0$) are characterized by a lack of precipitation in all seasons with the shape and size of the region of positive $e-p$ approximately matching the shape and size of the regions with $p<2$ mm/day. Seasonal variations of evaporation (Figure 3.8) are most noticeable in the subtropical maxima and in the peaks over western boundary currents. Both oceans show maxima of evaporation

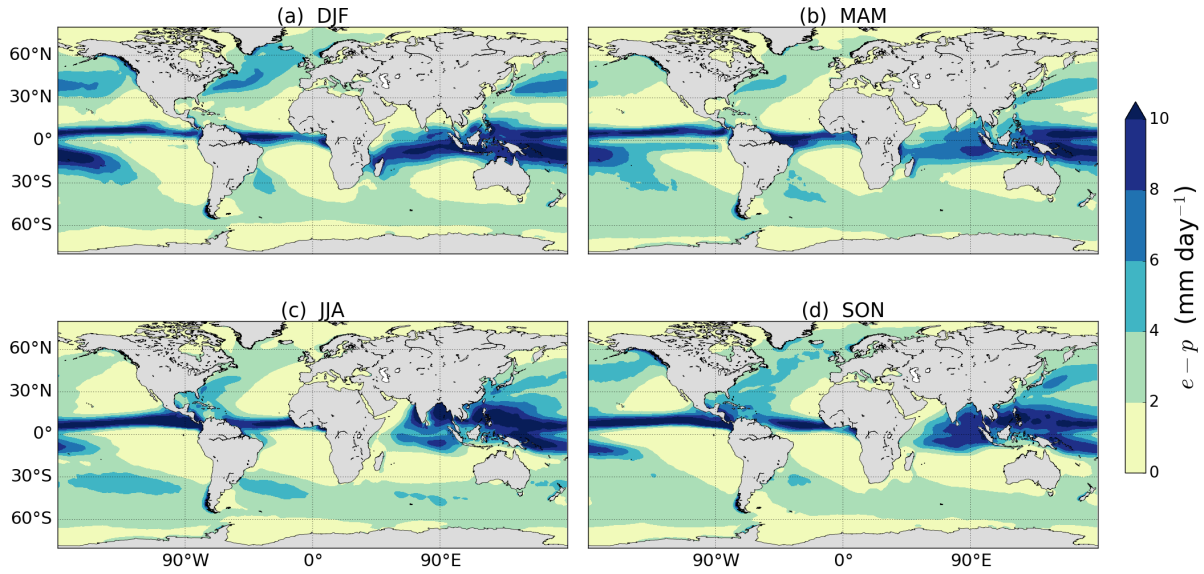

Figure 3.9: Climatological seasonal mean ERA-Interim precipitation 1980-2014 for (a) DJF, (b) MAM, (c) JJA and (d) SON.

in the northern hemisphere winter which is a result of increased wind speeds and the lower relative humidity. The advection of dry (subsaturated) winter air from continents to the oceans maintains high rate of evaporation, and therefore high wintertime latent heat flux, over the western part of basins, and notably over Western Boundary Currents such as the Gulf Stream and Kuroshio (Yu and Weller, 2007).

Further decomposing the seasonal cycle into latitudinal bands shows that the October/November peak in Atlantic $\bar{p}$ occurs in the northern hemisphere (Figure 3.10b). During autumn the water vapour content of the subtropics is higher due to increased evaporation (Figure 3.8d) and this is picked up by the storm tracks leading to increased meridional water vapour transport. D'Addezio and Bingham (2014) also attribute the autumn peak in subtropical North Atlantic precipitation to African easterly wave activity and tropical storm activity. Wang *et al.* (2013) highlights the influence of seasonal cycle of SSTs and the Atlantic Warm Pool (AWP) area, both of which peak in September along with $\bar{p}$ in the 15°N-35°N band (the AWP is a region of SST $>$ 28.5°C in the western tropical North Atlantic, 5°N-30°N). A minimum of SSS also occurs in the AWP region in September with a maximum in March when the AWP disappears (a month after the $E - P$ maximum). Initially the peak is in the subtropics but is later maintained at higher latitudes in winter (Figures 3.9a,d). The double peak in tropical Atlantic precipitation is a due to the seasonal migration of the ITCZ which dominates the tropical SSS seasonal cycle (Boyer and Levitus, 2002).

The annual cycle of Pacific $\bar{p}$ (Figure 3.11(b)) is also dominated by the northern hemisphere

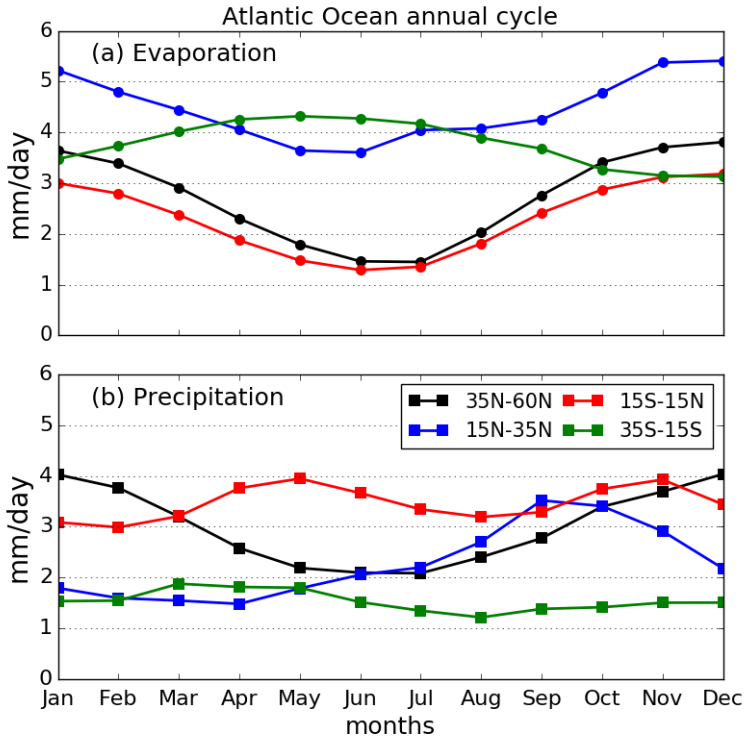

Figure 3.10: Climatological monthly means of ERA-Interim (1979-2014) Atlantic Ocean area-averaged (a) evaporation and (b) precipitation in latitude bands representing the tropics, subtropics and northern hemisphere extratropics.

(reflecting the fact that most of the domain used to define the Pacific in this study is in the northern hemisphere), with the May-July minimum occuring in the midlatitudes due to a relatively weak storm track. The peaks in $\bar{p}$ in the northern subtropics in August and during winter in the midlatitudes are due to the same process found in the subtropical North Atlantic at the same times of year.

3.5.3 Interannual variability

The interannual variability of evaporation, precipitation, $\bar{e} - \bar{p}$ and div$\mathbf{Q}$ are shown along with the GPCP estimate of precipitation (Adler *et al.*, 2003) as anomalies from their respective annual means in Figure 3.12. Precipitation time series are shown as $-\bar{p}$ in order to simplify the comparison with $\bar{e} - \bar{p}$ and div$\mathbf{Q}$. Until 2002, ERA-Interim precipitation appears to match GPCP variability well (particularly over the Atlantic) but the two datasets differ significantly in 2002-06. This is particularly evident over the Pacific where ERA-Interim $-\bar{p}$ increases sharply while $-$GPCP does not. This shift in precipitation is due to a problem with the assimilation of rain-affected radiances that caused an incorrect drying of the atmosphere (Dee *et al.*, 2011). Note the large offset between div$\mathbf{Q}$ and $\bar{e} - \bar{p}$ in the Pacific (Figure 3.12b). ERA-Interim does, however,

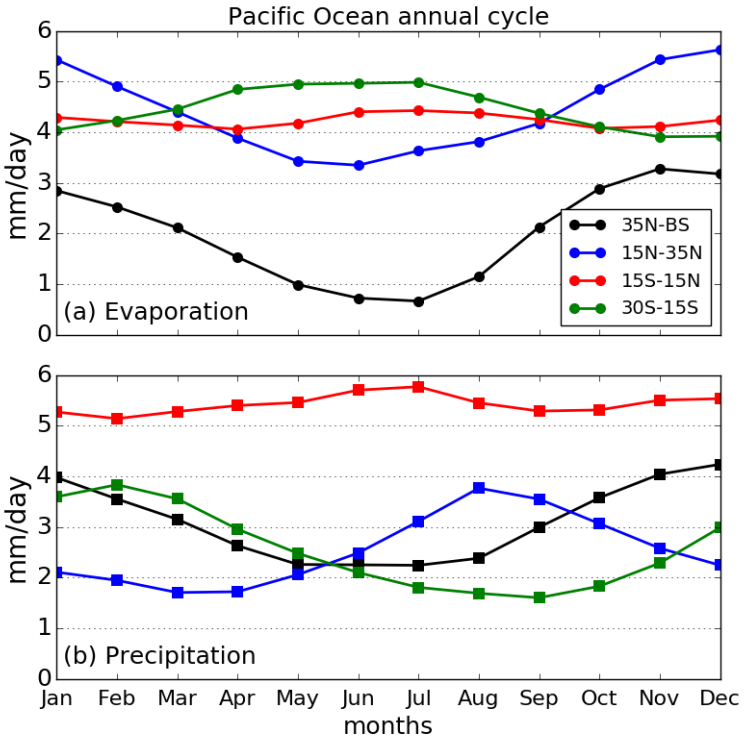

Figure 3.11: Climatological monthly means of ERA-Interim (1979-2014) of Pacific Ocean area-averaged (a) evaporation and (b) precipitation in latitude bands representing the tropics, subtropics and northern hemisphere extratropics.

capture some of the El Niño-driven variability *i.e.* the 1997-98 El Niño is shown by a dip in $-\bar{p}$ by both ERA-Interim and GPCP. The Atlantic appears to be less affected by the assimilation problems: the GPCP variability from 2004-06 is reproduced in $-\bar{p}$ while still offset from $-$GPCP by ~ 3 cm/yr. ERA-Interim also successfully reproduces the large $-\bar{p}$ decrease (a subsequent decrease in $\bar{e} - \bar{p}$) in 2010 associated with a record low North Atlantic Oscillation (NAO) Index and a 30% reduction in the AMOC (Roberts *et al.*, 2013; Bryden *et al.*, 2014). Increases in the area of the AWP on interannual timescales are shown to reduce $E - P$ due to increased SSTs and therefore increased moisture convergence into the region resulting in increased precipitation (Wang *et al.*, 2013). This then causes negative SSS anomalies which Wang *et al.* (2013) speculated may have an impact on the strength of the AMOC.

Evaporation appears to be less variable than precipitation in both basins and contributes less to the variability of ERA-Interim $\bar{e} - \bar{p}$. In the Pacific, however, evaporation changes contribute significantly to $\bar{e} - \bar{p}$ changes during the events such as the 1997-98 El Niño. This El Niño event is known to have caused an SSS decrease in the western equatorial Pacific and an SSS increase around the SPCZ, with precipitation considered to be one of the main mechanisms responsible for these SSS changes (Singh *et al.*, 2011). Increasing trends in $\bar{e}$ are evident

Table 3.3: Pearson correlations ($\widetilde{r}$) between annual means of ERA-Interim $\bar{e}$, $-\bar{p}$ and $\bar{e}-\bar{p}$ with div$\mathbf{Q}$ and standard deviations (σ, cm/yr) of $\bar{e}$, $-\bar{p}$, $\bar{e}-\bar{p}$ and div$\mathbf{Q}$.

	Atlantic		Pacific	
	$\widetilde{r}$	σ	$\widetilde{r}$	σ
$\bar{e}$	0.40	3.0	0.51	4.5
$-\bar{p}$	0.51	4.0	0.39	4.7
$\bar{e}-\bar{p}$	0.73	4.3	0.64	6.5
div$\mathbf{Q}$	1.0	3.0	1.0	2.1

in both basins throughout the ERA-Interim period. The Pacific trend is stronger than the Atlantic trend, with $\bar{e}$ increasing at a rate of 3.4 mm/yr/yr (least-squares linear fit) compared to 2.0 mm/yr/yr in the Atlantic. Increasing trends in oceanic evaporation are also present in other datasets (Iwasaki *et al.*, 2014; Su and Feng, 2015). Yu and Weller (2007) show that latent heat flux has increased in line with SSTs, resulting in an increase in evaporation rate of approximately 10 cm/yr from 1986-2005. This value compares well with ERA-Interim (Figure 3.12) for the same period over the Pacific. As well as increasing SSTs, increasing wind speed has also been noted to contribute to increasing evaporation rates (Yu, 2007; Iwasaki *et al.*, 2014). Column-integrated water vapour has also been increasing as shown by the Special Sensor Microwave Imager (SSM/I), a trend which is well represented by reanalyses (Zhang *et al.*, 2013). Such an increase in column-integrated water vapour would require a corresponding increase in oceanic evaporation. This suggests that, unlike the precipitation trends, evaporation trends in ERA-Interim may be real and capture a physical change (although Brown and Kummerow (2014) show that ERA-Interim overestimates tropical evaporation).

Table 3.3 shows the correlations of $\bar{e}$, $-\bar{p}$, $\bar{e}-\bar{p}$ with div$\mathbf{Q}$ and the standard deviations of each field. The correlations highlight the inconsistencies between the two methods of calculating the surface water flux. The moisture flux divergence is better correlated with $\bar{e}-\bar{p}$ over the Atlantic than the Pacific. In particular, $-\bar{p}$ and div$\mathbf{Q}$ are poorly correlated over the Pacific, as expected from Figure 3.12b. The standard deviations show that all Pacific fluxes are more variable than the Atlantic fluxes, with $-\bar{p}$ showing more interannual variablity than $\bar{e}$ over each ocean. Table 3.3 also shows that the asymmetry in $\bar{p}$ discussed in section 3.5.2 is also steady on interannual time scales, with Pacific $\bar{p}$ exceeding Atlantic $\bar{p}$ by approximately 40 cm/yr (not shown).

Although Figure 3.12 also shows that $\bar{e}-\bar{p}$ mainly follows the interannual variability of

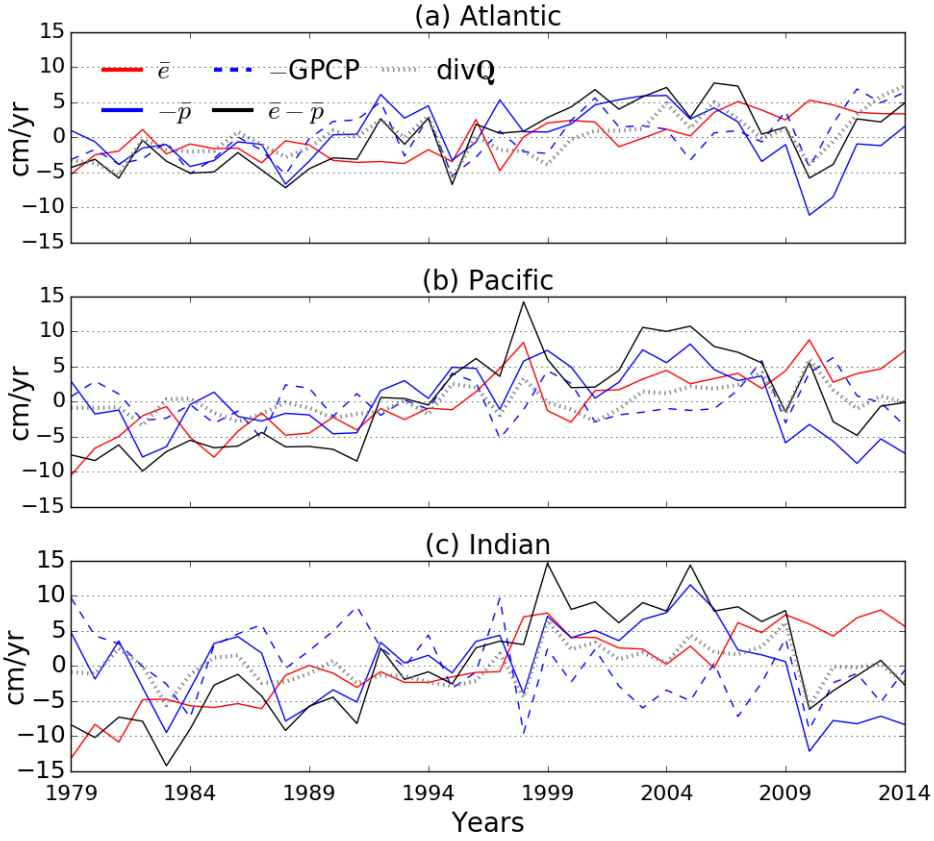

Figure 3.12: Yearly anomalies from the 1979-2014 area-averaged annual mean ERA-Interim $\bar{e}$, $-\bar{p}$, $\bar{e}-\bar{p}$, div$\mathbf{Q}$ and -GPCP for the (a) Atlantic, (b) Pacific and (c) Indian oceans at basin scale (first row of ERA-Interim columns in Table 3.1).

$-\bar{p}$, the variability and trends in ERA-Interim are, as discussed above, not robust. That said, in the Atlantic before 2002 when ERA-Interim $\bar{p}$ matches GPCP well (correlation coefficient of 0.82), $-\bar{p}$ correlates with div$\mathbf{Q}$ better than with $\bar{e}$ (0.59 with $-\bar{p}$ over both oceans and 0.11 and 0.32 for $\bar{e}$ in the Atlantic and Pacific respectively). This suggests that $\bar{p}$ may well dominate $\bar{e}-\bar{p}$ variability in the Atlantic (at least before 2002). In the Pacific, correlation between ERA-Interim and GPCP before 2002 are poorer (only 0.43), and the dominant factor in variability cannot be deduced.

3.6 Summary and conclusions

In this paper, we compare seven estimates of the net freshwater flux ($E-P-R$) over oceans, with a focus on the $E-P-R$ asymmetry between the Atlantic and Pacific oceans. Using ERA-Interim, which compares favourably with other estimates, we proceed on exploring the Atlantic/Pacific asymmetry on spatial (10° latitudinal bands) and temporal (seasonal, interannual) scales not accessible with some other datasets as well as investigating the role of pre-

cipitation, evaporation and runoff separately on the $E - P - R$ asymmetry. Our key findings are:

1. Net surface water fluxes estimated from atmospheric reanalyses are consistent with the ocean temperature and salinity observations used to estimate net freshwater fluxes from hydrographic section data. Both are also consistent with other datasets including recent ocean reanalyses. All estimates show that the Atlantic has greater positive $E-P-R$ than the Pacific. Pacific $E - P - R$ is approximately 0 Sv when the subpolar region is included and is approximately 0.4 Sv less than Atlantic $E - P - R$. Agreement between datasets is less strong in smaller latitude bands, however the $E - P - R$ still holds in the tropics and northern hemisphere although not in the southern hemisphere subtropics (due to the larger area of the Pacific).
2. We also find that ERA-Interim div$\mathbf{Q}$ and $E-P$ from surface forecast accumulations agree well when averaged globally or across ocean basins (consistent with Berrisford *et al.*, 2011) which establishes the validity of the ERA-Interim estimates for further diagnostics. Annual mean area-averaged evaporation, precipitation, runoff and $E - P - R$ across 10° latitude bands show that the asymmetry in $E - P - R$ in the high latitude northern hemisphere is mainly due to greater evaporation from the Atlantic (*e.g.* Warren, 1983; Emile-Geay *et al.*, 2003) but everywhere further south it appears that a stronger asymmetry in precipitation is more important in contributing to the asymmetry in $E - P - R$. At basin scale the $E - P - R$ asymmetry is largely caused by a precipitation asymmetry, rather than an evaporation asymmetry. One potential mechanism for this is linked to the patterns of stationary eddies over the two basins: the subtropical highs (areas of dry, descending air and low precipitation) cover a larger fraction of the Atlantic than the Pacific where ascending air (which leads to precipitation) covers a larger fraction of the basin. (Wills and Schneider, 2015).
3. The seasonal cycles of basin-averaged evaporation and precipitation show that the Atlantic/Pacific asymmetry exists throughout the year and is quite steady *i.e.* no particular season contributes to the asymmetry. Throughout the year, Pacific evaporation and precipitation are approximately equal but Atlantic precipitation is always less than evaporation. There is little difference between basin-averaged evaporation but basin-averaged precipitation is less in the Atlantic than the Pacific for all months.
4. Because of problems with the assimilation of satellite data described by Dee *et al.* (2011),

trends and interannual variability in precipitation are not robust (a conclusion supported by a comparison with GPCP precipitation). It is therefore problematic to explore the interannual variability of precipitation and its correlation with $E-P$. An upward trend in evaporation over recent decades in both basins appears to be consistent with the estimate from OAFlux. The interannual variability of the basin-averaged $E - P$ fluxes exhibit correlations with events such as large El Niño and NAO events.

Overall, a key finding of this study is that the $E - P - R$ asymmetry between the Atlantic and Pacific oceans exists at all latitudes, not just high-latitudes and that, outside of the high latitude northern hemisphere, an asymmetry in precipitation, rather than evaporation, has more influence on the asymmetry in $E - P - R$. Precipitation is largely driven by internal atmospheric processes (circulation patterns, atmospheric physics). This suggests that $E-P-R$ and possibly SSS and MOC asymmetries are caused by differences in atmospheric processes over the two basins. Some potential mechanisms have been suggested in the literature: the basin geometry (Schmitt *et al.*, 1989; Ferreira *et al.*, 2010; Nilsson *et al.*, 2013), the effect of mountain ranges (Schmittner *et al.*, 2011; Sinha *et al.*, 2012), variability and tilt of the Atlantic storm track (Czaja, 2009) and the patterns of stationary eddies (Wills and Schneider, 2015).

Considering on one hand the link between the high salinity of the Atlantic, the deep convection and the AMOC, and on the other the link between SSS distribution and $e-p-r$ pattern, we argue that any theory for the localization of the MOC in the Atlantic should provide an explanation for the $E-P-R$ asymmetry, and thus for the deficit of precipitation over the Atlantic. It is worth emphasizing that an $E - P - R$ asymmetry may not be neccessary to localize deep water formation in the Atlantic and favour an AMOC. This is notably the case in the presence of multiple equilibria of the MOC where localization is possible with no asymmetry or reversed asymmetry (smaller $E - P - R$ in the sinking basin, see Huisman *et al.* 2009). However, even if the real ocean is in this dynamical regime, the observed $E - P - R$ asymmetry provides a significant reinforcement of the AMOC (an atmospheric feedback or perhaps just a coincidence *e.g.* due to geometrical factors), and should be accounted for.

Chapter 4

Linking $P - E$ mean state and variability to moisture fluxes across basin boundaries

It was shown in the previous chapter that an asymmetry in area-averaged precipitation rate is the main contribution to the asymmetry in the moisture budgets between the Atlantic and Pacific Oceans, where area-averaged precipitation is greater over the Pacific than over the Atlantic and there is little difference in evaporation rates per unit area. This result implies that atmospheric moisture transport plays a crucial role in setting the asymmetry in the moisture budgets. In this chapter, the relationships between the mean state and variability of $P - E$ of each ocean drainage basin (defined in chapter 2) and the adjacent moisture fluxes are analyzed with a view to determining which transports are most important in setting the asymmetry.

4.1 Introduction

4.1.1 Mathematical concepts

The horizontal moisture flux is calculated by weighting the horizontal wind vector ($\mathbf{v}$) by specific humidity (q) such that $\mathbf{Q} = q\mathbf{v}$. The horizontal moisture flux is linked to $E - P$ through Divergence Theorem where the integral of the moisture fluxes normal to the boundary of an

ocean drainage basin is equal to the volume integral of moisture flux divergence:

$$\iiint_V \nabla \cdot \mathbf{Q} \, \mathrm{d}V = \frac{1}{g} \oiint_{\partial V} \mathbf{Q} \cdot \hat{\mathbf{n}} \, \frac{\partial \tilde{p}}{\partial \eta} \, \mathrm{d}\eta \, \mathrm{d}l, \tag{4.1}$$

where V is volume, $g = 9.81$ m s^{-2} is acceleration due to gravity, $\hat{\mathbf{n}}$ is a unit normal vector, ∂V is the boundary, η is the hybrid vertical co-ordinate, $\tilde{p}$ is pressure (hPa) and dl is the length of the boundary. From equation (3.1),

$$E - P = \frac{1}{g} \oiint_{\partial V} \mathbf{Q} \cdot \hat{\mathbf{n}} \, \frac{\partial \tilde{p}}{\partial \eta} \, \mathrm{d}\eta \, \mathrm{d}l. \tag{4.2}$$

In this chapter the vertically-integrated moisture flux normal to the catchment boundaries of the ocean drainage basins is calculated from monthly mean ERA-Interim zonal (qu) and meridional (qv) moisture flux fields and used to discover the boundaries that contribute most to the differences in area-averaged precipitation for the ocean basins.

4.1.2 The Role of Central America

The current understanding of the role of atmospheric moisture transport in the moisture budget asymmetry is that strong moisture transport in the trade winds across Central America is the primary cause of the moisture budget asymetry between the Atlantic and Pacific Oceans. This theory first appears in Dietrich (1963) where it is stated that moisture evaporated from the Atlantic is transported in the trade winds and contributes to high precipitation and therefore low SSS in the Gulf of Panama. Weyl (1968) suggests that that the Isthmus of Panama (a very narrow strip of land) is the primary location for this moisture transport. SSS is indeed lower in the eastern Pacific off the west coast of Panama (Figure 1.1) but it seems unlikely that moisture transport through such a narrow gap and precipitation over such a small area could have such substantial effects on the moisture budget and SSS asymmetries of the entire ocean basins. It is not clear from the literature if there is consensus as to whether the Isthmus of Panama or Central America in general is the main location for the Atlantic-to-Pacific moisture transport as some authors name the Isthmus of Panama specifically (Zaucker and Broecker, 1992; Lohmann, 2003; Leduc *et al.*, 2007; Sinha *et al.*, 2012) where as others refer to Central America in general (Broecker, 1991; Richter and Xie, 2010; Schmittner *et al.*, 2011; Wang *et al.*, 2013).

The supposed predominance of the Central American moisture transport on the Atlantic/Pacific moisture budget asymmetry was highlighted by Broecker (1991) with an esti-

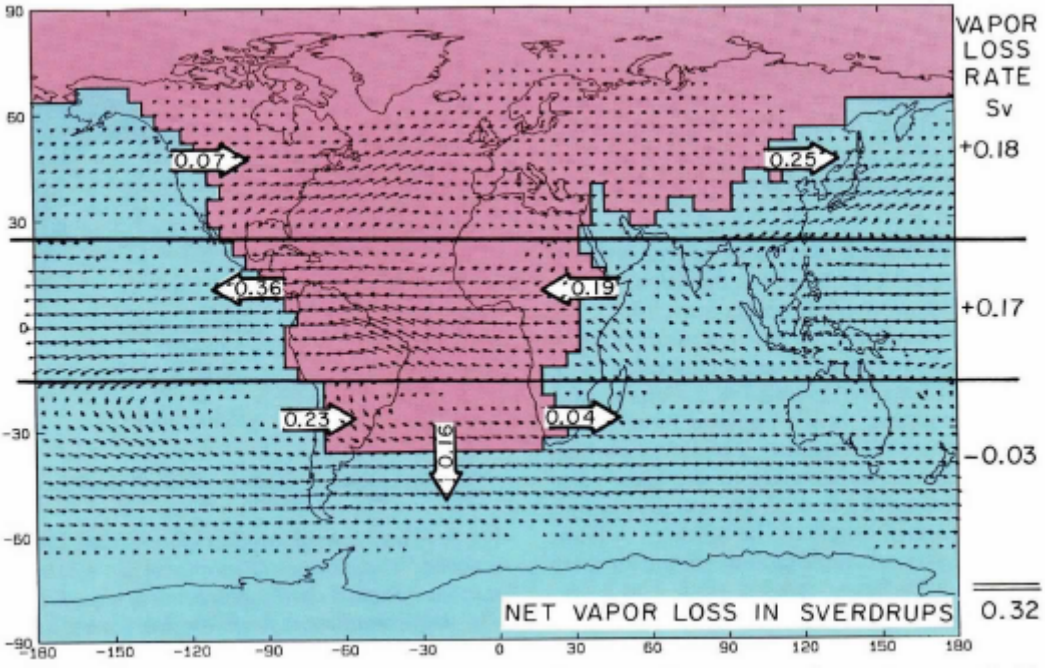

Figure 4.1: Map of atmospheric moisture fluxes between the Atlantic/Arctic drainage basin (red) and rest-of-the-world (blue) from Broecker (1991). The moisture fluxes were calculated using winds and humidity data from Oort (1983) on a $4^\circ \times 5^\circ$ grid and 11 vertical levels. The large white arrows represent the integrated moisture flux (Sv) normal to the catchment boundary surrounding the Atlantic/Arctic drainage basin and the small black arrows are the moisture flux vectors. The column down the right-hand side of the figure shows the water vapour loss rate (Sv) for each region of the Atlantic/Arctic drainage basin with the net water vapour loss rate shown at the bottom of the column. Broecker (1991) interprets the water vapour loss rate from this figure as $\overline{P - E}$ (see point 1 in section 4.1.3).

mate of moisture fluxes between the Atlantic/Arctic drainage basin and the 'rest of the world' (Figure 4.1). The loss rate of the tropical band in Figure 4.1 is the difference between the incoming flux across Africa and the outgoing flux across Central America ($0.36 - 0.19 = 0.17$ Sv). Therefore the tropical Atlantic loses 0.17 Sv water vapour to the rest of the world. From this, Broecker (1991) concluded that since the outgoing moisture flux across Central America is the largest transport of moisture in the atmosphere around the Atlantic/Arctic drainage basins, this flux is the primary cause of the aysmmetries in moisture budget and salinity between the Atlantic and Pacific Oceans. This interpretation was built upon in subsequent studies (Zaucker and Broecker, 1992; Zaucker *et al.*, 1994).

There is indeed strong moisture transport across Central America (ranging between 0.29 Sv and 0.72 Sv; Richter and Xie, 2010) as the easterly trade winds converge along the ITCZ where they become zonal (Figure 1.5). The orography in Central America is generally lower than orgography in the mountain ranges of North and Central America (Figure 2.12(a)) therefore the rain shadow effect is reduced. The Carribean LLJ is the major mechanism for moisture

transport in the region and is the main contributor towards Central American precipitation (Duran-Queseda *et al.*, 2010). Moisture transport across Central America is particularly strong in three valleys, namely Tehuantepec, Papagayo and Panama, where strong gap wind jets exist, and a regional climate model has shown that moisture transport above Lake Nicaragua in the Papagayo jet is stronger than the transport across Panama (Xu *et al.*, 2005).

4.1.3 Problems with focus on Central American moisture flux

Although Broecker (1991) and Figure 4.1 have influenced the common understanding of the moisture budget asymmetry, there are three significant flaws to the interpretation of Figure 4.1:

1. Divergence Theorem is not satisfied as the meridional fluxes across 25°N and 15°S are not included in Figure 4.1 - see equation (4.2). Therefore the rate of water vapour loss from the tropical Atlantic cannot be 0.17 Sv (unless the meridional fluxes sum to zero). It can be seen from more recent estimates (Figures 4.4 and 4.5) that these transports are far from negligible.
2. As discussed by Ferreira *et al.* (2018), the moisture flux across the Americas is approximately as large as the zonal mean zonal moisture flux ($[\overline{uq}]$, overbar denotes time mean). Therefore suggesting that the $\overline{P-E}$ asymmetry exists because the moisture flux across the Americas is anomalously large may be misleading.
3. Understanding the fluxes in Figure 4.1 simply as transports from one ocean basin to the next may be incorrect. This is a purely Eulerian understanding of the hydrological cycle and cannot take into account remote sources of moisture. For example, the moisture flux across Central America may not be of purely Atlantic origin and may include moisture with origin in the other ocean basins.

4.2 New estimate of moisture fluxes normal to catchment boundaries

In Figure 4.2 an updated map of $\overline{\mathbf{Q}} \cdot \hat{\mathbf{n}}$ on catchment boundaries and the atmospheric moisture budgets ($\overline{P-E}$) for each ocean drainage basin is presented. This uses the catchment boundaries defined in chapter 2 (Figure 2.11) and annual mean (1979-2014) ERA-Interim vertically integrated moisture fluxes. No mass adjustment was applied to the moisture fluxes for these calculations as Berrisford *et al.* (2011) say it is not neccessary to do so in ERA-Interim.

The fluxes shown in Figure 4.2 show what would be expected from Figure 1.5. Westward

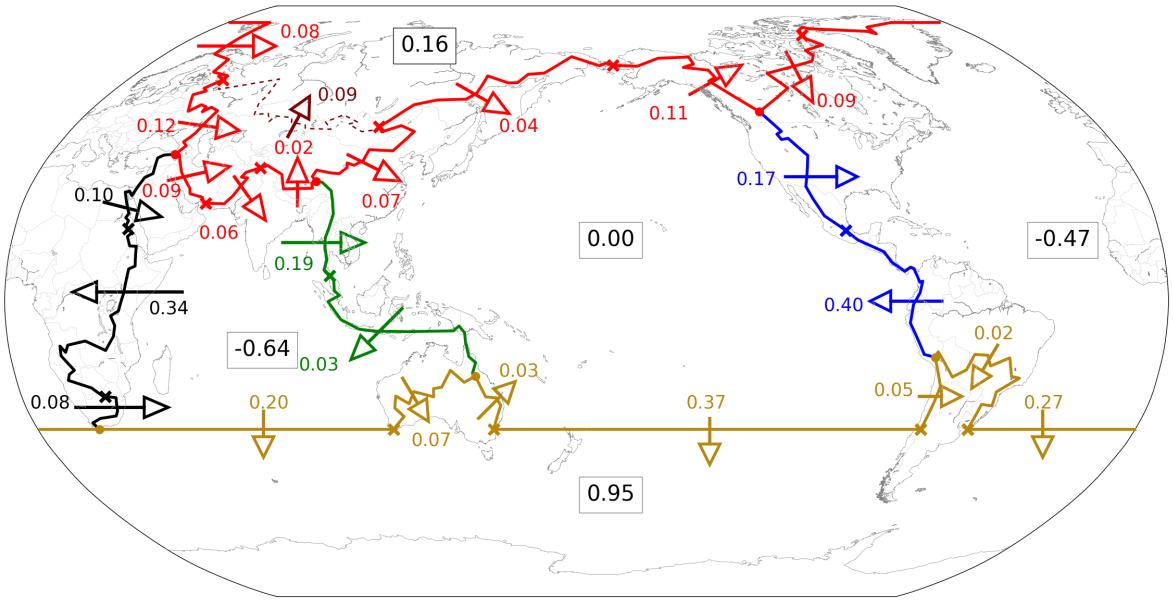

Figure 4.2: Vertically- and horizontally-integrated annual mean (1979-2014) ERA-Interim moisture fluxes normal to each catchment boundary ($\overline{\mathbf{Q}} \cdot \hat{\mathbf{n}}$) and basin-integrated precipitation minus evaporation ($\overline{P-E}$, boxes) calculated from $\overline{\mathbf{Q}} \cdot \hat{\mathbf{n}}$ using equation (4.2). Note that $\hat{\mathbf{n}}$ is inward pointing which gives a change in sign of the moisture budget from the previous chapter. The catchment boundaries are split into smaller sections (at the crosses) either at the locations where $\overline{\mathbf{Q}} \cdot \hat{\mathbf{n}}$ changes direction (Figure 4.3) or at specific geographic locations. The large dots indicate the end points of each sector of the Arctic (red) and Southern Ocean (gold) catchment boundaries where they meet the American (blue), African (black) and South-East Asian (green) catchment boundaries. All units are Sverdrups (1 Sv $\equiv 10^9$ kg s^{-1}).

atmospheric moisture transport in the tropics across the Americas due to the trade winds is partially offset by eastward moisture transport in the midlatitudes. Across the northern section of the South-East Asian catchment boundary there is an eastward moisture flux associated with the annual mean westerly flow across India and the Bay of Bengal. The $\overline{P-E}$ values for the Atlantic, Indian and Pacific Oceans in Figure 4.2 and the size of the Pacific/Atlantic asymmetry are consistent with the estimates presented in Figure 3.2.

The peak in Americas $\overline{\mathbf{Q}} \cdot \hat{\mathbf{n}}$ (-265 kg m^{-1} s^{-1}) occurs over Lake Nicaragua at 11°N (Figure 4.3(a)) in the Papagayo jet (Clarke, 1988). There are two other extrema in $\overline{\mathbf{Q}} \cdot \hat{\mathbf{n}}$ across Central America: at 17°N through the Chivela Pass from the Tehuantepec jet and at 10°N from the Panama jet (Steenburgh *et al.*, 1998). Note that the Panama jet has the weakest of the three main Atlantic-to-Pacific moisture transports across Central America. South of Panama at 5°N there is a positive maximum of 42 kg m^{-1} s^{-1} indicating a net transport from Pacific to Atlantic. This occurs at the same latitude as the core of the Choco LLJ which contributes to very high annual precipitation in Colombia (Poveda and Mesa, 2000). At the end of this catchment boundary the profile of $\overline{\mathbf{Q}} \cdot \hat{\mathbf{n}}$ is flat along zero (no net transport between Atlantic/Pacific) as the Andes are high enough to block moisture transport.

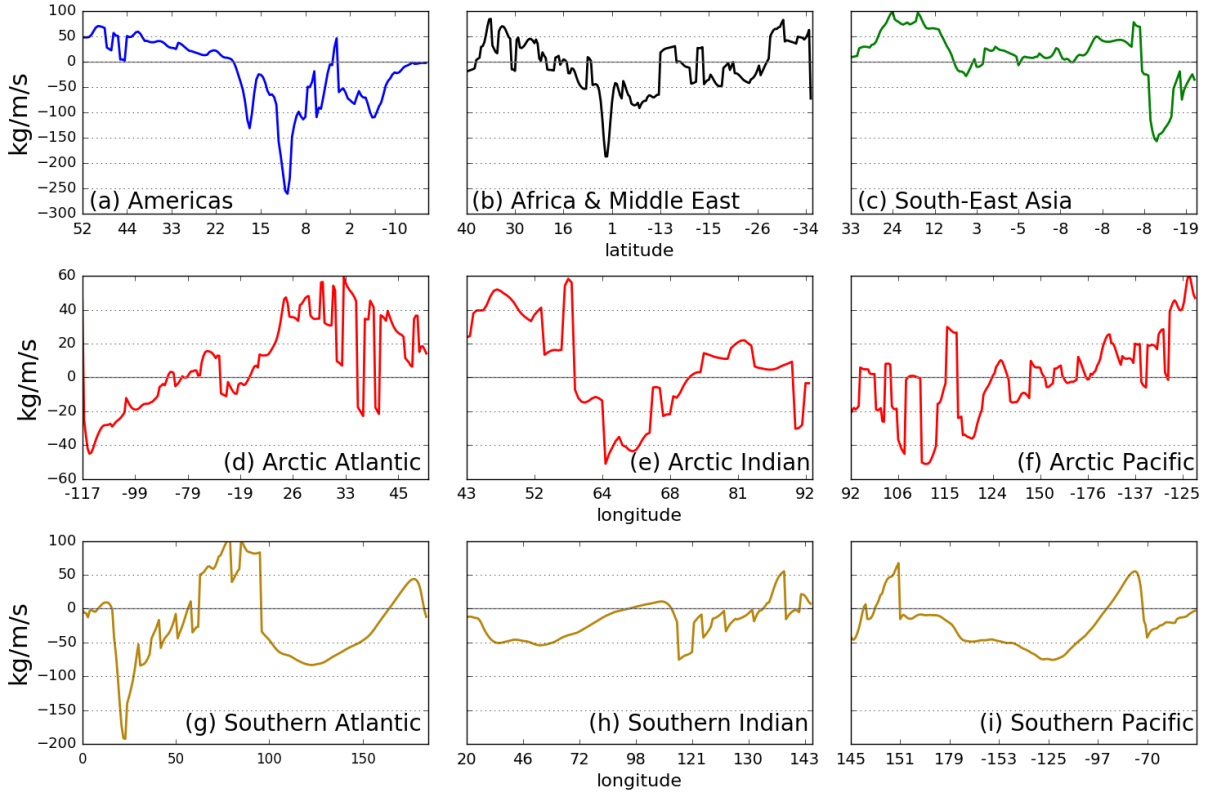

Figure 4.3: Annual mean (1979-2014) vertically-integrated ERA-Interim moisture fluxes normal to the catchment boundaries. The normal vector, $\hat{\mathbf{n}}$, is oriented such that positive fluxes are northward/eastward and negative fluxes are southward/westward. In each panel the $\overline{\mathbf{Q}} \cdot \hat{\mathbf{n}}$ profile is plotted linearly against distance along the catchment boundary then labelled by (a)-(c) latitude or (d)-(i) longitude. The thin, solid line in each panel highlights where $\overline{\mathbf{Q}} \cdot \hat{\mathbf{n}} = 0$. Units are kg/m/s.

Across the African catchment boundary the maximum transport of -210 kg m^{-1} s^{-1} occurs at 3°N in northern Kenya (Figure 4.3(b)) in the Turkana LLJ between the Ethiopian Highlands and East African Highlands (Nicholson, 2016). The profile of African $\overline{\mathbf{Q}} \cdot \hat{\mathbf{n}}$ (Figure 4.3(b)) shows a lot of small-scale fluctuations and has more changes of sign than the American profile due to the path the catchment boundary follows (Figure 2.11) as changes in the orientation of the boundary result in changes in sign of $\hat{\mathbf{n}}$. This is particularly noticeable around the Zambezi basin in the south of the continent.

Across the northern section of the South-East Asian catchment boundary there is strong eastward moisture transport across the Bay of Bengal and Thailand, peaking at 100 kg/m/s (Figure 4.3(c)) resulting in a net moisture flux of 0.19 Sv from the Indian to the Pacific Ocean drainage basin (Figure 4.2). Strong westward transport above the Torres Strait between Papua New Guinea and Australia peaking at 150 kg/m/s (Figures 1.5, 4.3(c)) results in weak net moisture flux across the Maritime Continent from the Pacific to the Indian Ocean drainage basin (0.03 Sv, Figure 4.2). This moisture transport above the Torres Strait dominates the net

moisture flux between 7°N in Malaysia and 8°S in Papua New Guinea where $\overline{\mathbf{Q}} \cdot \hat{\mathbf{n}}$ is close to zero (Figure 4.3(c)). This is because the flow is almost parallel to the catchment boundary in this region (Figure 1.5).

Around the Arctic catchment boundary there is a complex picture of cancelling fluxes. Along the Atlantic sector (Canada to Turkey) there is a weak import of moisture across Canada from the Arctic (0.09 Sv) which is almost entirely matched by net moisture export between Greenland and Russia at the end of the North Atlantic storm track (Dufour *et al.* (2016), Figures 1.5, 4.3(d)). The exchange of atmospheric moisture between the Atlantic and Arctic drainage basins is therefore dominated by zonal moisture transport (Figure 1.5) across Europe between Russia and Turkey (0.12 Sv, Figure 4.2). Along the Pacific sector, between Tibet and Mongolia (eastern boundary of the Central Asian endorheic basin), largely zonal flow (Figure 1.5) transports 0.07 Sv of atmospheric moisture into the Pacific drainage basin. Note that the sum of the fluxes around the boundaries of the Central Asian endorheic basin is 0.01 Sv, a value close to what would be expected as for such regions $\overline{P - E} \approx 0$ (Stohl and James, 2005; Rodriguez *et al.*, 2011).

Due to the fairly straightforward nature of the Southern Ocean catchment boundary, the moisture fluxes around it are simpler to understand. Across 35°S in each sector there is a large net southward transport which is largest along the Pacific sector and weakest along the Indian sector (Figure 4.2). Progressing eastward along 35°S for each sector, the profiles of $\overline{\mathbf{Q}} \cdot \hat{\mathbf{n}}$ (Figure 4.3(g)-(i)) show a southward flux which gradually transitions into a northward flux. The subtropical anticylones above the South Atlantic and South Pacific Oceans (Figure 1.5) influence the moisture fluxes around the catchment boundary of the River Plate basin (section 2.3.4.5). This results in a net transport across the Andes from the Pacific and limiting import from the Atlantic (Figure 4.2) as north-westerly flow trasports moisture across the South American coast out of the River Plate basin (Figure 1.5).

4.2.1 Comparison to previous estimates

Figures 4.4-4.6 show three other recent estimates (Rodriguez *et al.*, 2011; Levang and Schmitt, 2015; Singh *et al.*, 2016) of annual mean $\overline{\mathbf{Q}} \cdot \hat{\mathbf{n}}$ and $\overline{P - E}$ calculated from ECMWF reanalysis data. Each estimate uses a different method to define the catchment boundaries of the ocean drainage basins (see the figure captions for details). Compared to Figure 4.2, Rodriguez *et al.* (2011) (Figure 4.4) find a weaker Atlantic/Pacific moisture budget asymmetry of 0.3 Sv (com-

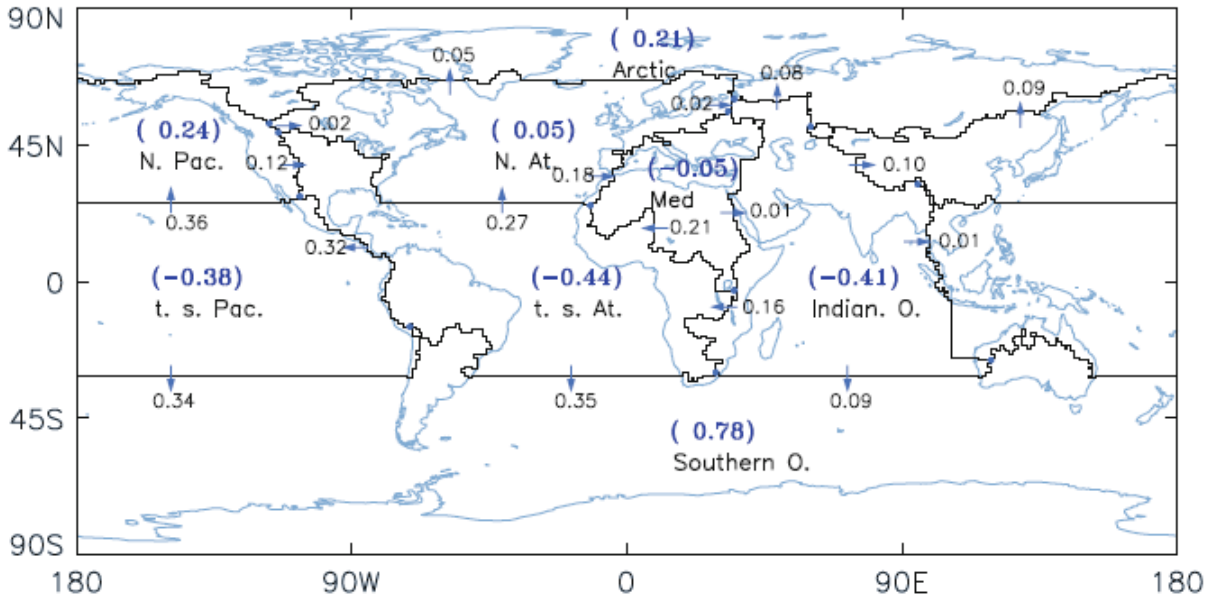

Figure 4.4: Estimates of annual mean (1979-2000) $\overline{\mathbf{Q}} \cdot \hat{\mathbf{n}}$ (arrows) and $\overline{P-E}$ (parenthesis) from Rodriguez *et al.* (2011) using ERA-40. The catchment boundaries were constructed the boundaries of the ocean drainage basins using a network of global river channels (Oki and Sud, 1998). Rodriguez *et al.* (2011) also presented similar maps for the NCEP renalysis and various versions of the Hadley Centre Climate Model which are not shown here. Reprinted by permission from Springer Nature Customer Care Centre GmbH: Springer, Climate Dynamics ©2016.

pared to 0.17 Sv). Singh *et al.* (2016) (Figure 4.6) only focused on moisture fluxes in/out of the Atlantic drainage basin but their estimate of $\overline{P-E} = 0.47$ Sv matches Figure 4.2. As Levang and Schmitt (2015) include the Arctic and North Atlantic in the same drainage basin it is not possible to estimate a basin-scale asymmetry from Figure 4.5.

Differences in estimates of $\overline{P-E}$ are due to the differing extents of the ocean drainage basins defined in each of these studies. One particularly clear issue is the catchment boundary along Central America from Singh *et al.* (2016) which crosses the Caribbean Sea and rejoins the continent on the eastern branch of the Andes in Colombia (Figure 4.6), but the land between the eastern and western branches of the Andes actually drains into the Caribbean Sea (Figure 2.6) which is part of the Atlantic drainage basin (Figure 2.11). This is caused by Singh *et al.* (2016) using the maximum topography in a longitude range to define the catchment boundaries and results in a larger westward $\overline{\mathbf{Q}} \cdot \hat{\mathbf{n}}$ (0.46 Sv, Figure 4.6) compared to this estimate (0.40 Sv, Figure 4.2).

The most notable difference in $\overline{\mathbf{Q}} \cdot \hat{\mathbf{n}}$ between these estimates occurs along the South-East Asian catchment boundary. The net eastward $\overline{\mathbf{Q}} \cdot \hat{\mathbf{n}}$ in Figure 4.2 (0.16 Sv) is much stronger than the eastward $\overline{\mathbf{Q}} \cdot \hat{\mathbf{n}}$ from Rodriguez *et al.* (2011) and Levang and Schmitt (2015) (0.01 Sv and 0.07 Sv respectively, Figures 4.4-4.5). This discrepancy is caused by different placements of

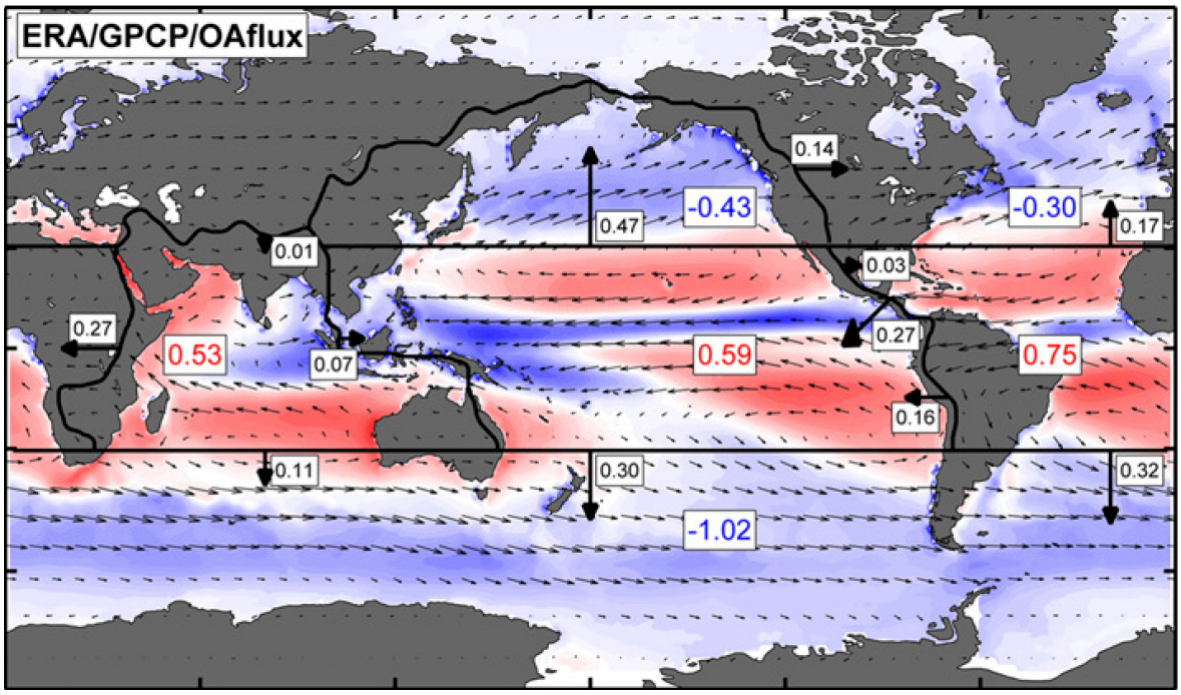

Figure 4.5: Estimates of annual mean (1979-2014) $\overline{\mathbf{Q}} \cdot \hat{\mathbf{n}}$ and $E - P - R$ from Levang and Schmitt (2015) using ERA-Interim winds and humidity for $\overline{\mathbf{Q}} \cdot \hat{\mathbf{n}}$ (arrows) and OAFlux, GPCP and Dai and Trenberth (2002) runoff for $E - P - R$ (boxes). The colours show $e - p$ from OAFlux and GPCP. The boundaries of the ocean drainage basins were defined using topographical maxima. ©American Meteorological Society. Used with permission.

the catchment boundary, where the Rodriguez *et al.* (2011) catchment boundary leaves the Maritime Continent surprisingly early and heads due south before turning due east towards Australia (Figure 4.4); and the catchment boundary from Levang and Schmitt (2015) cuts through the Maritime Continent further to the north than this estimate's South-East Asian catchment boundary (Figure 2.8). The Levang and Schmitt (2015) catchment boundary passes through the region of moisture flux convergence (Figure 4.5) which net South-East Asian $\overline{\mathbf{Q}} \cdot \hat{\mathbf{n}}$ is strongly affected by.

Further issues with South-East Asian $\overline{\mathbf{Q}} \cdot \hat{\mathbf{n}}$ are found in the NCEP reanalysis (Rodriguez *et al.*, 2011; not shown) and Coupled Model Intercomparison Project Phase 5 (CMIP5) models (Levang and Schmitt, 2015; not shown) where $\overline{\mathbf{Q}} \cdot \hat{\mathbf{n}}$ is westward from the Pacific to the Indian Ocean - the opposite direction from ERA40 and ERA-Interim (Figures 4.2 and 4.4-4.5). The discrepancies between climate model and NCEP reanalysis compared to ERA-Interim may be a result of coarser resolution. For example, Schiemann *et al.* (2014) showed that the Walker circulation is enhanced and moisture flux convergence increases over the Maritime Continent in an atmosphere-only GCM when the resolution is increased from 350 km to 110 km. Goswami and Sengupta (2003) highlighted deficiencies in the older, low resolution NCEP reanalysis (used

by Rodriguez *et al.*, 2011) winds over the equatorial Indian Ocean and linked these errors to deficencies in the precipitation estimate. The latest higher resolution NCEP reanalysis (CFSR; climate forecast system reanalysis) appears to have made advances in this region with a more realistic distribution of precipitation and improved circulation features (Chaudhari *et al.*, 2014).

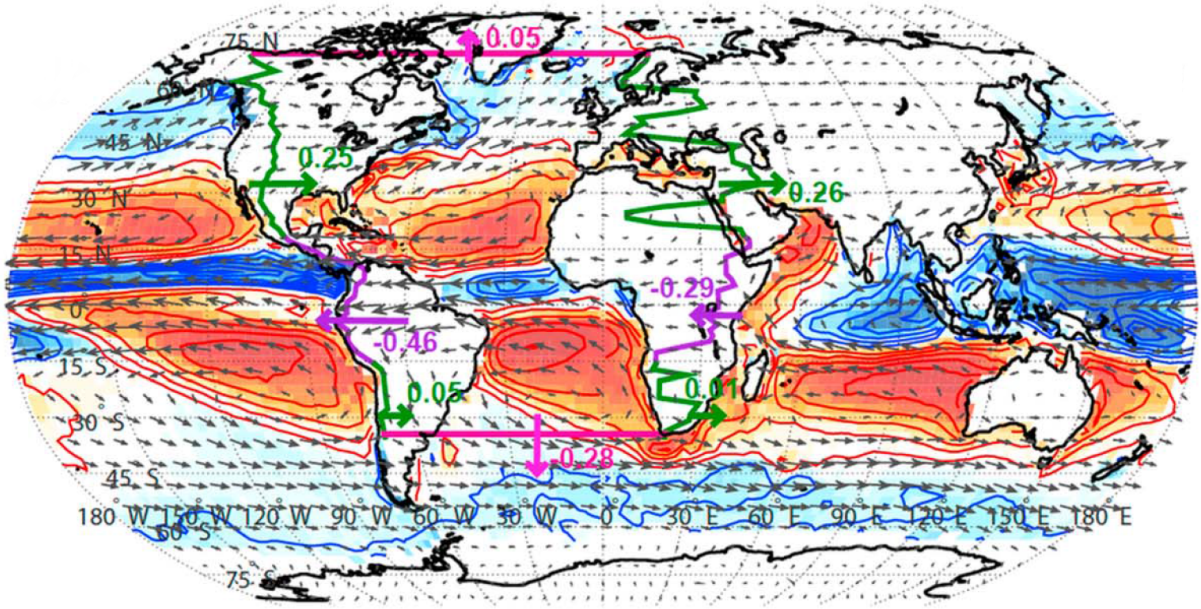

Figure 4.6: Estimates of annual mean (1979-2009) $\overline{\mathbf{Q}} \cdot \hat{\mathbf{n}}$ (coloured arrows) from Singh *et al.* (2016) using ERA-Interim. Also shown are $\overline{\mathbf{Q}}$ vectors (grey arrows), div$\overline{\mathbf{Q}}$ (colours) and $e - p$ (contours). Singh *et al.* (2016) considered only the moisture fluxes in and out of the Atlantic drainage basin which was defined at the western and eastern edges using maximum topography over the American continents and between the prime meridian and 30°E, the northern boundary is taken at 70°N and the southern boundary at 35°S.

4.2.2 Reynolds averaging

To understand differences in the moisture fluxes, the annual mean zonal ($\overline{qu}$) and meridional ($\overline{qv}$) moisture fluxes are decomposed into their mean flow and transient parts:

$$\overline{q\mathbf{v}} = \overline{q}\,\overline{\mathbf{v}} + \overline{q'\mathbf{v}'} \tag{4.3}$$

where $\overline{q}\,\overline{\mathbf{v}}$ is the moisture flux explained by the annual mean flow (and includes the seasonal cycle) and $\overline{q'\mathbf{v}'}$ is the moisture flux explained by transient processes (on timescales shorter than a month). Features such as the trade winds and subtropical highs are evident in the mean flow and storm tracks are highlighted in the eddy fluxes (Figure 4.7). The mean flow and transient

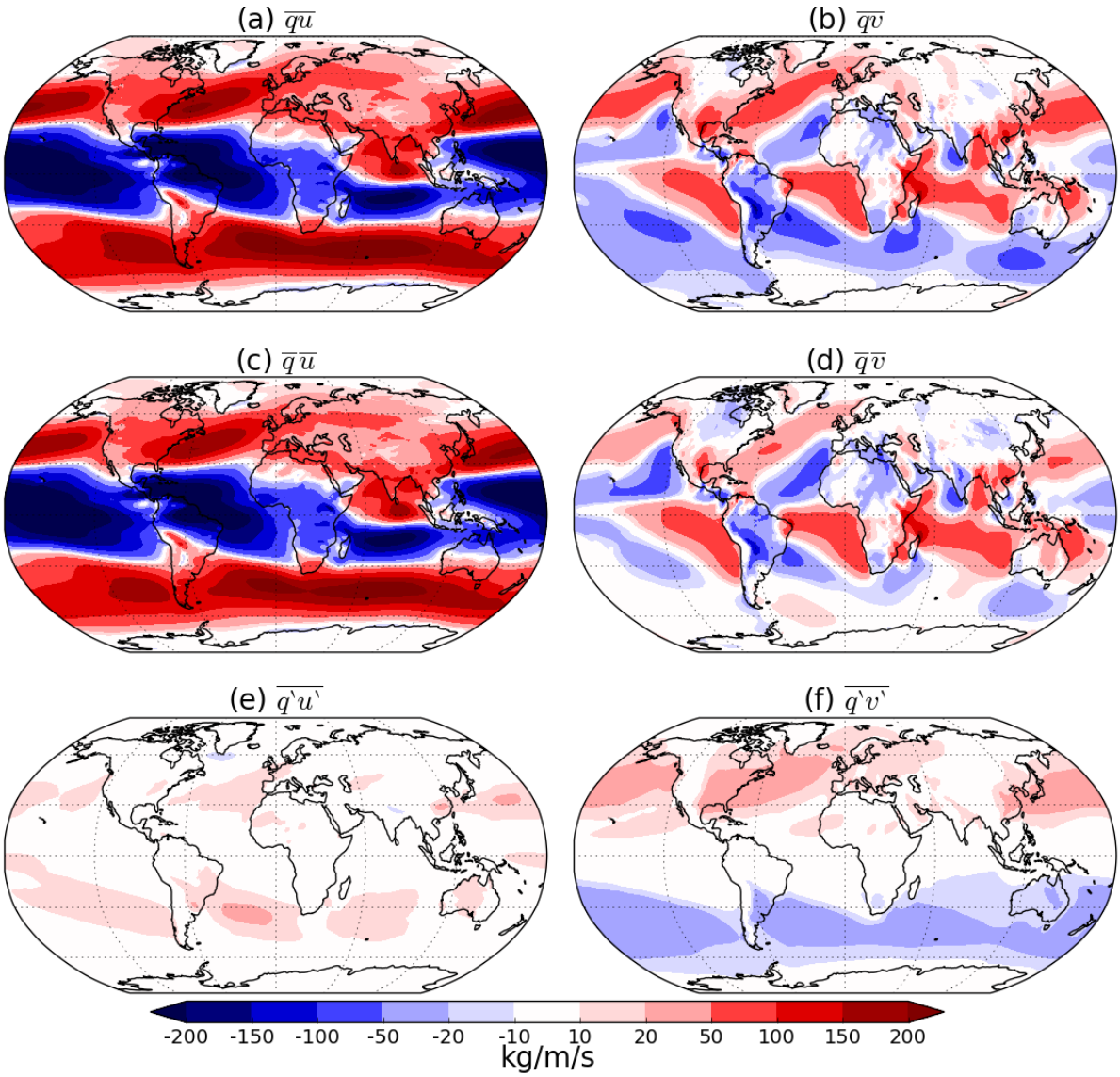

Figure 4.7: Reynolds decomposition of vertically integrated zonal and meridional moisture fluxes (equation (4.3)). Units are kg/m/s.

moisture fluxes normal to the catchment boundaries can then be calculated,

$$\overline{\mathbf{Q}} \cdot \hat{\mathbf{n}} = \overline{q}\,\overline{\mathbf{v}} \cdot \hat{\mathbf{n}} + \overline{q'\mathbf{v}'} \cdot \hat{\mathbf{n}}, \tag{4.4}$$

which can then be linked to the moisture budgets of each drainage basin (Figure 4.8) where

$$\overline{P-E} = (\overline{P-E})_{\overline{q}\,\overline{\mathbf{v}}} + (\overline{P-E})_{\overline{q'\mathbf{v}'}} \tag{4.5}$$

after equation (4.3), and

$$(\overline{P-E})_{\overline{q}\,\overline{\mathbf{v}}} = \oiint_{\partial V} \overline{q}\,\overline{\mathbf{v}} \cdot \hat{\mathbf{n}}\,\mathrm{d}\tilde{p}\,\mathrm{d}l \tag{4.6a}$$

$$(\overline{P-E})_{\overline{q'\mathbf{v}'}} = \oiint_{\partial V} \overline{q'\mathbf{v}'} \cdot \hat{\mathbf{n}}\,\mathrm{d}\tilde{p}\,\mathrm{d}l \tag{4.6b}$$

after equation (4.2).

The moisture budgets of the Arctic and Southern Oceans are dominated by poleward transient fluxes (Figures 4.7,4.8). Much of the Arctic catchment boundary is at the end of the North Atlantic and Pacific storm tracks which actually make small contributions to Arctic $(\overline{P-E})_{\overline{q'\mathbf{v}'}}$. The reason for dominance of $\overline{q'\mathbf{v}'}$ in Arctic $\overline{P-E}$ is that poleward eddy fluxes result in moisture import to the Arctic all around the catchment boundary. Although $\overline{q}\,\overline{\mathbf{v}} \cdot \hat{\mathbf{n}}$ tends to be stronger it is approximately balanced by the downwind $\overline{q}\,\overline{\mathbf{v}} \cdot \hat{\mathbf{n}}$ at the other side of a continent or ocean basin (Figure 4.8(a)).

Pacific $\overline{P-E}$ has equal contributions of opposing sign from $\overline{q}\,\overline{\mathbf{v}}$ and $\overline{q'\mathbf{v}'}$ (Figure 4.8) with $\overline{q}\,\overline{\mathbf{v}}$ causing net precipitation and $\overline{q'\mathbf{v}'}$ causing net divergence. The main locations for $\overline{q}\,\overline{\mathbf{v}} \cdot \hat{\mathbf{n}}$ entering the Pacific basin are across the tropical Americas and South-East Asia (Figure 4.8) although export in the midlatitudes across North America almost balances import of $\overline{q}\,\overline{\mathbf{v}}$ across South-East Asia. The main export of $\overline{q'\mathbf{v}'}$ from the Pacific is across 35°S. Eddy fluxes are dominant in $\mathbf{Q} \cdot \hat{\mathbf{n}}$ across 35°S for each sector of the Southern Ocean catchment boundary (Figure 4.7(e,f) although $\overline{q}\,\overline{\mathbf{v}} \cdot \hat{\mathbf{n}}$ on the Atlantic sector plays a larger role in $\overline{\mathbf{Q}} \cdot \hat{\mathbf{n}}$ than for the other two sectors and is seven times stronger.

Atlantic $\overline{P-E}$ is approximately split in half between export from mean flow and eddy fluxes with a slight dominance for the mean flow (Figure 4.8). The map for $\overline{q}\,\overline{\mathbf{v}} \cdot \hat{\mathbf{n}}$ around the Atlantic is very similar to the map for $\overline{\mathbf{Q}} \cdot \hat{\mathbf{n}}$ (Figure 4.2) with the transports across the Americas and Africa in the mean flow very similar to those from the full field. Indian Ocean $\overline{P-E}$ is dominated by net evaporation caused by $\overline{q}\,\overline{\mathbf{v}}$ with export across Africa and South-East Asia dominating $(\overline{P-E})_{\overline{q}\,\overline{\mathbf{v}}}$. Transient moisture fluxes make a secondary yet significant contribution to Indian Ocean net evaporation with transport across 35°S and Australia dominating $(\overline{P-E})_{\overline{q'\mathbf{v}'}}$ (Figure 4.8(b)).

Overall, meridional $\overline{q'\mathbf{v}'} \cdot \hat{\mathbf{n}}$ (Figure 4.8(b)) is always polewards (Arctic and Southern Ocean catchment boundaries) and zonal $\overline{q'\mathbf{v}'} \cdot \hat{\mathbf{n}}$ is always small (American, African and South-East Asian catchment boundaries) so $\overline{q'\mathbf{v}'}$ causes net moisture export from the Atlantic, Indian and

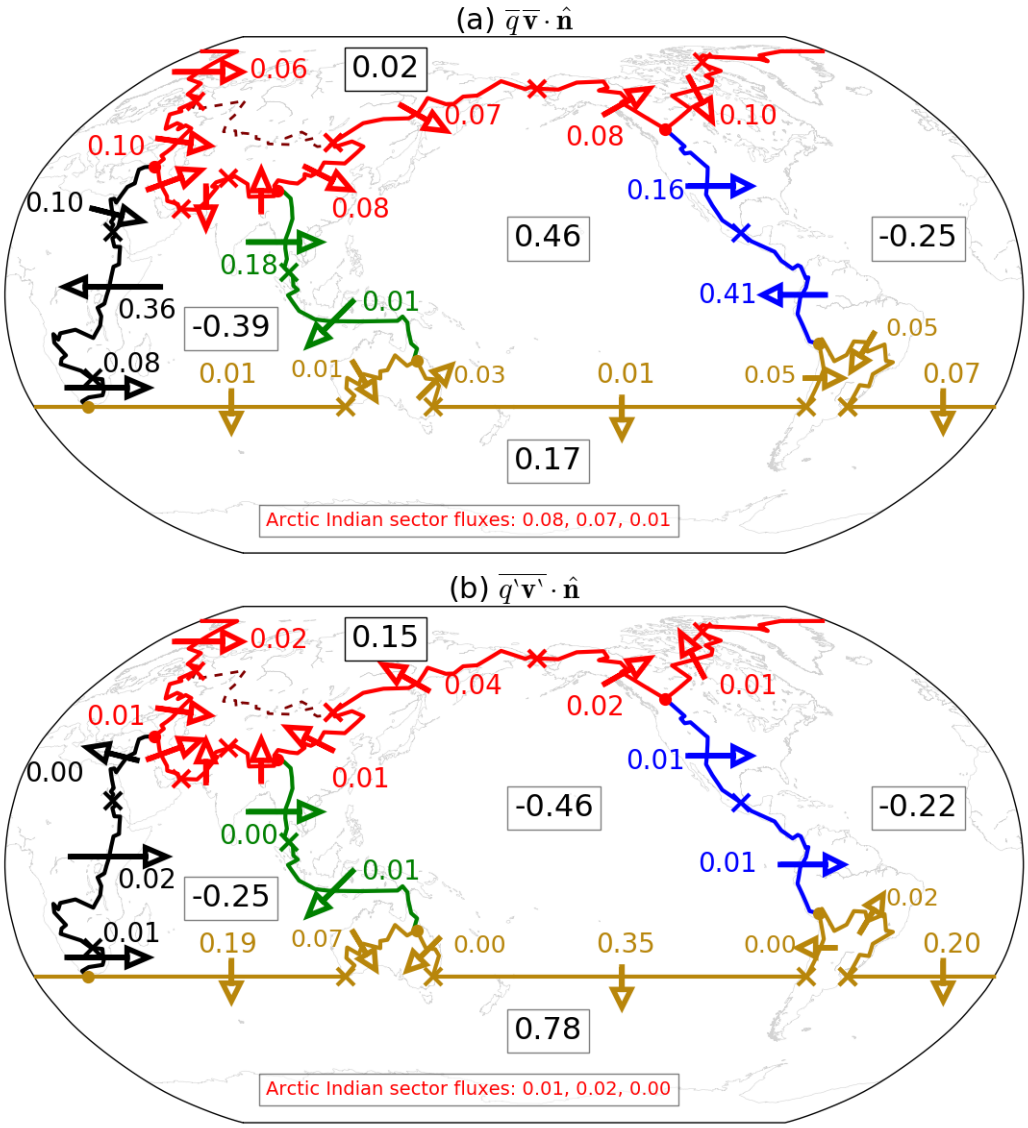

Figure 4.8: Reynolds decomposition of moisture fluxes normal to catchment boundaries (arrows) and $\overline{P - E}$ (boxes) into (a) mean flow and (b) eddy flux contributions. All values are in Sverdrups.

Pacific drainage basins. The $\overline{P - E}$ asymmetry is ultimately dominated by $\overline{q}\,\overline{\mathbf{v}}$ (Figure 4.8(a)) as $\overline{q}\,\overline{\mathbf{v}}$ results in a net import of moisture to the Pacific drainage basin on 0.46 Sv but exports 0.25 Sv and 0.39 Sv from the Atlantic and Indian basins respectively.

4.2.3 Seasonal Cycle

The most notable changes in the seasonal cycle of TCWV and the moisture fluxes (Figure 4.9) are those associated with the monsoon across the Indian and Pacific Oceans where the direction of the vertically-integrated moisture fluxes over the Indian Ocean reverses from DJF to JJA with the formation of the Somali jet in JJA diverting moisture away from Africa towards India and the Maritime Continent. In DJF the ITCZ extends across the Indian Ocean (Figure 3.9) but is

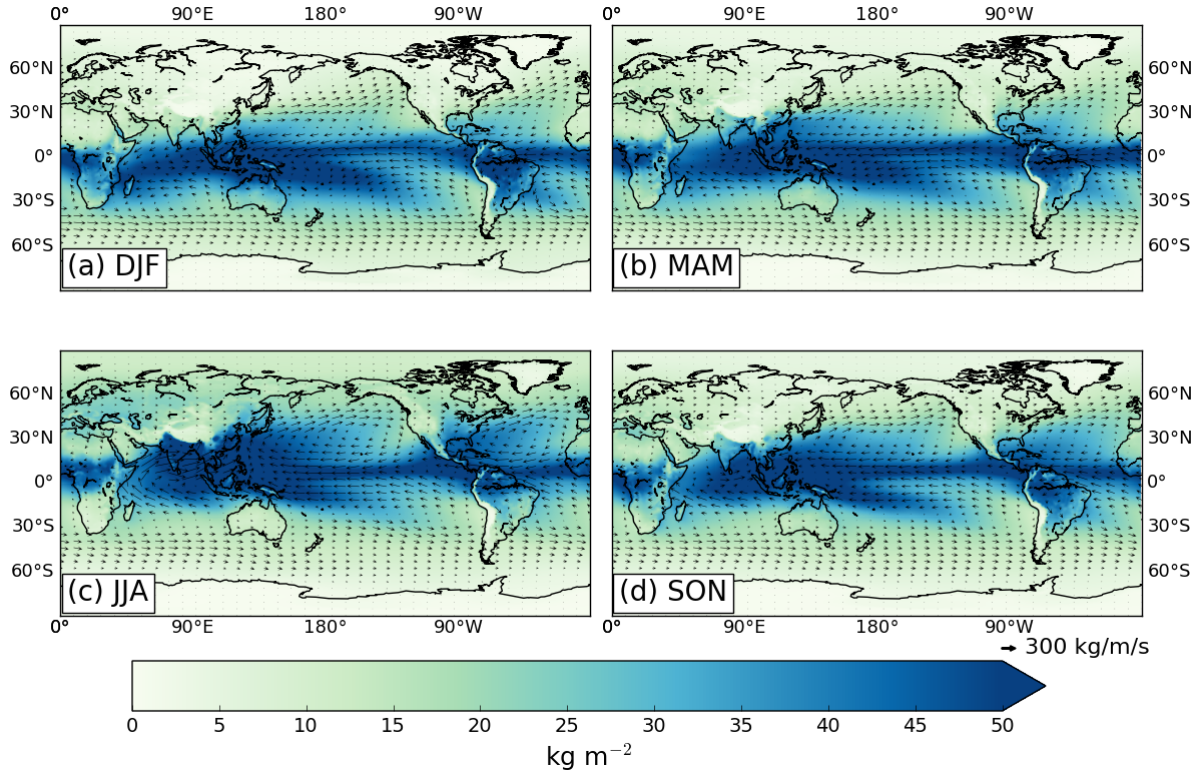

Figure 4.9: Total column water vapour (colours, in kg m^{-2}) and vertically-integrated moisture fluxes (arrows, in kg/m/s) from ERA-Interim for each season (1979-2014).

interrupted by the Somali jet in JJA. In the same season, TCWV peaks over the western North Pacific as more moisture is transport into the region (Figure 4.9(c)). It was these changes that Emile-Geay *et al.* (2003) suggested were the primary cause of net precipitation over the subpolar North Pacific as low level winds in JJA converged moisture from the region of high TCWV into the Aleutian Low. The increase in moisture transport in the northern hemisphere midlatitude westerlies is also notable in DJF (Figure 4.9(a)). The change in the midlatitude westerlies is also noticeable where they are largely zonal in summer but become more tilted in winter due to poleward deflection of the storm tracks (Orlanski, 1998).

The Pacific/Atlantic $\overline{P-E}$ asymmetry is strongest in JJA (> 1 Sv) when eastward South-East Asian $\overline{\mathbf{Q}} \cdot \hat{\mathbf{n}}$ associated with the Asian Monsoon peaks (0.59 Sv) at the same time as peak American $\overline{\mathbf{Q}} \cdot \hat{\mathbf{n}}$ (0.38 Sv) with the maximum strength of the Caribbean LLJ (Wang *et al.*, 2013) both act to converge atmospheric moisture into the Pacific basin resulting in net precipitation of 0.55 Sv (Figure 4.10(c)). The peak in American $\overline{\mathbf{Q}} \cdot \hat{\mathbf{n}}$ in JJA coincides with minimum African $\overline{\mathbf{Q}} \cdot \hat{\mathbf{n}}$ (0.08 Sv) as the Somali LLJ diverts moisture away from Africa (Figure 4.9), thus contributing to peak Atlantic net evaporation (0.63 Sv).

The seasonal cycle of the Pacific/Atlantic $\overline{P-E}$ asymmetry is therefore strongly influ-

enced by the meteorology of the Indian Ocean and the dynamics of the Asian Monsoon. The annual mean moisture flux field (Figure 1.5) of the Indian Ocean, Maritime Continent and North-West Pacific appear to be dominated by JJA, as does the Pacific moisture budget as it is net evaporative during the rest of the year but JJA pushes it towards neutral or net precipitation (Figure 4.10(c)).

There also appears to be a link between the African wet seasons and the Pacific/Atlantic $\overline{P-E}$ asymmetry. African $\overline{\mathbf{Q}} \cdot \hat{\mathbf{n}}$ reaches its minimum in JJA as the Somali LLJ diverts moisture away from Africa, thus enhancing Atlantic net evaporation along with peak American $\overline{\mathbf{Q}} \cdot \hat{\mathbf{n}}$. The minimum in African $\overline{\mathbf{Q}} \cdot \hat{\mathbf{n}}$ coincides with a weaker Turkana LLJ in JJA (Nicholson, 2016), but the MAM and SON maxima occur when there is strong south-easterly flow (Figure 4.9(b,d)). In MAM and SON East Africa has two distinct wet seasons (Liebmann *et al.*, 2012) which are caused by ITCZ movements (Dunning *et al.*, 2016). The peaks in African $\overline{\mathbf{Q}} \cdot \hat{\mathbf{n}}$ contribute towards minima in Atlantic $\overline{P-E}$ but not maximum Indian Ocean $\overline{P-E}$ as its seasonal cycle is dominated by South-East Asian $\overline{\mathbf{Q}} \cdot \hat{\mathbf{n}}$.

The lowest Pacific/Atlantic $\overline{P-E}$ asymmetry occurs in SON (Figure 4.9(d)) when eastward South-East Asian $\overline{\mathbf{Q}} \cdot \hat{\mathbf{n}}$ is near zero and American $\overline{\mathbf{Q}} \cdot \hat{\mathbf{n}}$ reaches its minimum due to stronger westward transport in the midlatitudes and the maximum extent of the Atlantic Warm Pool (AWP, Wang *et al.*, 2013). The AWP is a region in the Caribbean Sea, Gulf of Mexico and Tropical North Atlantic with SST > 28.5°C (Wang and Enfield, 2001) which reaches its maximum extent in SON. The increased SSTs result in a low pressure anomaly and therefore increased convergence over the region leading to increased local precipitation. Moisture transport across Central America is therefore inhibited by the AWP and the Pacific/Atlantic $\overline{P-E}$ asymmetry is diminished.

Moisture transports to and from the Arctic/Southern Ocean drainage basins do not appear to significantly impact the seasonal cycle of the Pacific/Atlantic $\overline{P-E}$ asymmetry. However, one interesting aspect of the seasonal cycles of the Southern Ocean catchment boundary $\overline{\mathbf{Q}} \cdot \hat{\mathbf{n}}$ is that moisture transport across the Atlantic and Pacific sectors of 35°S peak in JJA but this is not true for the Indian sector. The Atlantic and Pacific sector maxima are likely caused by enhanced poleward moisture transport associated with a stronger southern hemisphere storm track in austral winter. Atlantic net evaporation is enhanced by this but Pacific net precipitation is dampened, so there may only be a small net affect on the $\overline{P-E}$ asymmetry. The lack of Indian sector maximum may be explained by the existence of the Somali LLJ and its cross-

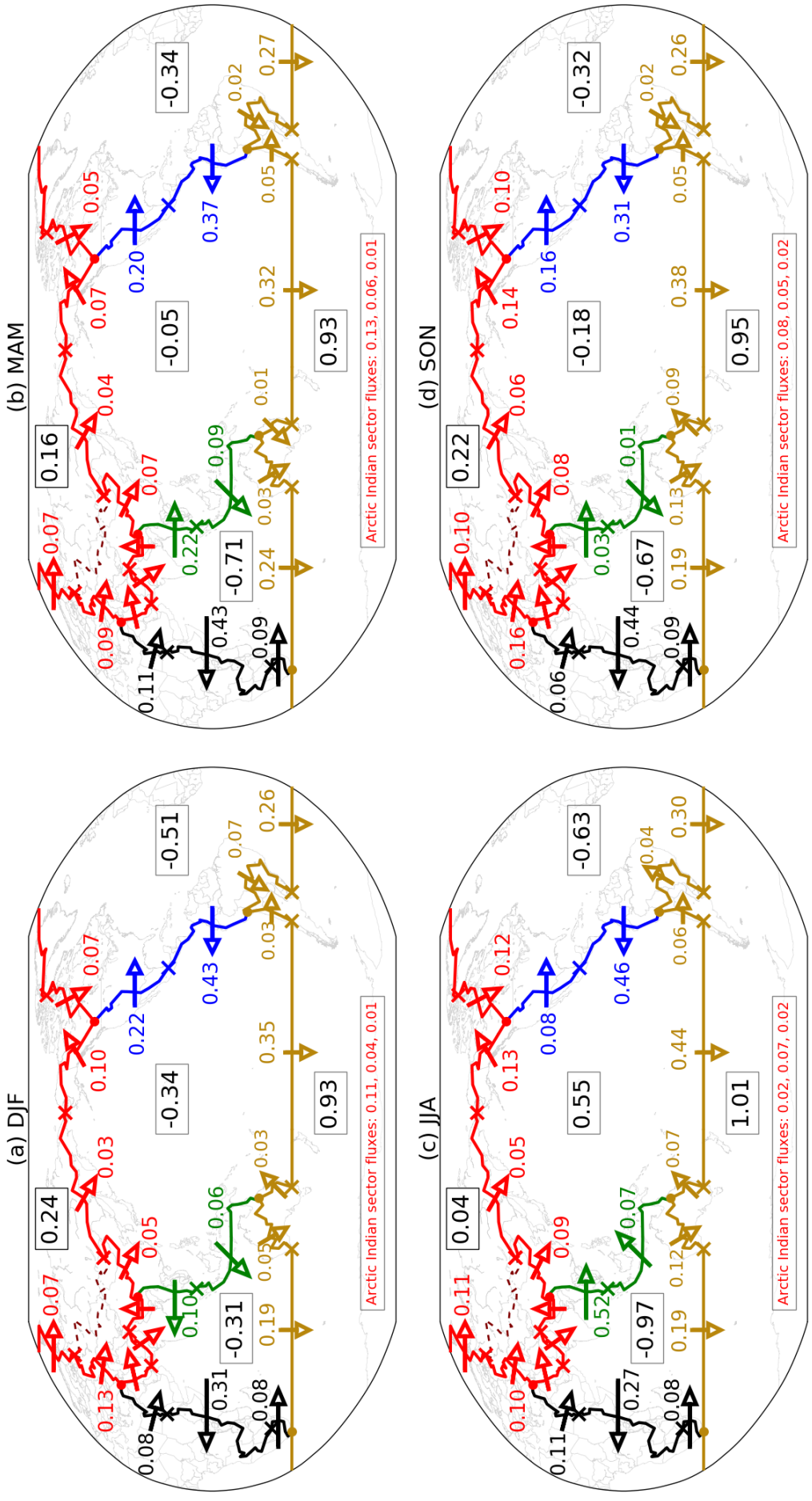

Figure 4.10: Climatological seasonal means (1979-2014) of $P - E$ (boxes) and vertically- and horizontally-integrated moisture fluxes normal to each catchment boundary (arrows) split into sections based on geographic locations or change in the net direction of annual mean $\mathbf{Q} \cdot \hat{\mathbf{n}}$ (Figure 4.3). All values are in Sverdrups (1 Sv$\equiv 10^9$ kg s^{-1}).

equatorial moisture transport (Rodwell and Hoskins, 1995) inhibiting transport across 35°S.

The seasonal cycles of $\overline{\mathbf{Q}} \cdot \hat{\mathbf{n}}$ and $\overline{P - E}$ point towards the significance of the atmospheric dynamics above the Indian Ocean associated with the Somali LLJ and Asian Summer Monsoon. This is a region previously unaccounted for in theories regarding the basin-scale $\overline{P - E}$ asymmetry despite its apparent role as a moisture source for Pacific precipitation in JJA.

4.3 Understanding the $P - E$ asymmetry from an annual mean perspective

The question of why such a large contrast between the Atlantic and Pacific atmospheric moisture budgets exists is often framed as one where the Atlantic is anomalous compared to the Pacific *i.e.* an MOC exists in the Atlantic but there is nothing to explain in the Pacific, and enhanced heat transport in the AMOC leads to Atlantic evaporation (*e.g.* Weijer *et al.*, 1999).

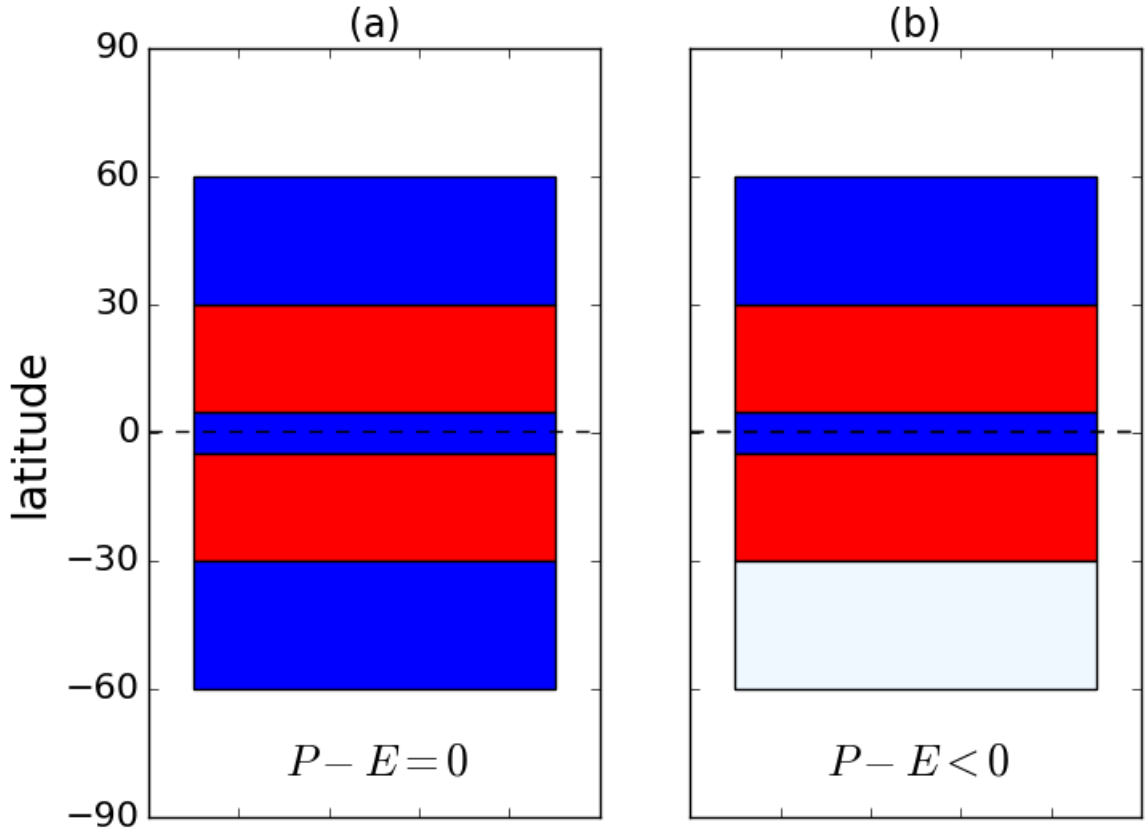

Figure 4.11: Schematic of two ocean basins with (a) two subpolar regions, two subtropical regions and an ITCZ; and (b) one subpolar region, two subtropical regions and an ITCZ. Blue regions represent $P - E > 0$ (net precipitation, ITCZ/subpolar regions) and red regions represent $P - E < 0$ (net evaporation, subtropics). Basin (a) represents an idealized ocean basin with $P - E = 0$ and basin (b) represents an idealized ocean basin similar to the Atlantic and Pacific but with $P - E < 0$ (closer to the Pacific). The pale blue rectangle in basin (b) indicates the missing southern subpolar region.

However, first consider an ocean basin extending from 60°S to 60°N (Figure 4.11(a)) with two subpolar regions ($P - E > 0$), two subtropical regions ($P - E < 0$) and an ITCZ ($P - E > 0$). In such a basin, the net atmospheric moisture budget is expected to be approximately neutral ($P - E \approx 0$). If one considers the area extending from 30°S to 60°N (Figure 4.11(b); only one subpolar region) the net atmospheric moisture budget is expected to be $P - E < 0$ (net evaporation). This is what is found in the Atlantic. The Pacific, however, with the two subtropical regions and one subpolar region has net $P - E \approx 0$ and does not match expectations.

The basins depicted in Figure 4.11 implicitly assume that moisture is transported westward in the tropics by trade winds and eastward in the midlatitude storm tracks. The existence of converging $\overline{\mathbf{Q}} \cdot \hat{\mathbf{n}}$ on both the eastern and western boundaries of the Pacific drainage basin therefore appears to cause abnormally strong precipitation within 20° latitude of the equator when compared to the Atlantic (Figure 3.5), mostly on the western side of the basin (Figure 3.9). The Indian Ocean, which could be approximated as one ITCZ and two subtropical regions, is net evaporative as expected, although its net evaporation may be abnormally strong due to the strong export of moisture associated with the Asian Summer Monsoon.

4.3.1 Transport across 35°S

There is also an important asymmetry in atmospheric moisture exports to the Southern Ocean (Table 4.1). As can be seen in Figure 4.2 the moisture transport across 35°S is greatest in the Pacific sector (-0.37 Sv) and lowest in the Indian sector. Although it is expected that the atmospheric moisture export from the Pacific drainage basin to the Southern Ocean drainage basin would be the largest of the three as it is much wider than the other two basins (Table 4.1). If the atmosphere was equally efficient at exporting moisture across 35°S from the Atlantic, Indian and Pacific then it would be expected that Pacific $\overline{\mathbf{Q}} \cdot \hat{\mathbf{n}}$ on 35°S would be double that on the Atlantic sector. However, Table 4.1 shows that transport across the Atlantic sector is 37% more efficient than transport across the Pacific sector with moisture transport across the Indian sector being the least efficient. The transient fluxes per unit length are approximately equal and do not make a significant contribution towards the asymmetry in transport across 35°S. The asymmetry in efficency of $\overline{\mathbf{Q}} \cdot \hat{\mathbf{n}}$ is mostly found in the mean flow where moisture transport across the Atlantic sector of 35°S is an order of magnitude more efficient than the transport across the Indian sector, and two orders of magnitude more efficent than transport across the Pacific sector.

Potential reasons for the greater efficiency across the Atlantic sector are:

1. A greater fraction of the Atlantic, which is the narrower basin, is occupied by southward $\overline{q}\,\overline{v}$ but in the Pacific the region of southward/northward transport (subtropical high) is confined to the west of the basin. There is even an additional region of northward $\overline{q}\,\overline{v}$ between Australia and New Zealand.
2. The easterly trade winds are deflected to the south by the Andes resulting in strong southward $\overline{q}\,\overline{v}$ over South America and a region off the coast with stronger $\overline{q}\,\overline{v}$ than is found in the South Pacific (Figure 4.7(d)).
3. The SPCZ may weaken $\overline{q}\,\overline{v}$ in the South Pacific as it causes anomalous moisture flux convergence into a region which has no analogue in the Atlantic.

4.3.2 Moisture exchange with the Arctic

Moisture exchange with the Arctic drainage basin also plays a role in the overall moisture budget asymmetry. Moisture imported by the atmosphere into the Pacific drainage basin across Asia between the Himalyas and the Bering Strait (0.11 Sv, Figure 4.2) is balanced by moisture exported across Canada and Alaska in the mid-latitude westerlies. Therefore net $\overline{\mathbf{Q}} \cdot \hat{\mathbf{n}}$ across the Arctic Pacific catchment boundary is approximately zero. For the Atlantic sector of the Arctic catchment boundary, moisture imported across Canada into the Atlantic drainage basin (0.09 Sv) is almost balanced by atmospheric moisture export to the Arctic (0.08 Sv) at the end of the North Atlantic storm track. However, net $\overline{\mathbf{Q}} \cdot \hat{\mathbf{n}}$ for the Arctic Atlantic catchment boundary is dominated by zonal transport across Europe into the Central Asian endorheic basin (0.12 Sv), thus resulting in a net export of moisture from the Atlantic drainage basin to the Arctic. This contributes 0.11 Sv to the overall $\overline{P - E}$ asymmetry.

This asymmetry related to the shape of the Arctic catchment boundary. Around the Pacific

Table 4.1: Net (Sv) and length-averaged (Sv m^{-1}) atmospheric moisture fluxes across each sector of 35°S.

		$\overline{\mathbf{Q}} \cdot \hat{\mathbf{n}}$		$\overline{q}\,\overline{\mathbf{v}} \cdot \hat{\mathbf{n}}$		$\overline{q'\mathbf{v}'} \cdot \hat{\mathbf{n}}$	
	length (km)	Sv	Sv m^{-1}	Sv	Sv m^{-1}	Sv	Sv m^{-1}
Atlantic	6773.4	-0.26	-3.99×10^{-8}	-0.07	-1.03×10^{-8}	-0.20	-2.95×10^{-8}
Indian	8714.4	-0.20	-2.30×10^{-8}	-0.01	-1.15×10^{-9}	-0.19	-2.18×10^{-8}
Pacific	12670.4	-0.37	-2.92×10^{-8}	-0.01	-7.89×10^{-10}	-0.35	-2.76×10^{-8}

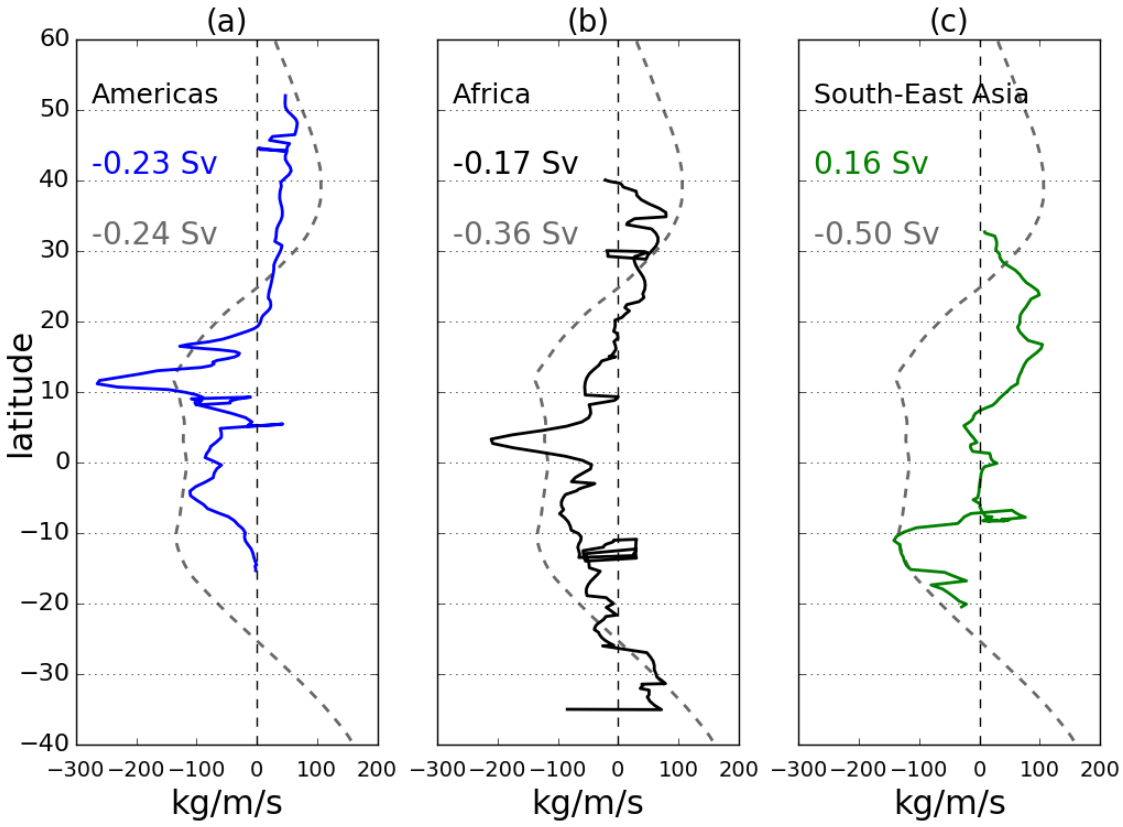

Figure 4.12: Comparison between the zonal mean zonal moisture flux ($[\overline{qu}]$, dashed lines) and the profile of the moisture flux normal to the (a) American, (b) African and (c) South-East Asian catchment boundaries ($\overline{\mathbf{Q}} \cdot \hat{\mathbf{n}}$, solid lines). The coloured numbers show the integrated $\mathbf{Q} \cdot \hat{\mathbf{n}}$ for each catchment boundary and the grey numbers show the integral of $[\overline{qu}]$ between the corresponding latitudes of each catchment boundary

it extends from the eastern Himalayas to the Rockies, and around the Atlantic it extends from the Rockies to northern Turkey (Figure 2.11). Therefore zonal moisture fluxes ($\overline{qu}$, Figure 4.7(a)) act to export atmospheric moisture from the Atlantic to the Arctic across Eastern Europe into Central Asia and import moisture from the Arctic to Pacific across the Tibetan Plateau. If the northern extent of the American catchment boundary were located further south (to approximately the same latitude as the northern extents of the African and South-East Asian catchment boundaries), then Pacific export to the Arctic and Arctic export to the Atlantic would increase thus bringing net Atlantic and Pacific sector $\mathbf{Q} \cdot \hat{\mathbf{n}}$ closer together.

4.3.3 Deviations from the zonal mean zonal moisture flux

Ferreira *et al.* (2018) point out that the net moisture transport across the Americas is close to what would be expected from the zonal mean zonal moisture flux ($[\overline{qu}]$) and that freshening of the Pacific occurs because zonally anomalous Monsoon circulations prevent moisture leaving across the western boundary of the Pacific drainage basin. The profile of Americas $\overline{\mathbf{Q}} \cdot \hat{\mathbf{n}}$

does indeed bear some resemblance to the zonal mean zonal moisture flux ($[\overline{qu}]$) (eastward in midlatitudes, westward in the tropics, Figure 4.12). African $\overline{\mathbf{Q}} \cdot \hat{\mathbf{n}}$ also shows some similarities to $[\overline{qu}]$ but is frequently closer to zero. South-East Asian $[\overline{qu}]$, however, is of opposing sign to $[\overline{qu}]$ from 28°N to 7°N and then remains close to zero until 7°S. These deviations from $[\overline{qu}]$ are reflected in the integrals where net American $\overline{\mathbf{Q}} \cdot \hat{\mathbf{n}}$ is close to the integral of $[\overline{qu}]$, net African $\overline{\mathbf{Q}} \cdot \hat{\mathbf{n}}$ is of the same sign but somewhat weaker and, crucially, net South-East Asian $\overline{\mathbf{Q}} \cdot \hat{\mathbf{n}}$ is of opposing sign to the zonal mean (Figure 4.12).

It is therefore likely that deviations from $[\overline{qu}]$ can explain the $\overline{P - E}$ asymmety. Replacing $\overline{\mathbf{Q}} \cdot \hat{\mathbf{n}}$ across the catchment boundaries discussed above (Figure 4.13) with the respective integrals of $[\overline{qu}]$ between corresponding latitudes gives an idealized distribution of $\overline{P - E}$ where each ocean basin is net evaporative ($\overline{P - E} < 0$) as would be expected from Figure 4.11. All the zonal $\overline{\mathbf{Q}} \cdot \hat{\mathbf{n}}$ are now westward (Figure 4.13(d)) as would be expected from $[\overline{qu}]$ ((Figure 4.12). The Pacific therefore no longer has converging $\overline{\mathbf{Q}} \cdot \hat{\mathbf{n}}$ across both western and eastern boundaries and the Indian Ocean no longer has diverging $\overline{\mathbf{Q}} \cdot \hat{\mathbf{n}}$ across both western and eastern boundaries. The Atlantic receives increased $\overline{\mathbf{Q}} \cdot \hat{\mathbf{n}}$ across its eastern boundary (Africa) but its export across its western boundary (Americas) is almost unchanged as the integral of $\overline{\mathbf{Q}} \cdot \hat{\mathbf{n}}$ almost matches the integral of $[\overline{qu}]$. The resulting idealized $\overline{P - E}$ give a Pacific Ocean with very strong net evaporation (-0.65 Sv) which is entirely a result of changing South-East Asian $\overline{\mathbf{Q}} \cdot \hat{\mathbf{n}}$. The Indian Ocean now has net evaporation ($\overline{P - E} = -0.18$ Sv) about 30% weaker than its "real world" value as it now imports moisture across South-East Asia and exports more across Africa. Atlantic net evaporation is about 0.2 Sv weaker than in the "real world" due to the increased import of moisture across Africa. The asymmetry in $\overline{P - E}$ between not only the Atlantic and Pacific Oceans, but also the Indian and Pacific Oceans, can therefore be entirely

Table 4.2: Basin-integrated and area-averaged $\overline{P - E}$ for the Atlantic, Indian and Pacific Oceans from ERA-Interim (Figure 4.13(a)) and the idealized state (Figure 4.13(d)). The areas (second row) are for the oceans only and do not include the land part of the drainage basins. Therefore $(\overline{P - E})_{\text{land}}$ is assumed to enter the oceans as runoff.

		Atlantic	Indian	Pacific
	Area (m^2)	0.746×10^{14}	0.450×10^{14}	1.405×10^{14}
ERA-Interim	$\overline{P - E}$ (Sv)	-0.47	-0.64	0.00
	area average (Sv/m^2)	-0.630×10^{-14}	-1.422×10^{-14}	0.00
Idealized	$\overline{P - E}$ (Sv)	-0.27	-0.18	-0.66
	area average (Sv/m^2)	-0.362×10^{-14}	-0.400×10^{-14}	-0.467×10^{-14}

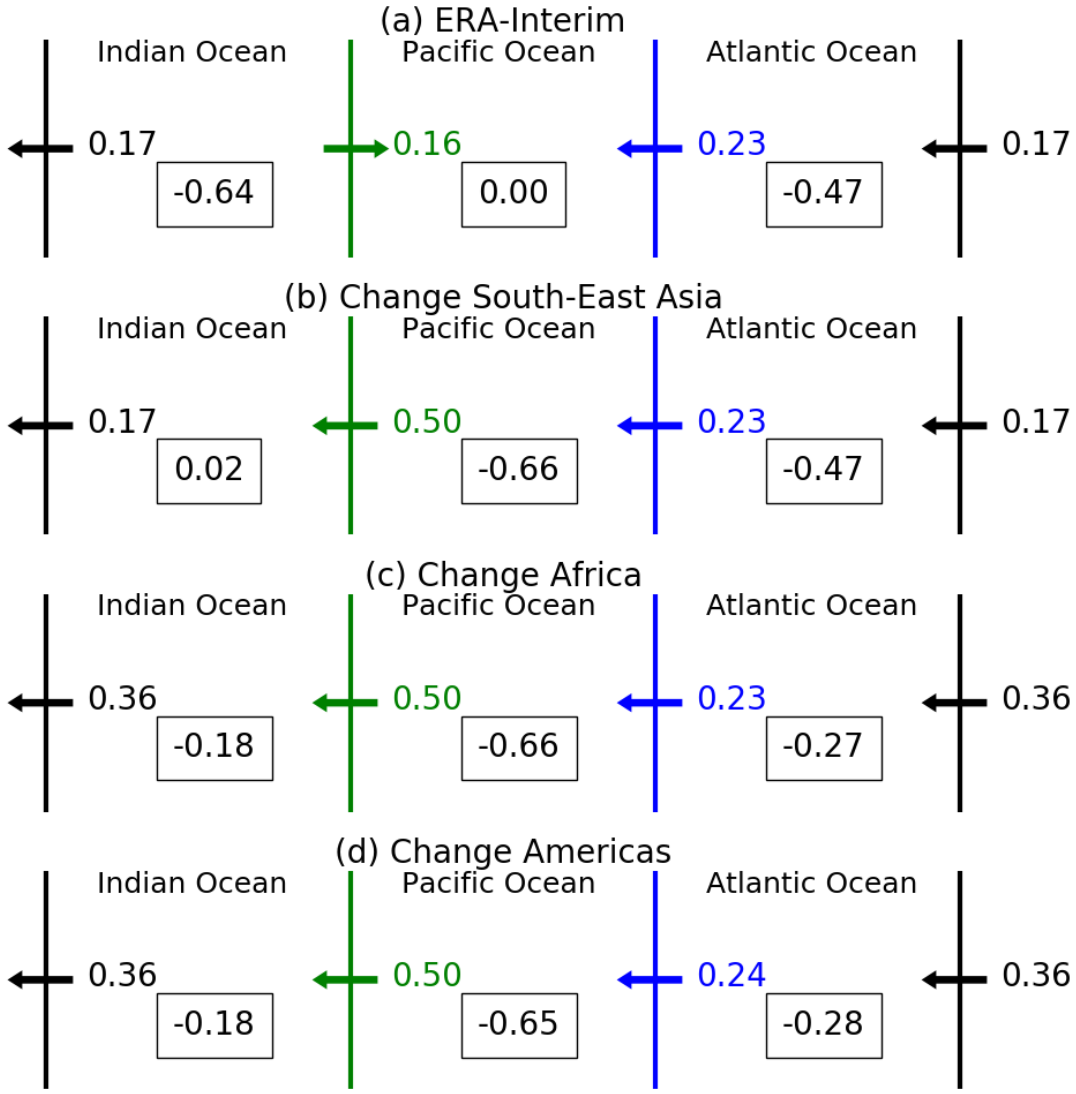

Figure 4.13: Changing $\overline{\mathbf{Q}} \cdot \hat{\mathbf{n}}$ on the African (black line), South-East Asian (green line) and American (blue line) catchment boundaries to match the integrals of $[\overline{qu}]$ between corresponding latitudes. Starting with the "real world" state from ERA-Interim (a) and finishing with the idealized state where each $\overline{\mathbf{Q}} \cdot \hat{\mathbf{n}}$ matches $[\overline{qu}]$ (d). Note that atmospheric moisture transports to/from the Arctic and Southern Oceans remain unchanged.

explained in terms of deviations from the zonal mean zonal moisture flux.

On first inspection in may appear that the $\overline{P - E}$ asymmetry between the Atlantic and Pacific has simply been reversed by changing each $\overline{\mathbf{Q}} \cdot \hat{\mathbf{n}}$ to match $[\overline{qu}]$. However, the Pacific is approximately double the size of the Atlantic so if the moisture budgets matched the state in Figure 4.11 then the Pacific would be expected to have stronger net evaporation than the Atlantic. To check if the oceans are indeed in a similar state it is useful to look at area-averaged $\overline{P - E}$ (Table 4.2). Changing to the idealized state brings each area-averaged $\overline{P - E}$ much closer together and closer to what would be expected from Figure 4.11(b).

4.4 Interannual variability of the $P - E$ asymmetry

This section focuses on the interannual variability (1979-2014) of the Pacific/Atlantic and Pacific/Indian $P - E$ asymmetries and the dominant $\mathbf{Q} \cdot \hat{\mathbf{n}}$ affecting the interannual variability of each basin's $P - E$ and the asymmetries. As it was established in the previous section that the $P - E$ asymmetries are entirely explained by deviations from $[\overline{qu}]$ along the American, African and South-East Asian catchment boundaries, this section will focus on the interannual variability of $\mathbf{Q} \cdot \hat{\mathbf{n}}$ on these catchment boundaries and Atlantic, Pacific and Indian $P - E$. For completeness, results for the Arctic and Southern Ocean catchment boundaries/basins will be presented but any discussion relating to them will be minimal.

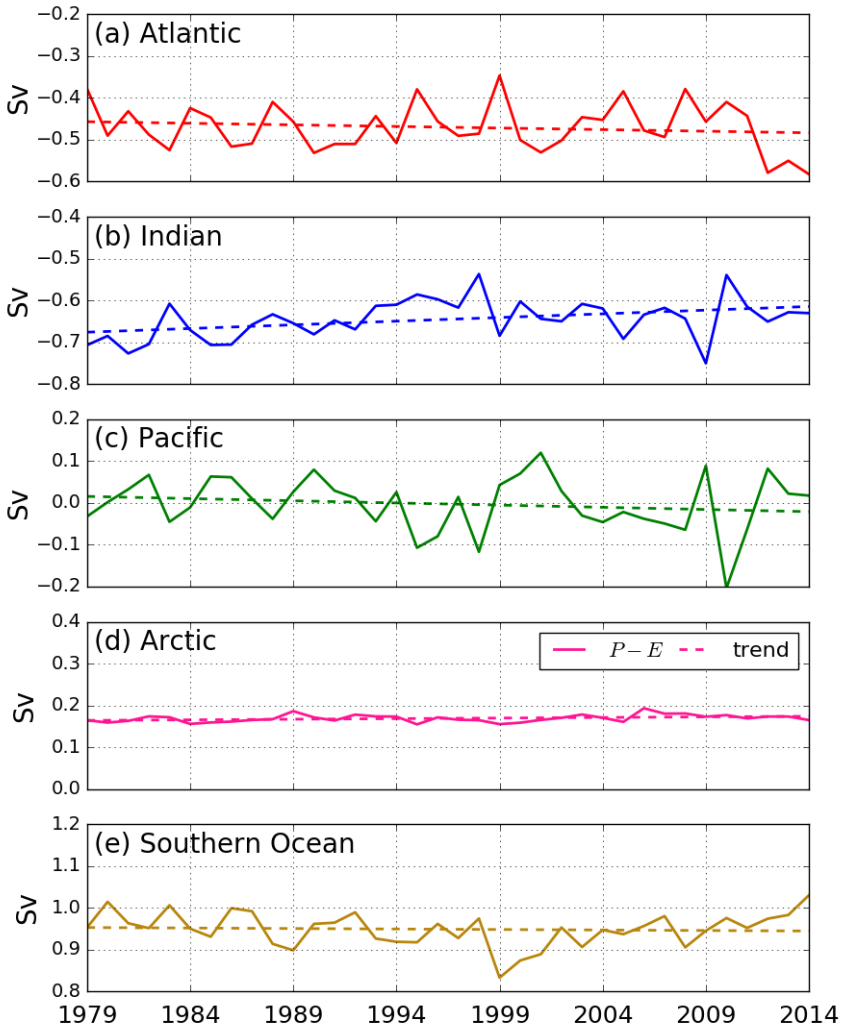

Figure 4.14: Interannual variability of $P - E$ for each ocean drainage basin (solid lines) and trends (dashed lines). Only Indian and Arctic trends are statistically significant at the 90% level. Each $P - E$ is calculated from the sum of the surrounding $\mathbf{Q} \cdot \hat{\mathbf{n}}$ (equation (4.2)).

4.4.1 Interannual variability of $P - E$ and $\mathbf{Q} \cdot \hat{\mathbf{n}}$

Atlantic, Indian and Pacific $P - E$ appear to be fairly steady around their respective annual means with weak trends (Figure 4.14). However, Atlantic $P - E$ exhibits an increasing trend (stronger net evaporation) and Indian $P - E$ exhibits a decreasing trend (weaker net evaporation) with the trend in Pacific $P - E$ almost indistinguishable from zero. From these results it would appear that the Pacific/Atlantic $P - E$ asymmetry has increased over the ERA-Interim period which is consistent with an intensified hydrological cycle with recent increases in global temperatures and the observed amplification in the SSS asymmetry (Durack and Wijffels, 2010; Skliris *et al.*, 2014).

Despite having almost no trend, Pacific $P - E$ is the most variable with a range slightly in excess of 0.3 Sv and frequent changes of sign (and therefore from net convergence to net divergence) from year-to-year (Figure 4.14(c)). The greatest changes in Pacific $P - E$ occur between 2009 and 2011, when $P - E$ drops from 0.1 Sv in 2009 to -0.2 Sv in 2010 before recovering to 0.1 Sv in 2011. These fluctuations coincide with large oscillations in South-East Asian $\mathbf{Q} \cdot \hat{\mathbf{n}}$ (Figure 4.15(c)) which drops from 0.24 Sv in 2009 to 0.05 Sv in 2010. This appears to be a direct result of the 2010-11 El Niño as the Somali LLJ is weaker during the warm phase of ENSO (Halpern and Woiceshyn, 2001) which reduces the moisture transport across South-East Asia. El Niño events therefore act to decrease the Pacific/Indian $P - E$ asymmetry by reducing South-East Asian $\mathbf{Q} \cdot \hat{\mathbf{n}}$ which decreases Indian Ocean net evaporation and switches the Pacific Ocean into a net evaporative state. La Niña events have the opposite effect on South-East Asian $\mathbf{Q} \cdot \hat{\mathbf{n}}$ and therefore amplify the Pacific/Indian $P - E$ asymmetry.

African hydroclimate is well-known to be affected by ENSO (Camberlin *et al.*, 2001; Giannini *et al.*, 2008) with wet anomalies over Kenya (September-January) and dry anomalies over the Sahel (July-September) during El Niño events, while La Niña causes wet anomalies over the Sahel. However, it is very difficult to find any direct impacts of ENSO on the interannual variability of African $\mathbf{Q} \cdot \hat{\mathbf{n}}$ (Figure 4.14(b)) due to the length of the catchment boundary as ENSO-induced changes in $\mathbf{Q} \cdot \hat{\mathbf{n}}$ are likely to be cancelled out. A recent abrupt decrease since 2008 may be linked to recent failures in seasonal precipitation in African (Lyon and DeWitt, 2012).

The interannual variability of American $\mathbf{Q} \cdot \hat{\mathbf{n}}$ (Figure 4.15(a)) has three particularly notable minima in 1995, 2005 and 2010 which coincide with maxima in the extent of the JJA AWP (see

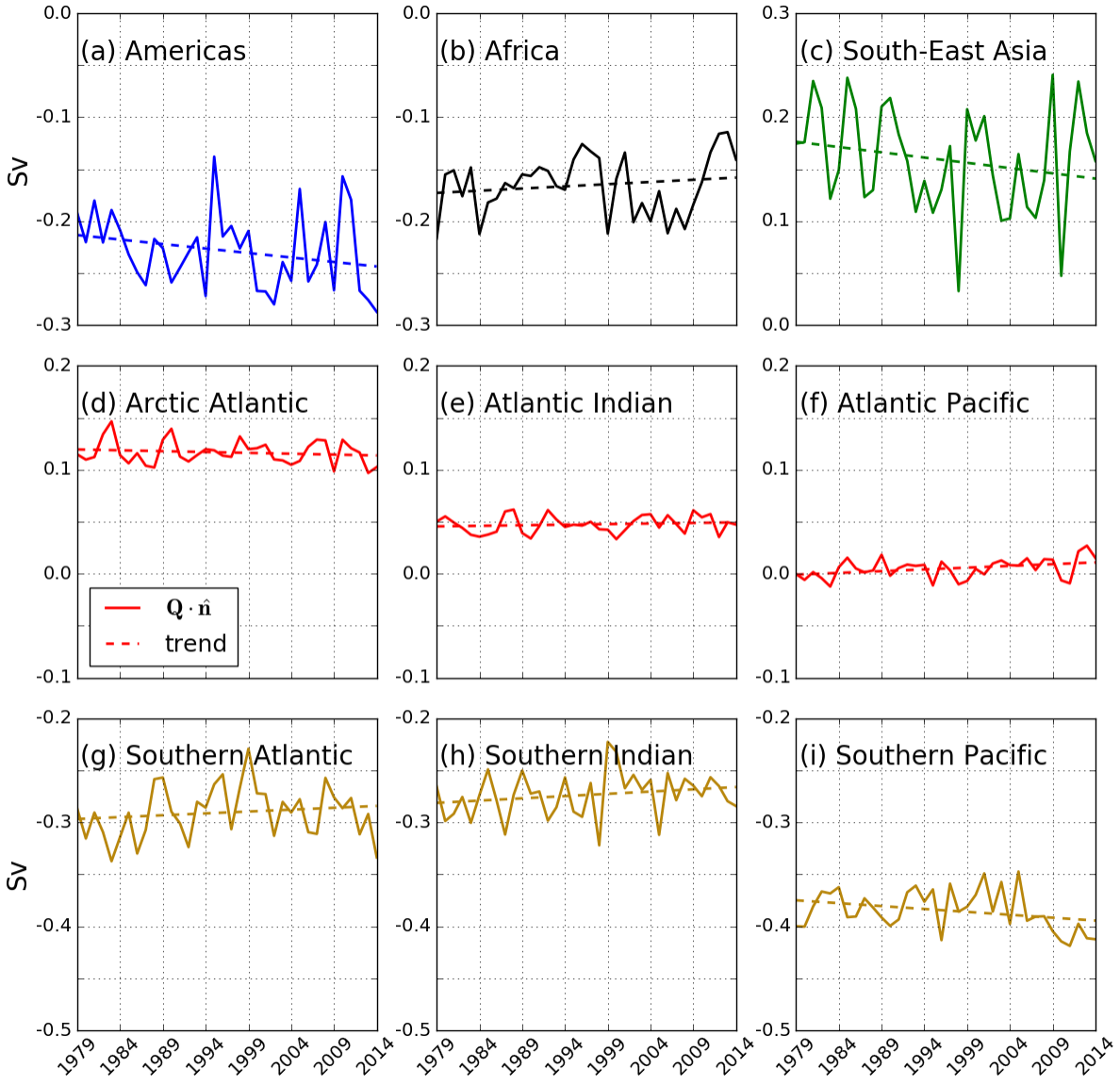

Figure 4.15: Interannual variability (1979-2014) of vertically- and horizontally-integrated ERA-Interim moisture fluxes normal to each catchment boundary (solid lines) and trends (dashed lines). Note that only the trends for the Arctic Pacific (f) and Southern Pacific (i) are statistically significant at the 90% level. The normal vector is defined to be positive in an eastward/northward direction and negative in a westward/southward direction.

section 4.2.3). During years with weakest $\mathbf{Q} \cdot \hat{\mathbf{n}}$ the AWP is large and extends into the tropical west Atlantic (Figure 4.16). Positive SST anomalies in this region result in low pressure anomalies resulting in increased convergence and therefore enhanced precipitation (Wang *et al.*, 2013). Increased convergence on the Atlantic side of the catchment boundary results in a reduction of the transport across Central America, thus reducing net evaporation over the Atlantic and inducing a tendency towards net evaporation over the Pacific (Figure 4.14(a,c)). A large AWP therefore reduces the Pacific/Atlantic $P - E$ asymmetry and a small AWP enhances it.

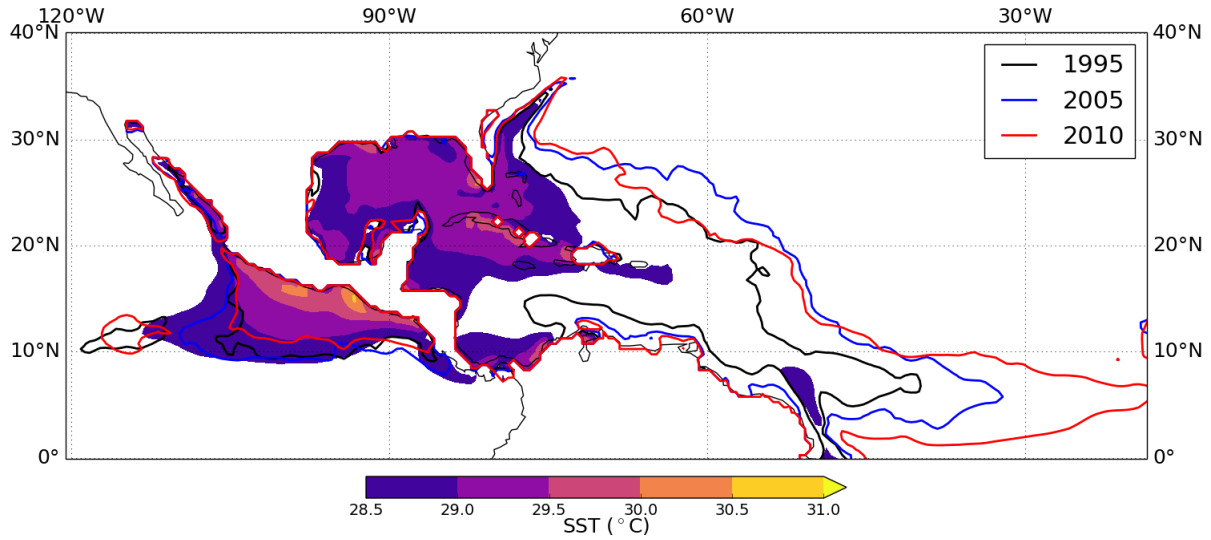

Figure 4.16: Annual mean (1980-2014) JJA Atlantic Warm Pool (filled contours; region of 28.5°C and above) from SODA (section 2.1.5) SST. The line contours show the extent of the JJA Atlantic Warm Pool in the years with the three lowest values of American $\mathbf{Q} \cdot \hat{\mathbf{n}}$ from Figure 4.15(a): 1995 (black), 2005 (blue) and 2010 (red).

4.4.2 Statistical relationships between $\mathbf{Q} \cdot \hat{\mathbf{n}}$ and $P - E$

Table 4.3 shows the Pearson correlation coefficients (r) and regression coefficients (m) between $\mathbf{Q} \cdot \hat{\mathbf{n}}$ on each catchment boundary and $P - E$ for each ocean drainage basin. The drainage basins tend to have strongest (and statistically significant) relationships with $\mathbf{Q} \cdot \hat{\mathbf{n}}$ on surrounding catchment boundaries although there are some exceptions. For example, each sector of the Arctic catchment boundary has a statistically significant (albeit weak) relationship with $P - E$ in the drainage basin to the east (*e.g.* r and m are statistically significant for Arctic Atlantic $\mathbf{Q} \cdot \hat{\mathbf{n}}$ and Indian $P - E$). Note that the three (Arctic/Southern) or four (Atlantic/Indian/Pacific) regression coefficients for the $\mathbf{Q} \cdot \hat{\mathbf{n}}$ around each drainage basin should sum to approximately one in each case.

The strongest statistical relationships are found between South-East Asian $\mathbf{Q} \cdot \hat{\mathbf{n}}$ and Indian $P - E$ ($r = -0.81$ and $m = 0.84$) and Pacific $P - E$ ($r = 0.84$ and $m = 0.65$). Americas $\mathbf{Q} \cdot \hat{\mathbf{n}}$ has strong and statistically significant relationships with both Atlantic and Pacific $P - E$, but the relationships with Atlantic $P - E$ are stronger. South-East Asian $\mathbf{Q} \cdot \hat{\mathbf{n}}$ therefore dominates the interannual variability of the $P - E$ asymmetry between the Indian and Pacific Oceans (which is also true of the seasonal cycle, Figure 4.10). With the interannual variability of Pacific $P - E$ dominated by the interannual variability of South-East Asian $\mathbf{Q} \cdot \hat{\mathbf{n}}$, it appears that South-East Asian $\mathbf{Q} \cdot \hat{\mathbf{n}}$ also dominates the interannual variability of the $P - E$ asymmetry between the Atlantic and Pacific Oceans. The interannual variability of Americas $\mathbf{Q} \cdot \hat{\mathbf{n}}$, appears to have only

a secondary role in the interannual variability of the Atlantic/Pacific $P - E$ asymmetry. This is not neccessarily surprising considering the relative sizes of the fluctuations from year-to-year in American and South-East Asian $\mathbf{Q} \cdot \hat{\mathbf{n}}$ (Figure 4.15(a,c)).

Interannual variability in both American and African $\mathbf{Q} \cdot \hat{\mathbf{n}}$ is dominated by interannual variability in the tropical regions of these catchment boundaries with very strong m and r for both (Tables 4.4 and 4.5). The tropical American $\mathbf{Q} \cdot \hat{\mathbf{n}}$ (20°N-15°S, AM1) also has strong statistical relationships with Atlantic and Pacific $P - E$ (Table 4.4) which highlights the dominance of the tropics in the Atlantic/Pacific $P - E$ asymmetry introduced in chapter 3 where the asymmetry is dominated by greater annual mean tropical precipitation in the Pacific compared to the Atlantic (Figure 3.5). The statistical relationships between tropical African $\mathbf{Q} \cdot \hat{\mathbf{n}}$ (20°N-26°S, AF2) and the neighbouring $P - E$ (Table 4.5) are weaker than the tropical American $\mathbf{Q} \cdot \hat{\mathbf{n}}$. This reflects the statistical relationships between net African $\mathbf{Q} \cdot \hat{\mathbf{n}}$ and neighbouring $P - E$ (Table 4.3) which is secondary to that of American and South-East Asian $\mathbf{Q} \cdot \hat{\mathbf{n}}$.

For the South-East Asian catchment boundary, $\mathbf{Q} \cdot \hat{\mathbf{n}}$ across both sections have strong and statistically significant relationships with net $\mathbf{Q} \cdot \hat{\mathbf{n}}$ and the neighbouring $P - E$ (Table 4.6). These statistics are generally stronger for the southern section (7°N-20°S, EA2) than the northern section (32°N-7°N, EA1) despite EA1 having much stronger $\mathbf{Q} \cdot \hat{\mathbf{n}}$ (Figure 4.2) with greater year-to-year fluctuations (not shown). The perhaps surprisingly strong statistics associated with the EA2 section is due to the tendency of its $\mathbf{Q} \cdot \hat{\mathbf{n}}$ to change sign from year-to-year (not shown) this having the effect of either reducing or increasing the neighbouring $P - E$ and the

Table 4.3: Correlation coefficients (r) and regression coefficients (m, Sv/Sv) for $\mathbf{Q} \cdot \hat{\mathbf{n}}$ (first column) and $P - E$ (top row). Values in bold are significant at the 90% level.

	Atlantic		Indian		Pacific		Arctic		Southern	
	r	m	r	m	r	m	r	m	r	m
Americas	**0.72**	**0.46**	0.13	0.10	**-0.61**	**0.34**	-0.22	-0.93	-0.12	-0.11
Africa	**-0.52**	**0.26**	**0.34**	**0.20**	0.05	0.02	-0.08	-0.26	**0.28**	**0.20**
SE Asia	-0.18	-0.16	**-0.81**	**0.87**	**0.84**	**0.65**	-0.22	-1.27	-0.14	-0.17
Arctic A	-0.01	0.00	**0.29**	**0.07**	-0.18	-0.03	0.25	0.32	-0.08	-0.02
Arctic I	0.15	0.02	0.03	-0.01	**-0.30**	**-0.04**	0.24	0.23	0.20	0.04
Arctic P	**-0.28**	**-0.05**	-0.20	-0.04	**0.33**	**-0.05**	**0.41**	**0.45**	0.00	0.00
Southern A	**0.64**	**0.28**	0.16	0.08	-0.18	-0.07	-0.08	-0.22	**-0.77**	**0.48**
Southern I	0.16	0.06	-0.13	-0.06	**-0.34**	**0.11**	0.11	0.26	**-0.65**	**0.34**
Southern P	0.14	0.05	-0.04	-0.02	0.18	0.05	-0.22	-0.48	**-0.40**	**0.19**

Table 4.4: Correlation (r) and regression (m) coefficients for interannual variability of American $\mathbf{Q}\cdot\hat{\mathbf{n}}$ split into smaller sections (first column) and net Americas $\mathbf{Q}\cdot\hat{\mathbf{n}}$, Atlantic $P-E$ and Pacific $P-E$ (top row). The smaller sections of the American catchment boundary (Figure 4.2) are based on the change in net direction of $\overline{\mathbf{Q}}\cdot\hat{\mathbf{n}}$ (Figure 4.3(a)). Values in bold are statistically significant at the 90% level.

	Americas $\mathbf{Q}\cdot\hat{\mathbf{n}}$		Atlantic $P-E$		Pacific $P-E$	
	r	m	r	m	r	m
AM1 (52°N-20°N)	-0.06	-0.02	-0.35	**-0.07**	-0.32	**-0.06**
AM2 (20°N-15°S)	**0.96**	**1.02**	0.78	**0.53**	0.67	**0.40**

Table 4.5: Correlation (r) and regression (m) coefficients for interannual variability of African $\mathbf{Q}\cdot\hat{\mathbf{n}}$ split into smaller sections (first column) and net African $\mathbf{Q}\cdot\hat{\mathbf{n}}$, Indian $P-E$ and Atlantic $P-E$ (top row). The smaller sections of the African catchment boundary (Figure 4.2) are based on the change in net direction of $\overline{\mathbf{Q}}\cdot\hat{\mathbf{n}}$ (Figure 4.3(b)). Values in bold are statistically significant at the 90% level.

	Africa $\mathbf{Q}\cdot\hat{\mathbf{n}}$		Indian $P-E$		Atlantic $P-E$	
	r	m	r	m	r	m
AF1 (40°N-20°N)	0.18	0.05	-0.18	-0.03	0.02	0.00
AF2 (20°N-26°S)	**0.93**	**0.92**	**0.37**	**0.22**	**-0.52**	**0.26**
AF3 (26°S-35°S)	0.11	0.03	0.08	0.01	-0.03	0.00

Table 4.6: Correlation (r) and regression (m) coefficients for interannual variability of South-East Asian $\mathbf{Q}\cdot\hat{\mathbf{n}}$ split into smaller sections (first column) and net South-East Asian $\mathbf{Q}\cdot\hat{\mathbf{n}}$, Pacific $P-E$ and Indian $P-E$ (top row). The smaller sections of the South-East Asian catchment boundary (Figure 4.2) are based on the change in net direction of $\overline{\mathbf{Q}}\cdot\hat{\mathbf{n}}$ (Figure 4.3(c)). Values in bold are statistically significant at the 90% level.

	SE Asia $\mathbf{Q}\cdot\hat{\mathbf{n}}$		Pacific $P-E$		Indian $P-E$	
	r	m	r	m	r	m
EA1 (32°N-7°N)	**0.68**	**0.33**	**0.70**	**0.26**	**-0.60**	**0.31**
EA2 (7°N-20°S)	**0.88**	**0.67**	**0.67**	**0.39**	**-0.68**	**0.55**

Pacific/Indian $P-E$ asymmetry. That the statistics for both sections are strong and significant should necessarily be surprising as the region is very sensitive to ENSO-induced interannual variability and also interannual variability in the strengths of the Asian (EA1) and Australian (EA2) Monsoons.

4.4.3 Dominant locations of $p-e$ interannual variability

Figures 4.17-4.19 show the regression maps for $\mathbf{Q}\cdot\hat{\mathbf{n}}$ (integrated between the end points of the catchment boundary), $P-E$ and the local surface water flux, $p-e$, for the Atlantic, Indian

and Pacific Ocean drainage basins. Regression maps for $\mathbf{Q} \cdot \hat{\mathbf{n}}$ across the American, African and South-East Asian catchment boundaries are presented as it has been shown that these fluxes dominate the $P - E$ asymmetries (section 4.3.3). Regression coefficients are shown instead of correlation coefficients to provide information about the size of the relationships. The normal vector, $\hat{\mathbf{n}}$, is oriented inward for each $\mathbf{Q} \cdot \hat{\mathbf{n}}$ such that $\mathbf{Q} \cdot \hat{\mathbf{n}}$ is positive when entering a drainage basin and negative when leaving. The regression maps should therefore be interpreted differently for $\mathbf{Q} \cdot \hat{\mathbf{n}}$ entering and leaving a drainage basin:

1. $\mathbf{Q} \cdot \hat{\mathbf{n}}$ entering drainage basin:
   - a positive statistical relationship (red contours) implies that as $\mathbf{Q} \cdot \hat{\mathbf{n}}$ increases (becomes more positive) $p - e$ increases *i.e.* with a stronger moisture flux into the basin there is a stronger tendency towards net precipitation
   - a negative statistical relationship (blue contours) implies that as $\mathbf{Q} \cdot \hat{\mathbf{n}}$ increases (becomes less positive) $p - e$ decreases *i.e.* with a weaker moisture flux into the basin there is a stronger tendency towards net evaporation

2. $\mathbf{Q} \cdot \hat{\mathbf{n}}$ leaving drainage basin
   - a positive statistical relationship (red contours) implies that as $\mathbf{Q} \cdot \hat{\mathbf{n}}$ decreases (becomes more negative) $p - e$ decreases *i.e.* with a stronger moisture flux out of the basin there is a stronger tendency towards net evaporation
   - a negative statistical relationship (blue contours) implies that as $\mathbf{Q} \cdot \hat{\mathbf{n}}$ increases (becomes less negative) $p - e$ increases *i.e.* with a weaker moisture flux out of the basin there is a stronger tendency towards net precipitation.

The regression maps relating basin-integrated $P - E$ to $p - e$ should simply be interpreted as an increase in $P - E$ having a positive relationship with increases in $p - e$.

Increases in American $\mathbf{Q} \cdot \hat{\mathbf{n}}$ leaving the Atlantic are associated with a stronger tendency towards net evaporation (reduced net precipitation) across the Gulf of Mexico, Caribbean Sea and western tropical North Atlantic (Figure 4.17(a)). This relationship is not particularly surprising given the link between SSTs in the AWP region and American $\mathbf{Q} \cdot \hat{\mathbf{n}}$ (Wang *et al.*, 2013). Interannual variability of African $\mathbf{Q} \cdot \hat{\mathbf{n}}$ entering the Atlantic is associated with changes in $p - e$ across the equatorial Atlantic (Figure 4.17(b)), with strong $\mathbf{Q} \cdot \hat{\mathbf{n}}$ linked to increased net precipi-

tation over the Congo basin and the western equatorial Atlantic. The influences of interannual variability of American and African $\mathbf{Q} \cdot \hat{\mathbf{n}}$ on the relationship between the interannual variability of $P - E$ appear to be independent of one another and related to different regions of the basin (Figure 4.17(c)). Ultimately the two main regions affecting interannual variability of Atlantic $P - E$ are the Caribbean Sea and western tropical North Atlantic (AWP region; Wang *et al.*, 2013) and the western equatorial Atlantic.

The relationship between interannual variability of African $\mathbf{Q} \cdot \hat{\mathbf{n}}$ leaving the Indian Ocean basin and $p - e$ is dominated by stronger tendencies towards net evaporation (reduced net precipitation) across the Bay of Bengal and eastern Indian Ocean (Figure 4.18(a)). This may be a signature of the Indian Ocean Dipole (IOD) where, in the positive phase, positive SST and precipitation anomalies are found in the west of the basin and the same anomalies occur in the east during the negative phase (Saji *et al.*, 1999). If Figure 4.18(a) does indeed show an IOD signature then the positive phase coincides with more moisture leaving the basin across Africa and decreased $p - e$ across the eastern Indian Ocean. Increases in South-East Asian $\mathbf{Q} \cdot \hat{\mathbf{n}}$ are also associated with stronger tendencies towards net evaporation around India and the eastern Indian Ocean (Figure 4.18(b)). This is reflected in the regression map for $P - E$ (Figure 4.18(c)) where increases in $P - E$ occur around the edges of the basin and are offset by decreasing $p - e$ in the centre of the Indian Ocean.

Pacific $p - e$ has very similar spatial relationships with both South-East Asian and American $\mathbf{Q} \cdot \hat{\mathbf{n}}$ (both of which converge into the Pacific basin). As each $\mathbf{Q} \cdot \hat{\mathbf{n}}$ increases (more moisture entering the basin) $p - e$ north of the equator also increases (enhanced net precipitation) and $p - e$ south of the equator decreases (Figure 4.19(a,b)). This may be associated with ITCZ movements and the structure of these regression maps is very similar to the maps of $e - p$ (Figures 1.4 and 3.1). The $p - e$ regression map for American $\mathbf{Q} \cdot \hat{\mathbf{n}}$ (Figure 4.19(b)) may also hint at ENSO-associated interannual variability with dry anomalies over the Maritime Continent with increased American $\mathbf{Q} \cdot \hat{\mathbf{n}}$ and stronger net precipitation east of Papua New Guinea. The regression map for Pacific $P - E$ variability (Figure 4.19(c)) also shows the dominance of tropical Pacific $p - e$ variability with increases in $P - E$ associated with stronger net precipitation north of the equator across the basin.

Overall, the regression maps in Figures 4.17-4.19 emphasize the dominance of the tropics in the $P - E$ asymmetries. This is particularly the case for the Pacific/Atlantic asymmetry with the tropical $p - e$ variability dominating the variability of basin-integrated $P - E$ in each

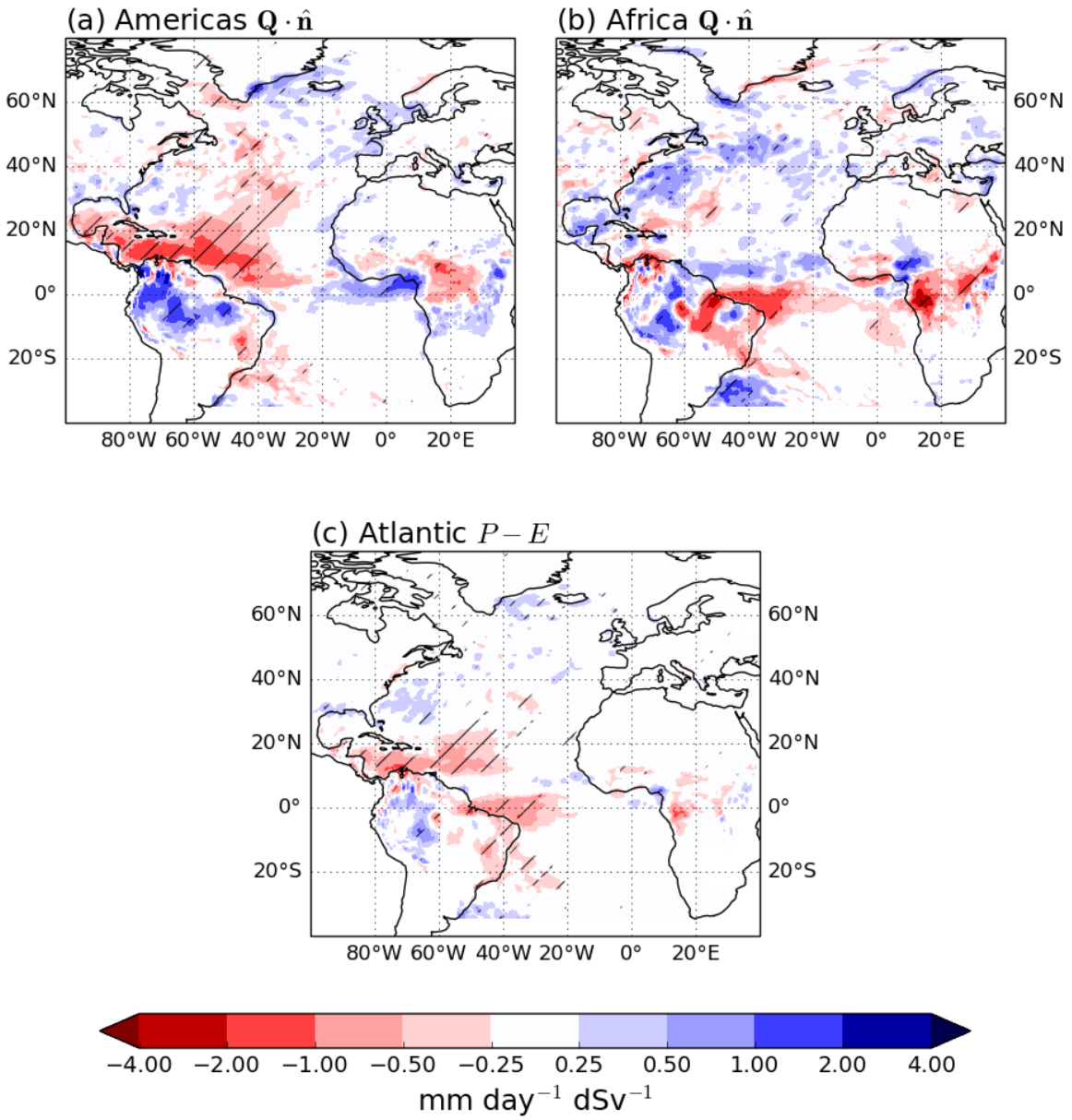

Figure 4.17: Regression maps for Atlantic $p - e$ with (a) Americas $\mathbf{Q} \cdot \hat{\mathbf{n}}$ (leaving the basin, therefore $\mathbf{Q} \cdot \hat{\mathbf{n}} < 0$), (b) African $\mathbf{Q} \cdot \hat{\mathbf{n}}$ (entering the basin, therefore $\mathbf{Q} \cdot \hat{\mathbf{n}} > 0$), and (c) Atlantic $P - E$. A positive statistical relationship (red contours) implies that as $\mathbf{Q} \cdot \hat{\mathbf{n}}$ decreases, $p - e$ decreases, and a negative statistical relationship (blue contours) implies that as $\mathbf{Q} \cdot \hat{\mathbf{n}}$ decreases, $p - e$ increases. See text for how these maps should be interpreted differently for $\mathbf{Q} \cdot \hat{\mathbf{n}}$ entering and leaving the basin. The units are mm day^{-1} dSv^{-1} (1 dSv $\equiv 10^{-1}$ Sv). Hatching indicates regions of 90% statistical significance.

basin. These findings support the results from chapter 3 where a large contrast in area-averaged tropical precipitation dominates the annual mean Pacific/Atlantic asymmetry (Figure 3.5). By linking interannual $p - e$ variability to $\mathbf{Q} \cdot \hat{\mathbf{n}}$, is is clearer which specific regions drive variability in the $P - E$ asymmetries but it remains unclear whether this variability is dominated by p or e as SST-driven variability in e appears to play a key role in some regions.

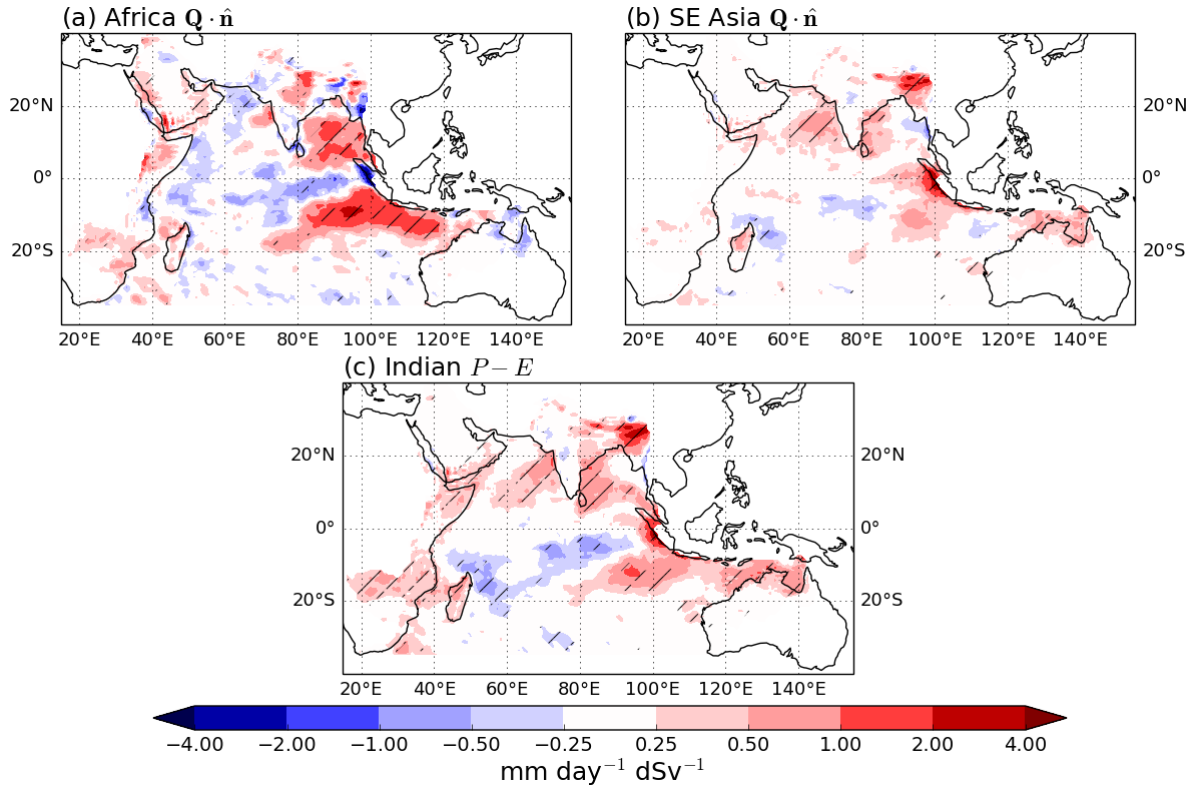

Figure 4.18: Regression maps for Indian $p-e$ and (a) African $\mathbf{Q}\cdot\hat{\mathbf{n}}$ (leaving the basin, therefore $\mathbf{Q}\cdot\hat{\mathbf{n}}<0$), (b) South-East Asian $\mathbf{Q}\cdot\hat{\mathbf{n}}$ (leaving the basin, therefore $\mathbf{Q}\cdot\hat{\mathbf{n}}<0$) and (c) Indian $P-E$. A positive statistical relationship (red contours) implies that as $\mathbf{Q}\cdot\hat{\mathbf{n}}$ decreases, $p-e$ decreases, and a negative statistical relationship (blue contours) implies that as $\mathbf{Q}\cdot\hat{\mathbf{n}}$ decreases, $p-e$ increases. See text for how these maps should be interpreted differently for $\mathbf{Q}\cdot\hat{\mathbf{n}}$ entering and leaving the basin. The units are mm day^{-1} dSv^{-1} (1 dSv $\equiv 10^{-1}$ Sv). Hatching indicates regions of 90% statistical significance.

4.4.4 Interannual variability of salinity

With $P-E$ and atmospheric moisture transport widely regarded to play a role in the variability of SSS and in the Atlantic/Pacific SSS asymmetry (Broecker, 1991; Leduc *et al.*, 2007) it is useful to find out if there are any statistical relationships between SSS and $\mathbf{Q}\cdot\hat{\mathbf{n}}$ and $P-E$ on interannual timescales. Figure 4.20 shows regression maps relating interannual variabilty in SODA SSS to $\mathbf{Q}\cdot\hat{\mathbf{n}}$ and $P-E$ for the Pacific Ocean. The spatial relationships shown in Figure 4.20 do have coherent structure to them, particularly along the equator. The region with a statistically significant negative relationship between SSS and South-East Asian $\mathbf{Q}\cdot\hat{\mathbf{n}}$ (SSS decreases as $\mathbf{Q}\cdot\hat{\mathbf{n}}$ entering the basin increases) could be considered realistic due to the heavy precipitation in the region (Figure 3.9). However, the bands of statistically significant positive relationships between SSS and $\mathbf{Q}\cdot\hat{\mathbf{n}}$ along the equator are counter-intuitive as increased $p-e$ (Figure 4.19) cannot lead to increased SSS - see first term on RHS of equation (1.1). Similar maps were produced for the other oceans using the same data (not shown) and two other SSS datasets:

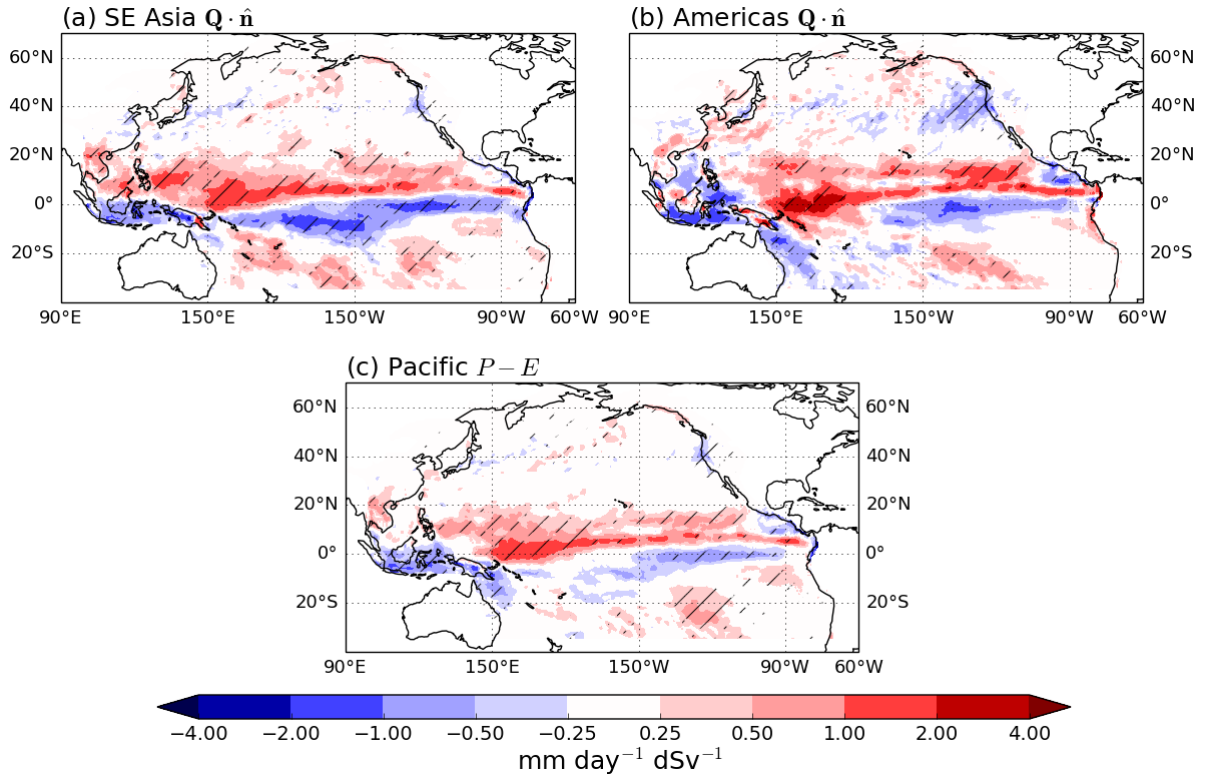

Figure 4.19: Regression maps for Pacific $p-e$ and (a) South-East Asian $\mathbf{Q}\cdot\hat{\mathbf{n}}$ (entering the basin, therefore $\mathbf{Q}\cdot\hat{\mathbf{n}}>0$), (b) American $\mathbf{Q}\cdot\hat{\mathbf{n}}$ (entering the basin, therefore $\mathbf{Q}\cdot\hat{\mathbf{n}}>0$) and (c) Pacific $P-E$. A positive statistical relationship (red contours) implies that as $\mathbf{Q}\cdot\hat{\mathbf{n}}$ decreases, $p-e$ decreases, and a negative statistical relationship (blue contours) implies that as $\mathbf{Q}\cdot\hat{\mathbf{n}}$ decreases, $p-e$ increases. See text for how these maps should be interpreted differently for $\mathbf{Q}\cdot\hat{\mathbf{n}}$ entering and leaving the basin. The units are mm day^{-1} dSv^{-1} (1 dSv $\equiv 10^{-1}$ Sv). Hatching indicates regions of 90% statistical significance.

ECCOv4 and EN4 (Good *et al.*, 2013). The results from these (not shown) were broadly similar to SODA with no clear link beween the interannual variability of SSS and moisture fluxes.

The lack of a clear link between the interannual variablity of SSS and $P-E$ found here is not surprising and seems consistent with previous findings. For example, Vinogradova and Ponte (2013) point out that, due to variability of oceanic fluxes, a one-to-one correspondence between local SSS tendency and freshwater fluxes cannot be expected on interannual timescales. Oceanic and freshwater fluxes are generally poorly correlated so they found that simple linear regression models could only capture a small amount of the variability in $E-P-R$ at scales of at least 100 km.

Bingham and Lee (2017) found that SSS tends to have shorter decorrelation timescales than freshwater fluxes which implies that there is no distinct relationship between SSS and $P-E$. When Bingham and Lee (2017) removed the seasonal cycle from these time scales they found that freshwater fluxes have a time scale in the range 150-250 days, with SSS time scales less than

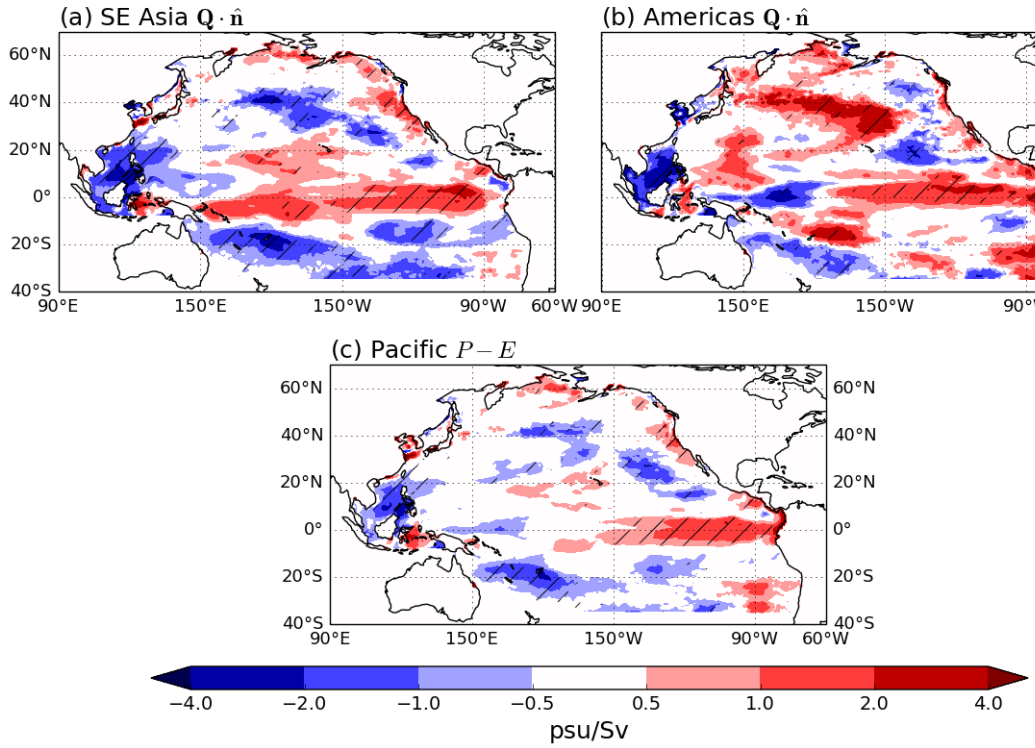

Figure 4.20: Regression maps for Pacific SODA SSS and (a) South-East Asian $\mathbf{Q}\cdot\hat{\mathbf{n}}$, (b) American $\mathbf{Q}\cdot\hat{\mathbf{n}}$ and (c) Pacific Ocean $P-E$. For $\mathbf{Q}\cdot\hat{\mathbf{n}}$ in (a) and (b) $\hat{\mathbf{n}}$ is oriented inward. Hatching indicates regions of 90% statistical significance.

20 days. Their results showed that SSS changes as a proxy for $P-E$ changes do not apply over the global ocean for short time scales. They speculated that momentum and vorticity fluxes may matter more than freshwater fluxes in determining SSS variability.

Zika *et al.* (2015) showed that, in both models and observations, that a mixing time scale of approximately 50 years exists on which freshwater fluxes affects the volumetric salinity distribution. Ferreira *et al.* (2018) find a similar mixing timescale (T) by considering a fractional salinity contrast multiplied by the ratio betwen the depth of a water column (H) and a north-south freshwater forcing contrast ($\Delta\tilde{P}$):

$$T \sim \frac{\Delta S}{S}\frac{H}{\Delta\tilde{P}}. \tag{4.7}$$

They also speculate that wind-driven and shallow overturning circulations could transport and mix salinity on decadal timescales. There is evidence for changes in near surface salinity in response to freshwater flux changes on decadal time scales (Durack and Wijffels, 2010; Skliris *et al.*, 2014). Both studies report an increasing trend in the Atlantic and a freshening trend in the Pacific.

The timescales considered in this study are therefore too short for the hydrological cycle to

have substantially influenced SSS and the 35 year record is not long enough. As a result, any attempts at making connections between the interannual variability of SSS and the hydrological cycle will produce results of limited use. However, it is not implausible that the changes to moisture transports on centennial to millenial timescales discussed in paleoclimate studies (Lohmann, 2003; Leduc *et al.*, 2007; Prange *et al.*, 2010) since correlation seems to increase with timescale (Durack and Wijffels, 2010).

4.5 Summary

It has been shown that the annual mean state of the $\overline{P-E}$ asymmetry between the Pacific and Atlantic Oceans, plus an additional $\overline{P-E}$ asymmetry between the Pacific and Indian Oceans, is a result of the following asymmetries in moisture transport:

1. A large deviation from the zonal mean zonal moisture flux ($[\overline{qu}]$) along the South-East Asian catchment boundary (Figure 4.12(c)) is the leading cause of the near neutral annual mean Pacific moisture budget and the strongly net evaporative Indian Ocean moisture budget (Figure 4.13.) This also appears to cause the strong area-averaged tropical Pacific precipitation (Figure 3.5).
2. Weaker than expected ($\overline{\mathbf{Q}}\cdot\hat{\mathbf{n}}$) along the African catchment boundary (Figure 4.12(b)) plays a secondary role but enhances the Pacific/Atlantic asymmetry as the Atlantic Ocean recieves less atmospheric moisture across its eastern boundary than it should according to $[\overline{qu}]$. This is a likely cause of the weak area-averaged tropical Atlantic precipitation (Figure 3.5).
3. The atmosphere is more efficient at exporting moisture between the Atlantic and Southern Oceans across 35°S than it is between the Pacific/Indian and Southern Oceans (Table 4.1). This appears to be due to stronger $\overline{q}\,\overline{v}$ (Figures 4.7(d),4.8(a)), the relative widths of the basins, the southward deflection of flow by the ITCZ and the existence of the SPCZ. Note that although atmospheric transport across 35°S is the least efficient of the three, Indian Ocean $P - E$ is dominated by moisture export across South-East Asia.
4. Due to the shape of the Arctic catchment boundary around the Pacific and Atlantic, about 0.11 Sv moisture is exported out of the Atlantic drainage basin into the Arctic across Eastern Europe. Atmospheric moisture entering the Pacific drainage basin across Asia is balanced by export across Alaska and Canada.
5. The $P - E$ asymmetries are dominated by the annual mean flow ($\overline{q}\,\overline{\mathbf{v}}\cdot\hat{\mathbf{n}}$) as it causes a

net atmospheric moisture import of 0.46 Sv to the Pacific basin but net exports of 0.25 Sv and 0.39 Sv from the Atlantic and Indian basins respectively. Transient moisture fluxes ($\overline{q'\mathbf{v}'} \cdot \hat{\mathbf{n}}$) result in net export of atmospheric moisture from each of these basins (Figure 4.8).

6. The seasonal cycle of $\overline{\mathbf{Q}} \cdot \hat{\mathbf{n}}$ and $P - E$ (Figure 4.10) shows that the $P - E$ asymmetries are largest in JJA when Pacific $P - E = 0.55Sv$. This is caused by a South-East Asian $\overline{\mathbf{Q}} \cdot \hat{\mathbf{n}}$ of 0.52 Sv. The atmospheric moisture budget of the Pacific Ocean drainage basin, and the $P - E$ asymmetries, are therefore dominated by the Asian Summer Monsoon in JJA.

The interannual variability of each $P - E$ and $\mathbf{Q} \cdot \hat{\mathbf{n}}$ were also discussed in this chapter with regards to interannual variability of the $P - E$ asymmetries. The key findings were that South-East Asian $\mathbf{Q} \cdot \hat{\mathbf{n}}$ is the most variable (mostly ENSO-driven) and dominates interannual variability of Pacific and Indian Ocean $P - E$ (Table 4.3). Interannual variabilty of American $\mathbf{Q} \cdot \hat{\mathbf{n}}$ (primarily driven by the size of the Atlantic Warm Pool; Wang *et al.*, 2013) dominates interannual variability of Atlantic $P - E$ but is secondary to South-East Asian $\mathbf{Q} \cdot \hat{\mathbf{n}}$ for Pacific $P - E$ (Table 4.3). Moisture fluxes across South-East Asia therefore dominate both the mean state and interannual variability of the moisture budget asymmetries.

The interannual variability in American and African $\mathbf{Q} \cdot \hat{\mathbf{n}}$ is dominated by variability in westward $\mathbf{Q} \cdot \hat{\mathbf{n}}$ in the tropics (Tables 4.4 and 4.5) with $\mathbf{Q} \cdot \hat{\mathbf{n}}$ on both sections of the South-East Asian catchment boundaries showing strong statistical relationships with net $\mathbf{Q} \cdot \hat{\mathbf{n}}$ (Table 4.6). Regression maps linking interannual variabilty of basin-wide $p - e$ (Figures 4.17-4.19) to $\mathbf{Q} \cdot \hat{\mathbf{n}}$ and $P-E$ indicate specific regions in which $p-e$ variability dominated $P-E$ variability such as the Atlantic Warm Pool region and the tropical Pacific. These findings support the conclusion from chapter 3 that the annual mean Pacific/Atlantic moisture budget asymmetry is dominated by greater precipitation per unit area across the tropical Pacific (Figure 3.5). However, it was not possible to find clear statistical relationships between the interannual variability of moisture fluxes and SSS as interannual timescales are too short and oceanic processes play an important role (Bingham and Lee, 2017).

The understanding of the role of atmospheric moisture transport in the Atlantic/Pacific moisture budget asymmetry has previously focused on Central America: moisture evaporated from the Atlantic is transported across Central America in the trade winds and falls as precipitation over the Pacific Ocean (Dietrich, 1963; Weyl, 1968; Broecker, 1991). However, it was

shown that the net moisture flux across the American catchment boundary is only as large as would be expected from the zonal mean zonal moisture flux (Figure 4.12), with transport across Africa weaker than expected and transport across South-East Asia in the opposite direction to the zonal mean (Figure 4.12).

This chapter has shown that the mean state and interannual variability of the Pacific/Atlantic atmospheric moisture budget asymmetry is dominated by zonally anomalous moisture fluxes across South-East Asia. Replacing the vertically-integrated moisture fluxes normal to the American, African and South-East Asian catchment boundaries with the integrals of the zonal mean zonal moisture flux between the corresponding latitudes gives three net evaporative basins (Figure 4.13), which is expected from basins with these latitudes (Figure 4.11). The area-averaged atmospheric moisture budgets of the Atlantic, Indian and Pacific basins are also much closer than in the "real world" (Table 4.2) with Atlantic and Indian net evaporation cut by 43% and 72% respectively. These results suggest that the Pacific/Atlantic asymmetry should not be considered in isolation from the Indian Ocean, but that a Pacific/Indian asymmetry should also be included when attempting to understand basin-integrated atmospheric moisture budgets.

The role of weak moisture transport across Africa in the Pacific/Atlantic asymmetry is often neglected, or only referred to with respect to be being weaker than the net transport across the Americas (Broecker, 1991; Levang and Schmitt, 2015; Singh *et al.*, 2016). Schmittner *et al.* (2011) considered the Atlantic/Pacific asymmetries in moisture budget, SSS and MOC but focused only on atmospheric moisture transport across the tropical and midlatitude Americas. Wei and Bordoni (2016) conducted experiments with no African mountains and found counterintuitive results where JJA precipitation over India increased despite a weakening of the Somali jet. Removing the African mountains resulted in stronger westerly winds across the east African coast which would suggest that net moisture transport across Africa may decrease in the absence of mountains.

This chapter has focused on understanding the annual mean state and interannual variabilty of the Pacific/Atlantic and Pacific/Indian $P - E$ asymmetries by linking $\mathbf{Q} \cdot \hat{\mathbf{n}}$ on the catchment boundaries to $P - E$ for the ocean drainage basins. In section 4.1.3 three problems with the current interpretation of the Pacific/Atlantic $P - E$ asymmetry are presented. The first problem is one unique to Broecker (1991) and this chapter has dealt with the second problem, building on the findings of Emile-Geay *et al.* (2003) and Ferreira *et al.* (2018) to show highlight

the importance of South-East Asian $\mathbf{Q} \cdot \hat{\mathbf{n}}$ towards the $P - E$ asymmetries. The following chapter will approach the third of these problems (relating to moisture origins) by using Lagrangian diagnostics to build on the purely Eulerian understanding of the $P - E$ asymmetries from this chapter.

Chapter 5

Using trajectories to understand the atmospheric moisture budget asymmetries

The two previous chapters focused on understanding the atmospheric moisture budgets of the ocean basins from an Eulerian perspective. In this chapter the atmospheric moisture budgets of each ocean basin are studied from a Lagrangian perspective using an air mass trajectory model (Methven, 1997, see chapter 2).

5.1 Introduction

The moisture fluxes normal to the catchment boundaries of the ocean drainage basins ($\overline{\mathbf{Q}}\cdot\hat{\mathbf{n}}$) discussed in the previous chapter are often interpreted as a direct transport of moisture between neighbouring oceans across the dividing catchment boundary. Specifically, moisture transport between the Atlantic and Pacific drainage basins is often interpreted as moisture which has evaporated from the subtropics and transported across Central America in the trade winds and precipitated out over the Pacific Ocean (Dietrich, 1963; Weyl, 1968; Broecker, 1991; Zaucker and Broecker, 1992). However, simply interpreting these moisture fluxes as direct exchanges of moisture between two neighbouring ocean basins ignores any remote sources of moisture from other basins and cannot reveal the atmospheric phenomena responsible for the transport. For example, the moisture flux across Central America could be composed of moisture with origin in the Indian Ocean or from the Pacific Ocean which has travelled all the way round the hemi-

sphere westward, or moisture that was travelling eastward but has doubled back and returned westward. This chapter will therefore use Lagrangian techniques to partition each $\overline{\mathbf{Q}} \cdot \hat{\mathbf{n}}$ into the contributions from each ocean drainage basin and identify the main regions of moisture origins within each drainage basin and to identify some of the key dynamical phenomena responsible.

There have been two previous attempts to understand the Atlantic/Pacific atmospheric moisture budget asymmetry using Lagrangian techniques. Stohl and James (2005) looked at 10 day forward trajectories from each ocean basin and concluded that air from the North Pacific "produces" net evaporation over the North Atlantic and that air from the Indian Ocean "produces" net precipitation over the Pacific. Singh *et al.* (2016) used numerical water tracers to investigate how the moisture budget and salinity asymmetry amplify with global warming, finding that enhanced Atlantic-to-Pacific atmospheric moisture transport is due to greater distances between source and sink regions, and that moisture residence time increases.

There are many regional studies which use Lagrangian methods to trace precipitation origins (*e.g.* Iceland (Nieto *et al.*, 2007), Central America (Duran-Queseda *et al.*, 2010), England and Wales (de Leeuw *et al.*, 2017)) and two global studies (Gimeno *et al.*, 2010; van der Ent and Savenije, 2013). Both these studies show that most of the Atlantic Ocean provides moisture for continental precipitation despite using very different methods. However, van der Ent and Savenije (2013) found that only narrow regions of the eastern Pacific Ocean off the coasts of North and South America provide significant[1] moisture for continental precipitation, whereas Gimeno *et al.* (2010) identified both subtropical highs as major source regions. Across the Pacific it therefore seems that much of the evaporated moisture rains out before reaching land. The contrasting sizes of the Atlantic and Pacific source regions may be linked to the relative widths of the basins (Schmitt *et al.*, 1989; Ferreira *et al.*, 2010; Wills and Schneider, 2015) with the greater width of the Pacific basin resulting in low levels of moisture export by the atmosphere - a point which will be addressed in this chapter.

It is important to note that this study does not attempt to make a direct link between precipitation distributions over each ocean drainage basin and moisture origins. Instead, back trajectories are released from the catchment boundaries of the ocean drainage basins (Figure 2.11) to find the origins of $\overline{\mathbf{Q}} \cdot \hat{\mathbf{n}}$ crossing each catchment boundary. This allows $\overline{\mathbf{Q}} \cdot \hat{\mathbf{n}}$ to be partitioned into contributions from each drainage basin and the effect on basin-wide precipi-

[1] van der Ent and Savenije (2013) defined the major oceanic source regions for continental precipitation as regions where more than 250 mm/yr of oceanic evaporation is transported to the continent. This must be at least 20% of the total evaporation in the region

tation and the atmospheric moisture budget is inferred through conservation of moisture and Divergence Theorem (equations (4.1)-(4.2)).

5.2 Trajectory origin definitions

To find the moisture origins the method of de Leeuw (2014) and de Leeuw *et al.* (2017) is used. This method relates an air mass trajectory's thermodynamic properties to its last rapid interaction with the surface. Figure 5.1 shows the different origin types.

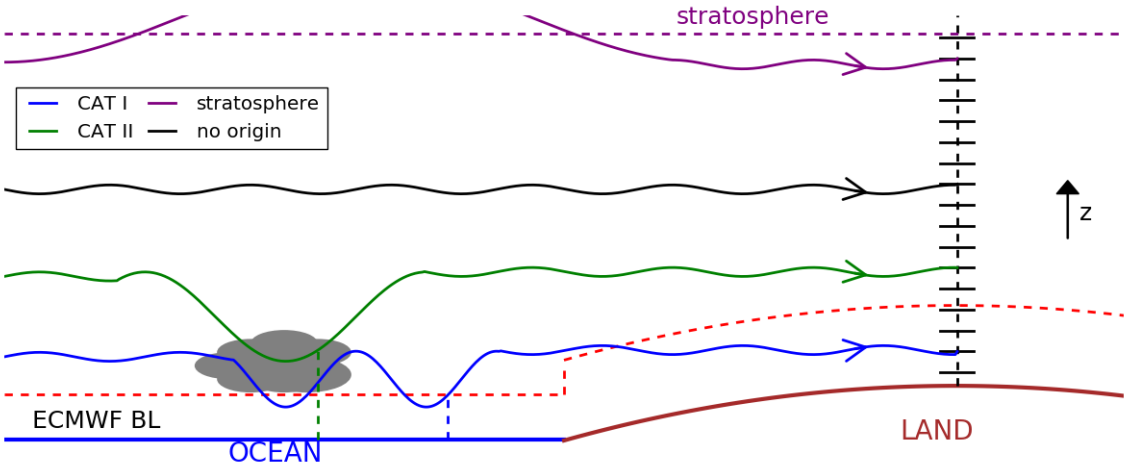

Figure 5.1: Schematic showing the different trajectory origin categories: boundary layer origin (CAT I, blue), partial mixing (CAT II, green), stratosphere (purple) and no origin (black). The trajectory with CAT I origin is assigned origin upon its last exit from the ocean BL. In this example the trajectory enters the BL above the land after exiting the ocean BL before arriving at the catchment boundary (black dashed line). The trajectory with CAT II origin experiences mixing in a cloud (dashed green line) above the top of the ECMWF BL (dashed red line) where θ_e and q both increase. The trajectory with stratospheric origin exits the stratosphere (bounded by the tropopause, dashed purple line) before arriving at the catchment boundary. The solid black lines at the catchment boundary are the η levels on which trajectories are initialized.

5.2.1 Boundary Layer origin

The first origin category (CAT I) identifies a trajectory's moisture origin at its last exit from the atmospheric boundary layer (BL). The BL height (z_{BL}) in ERA-Interim is defined in the IFS using the Bulk Richardson number ($R_{i_{b(z)}}$, an indicator of shear and stability) where z_{BL} is the first level above the surface where the Bulk Richardson number greater than a critical value. Below the critical value (0.25) the BL is well-mixed due to turbulence, but above the critical value turbulence does not occur. This definition of z_{BL} only takes dry dynamics into account. As latent heat release is not accounted for, this definition of z_{BL} only defines the dry boundary layer height which is approximately the same as the cloud base height. In unsaturated conditions the virtual potential temperature (θ_v) is well-mixed (Emmanuel, 1994) so air properties

at origin location are closely related to the air properies at the ocean surface. Note that CAT I origins are only assigned when a trajectory exits the BL above the ocean (as determined by the ERA-Interim land-sea mask) in order to link moisture fluxes to oceanic moisture origins (Figure 5.1), so if a trajectory crosses the coast in the BL it is assigned CAT I origin at the coast.

5.2.2 Partial Mixing origin

The second origin category (CAT II) assigns origins to trajectories within the cloud layer above the dry BL (Figure 5.1) that do not fall below z_{BL} (de Leeuw *et al.*, 2017). The criterion for CAT II origin is that equivalent potential temperature (θ_e) must increase by at least 2.5 K over three consexutive 6 hour time steps with an accompanying increase in q to exclude dry mixing (de Leeuw *et al.*, 2017). This assumes that θ_e at the origin location is approximately equal to θ_e at the surface as θ_e is well mixed in a moist BL. The Bolton (1980) formula is used to calculate θ_e :

$$\theta_e = \theta \exp\left(\left(\frac{3.376}{\Psi} - 0.00254\right) 10^3 w(1 + 0.81w)\right) \tag{5.1}$$

$$\Psi = \frac{2840}{3.5\log(T) - \log\left(\frac{100\,\tilde{p}\,w}{0.622+0.378w}\right) - 0.1988} + 55 \tag{5.2}$$

$$w = \frac{q}{1-q}, \tag{5.3}$$

where θ is potential temperature (K), w is the mixing ratio of water vapour (kg/kg), T is temperature (K), $\tilde{p}$ is pressure (Pa) and q is specific humidity (kg kg^{-1}). CAT II origins are permitted to occur over land if the criterion is met as it then includes any regions with high convective activity and moisture recycling (*e.g.* the Amazon and Congo rainforests).

5.2.3 Stratospheric origin

If a trajectory is in the stratosphere upon arrival at the catchment boundary or if it has recently been in the stratosphere before arrival (Figure 5.1) then it is assigned stratospheric origin. These trajectories are dry and do not contribute significantly to $\mathbf{Q} \cdot \hat{\mathbf{n}}$. A trajectory is diagnosed as being in the stratosphere if it is above the dynamical tropopause, *i.e.* $\theta > 380$ K or PV > 3 PVU (potential vorticity units; 1 PVU $\equiv 10^{-6}$ K m^2 kg^{-1} s^{-1}). Trajectories which fulfill either of these criteria were also checked to see if their height above surface when one of the criteria was met exceeded 6 km. This excluded low trajectories with high PV in the BL or at high latitudes.

5.2.4 Prioritization of origins

If a trajectory has been in the stratosphere more recently than it has fulfilled the criteria for either CAT I or CAT II origins then it will be assigned stratospheric origin. CAT I origins are given priority over CAT II origins as the relationship between θ_v at origin height and θ_v at 2 m height (for CAT I origins) is stronger than the relationship between θ_e at origin height and θ_e at height (for CAT II origins) (de Leeuw, 2014). This weaker relationship for CAT II is the reason a trajectory is considered to experience "partial mixing" where as CAT I trajectories undergo turbulent mixing in the BL. CAT I origins are given priority for the entire length of the trajectory, therefore even if CAT II occurs near to the trajectory's arrival it will be assigned CAT I origin if is has made contact the BL further back along the trajectory.

5.3 Trajectory length

5.3.1 Moisture Residence Time

Many studies investigating moisture origins using trajectories use 10 day back trajectories (e.g., Nieto *et al.*, 2007; Duran-Queseda *et al.*, 2010), a choice based on the global mean moisture residence time (Trenberth, 1998; Numaguti, 1999):

$$\tau \equiv \lambda^{-1} = \frac{w}{P}, \tag{5.4}$$

where λ^{-1} is the e-folding time constant for depletion of precipitable water (w) by precipitation (P). Trenberth (1998) found a global mean moisture residence time of 8-10 days. This global mean moisture residence time may not neccessarily be representative of the moisture residence time in each region for which 10 day trajectories have been used as the residence time is highly variable globally. For example, it can be as high as 24 days in the subtropics (Cau *et al.*, 2007).

Recent studies have revisited the global mean moisture residence time. For example, Läderach and Sodemann (2016) constructed a Lagrangian estimate of moisture residence time based on trajectories and a depletion constant which includes div$\mathbf{Q}$. They found a much shorter globally averaged moisture residence time of 4-5 days, but van der Ent and Tuinenburg (2017) argue that this is unphysical as it violates global mass balance due to the FLEXPART model's tendency to overestimate evaporation. van der Ent and Tuinenburg (2017) support the calculation of global mean moisture residence time using equation (5.4) and conclude that the traditional estimate of 8-10 days remains valid.

5.3.2 Evolution of proportion of moisture flux

For this study, the important factor in determining the trajectory length was how much of $\mathbf{Q} \cdot \hat{\mathbf{n}}$ can be attributed to an origin as trajectory length is increased. To find this, one month of 30-day back trajectories were released every 12 hours from the American catchment boundary on 17 evenly spaced η levels (from 0.95 to 0.15) to find a suitable trajectory length.

The proportion of trajectories which can be assigned an origin is a monotonically increasing quantity with trajectory length (Figure 5.2(a)). Initially, more trajectories have CAT II origin than CAT I but as the trajectory length is increased to 8 days the number of trajectories with CAT II orgins begins to decrease. At the same point the number of trajectories with CAT I origin increases more rapidly. This is because CAT II origins are reassigned to CAT I origins as trajectories make contact with the BL above the ocean and CAT I origins are prioritized over CAT II origins (section 5.2.4). Close inspection of Figure 5.2(a) reveals small oscillations on the total, CAT I and CAT II lines. These oscillations are caused by the diurnal cycle of the BL height which peaks in daytime so more trajectories can make contact with it. This can be seen more clearly on similar plots for a single release of trajectories (not shown). The oscillations also disappear with increasing trajectory length as the trajectories are spread out across different timezones and therefore less susceptible to the diurnal cycle of BL height.

To investigate the proportion of $\mathbf{Q} \cdot \hat{\mathbf{n}}$ explained with increasing trajectory length the mag-

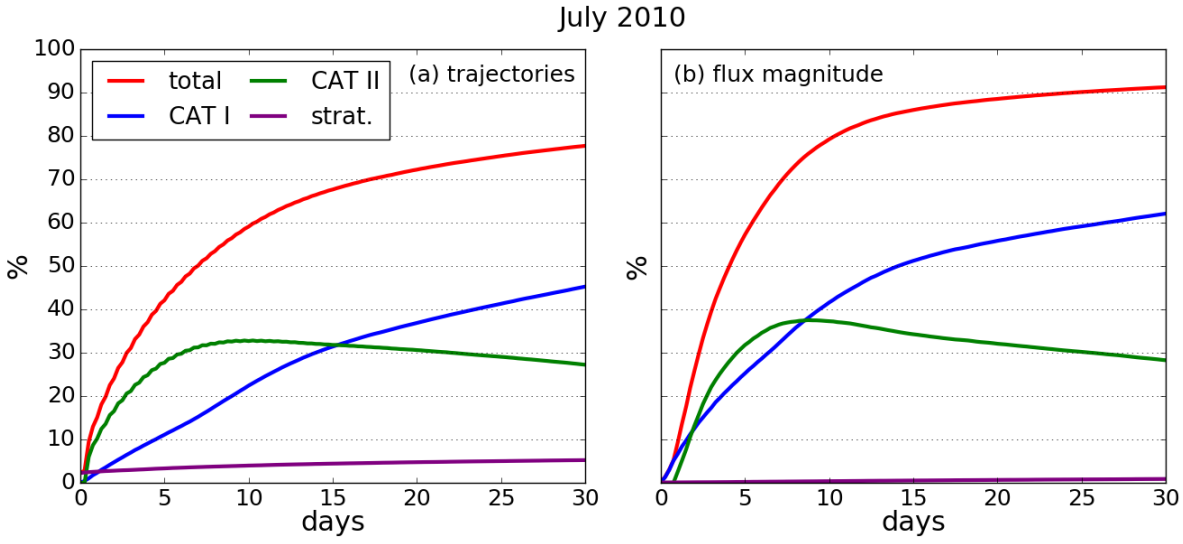

Figure 5.2: Evolution of proportion (a) of trajectories and (b) flux magnitude from trajectories with all origin types (red), CAT I origins (blue), CAT II origins (green) and stratospheric origins (purple) as trajectory length is increased. These results are averaged over trajectories released every 12 hours from the American catchment boundary in July 2010. The sum of the CAT I, CAT II and stratosphere lines is equal to the red line in both panels.

nitude of the moisture flux explained by trajectories with an assigned origin was calculated at each timestep, *i.e.*:

$$|\mathbf{Q}\cdot\hat{\mathbf{n}}| = \frac{1}{g}\oiint_{\partial V} q_{t=0}|\mathbf{v}|\cdot|\hat{\mathbf{n}}|\,\frac{\partial\tilde{p}}{\partial\eta}\,\mathrm{d}\eta\,\mathrm{d}l, \tag{5.5}$$

so that both components of $\mathbf{v}$ and $\hat{\mathbf{n}}$ are positive, and $q_{t=0}$ is specific humidity for each trajectory at the time the trajectory is initialized. The contribution to $|\mathbf{Q}\cdot\hat{\mathbf{n}}|$ from trajectories with stratospheric origin is very weak (less than 1%, Figure 5.2(b)) as these trajectories have a very low moisture content. The effect of reassigning CAT II origins to CAT I is also seen in the evolution of $|\mathbf{Q}\cdot\hat{\mathbf{n}}|$ but the CAT I $|\mathbf{Q}\cdot\hat{\mathbf{n}}|$ becomes dominant earlier than the evolution of trajectories does. The total $|\mathbf{Q}\cdot\hat{\mathbf{n}}|$ begins to level off after 20 days and becomes asymptotic to approximately 91%. Trajectories longer than 20 days will only provide diminishing returns to $|\mathbf{Q}\cdot\hat{\mathbf{n}}|$.

To see at what trajectory length the net $\mathbf{Q}\cdot\hat{\mathbf{n}}$ can be accurately calculated from all trajectories, the evolution of net $\mathbf{Q}\cdot\hat{\mathbf{n}}$ with increasing trajectory length was investigated along with the positive (westward/northward) and negative (eastward/southward) components of the flux (Figure 5.3) *i.e.*

$$\mathbf{Q}\cdot\hat{\mathbf{n}} = \mathbf{Q}\cdot\hat{\mathbf{n}}_+ + \mathbf{Q}\cdot\hat{\mathbf{n}}_-, \tag{5.6}$$

where $\mathbf{Q}\cdot\hat{\mathbf{n}}_+ > 0$ and $\mathbf{Q}\cdot\hat{\mathbf{n}}_- < 0$. The net $\mathbf{Q}\cdot\hat{\mathbf{n}}$ levels off between 10 and 15 days. For trajectories longer than 15 days $\mathbf{Q}\cdot\hat{\mathbf{n}}_+$ and $\mathbf{Q}\cdot\hat{\mathbf{n}}_-$ increase very slowly and at similar rates, which is evident by the flat line of the evolution of net $\mathbf{Q}\cdot\hat{\mathbf{n}}$. Therefore net $\mathbf{Q}\cdot\hat{\mathbf{n}}$ cannot be accurately calculated

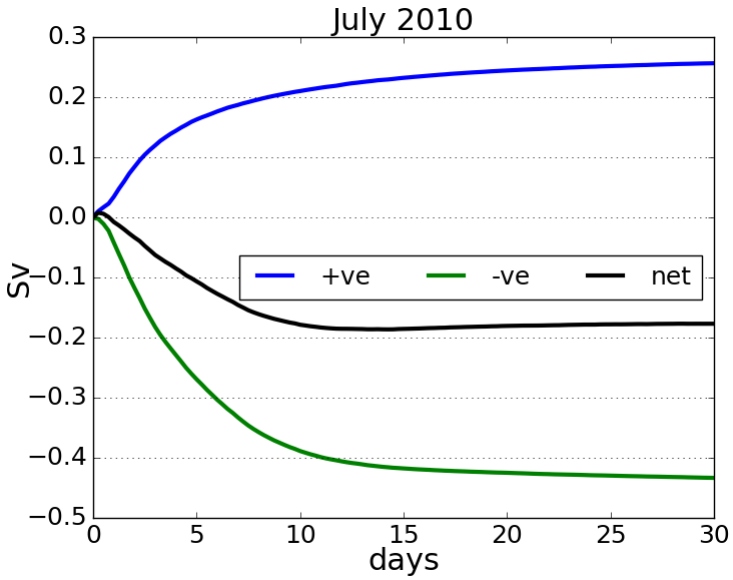

Figure 5.3: Evolution of the positive (blue; westward/northward), negative (green; eastward/southward) and net (black; sum of positive and negative) contributions to $\mathbf{Q}\cdot\hat{\mathbf{n}}$. These results are averaged over trajectories released every 12 hours from the American catchment boundary in July 2010.

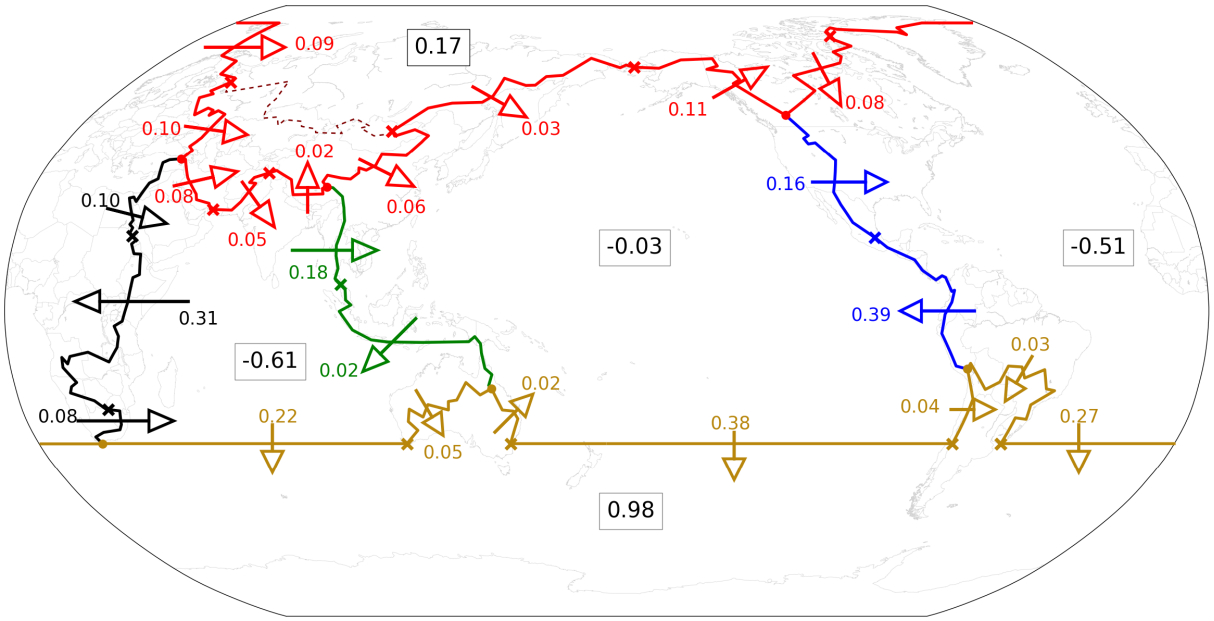

Figure 5.4: Vertically and horizontally integrated annual mean (2010-2014) ERA-Interim moisture fluxes normal to each catchment boundary ($\overline{\mathbf{Q}} \cdot \hat{\mathbf{n}}$, arrows) and basin-integrated $\overline{P-E}$ (boxes). All units are Sverdrups (1 Sv $\equiv 10^9$ kg s^{-1}). See the caption of Figure 4.2 for a full description.

from short trajectories and local sources of moisture close to the catchment boundary cannot sufficiently explain net $\mathbf{Q} \cdot \hat{\mathbf{n}}$.

Based on the results in this section, 14-day back trajectories were considered to be sufficient for the purposes of this study due to the proportion of $|\mathbf{Q} \cdot \hat{\mathbf{n}}|$ explained at this length and the length required to accurately calculate net $\mathbf{Q} \cdot \hat{\mathbf{n}}$. Note that these results are averaged over only one month and based on one catchment boundary. However, results in other months and on other catchment boundaries are broadly similar.

5.4 Model set-up

This study uses the ROTRAJ model (Methven (1997); described in chapter 2) to calculate offline trajectories from 6-hourly ERA-Interim data. Back trajectories (14 days long, see section 5.3) are released from the catchment boundaries surrounding each ocean drainage basin on 17 evenly spaced η levels (from 0.95 to 0.15) every 12 hours (at 0000 UTC and 1200 UTC) over the five year period 2010-2014. Trajectories are released from 00 UTC on 1st January 2010 to 00 UTC on 1st January 2015. Overall there are 101,508,135 trajectories. The annual mean atmospheric moisture budgets of each ocean drainage basin and the asymmetry between the Pacific and the Atlantic/Indian over this time period (Figure 5.4) are similar to the full 36-year ERA-Interim climatology (Figure 4.2).

To determine each trajectory's origin type, several attributes were interpolated to the trajectory's location at each 6 hour timestep: specific humidity (q), potential vorticity (PV), pressure ($\tilde{p}$), height (z), boundary layer height (z_{BL}) and temperature (T). Additonally, three further attributes were output at the trajectory's release time to help calculate $\mathbf{Q} \cdot \hat{\mathbf{n}}$: zonal wind ($u$), meridional wind ($v$) and surface pressure ($\tilde{p}_{\mathrm{surf}}$).

5.4.1 Discrepancies between trajectory model output and ERA-Interim pressure levels data

In this study, trajectories are released from 17 evenly spaced η levels from 0.95 to 0.15. At sea level these correspond to 950 hPa and 150 hPa respectively. The ECMWF model, however, has 60 η levels (Dee *et al.*, 2011) ranging from $\eta = 1$ at the surface to $\eta = 0$ at the top of the atmosphere, so it is likely that this vertical subsampling may cause problems with the calculation of vertically-integrated moisture fluxes from trajectory model output. To evaluate the potential effects of vertical subsampling the trajectory output is compared to ERA-Interim data interpolated to 37 pressure levels (from 1000 hPa to 1 hPa).

The vertical profiles of trajectory data agree well with the pressure levels data (Figure 5.5).

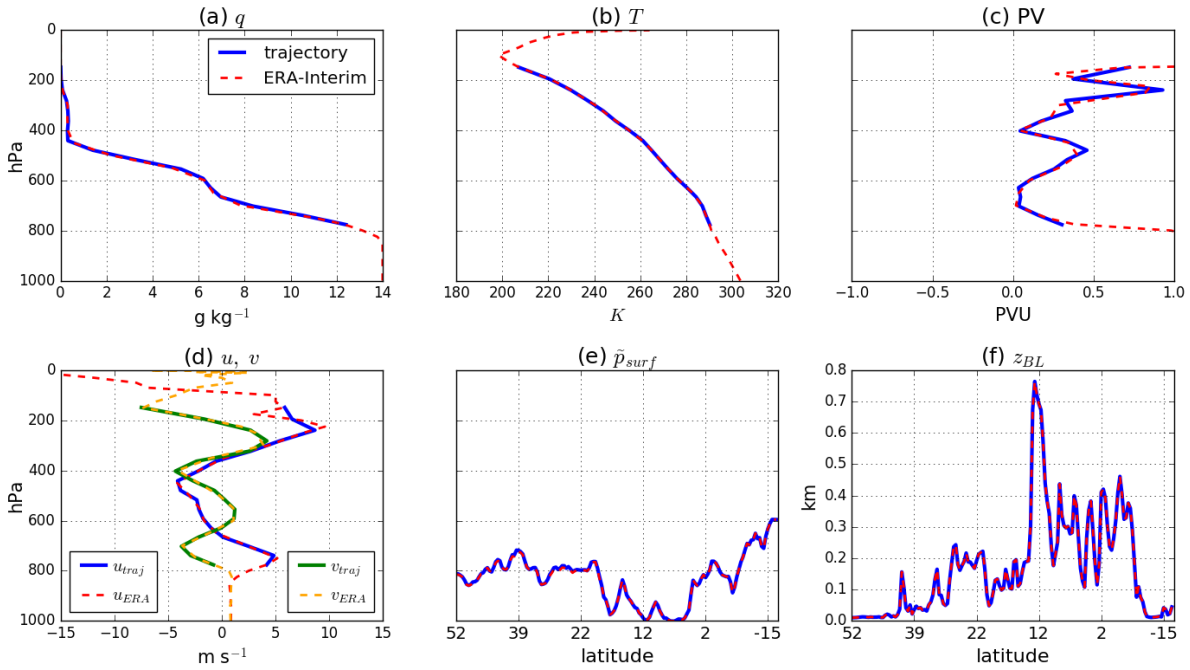

Figure 5.5: Comparison between vertical profiles of (a) specific humidity, (b) temperature, (c) potential vorticity, (d) zonal and meridional winds, horizontal profiles of (e) surface pressure and (f) boundary layer height from trajectory model output (solid blue/green lines) and ERA-Interim pressure levels (dashed red/orange lines) at 12 UTC on 1st July 2014 on the American catchment boundary at 108.24°E, 29.68°N. Panels (a)-(e) are plotted against pressure and (f) is plotted against height in km.

Some tight features in q, PV, u and v are not captured by the data on the trajectory release grid but the discrepancies are not large. The vertical profiles of these variables from trajectory data broadly match the pressure levels data almost perfectly, particularly for T (Figure 5.5(b)). The horizontal profiles of $\tilde{p}_{\text{surf}}$ and z_{BL} also match the ERA-Interim surface data almost perfectly (Figure 5.5(e,f)).

The horizontal profile of vertically-integrated $\mathbf{Q} \cdot \hat{\mathbf{n}}$ for a single trajectory release (Figure 5.6) is generally in good agreement with the vertical integral from ERA-Interim pressure levels data. However, the trajectory data struggles to capture some of the peaks in the profile of vertically-integrated $\mathbf{Q} \cdot \hat{\mathbf{n}}$. This is a direct consequence of the vertical subsampling. When provided on pressure levels, ERA-Interim has varying vertical resolution to have more levels closer to the ground where there is high stratification in the BL.

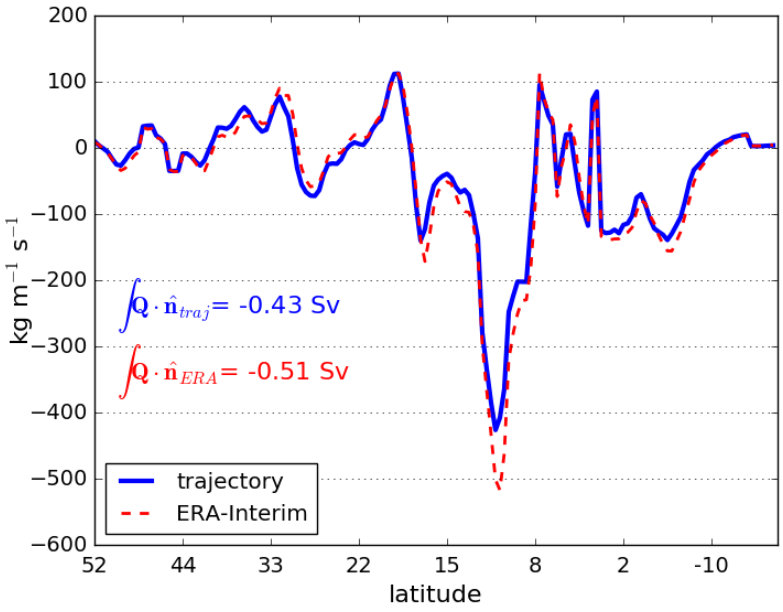

Figure 5.6: Comparison between the horizontal profile of vertically integrated $\mathbf{Q} \cdot \hat{\mathbf{n}}$ trajectory model output (solid blue line) and ERA-Interim pressure levels (dashed red line) at 12 UTC on 1st July 2014 on the American catchment boundary. The horizontal and vertical integrals of $\mathbf{Q} \cdot \hat{\mathbf{n}}$ for trajectory and ERA-Interim data are also shown.

The largest discrepancies between the trajectory and ERA-Interim pressure levels data occur in low-lying regions, particularly above Lake Nicaragua at 10°N (Figure 5.6). Above such locations the trajectory release spacing results in a coarse spacing in pressure and therefore a greater d$\tilde{p}$ than provided from the pressure level data. This results in zonal and meridional moisture fluxes which are far too strong at lower levels and also ignores the near-surface moisture flux between the surface and lowest η level. The vertical integrals of qu and qv are stronger by about 50 kg m^{-1} s^{-1} from pressure levels data when the whole column is included, but re-

moving the bottom 50 hPa causes the vertical integrals to be about 30 kg m^{-1} s^{-1} weaker than those from the trajectory data, a discrepancy which is easily explained by the erroneously strong flux around 900-750 hPa.

These discrepancies betwen trajectory model output and ERA-Interim pressure levels data result in a net $\mathbf{Q} \cdot \hat{\mathbf{n}}$ across the catchment boundary which is 0.08 Sv weaker when calculated from trajectory model output. The profile does still capture all the features despite underestimating the peaks in $\mathbf{Q} \cdot \hat{\mathbf{n}}$ (at its worst the trajectory data underestimates $\mathbf{Q} \cdot \hat{\mathbf{n}}$ by 17%). Net $\mathbf{Q} \cdot \hat{\mathbf{n}}$ is also underestimated by only 15%. These errors are low enough to proceed with the model set-up described in section 5.4.

5.5 Density of trajectory origins

To understand the trajectory origins the number density, ρ, can be calculated using a smooth kernel function of radius $R = 200$ km:

$$K_i(\mathbf{x}) = N\left(1 - \frac{r^2}{R^2}\right), \tag{5.7}$$

for $r < R$ or $r = 0$, where r (the great circle distance between trajectory origin location $\mathbf{x}_i$ and a neighouring location $\mathbf{x}$) is defined as,

$$r = a\phi \tag{5.8}$$

and

$$\cos(\phi) = \frac{\mathbf{x} \cdot \mathbf{x}_i}{a^2}, \tag{5.9}$$

where a is Earth's radius, ϕ is latitude and N is a constant such that

$$\iint K_i(\mathbf{x}) \ \cos\phi \ \mathrm{d}\phi \ \mathrm{d}\lambda = 1 \tag{5.10}$$

where λ is longitude. The number density distribution for n trajectories is defined as

$$\rho(\mathbf{x}) = \frac{1}{n}\sum_{i=1}^{n} K_i(\mathbf{x}) \tag{5.11}$$

after Silverman (1986) and Hodges (1996). This method is superior to simply plotting a 2D histogram which counts the number of origins in a latitude-longitude grid box as it is not sensitive to the map projection and produces a smoother field (Methven *et al.*, 2001).

The annual mean density maps for trajectories released from each catchment boundary is shown in Figure 5.7. The highest origin densities are found along or in the vicinity of all catchment boundaries. This is most notable along the South-East Asian catchment boundary where many trajectories with CAT I origin are in the boundary layer close to the catchment boundary. In this region the catchment boundary is mostly very near to the coast and also crosses open sea (Figure 2.11) which permits CAT I origins at the time of trajectory release (Figure 5.8). This is also a clear feature of the CAT I density fields for each sector of the Southern Ocean catchment boundary. CAT II origins are less numerous along these boundaries (Figure 5.9), partly because CAT I origins are given priority (section 5.2.4), but also because CAT II origin requires three successive increases in θ_e so it is not possible for CAT II origin to occur within the first two timesteps of a trajectory. On the continents the CAT II origin density is somewhat higher near the catchment boundaries (Figure 5.9). This is because CAT I origins cannot occur over land (section 5.2.1) and also transport across the oceans is likely to be somewhat faster due to higher wind speeds.

There are also clear coastal maxima in the overall and CAT I origin density fields (Figures 5.7,5.8), *e.g.* along the coasts of South America, west Africa and western Australia. This is a result of greater z_{BL} over land than above the oceans where there is horizontal transport across the coast (Figure 5.1), a phenomenon known as "coastal outflow" (Dacre *et al.*, 2007; Peake *et al.*, 2014). As CAT I origins are restricted to be ocean-only (section 5.2.1) much of the near-coastal origins are likely to be trajectories which are already in the BL above the continents and crossed the coast in the boundary layer, thus being assigned CAT I origin at the coast.

Two regions of high CAT I origin density are found in the North Atlantic and North Pacific for trajectories released from the respective sectors of the Arctic catchment boundary (Figure 5.8(d,f)). The boundary layer is much higher over these two regions than the surrounding ocean due to higher SSTs associated with the Gulf Stream and Kurishio Current, so trajectories exit the BL horizontally from these regions. In the North Atlantic, the region of high CAT I origin density curls around the region east of Newfoundland where the BL is about 1 km lower (due to cold SSTs from the Labrador Current) than over the Gulf Stream extension from Cape Hatteras.

Each trajectory which has CAT I or CAT II origin was also checked for its origin ocean drainage basin (Atlantic, Indian, Pacific, Arctic or Southern). Trajectories with origin on a catchment boundary at trajectory release time were assigned origin in the drainage basin the

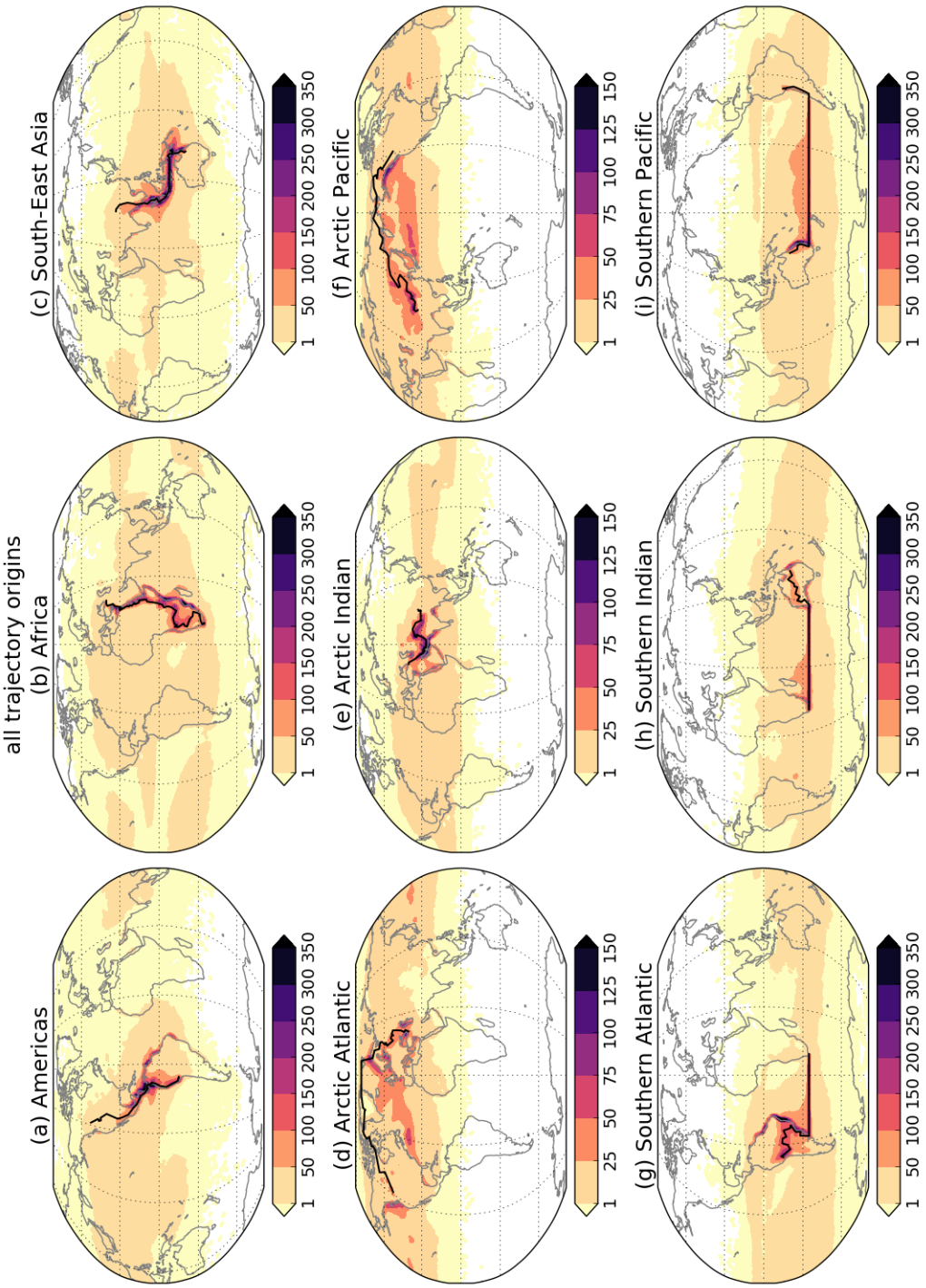

Figure 5.7: Annual mean (2010-2014) density maps of all origins of trajectories released from each catchment boundary (shown in black on each map).

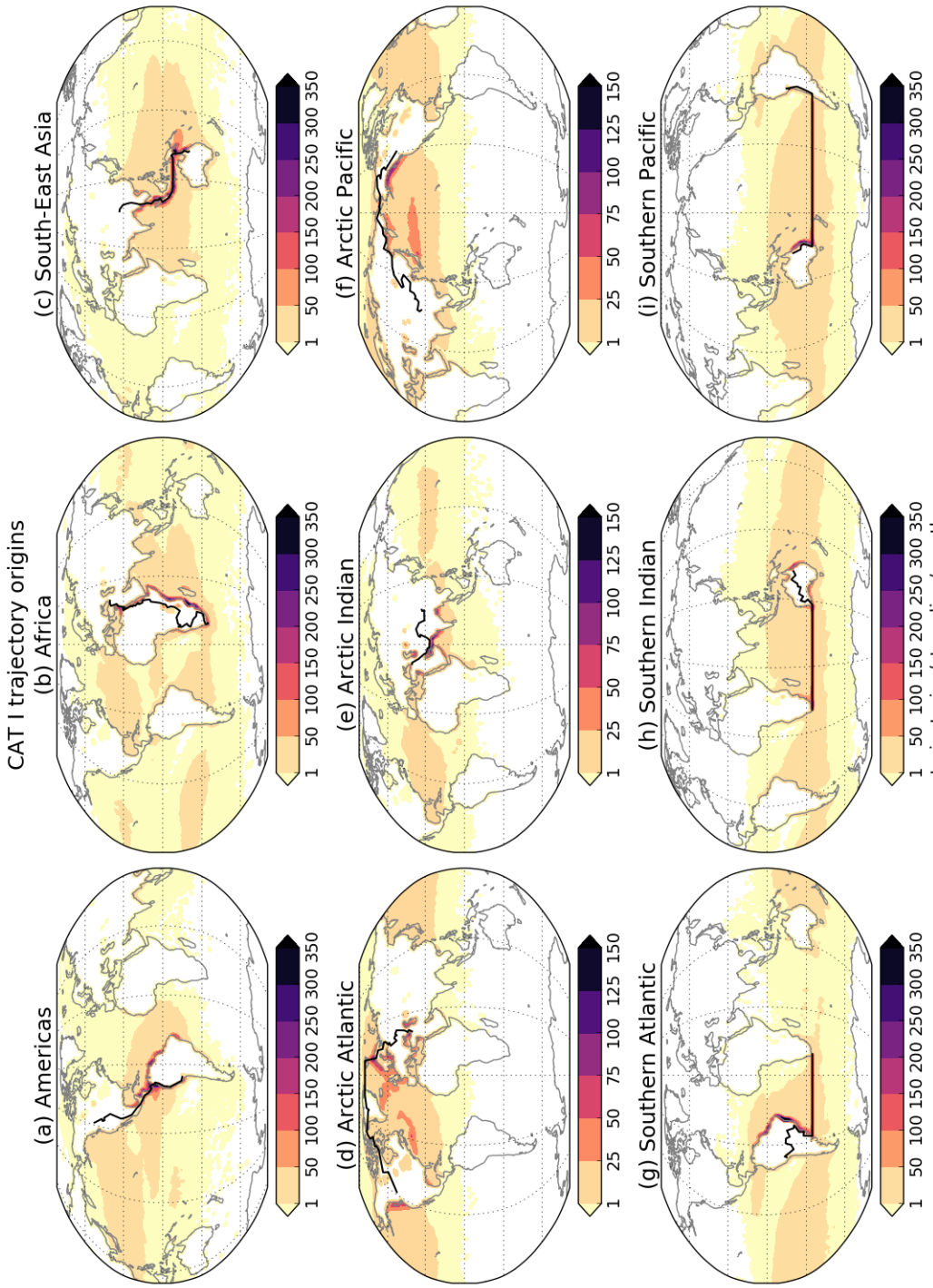

Figure 5.8: Annual mean (2010-2014) density maps of CAT I origins of trajectories released from each catchment boundary (shown in black on each map).

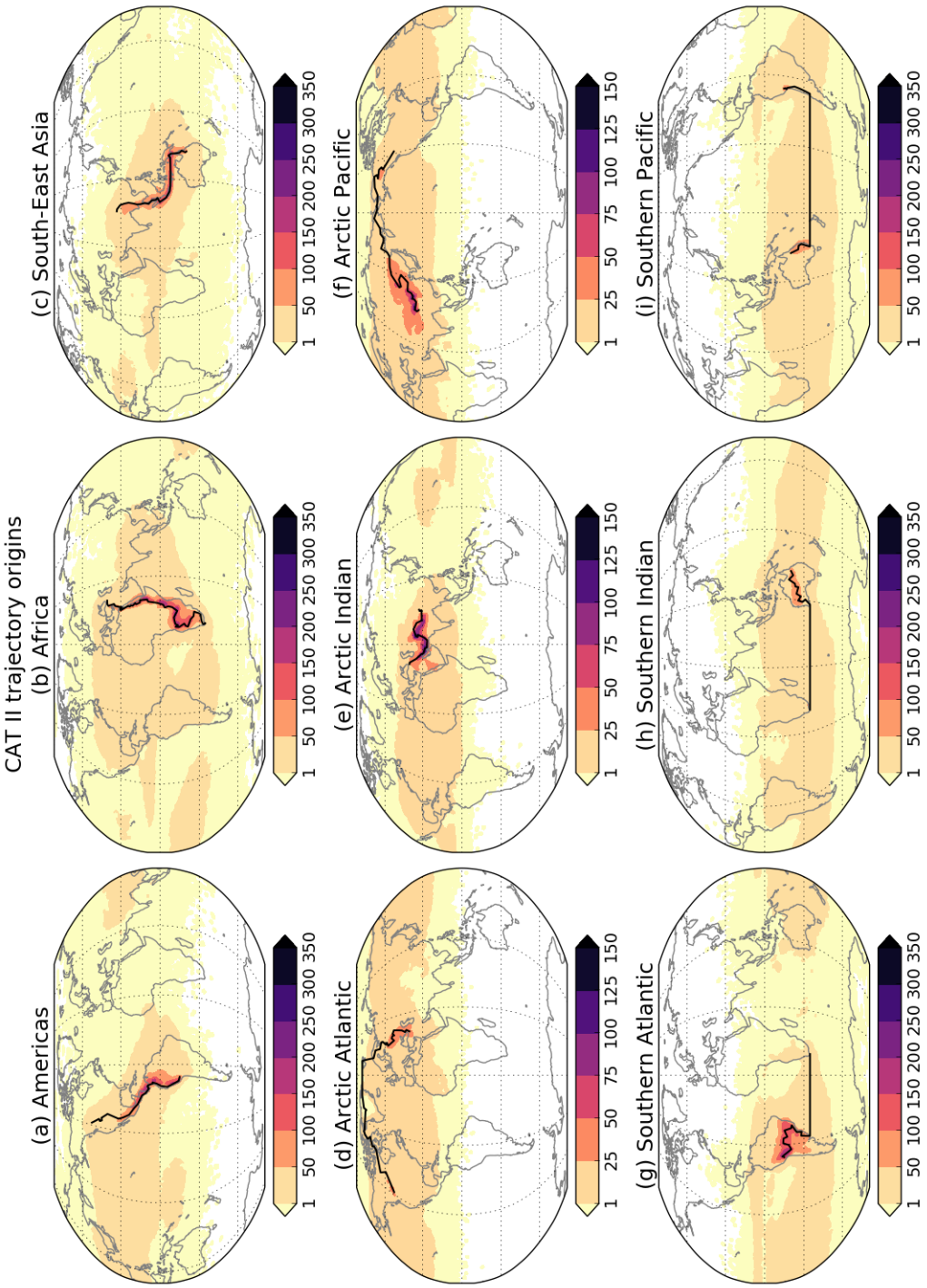

Figure 5.9: Annual mean (2010-2014) density maps of CAT II origins of trajectories released from each catchment boundary (shown in black on each map).

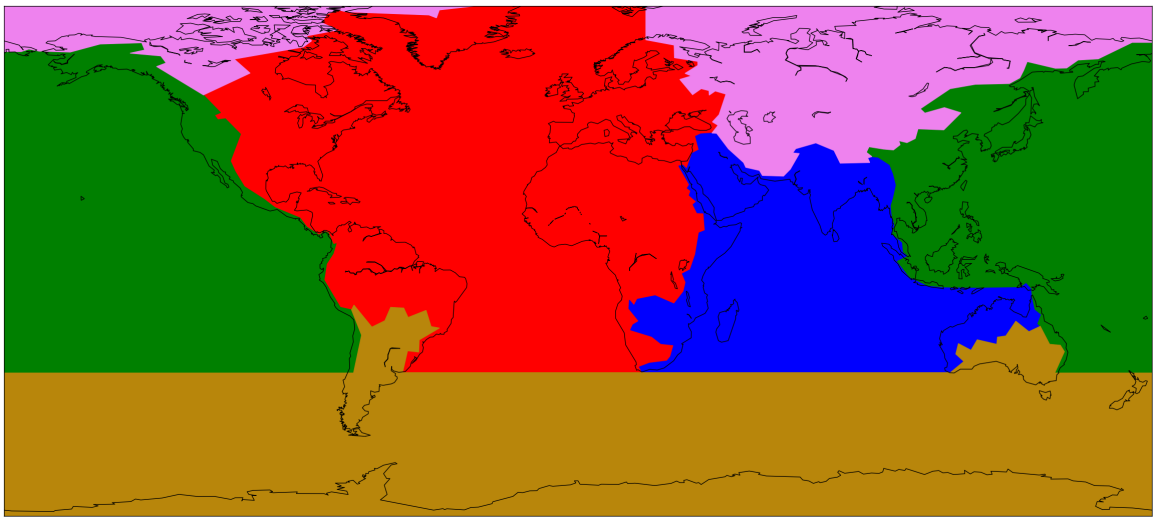

Figure 5.10: The five ocean drainage basins as defined by their catchment boundaries as described in chapter 2: Atlantic (red), Indian (blue), Pacific (green), Arctic (pink) and Southern (gold).

trajectory was in at the first timestep back along the trajectory. The proportions of trajectories with CAT I and CAT II origins released from the three catchment boundaries which take primarily north-to-south paths (Americas, Africa and South-East Asia) are dominated by the neighbouring basins, but the Arctic and Southern catchment boundaries have higher proportions of trajectories with origins in other drainage basins (Figure 5.11). The Arctic catchment boundary has the highest proportions of trajectories with stratospheric origin (almost as high as 25%) due to the high latitude (Russia/North America/Greenland) of the catchment boundary since the tropopause slopes down towards the poles which permits air to cross from the troposphere into the stratosphere.

The South-East Asian catchment boundary has the highest proportion of trajectories assigned to CAT I or CAT II origins which is due to the high tropopause. The large values of trajectories with no origin in 14 days are consistent with trajectory origin evolution plots similar to Figure 5.2(a). It will be shown in the following section that these trajectories do not contribute much to net $\overline{\mathbf{Q}} \cdot \hat{\mathbf{n}}$. Additionally, trajectories longer than 14 days are not required to get a good approximation of $\mathbf{Q} \cdot \hat{\mathbf{n}}$ (Figure 5.2(b)).

5.6 Flux-weighted density

To understand how the trajectory origin density fields relate to $\overline{\mathbf{Q}} \cdot \hat{\mathbf{n}}$ the density fields, $\rho(\mathbf{x})$, are weighted by $(1/g)q\mathbf{v} \cdot \hat{\mathbf{n}}\ \mathrm{d}\tilde{p}\ \mathrm{d}l$ from each trajectory:

$$\overline{\mathbf{Q}} \cdot \hat{\mathbf{n}}(\mathbf{x}) = \frac{1}{g} \sum_{i=1}^{n} (q\mathbf{v} \cdot \hat{\mathbf{n}}\ \mathrm{d}\tilde{p}\ \mathrm{d}l)_i\ K_i(\mathbf{x}) \tag{5.12}$$

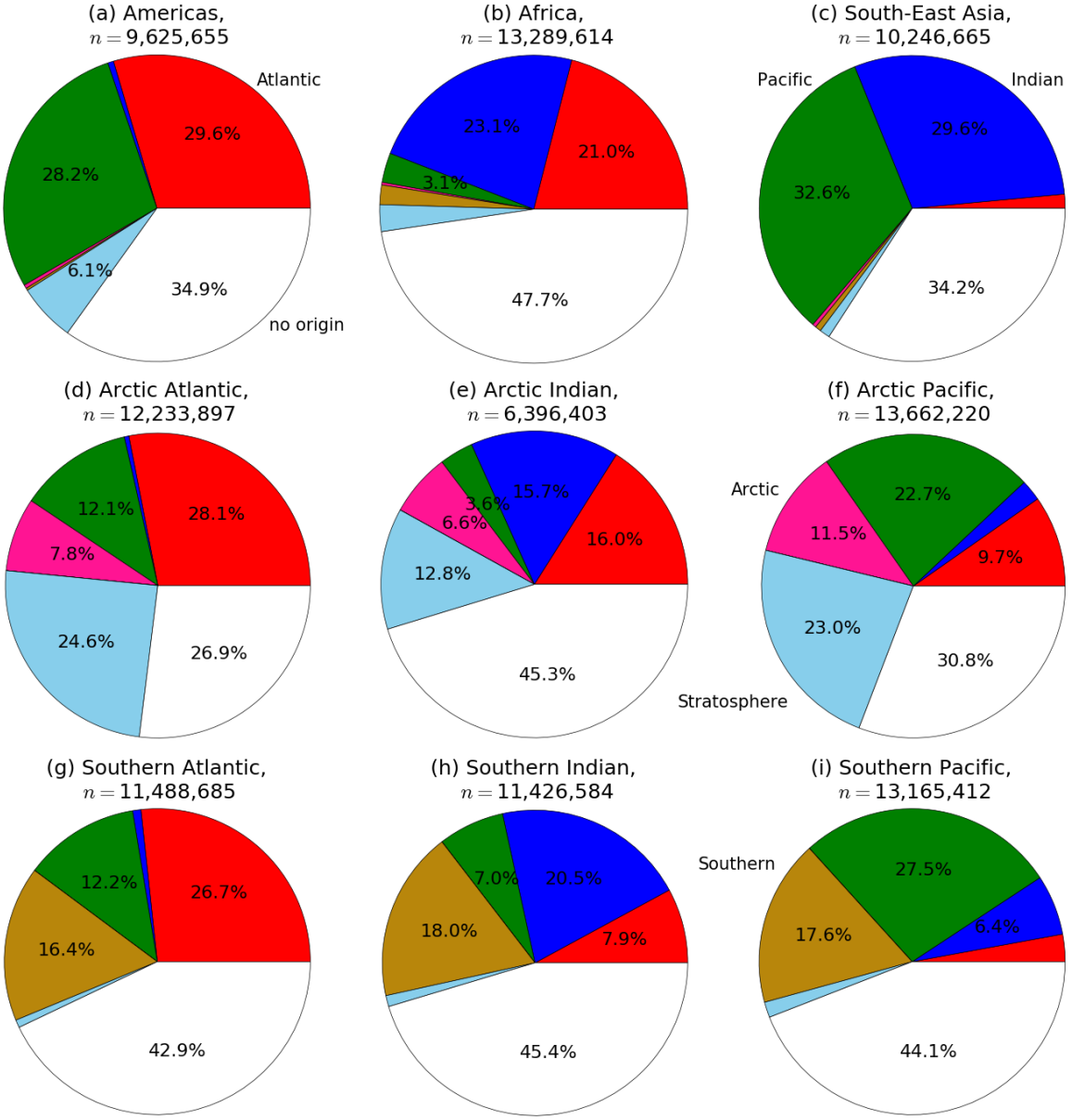

Figure 5.11: Proportions of all trajectories released from each catchment boundary with origin in the Atlantic (red), Indian (dark blue), Pacific (green), Arctic (pink), Southern (gold) drainage basins, stratosphere (light blue) or without origin (white). Only proportions of 3% or greater are labelled. The total number of trajectories (n) released from each catchment boundary over 2010-2014 is shown in each panel.

after Hodges (1996). The flux-weighted density maps for trajectories released from the catchment boundaries surrounding each of the five drainage basins (Figure 5.10) are shown in Figures 5.12-5.16 where blue/negative contours indicate moisture flux leaving the drainage basin (therefore reducing $\overline{P-E}$) and red/positive contours indicate moisture flux which is entering the drainage basin (therefore increasing $\overline{P-E}$). For brevity, only the flux-weighted density maps for all trajectories with origin are shown rather than separate CAT I and CAT II maps.

Flux-weighted densities are generally high along and close to the catchment boundaries,

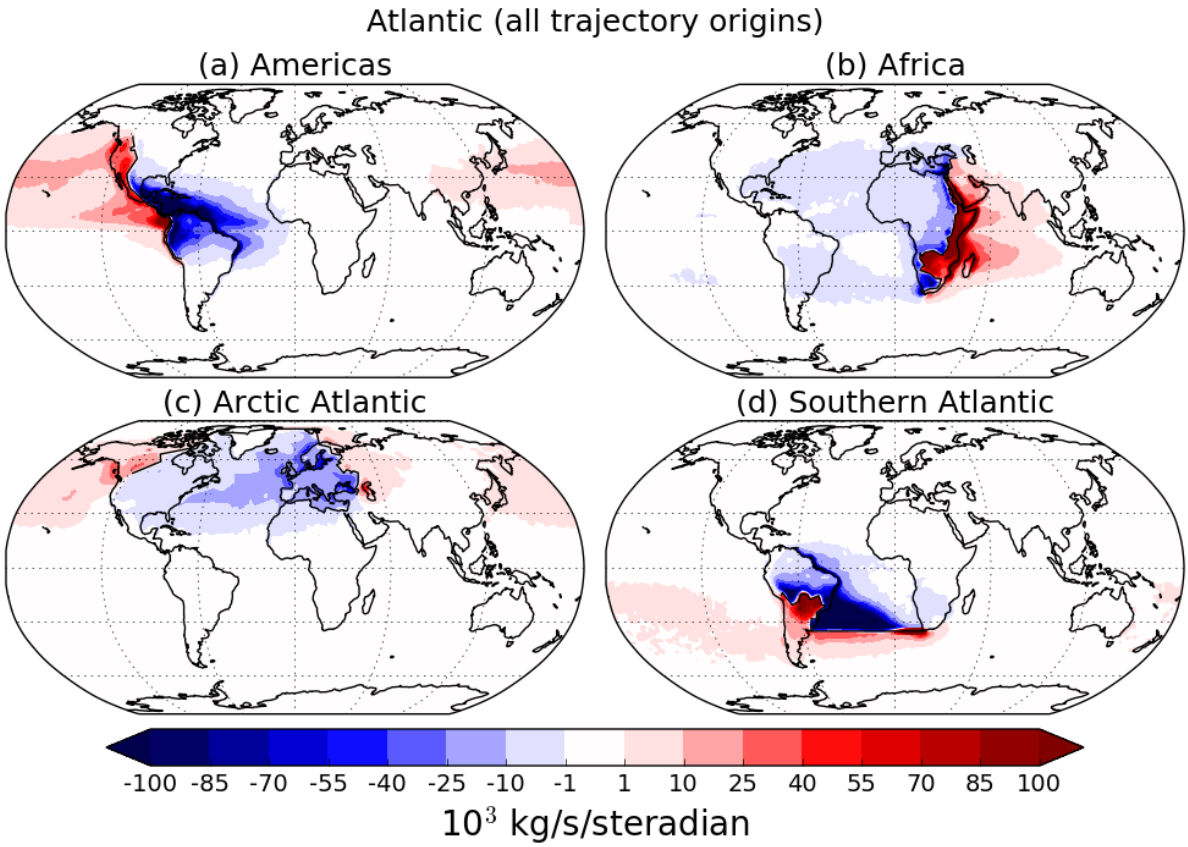

Figure 5.12: Flux-weighted density maps for all trajectories with origin released from catchment boundaries surrounding the Atlantic drainge basin: (a) Americas, (b) Africa, (c) Arctic Atlantic and (d) Southern Atlantic. Red/positive contours indicate moisture flux entering the basin across the catchment boundary and blue/negative contours indicate moisture flux leaving the basin across the catchment boundary.

particularly along the African catchment boundary, as would be expected from the trajectory origin density maps (Figures 5.7). The effect of coastal outflow can also be seen in the flux-weighted density maps, particularly along the South American and Indian coasts. The sub-tropical highs show up as regions with low to zero flux-weighted density where air is moving away from the catchment boundaries *e.g.* North Pacific for American catchment boundary, and South Atlantic for African catchment boundary. The northern hemisphere storm tracks are also clearly identifiable as narrow bands of 10-25 kg s^{-1} steradian^{-1} density across the North Atlantic and Pacific Oceans. Remote moisture origins appear to be very scarce with only small regions of low flux-weighted density notable in Figures 5.12-5.16 *e.g.* in the North Atlantic for eastward $\overline{\mathbf{Q}} \cdot \hat{\mathbf{n}}$ across South-East Asia, and in the South Pacific for eastward $\overline{\mathbf{Q}} \cdot \hat{\mathbf{n}}$ across Africa.

Some key features of the flux-weighted density fields specific to each basin are:

1. **Atlantic Ocean** (Figure 5.12): The North Pacific storm track imports moisture across North America and the North Atlantic storm track exports moisture across Europe. High

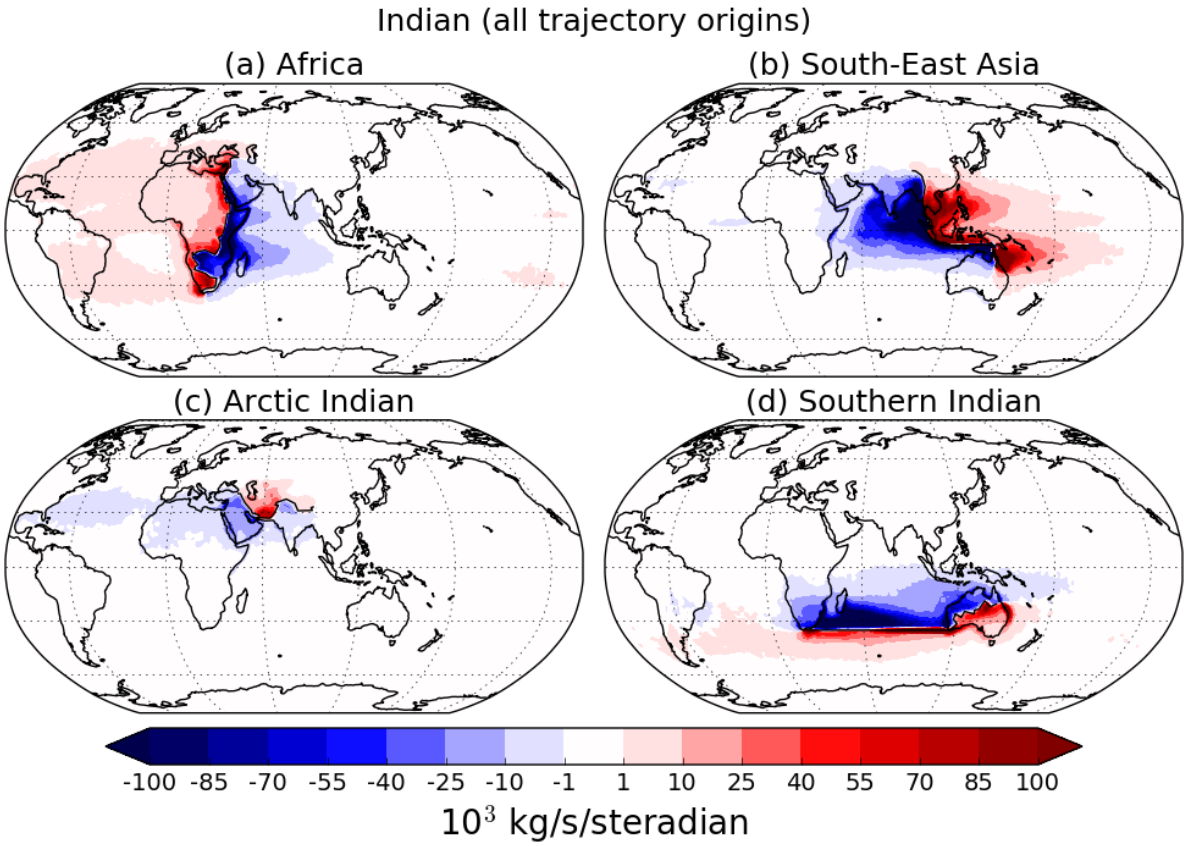

Figure 5.13: Flux-weighted density maps for all trajectories with origin released from catchment boundaries surrounding the Indian drainge basin: (a) Africa, (b) South-East Asia, (c) Arctic Indian and (d) Southern Indian. Red/positive contours indicate moisture flux entering the basin across the catchment boundary and blue/negative contours indicate moisture flux leaving the basin across the catchment boundary.

flux-weighted densities are found across the Caribbean Sea and tropical North Atlantic (similar to Duran-Queseda *et al.*, 2010) for westward $\overline{\mathbf{Q}} \cdot \hat{\mathbf{n}}$ across Central America which shows that the moisture transported from the Atlantic to the Pacific does indeed have origin in this region (Broecker, 1991; Leduc *et al.*, 2007). However, this methodology cannot directly link $\overline{\mathbf{Q}} \cdot \hat{\mathbf{n}}$ to Pacific precipitation.

2. **Indian Ocean** (Figure 5.13): For trajectories released from the South-East Asian catchment boundary, there is a narrow band of very low flux-weighted density off the coast of East Africa and the Arabian peninsula highlighting the path of the Somali LLJ. Flux-weighted density for $\overline{\mathbf{Q}} \cdot \hat{\mathbf{n}}$ leaving the Indian Ocean basin is greatest across the Bay of Bengal for trajectories released from the South Easr Asian catchment boundary, and east of Madagascar for trajectories released from the Indian sector of the Southern Ocean catchment boundary.
3. **Pacific Ocean** (Figure 5.14): The North Pacific storm track exports moisture across the northern end of the American catchment boundary and the eastern end of the Arctic

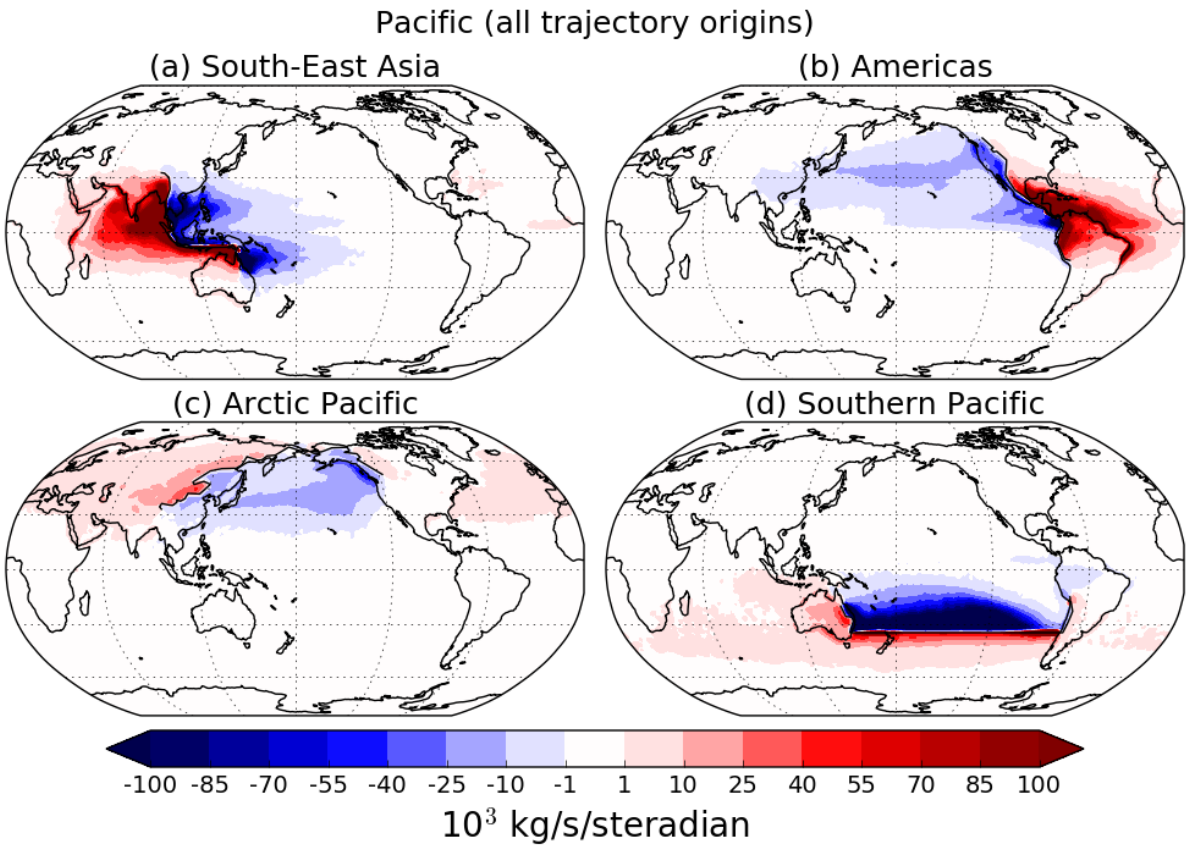

Figure 5.14: Flux-weighted density maps for all trajectories with origin released from catchment boundaries surrounding the Pacific drainge basin: (a) South-East Asia, (b) Americas, (c) Arctic Pacific and (d) Southern Pacific. Red/positive contours indicate moisture flux entering the basin across the catchment boundary and blue/negative contours indicate moisture flux leaving the basin across the catchment boundary.

(Pacific sector) catchment boundary with a weak import of moisture across Asia with origin from the North Atlantic storm track. Most of the South Pacific is occupied by a region of high flux-weighted density for southward $\overline{\mathbf{Q}} \cdot \hat{\mathbf{n}}$ across 35°S.

4. **Arctic Ocean** (Figure 5.15): The North Atlantic and North Pacific storm tracks import moisture to the Arctic, hence the dominance of transient moisture fluxes in the Arctic moisture budget (section 4.2.2). Across the Indian sector of the Arctic catchment boundary, $\overline{\mathbf{Q}} \cdot \hat{\mathbf{n}}$ into the Arctic has low-density origin across the subtropical North Atlantic and North Africa with higher densities around the Arabian peninsula.
5. **Southern Ocean** (Figure 5.16): High flux-weighted densities are found in the poleward part of the southern hemisphere subtropical highs. The contrasting shapes of these regions are a result of the differences in $\overline{q}\,\overline{v}$ between the basins (Figure 4.7(d)). Moisture fluxes leaving the Southern Ocean basin generally have origin within 20° latitude of the catchment boundary with the $\overline{\mathbf{Q}} \cdot \hat{\mathbf{n}}$ extending around the Southern Ocean, sometimes into the neighbouring basins.

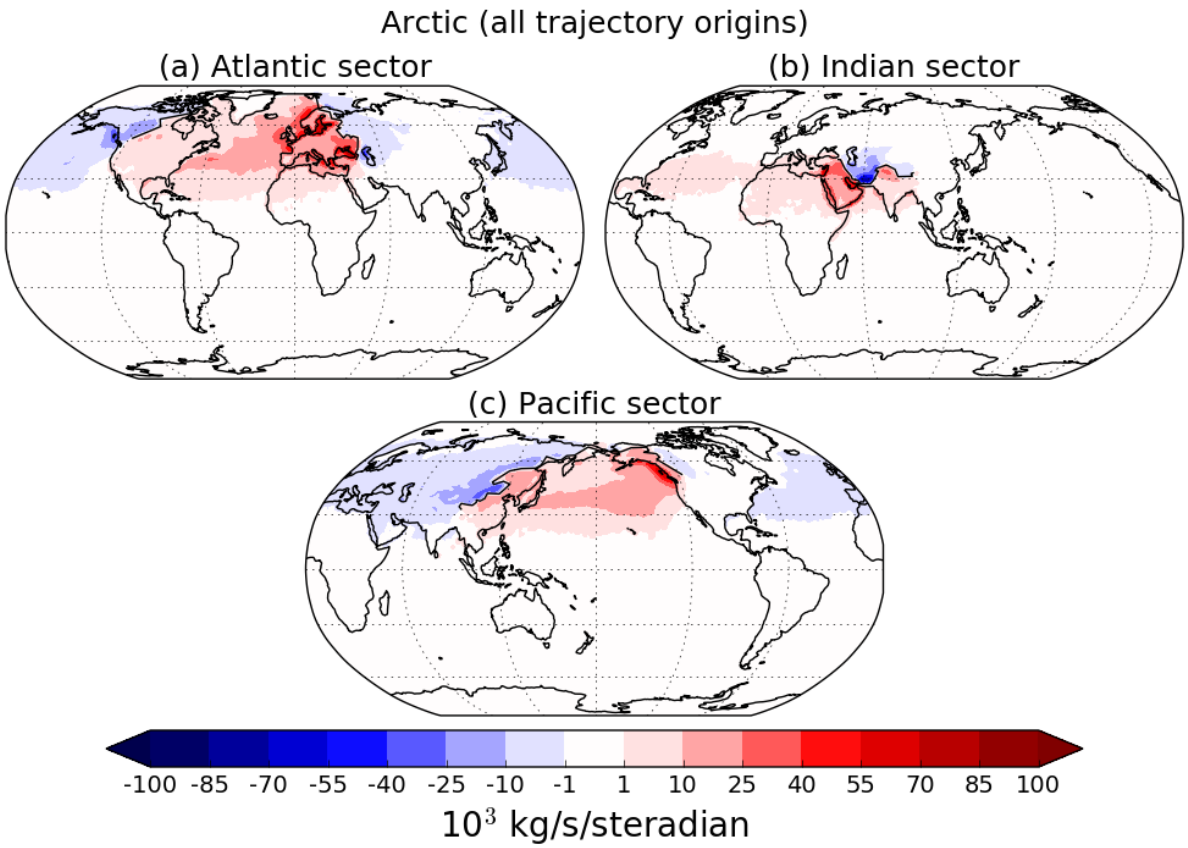

Figure 5.15: Flux-weighted density maps for all trajectories with origin released from catchment boundaries surrounding the Arctic drainge basin: (a) Atlantic sector, (b) Indian sector and (c) Pacific sector. Red/positive contours indicate moisture flux entering the basin across the catchment boundary and blue/negative contours indicate moisture flux leaving the basin across the catchment boundary.

5.7 Partitioning the moisture flux into origin drainage basins

The trajectories can be used to partition the moisture flux normal to the catchment boundaries ($\mathbf{Q}\cdot\hat{\mathbf{n}}$) into contributions from each drainage basin (Figure 5.10), from the stratosphere and flux from trajectories with no origin in 14 days:

$$\mathbf{Q}\cdot\hat{\mathbf{n}} = \mathbf{Q}\cdot\hat{\mathbf{n}}_{Atl} + \mathbf{Q}\cdot\hat{\mathbf{n}}_{Ind} + \mathbf{Q}\cdot\hat{\mathbf{n}}_{Pac} + \mathbf{Q}\cdot\hat{\mathbf{n}}_{Arc} + \mathbf{Q}\cdot\hat{\mathbf{n}}_{Sou} + \mathbf{Q}\cdot\hat{\mathbf{n}}_{Str} + \mathbf{Q}\cdot\hat{\mathbf{n}}_{none}, \quad (5.13)$$

where the subscripts refer to the origin drainage basin, the stratosphere (*Str*) and flux from trajectories with no assigned origin (*none*). The fluxes can be calculated either directly from trajectory model output or by integrating the flux-weighted density fields (Figures 5.12-5.16).

The contribution to $\overline{\mathbf{Q}}\cdot\hat{\mathbf{n}}$ from trajectories with stratospheric origin ($\overline{\mathbf{Q}}\cdot\hat{\mathbf{n}}_{Str}$) is negligible (Figure 5.17), even for the Arctic catchment boundary where the greatest proportions of trajectories with stratospheric origin are found (Figure 5.11). The moisture flux from trajectories with no origin ($\overline{\mathbf{Q}}\cdot\hat{\mathbf{n}}_{none}$) is substantially larger than $\overline{\mathbf{Q}}\cdot\hat{\mathbf{n}}_{Str}$ but still neglible compared to $\overline{\mathbf{Q}}\cdot\hat{\mathbf{n}}$. This

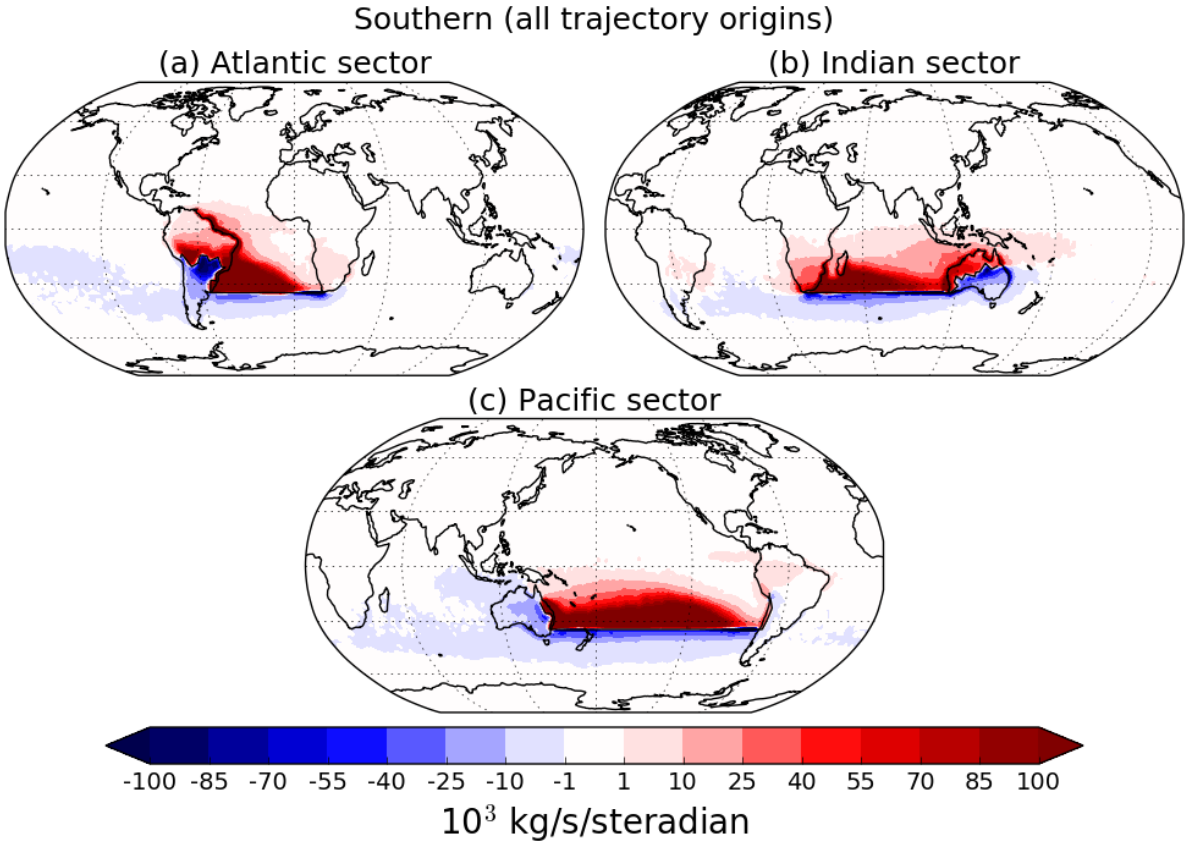

Figure 5.16: Flux-weighted density maps for all trajectories with origin released from catchment boundaries surrounding the Southern Ocean drainge basin: (a) Atlantic sector, (b) Indian sector and (c) Pacific sector. Convention is as per Figure 5.12.

is particularly true for the Atlantic sector of the Southern Ocean catchment boundary (Figure 5.17(g)) despite the high proportion of trajectories with no origin (42.9%, Figure 5.11(g)). For the Pacific sector of the Arctic catchment boundary, $\overline{\mathbf{Q}} \cdot \hat{\mathbf{n}}_{none}$ is stronger (and of opposite sign to) $\overline{\mathbf{Q}} \cdot \hat{\mathbf{n}}$ (Figure 5.17(f)). Trajectories with no origin are also more numerous than trajectories with origin in the stratosphere or any ocean drainage basin (Figure 5.11(f)). However, $\overline{\mathbf{Q}} \cdot \hat{\mathbf{n}}_{none}$ is weaker than $\overline{\mathbf{Q}} \cdot \hat{\mathbf{n}}_{Arc}$ and is only stronger than $\overline{\mathbf{Q}} \cdot \hat{\mathbf{n}}$ because moisture fluxes crossing the catchment boundary in opposing directions have the net effect of cancelling each other out.

Total $\overline{\mathbf{Q}} \cdot \hat{\mathbf{n}}$ for the American, African and South-East Asian catchment boundaries is dominanted by moisture flux with origin in two the drainage basins directly adjacent to each catchment boundary. For example, American $\overline{\mathbf{Q}} \cdot \hat{\mathbf{n}}$ is dominated by a westward $\overline{\mathbf{Q}} \cdot \hat{\mathbf{n}}_{Atl}$ about three times stronger than the eastward $\overline{\mathbf{Q}} \cdot \hat{\mathbf{n}}_{Pac}$. The dominance of westward transport across Africa ($\overline{\mathbf{Q}} \cdot \hat{\mathbf{n}}_{Ind}$) weaker, with eastward $\overline{\mathbf{Q}} \cdot \hat{\mathbf{n}}_{Atl}$ about half the strength of $\overline{\mathbf{Q}} \cdot \hat{\mathbf{n}}_{Ind}$. The partitioning for South-East Asia reveals opposing results. As is known from chapter 4, total $\overline{\mathbf{Q}} \cdot \hat{\mathbf{n}}$ is eastward and departs from $[\overline{q}\,\overline{u}]$ (Figure 4.12). Total South-East Asian $\overline{\mathbf{Q}} \cdot \hat{\mathbf{n}}$ is dominated by eastward $\overline{\mathbf{Q}} \cdot \hat{\mathbf{n}}_{Ind}$, 3-4 times stronger than the main eastward fluxes across the Americas and Africa. The

westward $\overline{\mathbf{Q}} \cdot \hat{\mathbf{n}}_{Pac}$ is comparable to the main westward fluxes across the Americas and Africa.

Total $\overline{\mathbf{Q}} \cdot \hat{\mathbf{n}}$ for each sector of the Arctic catchment boundary is not split into two dominant partitioned fluxes. Moisture fluxes with origin in three drainage basins make significant contributions to total $\overline{\mathbf{Q}} \cdot \hat{\mathbf{n}}$. Each sector has a southward $\overline{\mathbf{Q}} \cdot \hat{\mathbf{n}}_{Arc}$ which is strongest across the Pacific sector and weakest across the Indian sector, reflecting the relative widths of each sector, mountain ranges and the annual mean flow in these regions (Figure 1.5). The basin to the south of each sector makes a northward contribution to total $\overline{\mathbf{Q}} \cdot \hat{\mathbf{n}}$ which is always the strongest of the partitioned fluxes, as would be expected since the Arctic basin is a net sink of moisture. Significant contributions to total $\overline{\mathbf{Q}} \cdot \hat{\mathbf{n}}$ for each sector are made by $\overline{\mathbf{Q}} \cdot \hat{\mathbf{n}}_{Atl}$: northwards for the Atlantic and Indian sectors, southwards for the Pacific sector. This is reflected in the flux-weighted density maps for the Arctic catchment boundary (Figure 5.15) and the proportions of trajectories with Atlantic origin (Figure 5.11).

Moisture fluxes across each sector of the Southern Ocean catchment boundary are dominated by $\overline{\mathbf{Q}} \cdot \hat{\mathbf{n}}$ from trajectories with origin in the Southern Ocean and the ocean to the north. Contributions from other basins are negligible for the Southern Ocean catchment boundary, but more larger than for the American, African and South-East Asian catchment boundaries. The third largest contribution to total $\overline{\mathbf{Q}} \cdot \hat{\mathbf{n}}$ for each sector comes from the drainage basin to the west of each sector, although the sign of this contribution is negative for the Indian sector and positive for the other two sectors. The proportions of trajectories from the tertiary source basin are not insignificantly small, but the low values of $\overline{\mathbf{Q}} \cdot \hat{\mathbf{n}}$ for the tertiary sources implies these trajectories have very low q upon arrival at the catchment boundary.

5.8 Understanding the atmospheric moisture budgets from trajectory data

5.8.1 Recalculating the atmospheric moisture budgets from trajectory data

The partitioned moisture fluxes ($\overline{\mathbf{Q}} \cdot \hat{\mathbf{n}}_i$) can also be used to understand $\overline{P - E}$ (equation (4.2)) for each ocean drainage basin (Figure 5.18). Compared to the actual ERA-Interim estimates of $\overline{\mathbf{Q}} \cdot \hat{\mathbf{n}}$ and $\overline{P - E}$ for 2010-2014 (Figure 5.4), the estimates from trajectory model output agree reasonably well. The net direction of $\overline{\mathbf{Q}} \cdot \hat{\mathbf{n}}$ and the sign of $\overline{P - E}$ are captured by the trajectories. The Atlantic, Pacific and Arctic moisture budgets from trajectory model output are very close to the values presented in Figure 5.4. The size of the contrast between the Atlantic and Pacific

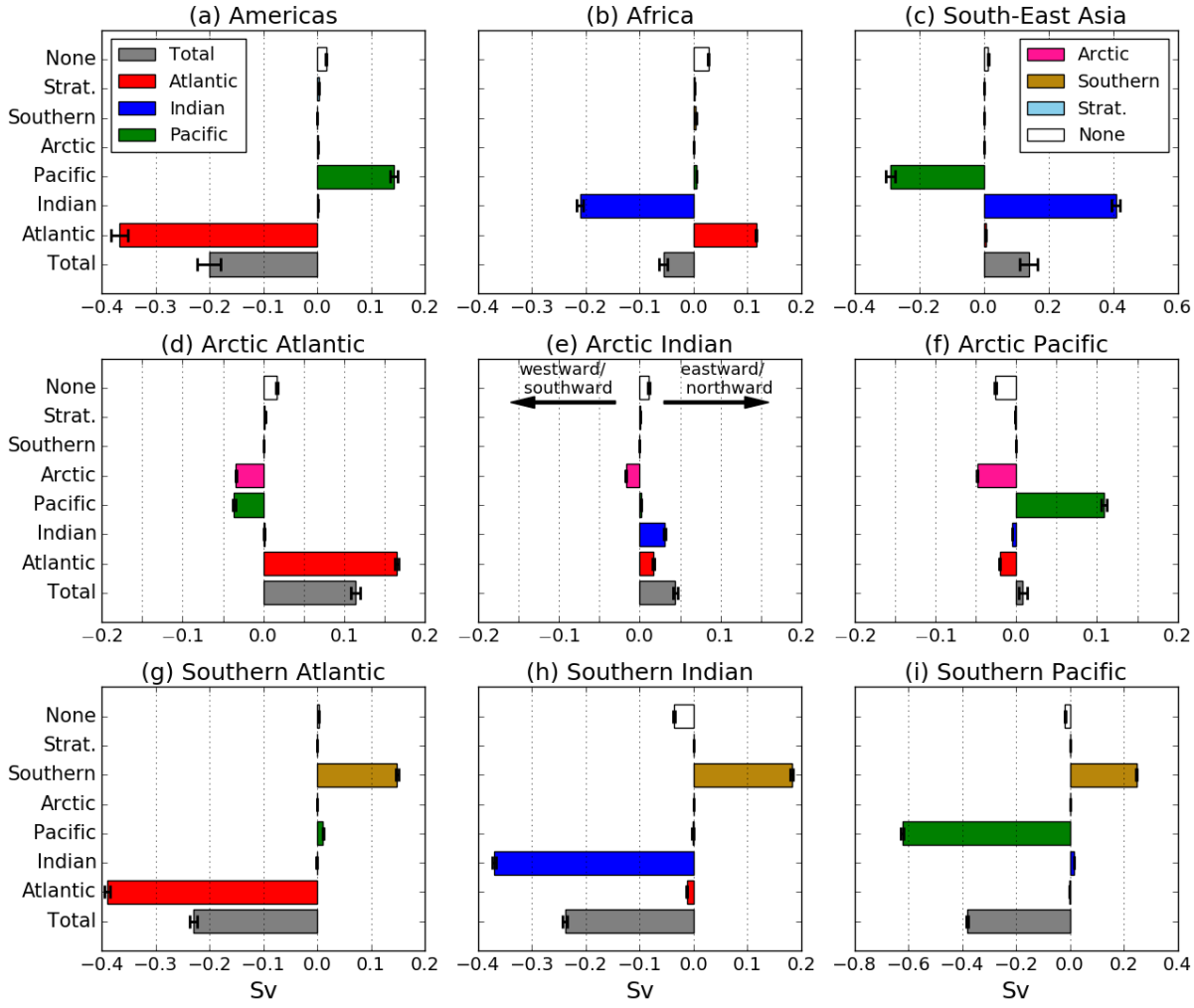

Figure 5.17: Vertically and horizontally integrated $\overline{\mathbf{Q}} \cdot \hat{\mathbf{n}}$ (2010-2014) on each catchment boundary partitioned into origin drainage basins (Atlantic, Indian, Pacific, Arctic, Southern), the stratospheric contribution and trajectories with no assigned origin. The sum of these seven $\overline{\mathbf{Q}} \cdot \hat{\mathbf{n}}$ is equal to the total $\overline{\mathbf{Q}} \cdot \hat{\mathbf{n}}$ (grey bars). All values are in Sverdrups (Sv). The error bars represent standard error of the mean. Positive fluxes represent moisture flux in a net eastward/northward direction and negative fluxes indicate moisture flux in a net westward/southward direction. The colours of the five drainage basins match those from Figure 5.10.

moisture budgets (0.44 Sv) is slightly underestimated compared to Figure 5.4 (0.48 Sv) but agrees with the estimates presented in Figure 3.2.

The trajectory model does, however, underestimate Indian Ocean $\overline{P-E}$ by 0.13 Sv. This appears to be mainly due to underestimation of African $\overline{\mathbf{Q}} \cdot \hat{\mathbf{n}}$. This is likely to be caused by two factors:

1. **Diurnal Aliasing**: trajectories are only released twice daily at 00 and 12 UTC (section 5.4) but maximum z_{BL} occurs in late afternoon/early evening between 15 and 18 UTC over the Sahara (Marsham *et al.*, 2013) and at about 17 UTC over South Africa (Korhonen *et al.*, 2014). Therefore many trajectories which could have been released in the BL at 18 UTC

and would have been assigned an origin soon after were not calculated. The Turkana LLJ is also weakest at 12 UTC and strongest between 00 and 06 UTC (Nicholson, 2016), so some of the maxima in this region may not have been captured.

2. **Vertical Subsamping**: trajectories are released from 17 evenly spaced η levels (0.95 to 0.15, section 5.4). This means that the vertical integrals of qu and qv do not capture the near surface flow and low-level flow given too large $\mathrm{d}\tilde{p}$ weighting (section 5.4.1). This systematically occurs along all catchment boundaries where $\overline{\mathbf{Q}} \cdot \hat{\mathbf{n}}$ peaks in low-lying regions (Figure 5.19). Vertical subsampling may also explain the high proportion of trajectories released from the African catchment boundary which cannot be assigned an origin in 14 days (Figure 5.11).

Southern Ocean $\overline{P-E}$ is also underestimated by the trajectories (Figure 5.18). This occurs all the way round the Southern Ocean catchment boundary as most of the transport is low-level due to the amount of ocean directly beneath the catchment boundary. The largest discrepancy occurs along the Atlantic sector (0.07 Sv) where transport into the River Plate basin is systematically underestimated (Figure 5.19). This may be partially due to diurnal aliasing of the South American LLJ which can peak at 06 UTC (Marengo *et al.*, 2004).

Despite underestimating Indian Ocean $\overline{P-E}$ and African $\overline{\mathbf{Q}} \cdot \hat{\mathbf{n}}$, the trajectories provide a acceptable representation of the moisture budgets with which to understand the asymmetries between the ocean drainage basins.

5.8.2 Total moisture fluxes in and out of the drainage basins

An advantage of using trajectories to study $\overline{\mathbf{Q}} \cdot \hat{\mathbf{n}}$ and $\overline{P-E}$ is that the total moisture fluxes entering (IN) and leaving (OUT) the ocean drainage basins can be calculated from $\overline{\mathbf{Q}} \cdot \hat{\mathbf{n}}_i$ (Figure 5.18). These cannot be calculated when attempting to understand $\overline{P-E}$ from an Eulerian perspective (chapter 4).

The Atlantic, Pacific and Indian basins all have similar OUT values exceeding 1 Sv (Figure 5.18) despite their different areas (Table 4.2). Pacific IN is very close to Pacific OUT, resulting in $\overline{P-E} = -0.05$ Sv. Atlantic and Indian IN fluxes are almost equal resulting in almost matching $\overline{P-E}$ values, but it should be noted that Indian OUT is underestimated due to underestimation of $\overline{\mathbf{Q}} \cdot \hat{\mathbf{n}}_{Ind}$ on the African catchment boundary (see section 5.8.1).

Comparing the IN and OUT fluxes as integrated values between the drainage basins gives

somewhat limited results as the drainage basins have very different sizes. It is therefore more informative to compare the IN and OUT fluxes as length-averages along the perimeter of the drainage basins (Table 5.1).

The OUT fluxes per unit length have similar values (Table 5.1) with the Indian slighly stronger than the other two and the Pacific the weakest. The Atlantic and Indian have similar IN fluxes per unit length but the Pacific's IN flux per unit length is about 75% and 65% stronger than the Atlantic and Indian IN fluxes respectively. Atmospheric moisture transport is therefore:

1. more efficient at importing moisture into the Pacific drainage basin than the Atlantic and Indian basins,
2. similarly efficient at exporting moisture from each of the drainage basins.

These findings are consistent with the findings in chapter 3 where there is little difference in area-averaged evaporation across the Atlantic and Pacific, but area-averaged precipitation is considerably greater across the Pacific (particularly south of 30°N, Figure 3.5).

Table 5.1: Total moisture fluxes entering (IN) and leaving (OUT) across the Atlantic, Indian and Pacific catchment boundaries and $\overline{P-E}$ for each drainage basin, all calculated as average fluxes per unit length (Sv m^{-1}). The lengths of the catchment boundaries in km are shown in the second row.

	Atlantic	Indian	Pacific
length (km)	51942.7	46068.4	54304.6
IN	1.10×10^{-8}	1.25×10^{-8}	2.06×10^{-8}
OUT	2.04×10^{-8}	2.29×10^{-8}	2.15×10^{-8}
$\overline{P-E}$	-9.42×10^{-9}	-1.04×10^{-8}	-9.21×10^{-10}

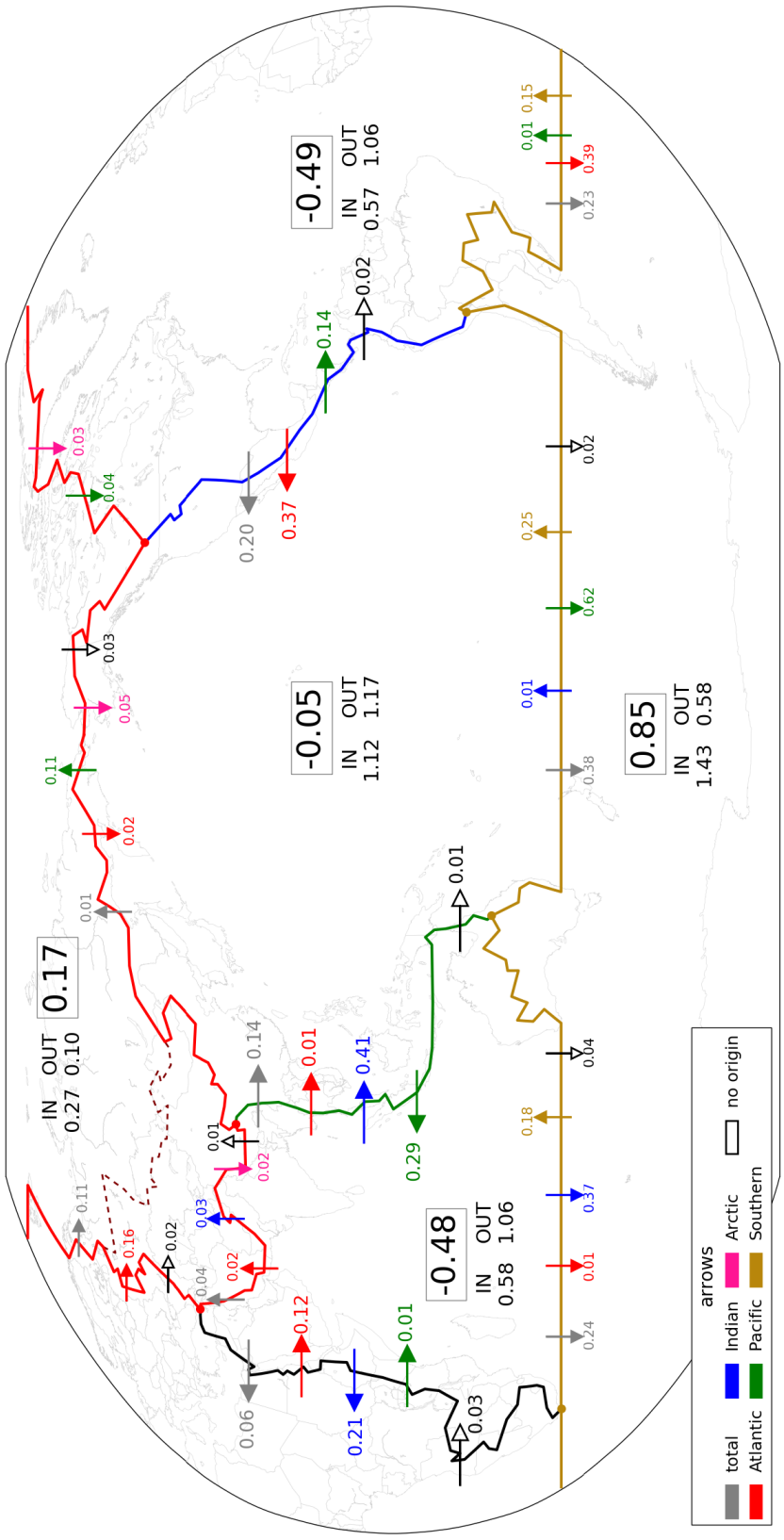

Figure 5.18: Map of vertically and horizontally integrated total $\overline{\mathbf{Q}} \cdot \hat{\mathbf{n}}$ (2010-2014) and $\overline{\mathbf{Q}} \cdot \hat{\mathbf{n}}$ partitioned into origin drainage basins (Atlantic, Indian, Pacific, Arctic, Southern) and $\overline{\mathbf{Q}} \cdot \hat{\mathbf{n}}$ from trajectories with no origin in 14 days. The colours of the catchment boundaries and moisture flux arrows are unrelated. The catchment boundary colours match those from Figure 2.11 and the colours of the arrows match the colours of the drainage basins in Figure 5.10. Only values (in Sv) which are non-zero when rounded to two significant figures are shown so there are discrepancies between the values of $P - E$ (boxes) and the sum of the surrounding $\overline{\mathbf{Q}} \cdot \hat{\mathbf{n}}$ (arrows). The stratospheric contribution to $\overline{\mathbf{Q}} \cdot \hat{\mathbf{n}}$ is non-zero for each catchment boundary but too small to be shown here (see Figure 5.17). Also shown are the net moisture fluxes entering (IN) and leaving (OUT) each drainage basin, calculated as the sum of the partitioned fluxes pointing inward and outward respectively. The size of the arrows does not represent the strength of $\overline{\mathbf{Q}} \cdot \hat{\mathbf{n}}$, only the direction, and the location of each arrow does not represent the precise location for $\overline{\mathbf{Q}} \cdot \hat{\mathbf{n}}_i$. Each arrow represents a $\overline{\mathbf{Q}} \cdot \hat{\mathbf{n}}$ integrated along the entire length of a catchment boundary between the two end points (dots at intersections between catchment boundaries).

The $\overline{P-E}$ values per unit length for each basin (Table 5.1) show that net moisture export across the perimeter of the Pacific catchment boundary is less efficient than for the Atlantic and Indian basins by an order of magnitude. These results are not neccessarily completely consistent with the area-averaged moisture budgets from Table 4.2 where area-averaged net evaporation from the Atlantic Ocean is stronger than from the Indian Ocean. However, the moisture budgets in this chapter are calculated over a shorter time period than in chapter 4. The length-averaged $\overline{P-E}$ for the Pacific is consistent with the area-average from Table 4.2 as both are approximately neutral and weaker than the Atlantic and Indian $\overline{P-E}$.

5.8.3 Partitioned transport across 35°S

In section 4.3.1 net $\overline{\mathbf{Q}} \cdot \hat{\mathbf{n}}$ across 35°S for each sector of the Southern Ocean catchment boundary was calculated as a flux per unit length to find which transports are most/least efficient at exporting moisture to the Southern Ocean drainage basin (Table 4.1). It was shown that net transport across the Atlantic sector is the most efficient and net transport across the Indian sector is the least efficient with contrasting $\overline{q}\,\overline{v}$ patterns (Figure 4.7(d)) causing the asymmetries in length-averaged $\overline{\mathbf{Q}} \cdot \hat{\mathbf{n}}$. Length-averaged net $\overline{\mathbf{Q}} \cdot \hat{\mathbf{n}}$ in Table 5.2 are generally consistent with the results from Table 4.1 with moisture flux across the Atlantic sector about 22% more efficient than moisture flux across the Pacific sector. The use of trajectories can further this analysis as each $\overline{\mathbf{Q}} \cdot \hat{\mathbf{n}}_i$ can also be calculated as a flux per unit length (Table 5.2).

Table 5.2: Net ($\overline{\mathbf{Q}} \cdot \hat{\mathbf{n}}$) and partitioned ($\overline{\mathbf{Q}} \cdot \hat{\mathbf{n}}_i$) moisture fluxes per unit length (top row) in 10^{-8} Sv m^{-1} across 35°S for each sector of the Southern Ocean catchment boundary (first column).

	$\overline{\mathbf{Q}} \cdot \hat{\mathbf{n}}$	$\overline{\mathbf{Q}} \cdot \hat{\mathbf{n}}_{Atl}$	$\overline{\mathbf{Q}} \cdot \hat{\mathbf{n}}_{Ind}$	$\overline{\mathbf{Q}} \cdot \hat{\mathbf{n}}_{Pac}$	$\overline{\mathbf{Q}} \cdot \hat{\mathbf{n}}_{Sou}$
Atlantic sector	-3.51	-4.42	-0.02	-0.07	1.37
Indian sector	-2.03	-0.13	-3.46	0.00	1.74
Pacific sector	-2.88	0.00	-0.03	-4.48	1.78

Partitioning $\overline{\mathbf{Q}} \cdot \hat{\mathbf{n}}$ reveals two key parts of the contrasting length-averaged moisture fluxes. Firstly, southward transport across 35°S is least efficient across the Indian sector ($\overline{\mathbf{Q}} \cdot \hat{\mathbf{n}}_{Ind}$) compared to the Atlantic and Pacific sectors by about 20% when the sum of all southward transports along each sector is considered. The relatively weak southward transport across 35°S from the Indian Ocean basin is a result of the JJA dominance of annual mean $\overline{q\mathbf{v}}$ across the Indian Ocean (Figures 1.5 and 4.9). The Somali LLJ results in anomalous cross-equatorial moisture transport

from the southern hemisphere subtropical high, thus restricting the development of a poleward component of the subtropical high (Figure 4.7) and preventing poleward moisture transport. This causes the $\overline{q\,\mathbf{v}}$ flow to be parallel to 35°S for the Indian sector whereas it is tilted across the Atlantic and Pacific sectors (Figure 1.5).

The second part of the contrast in net length-averaged $\overline{\mathbf{Q}} \cdot \hat{\mathbf{n}}$ comes from the northward moisture flux across 35°S ($\overline{\mathbf{Q}} \cdot \hat{\mathbf{n}}_{Sou}$) which is least efficient across the Atlantic sector. Along 35°S much of the Atlantic basin is occupied by the poleward part of the subtropical high with a much smaller fraction of the basin covered by the equatorward part of the basin comapared to the Pacific and Indian sectors (Figure 4.7). Northward atmospheric moisture flux across the Atlantic sector of 35°S is therefore severely restricted. Profiles of $\overline{\mathbf{Q}} \cdot \hat{\mathbf{n}}_i$ (Figure 5.19) show that $\overline{\mathbf{Q}} \cdot \hat{\mathbf{n}}_{Sou}$ are stronger across the widths of the Indian and Pacific basins than across the Atlantic basin.

5.8.4 Partitioning $P - E$

As well as partioning $\mathbf{Q} \cdot \hat{\mathbf{n}}$ into origin drainage basins, $P - E$ for each drainage basin can be paritioned into contributions from the other basins through an equation analogous to equation (5.13):

$$\begin{aligned} P - E = (P - E)_{Atl} + (P - E)_{Ind} + (P - E)_{Pac} + (P - E)_{Arc} \\ + (P - E)_{Sou} + (P - E)_{Str} + (P - E)_{none}, \end{aligned} \tag{5.14}$$

where each $(\overline{P - E})_i$ is calculated from Equation (4.2) using the associated $\overline{\mathbf{Q}} \cdot \hat{\mathbf{n}}_i$ from Figure 5.18. A basin's contribution to its own $P - E$ is approximately equal to its OUT moisture flux (Figure 5.18) but there can be a small contribution from $(P - E)_{none}$ (Table 5.3).

The key result from partitioning $\overline{P - E}$ (Table 5.3) is that Pacific $\overline{P - E}$ is dominated by $(\overline{P - E})_{Ind}$ which accounts for approximately 38% of the Pacific IN flux (Figure 5.18). Contributions from the Atlantic ($(P - E)_{Atl}$) and Southern ($(\overline{P - E})_{Sou}$) Oceans are significant but secondary to $(\overline{P - E})_{Ind}$. Therefore trajectories with origin in the Indian Ocean drainage basin induce a net precipitation of 0.43 Sv across the Pacific Ocean, similar to Stohl and James (2005). The $\overline{\mathbf{Q}} \cdot \hat{\mathbf{n}}_{Ind}$ crossing South-East Asia between the Indian and Pacific basin (0.41 Sv, Figure 5.18) also accounts for 38% of Indian Ocean OUT flux, whereas eastward $\overline{\mathbf{Q}} \cdot \hat{\mathbf{n}}_i$ from the Atlantic and Pacific only account for $\sim 11\%$ of their respective OUT fluxes. This result highlights how the anomalous eastward moisture fluxes across South-East Asia (chapter 4) affect the at-

Table 5.3: Contributions to total $\overline{P-E}$ for each drainage basin from moisture fluxes from trajectories with origin in each drainage basin and from trajectories with no origin in 14 days. Contributing $\overline{P-E}$ is denoted $(\overline{P-E})_i$ and shown to 2 significant figures in Sverdrups. Moisture fluxes from trajectories with stratospheric origin are too small to contribute a large enough $(\overline{P-E})_i$ worth presenting. Note that each $(\overline{P-E})_i$ is calculated from the corresponding $\overline{\mathbf{q}} \cdot \hat{\mathbf{n}}_i$ on all catchment boundaries surrounding the drainage basin.

		drainage basins				
		Atlantic	Indian	Pacific	Arctic	Southern
$(\overline{P-E})_i$	Atlantic	-1.04	0.08	0.39	0.16	0.4
	Indian	0.21	-1.02	0.43	0.03	0.36
	Pacific	0.18	0.29	-1.16	0.07	0.61
	Arctic	0.03	0.02	0.05	-0.10	0.00
	Southern	0.15	0.19	0.25	0.00	-0.58
	None	-0.03	-0.03	0.00	0.00	0.05

mospheric moisture budgets of the Pacific and Indian Oceans, and is also the leading cause of the Pacific/Atlantic and Pacific/Indian $\overline{P-E}$ asymmetries.

5.9 Major processes influencing moisture transports

In the previous section the $\overline{P-E}$ asymmetry was understood from a Lagrangian perspective using airmass trajectories. In this section the trajectories will be used to elucidate the dominant dynamical processes affecting $\overline{\mathbf{Q}} \cdot \hat{\mathbf{n}}$ and highlight the locations where the strongest $\overline{\mathbf{Q}} \cdot \hat{\mathbf{n}}$ are found with respect to the $\overline{P-E}$ asymmetry. As it was shown in chapter 4 that deviations from $[\overline{qu}]$ on the American, African and South-East Asian catchment boundaries is most important in setting the $\overline{P-E}$ asymmetries this section will focus on $\overline{\mathbf{Q}} \cdot \hat{\mathbf{n}}$ on these catchment boundaries.

5.9.1 Locations of peaks in $\overline{\mathbf{Q}} \cdot \hat{\mathbf{n}}$

In chapter 4 profiles of vertically-integrated $\overline{\mathbf{Q}} \cdot \hat{\mathbf{n}}$ (Figure 4.3) were used to pick out maxima in $\overline{\mathbf{Q}} \cdot \hat{\mathbf{n}}$ and some key dynamical features were inferred from the locations of the $\overline{\mathbf{Q}} \cdot \hat{\mathbf{n}}$ maxima. However, these profiles were calculated using only vertical integrals of $\overline{qu}$ and $\overline{qv}$ so there was no information about the vertical profiles of $\overline{\mathbf{Q}} \cdot \hat{\mathbf{n}}$ along the catchment boundaries. In this chapter trajectories are released on 17 η levels which permits the calculation of cross-sections of $\overline{\mathbf{Q}} \cdot \hat{\mathbf{n}}$ along the catchment boundaries (Figure 5.20).

Some key points are:

- **Atlantic to Pacific transport** across the Americas (Figures 5.19(a) and 5.20(a)). Net $\overline{\mathbf{Q}} \cdot \hat{\mathbf{n}}$

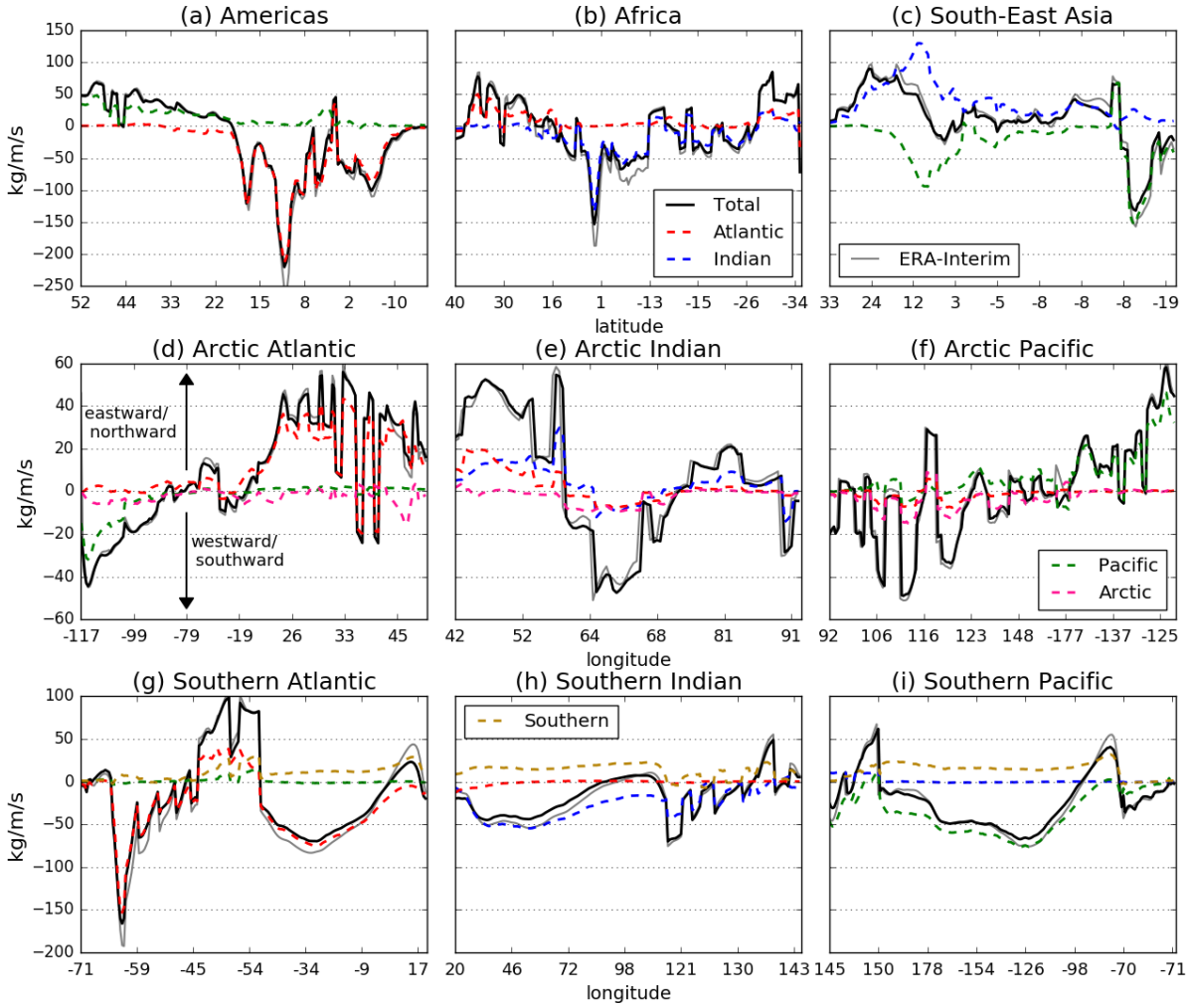

Figure 5.19: Vertically integrated $\overline{\mathbf{Q}} \cdot \hat{\mathbf{n}}$ (2010-2014) profiles along each catchment boundary paritioned into origin drainage basins (Atlantic, Indian, Pacific, Arctic, Southern). Only the significant paritioned fluxes (Figure 5.17) are shown. The sum of the partitioned fluxes is approximately equal to the total moisture flux (solid black line). The thin grey line shows the annual mean ERA-Interim $\overline{\mathbf{Q}} \cdot \hat{\mathbf{n}}$ for the same time period (similar to Figure 4.3). All units are kg m^{-1} s^{-1}. Positive fluxes represent moisture flux in a net eastward/northward direction and negative fluxes indicate moisture flux in a net westward/southward direction. The colours of the five drainage basins match those from Figure 5.10.

is dominated by westward $\overline{\mathbf{Q}} \cdot \hat{\mathbf{n}}_{Atl}$ south of 20°N. The profile of $\overline{\mathbf{Q}} \cdot \hat{\mathbf{n}}_{Atl}$ is characterized by three distinct maxima at 17°N through the Chivela Pass (Tehuantepec jet, Steenburgh *et al.*, 1998), 11°N above Lake Nicaragua (Papagayo jet, Clarke, 1988) and 10°N for the Panama jet (Steenburgh *et al.*, 1998). These maxima occur between 850 hPa and 900 hPa, the approximate pressure levels of these gap winds, similar to cross-sections of velocity and water vapour mixing ratio from Xu *et al.* (2005).

- **Indian to Atlantic transport** across Africa (Figures 5.19(b) and 5.20(b)). Net $\overline{\mathbf{Q}} \cdot \hat{\mathbf{n}}$ is dominated by westward $\overline{\mathbf{Q}} \cdot \hat{\mathbf{n}}_{Ind}$ between 20°N and 26°S. The peak in the $\overline{\mathbf{Q}} \cdot \hat{\mathbf{n}}_{Ind}$ profile occurs at 3°N in the Turkana Channel and at 850-875 hPa, which is the same level as the Turkana

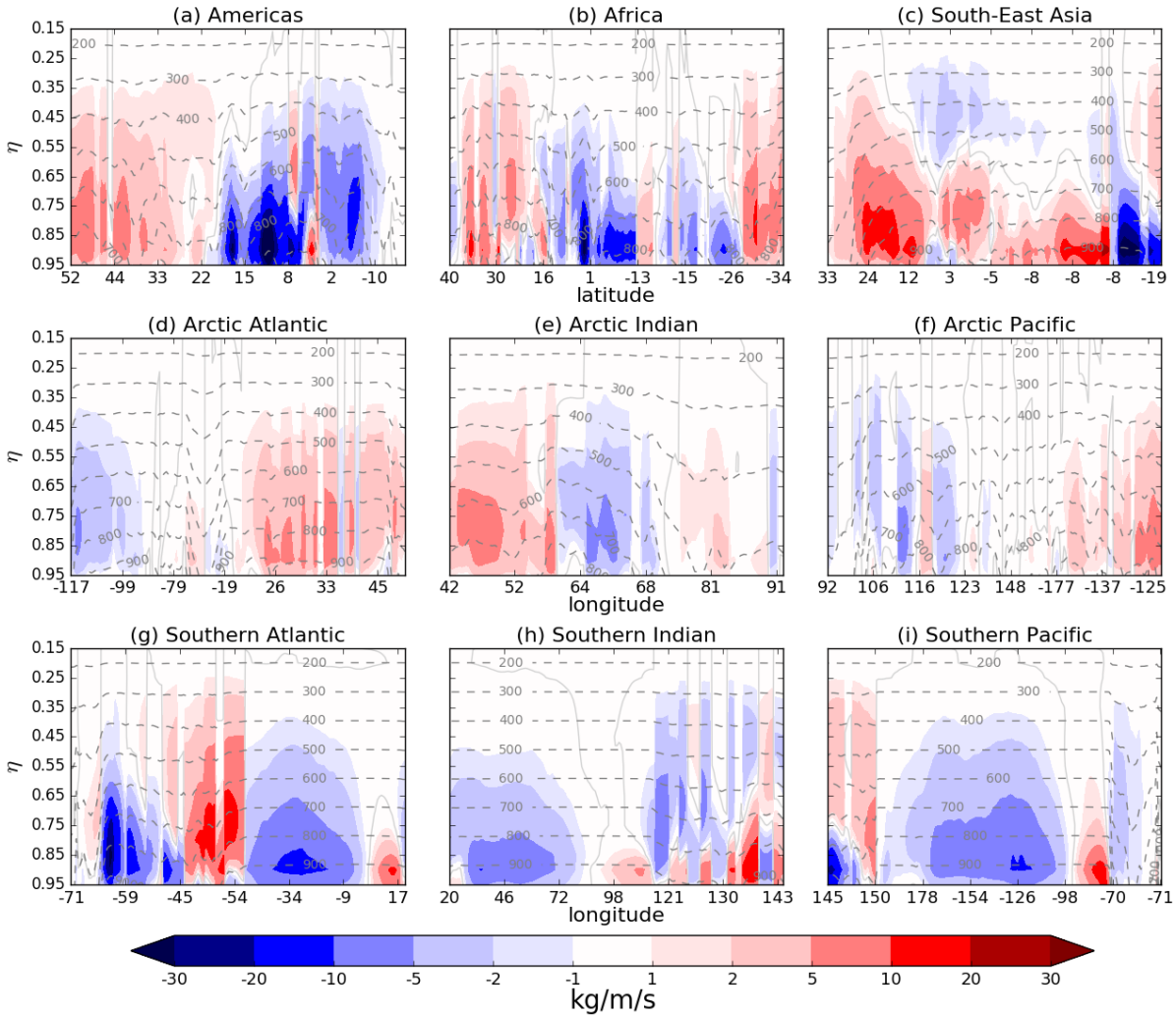

Figure 5.20: Cross-sections of $\overline{\mathbf{Q}} \cdot \hat{\mathbf{n}}$ (not weighted by dl) for each catchment boundary (2010-2014) from trajectory output on model (η) levels. Red/positive contours indicate moisture flux in a net northward/eastward direction and blue/negative contours indicate moisture flux in a net southward/westward direction. Moisture flux units are kg m^{-1} s^{-1}. The solid grey contour shows where the moisture flux is equal to zero and the dashed grey contours show the pressure levels in hPa.

LLJ (Nicholson, 2016). South of the Turkana Channel there is $\overline{\mathbf{Q}} \cdot \hat{\mathbf{n}}_{Ind}$ of approximately -50 kg/m/s at 750 hPa until 13°S (above the African Great Lakes). This is linked to moisture transport from the Indian Ocean to the Ethiopian Highlands (Viste and Sorteberg, 2011).

- **Pacific to Indian transport** across South-East Asia (Figures 5.19(c) and 5.20(c)). The net $\overline{\mathbf{Q}} \cdot \hat{\mathbf{n}}$ profile is dominated by eastward $\overline{\mathbf{Q}} \cdot \hat{\mathbf{n}}_{Ind}$ with westward $\overline{\mathbf{Q}} \cdot \hat{\mathbf{n}}_{Pac}$ only dominating above the Torres Strait. It is the eastward $\overline{\mathbf{Q}} \cdot \hat{\mathbf{n}}_{Ind}$ that causes deviations from $[\overline{qu}]$ that dominate the $\overline{P-E}$ asymmetries.The $\overline{\mathbf{Q}} \cdot \hat{\mathbf{n}}$ cross-section shows westward moisture flux at 600-300 hPa between 3°N and 5°S caused by the upper branch of the Walker Circulation which is westward over the Indian Ocean.

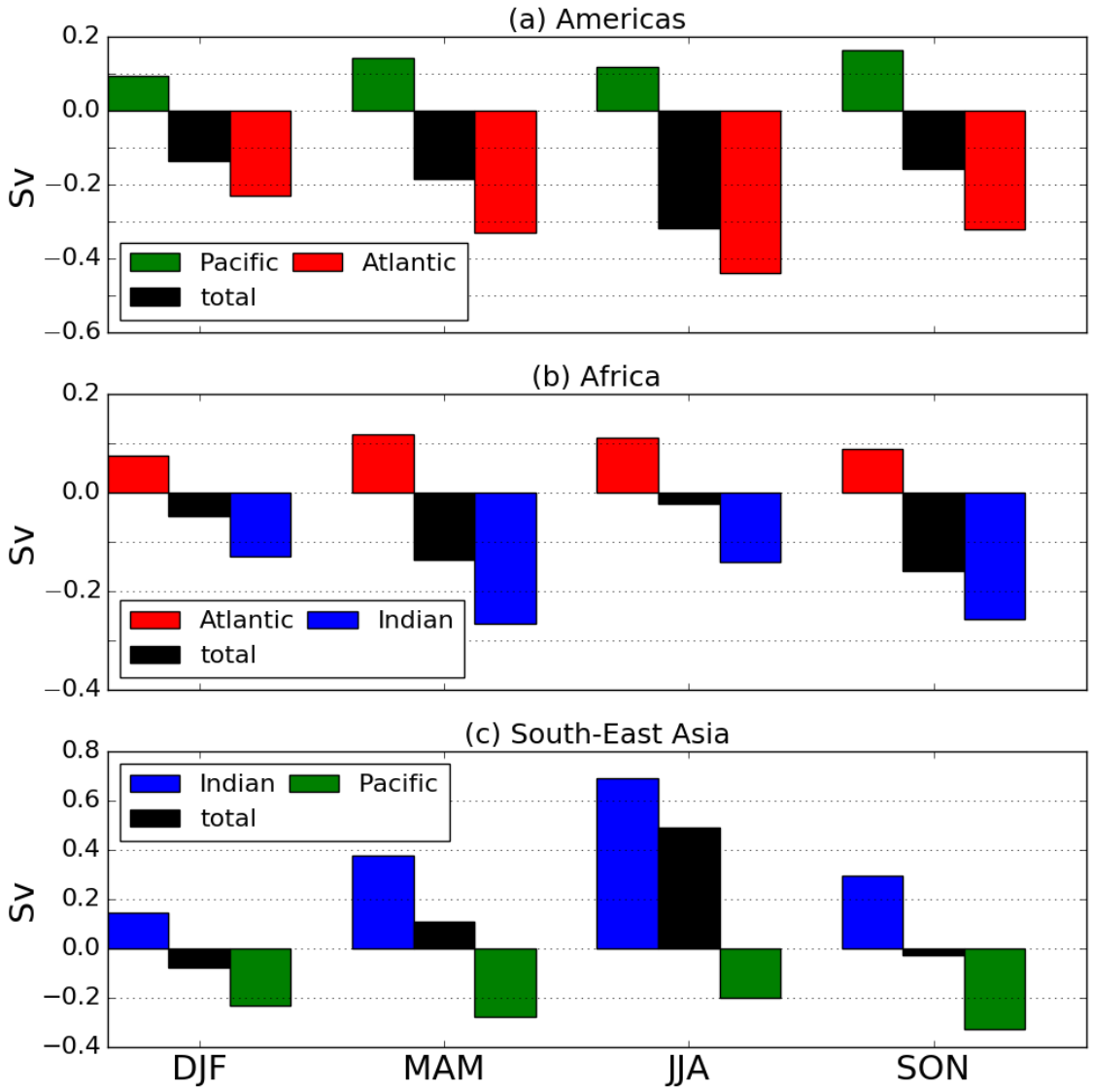

Figure 5.21: Vertically and horizontally integrated 2010-2014 climatological seasonal mean $\overline{\mathbf{Q}} \cdot \hat{\mathbf{n}}$ for the (a) American, (b) African and (c) South-East Asian catchment boundaries. The total $\overline{\mathbf{Q}} \cdot \hat{\mathbf{n}}$ (black) and $\overline{\mathbf{Q}} \cdot \hat{\mathbf{n}}$ from trajectories with origin in the two adjacent basins to each catchment boundary are shown (Atlantic: red, Pacific: green, Indian: blue). These values (in Sv) are calculated from the flux-weighted density fields in Figures 5.25-5.23.

5.9.2 Seasonal Cycles of partitioned $\overline{\mathbf{Q}} \cdot \hat{\mathbf{n}}$

Some of the processes discussed in section 5.9.1 are not persistent year-round features of the atmospheric circulation and moisture transport are very sensitive to the seasonal cycle (section 4.2.3). Figure 5.21 shows the seasonal cycles of net $\overline{\mathbf{Q}} \cdot \hat{\mathbf{n}}$ and the significant $\overline{\mathbf{Q}} \cdot \hat{\mathbf{n}}_i$ for the American, African and South-East Asian catchment boundaries with the seasonal cycle of each net $\overline{\mathbf{Q}} \cdot \hat{\mathbf{n}}$ is approximately consistent with Figure 4.10. The key result from Figure 5.21 is that the seasonal cycle of $\overline{\mathbf{Q}} \cdot \hat{\mathbf{n}}_{Ind}$ dominates the seasonal cycle of net $\overline{\mathbf{Q}} \cdot \hat{\mathbf{n}}$ on the African and South-East Asian catchment boundaries.

The seasonal cycles of moisture origins for the African and South-East Asian catchment boundaries (Figures 5.22 and 5.23) show that the seasonal cycles of each $\overline{\mathbf{Q}} \cdot \hat{\mathbf{n}}_{Ind}$ are closely linked to the dynamics of the Somali LLJ and the Asian Monsoon. The meridional (cross-equatorial) branch of the Somali LLJ forms in April/May (Riddle and Cook, 2008) and transports moisture from the Indian Ocean around Madagascar towards East Africa (Figure 5.22(c)). In June the zonal branch of the Somali LLJ forms and diverts moisture eastward away from the Horn of Africa towards the monsoon rains over India (note the empty region across the Horn of African and adjacent ocean in Figure 5.22(c)). The seasonal reversal of winds and vertically-integrated moisture fluxes (Figure 4.9) result in the origin region of South-East Asian $\overline{\mathbf{Q}} \cdot \hat{\mathbf{n}}_{Ind}$ expanding across the Indian Ocean from DJF to JJA (Figure 5.23) and therefore the change in sign of net South-East Asian $\overline{\mathbf{Q}} \cdot \hat{\mathbf{n}}$ (Figure 5.21).

The seasonal cycle of moisture fluxes leaving the Indian Ocean drainage basin across Africa and South-East Asia is therefore strongly affected by the continental geometry and topo-

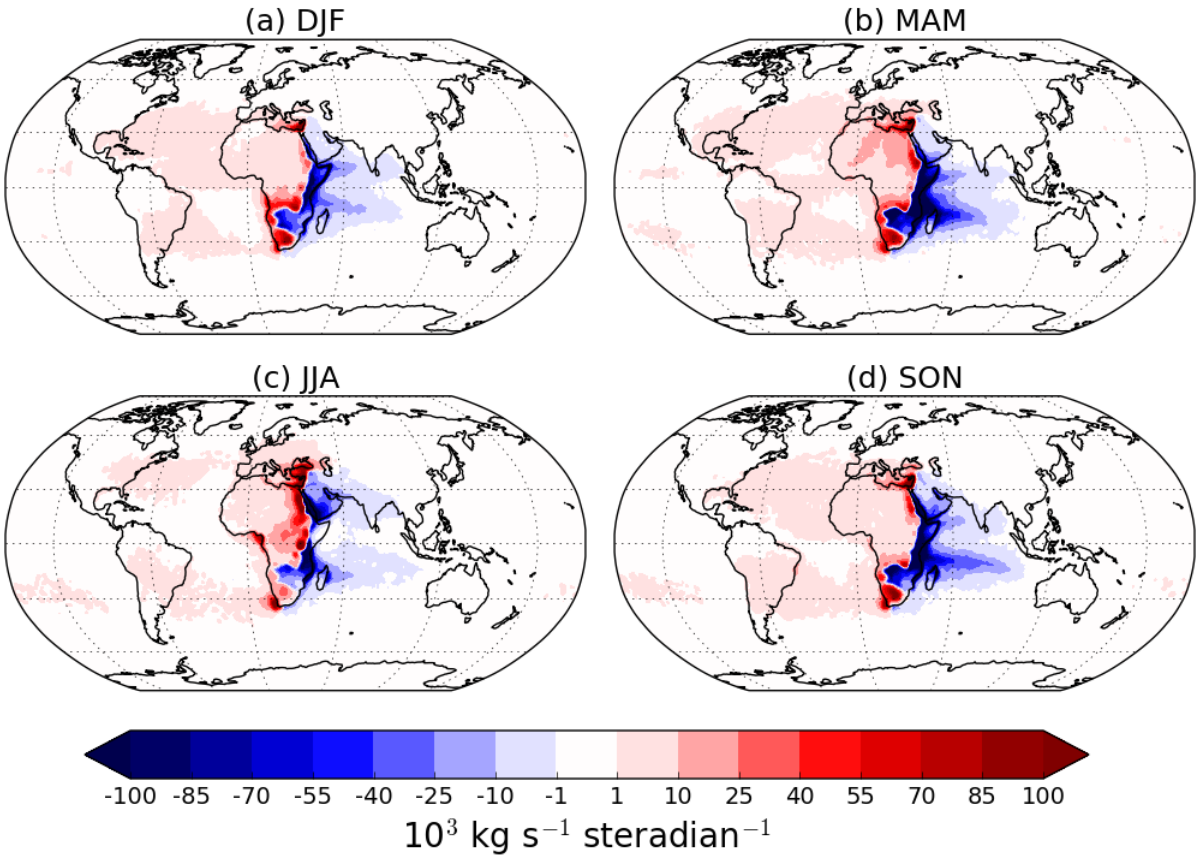

Figure 5.22: Flux-weighted density maps for the 2010-2014 climatological seasonal means of all trajectories with origin released from the African catchment boundary. Red/positive contours indicate moisture flux which crosses the catchment boundary in a northward/eastward direction, and blue/negative contours indicate moisture flux which crosses the catchment boundary in a southward/westward direction.

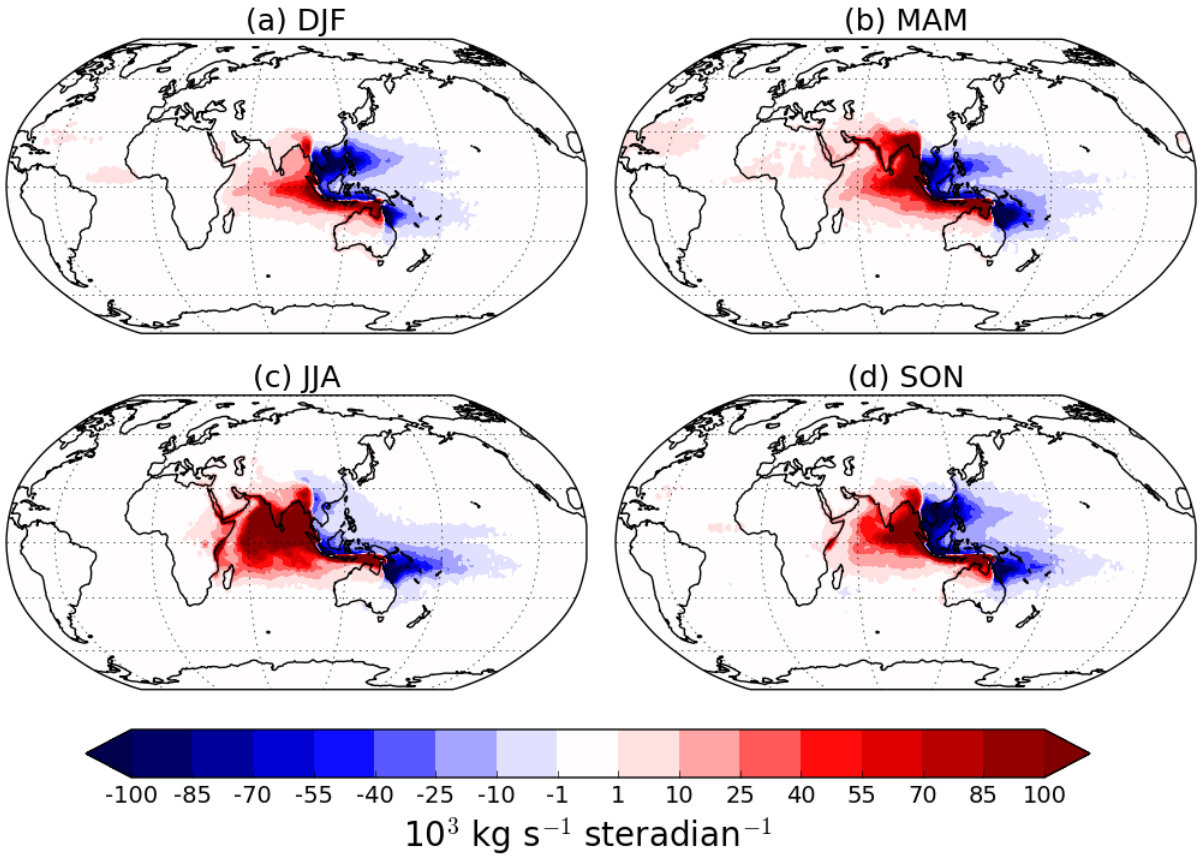

Figure 5.23: Flux-weighted density maps for the 2010-2014 climatological seasonal means of all trajectories with origin released from the South-East Asian catchment boundary. Red/positive contours indicate moisture flux which crosses the catchment boundary in a northward/eastward direction, and blue/negative contours indicate moisture flux which crosses the catchment boundary in a southward/westward direction.

graphic features of the basin. Land-sea temperature contrasts are considered to play a role in the seasonal reversal of surface winds, as is the seasonal migration of the ITCZ (Gadgil, 2003; Bordoni and Schneider, 2008). As the ITCZ moves northward the East African Highlands and land-sea friction contrasts concentrate the Somali LLJ into a narrow longitudinal band (Rodwell and Hoskins, 1995). The difference between the atmospheric dynamics in January and June can be seen from the trajectories in Figure 5.24, with a fully formed Somali LLJ dominating the lower troposphere in June and nonexistant in January. Note that few of the origins for South-East Asian $\overline{\mathbf{Q}} \cdot \hat{\mathbf{n}}_{Ind}$ are located directly below the Somali LLJ but instead along the coast of India or to the south of the subcontinent (Figure 5.24(c)) where the trajectories exit the boundary layer or experience mixing. However, Rodwell and Hoskins (1995) estimated that 60-80% of moisture transported by the Somali LLJ is from the southern hemisphere subtropical high.

The seasonal cycle of American net $\overline{\mathbf{Q}} \cdot \hat{\mathbf{n}}$ is dominated by westward $\overline{\mathbf{Q}} \cdot \hat{\mathbf{n}}_{Atl}$ which peaks in JJA (Figure 5.21(a)). The $\overline{\mathbf{Q}} \cdot \hat{\mathbf{n}}_{Atl}$ origin region extends across the tropical Atlantic onto North

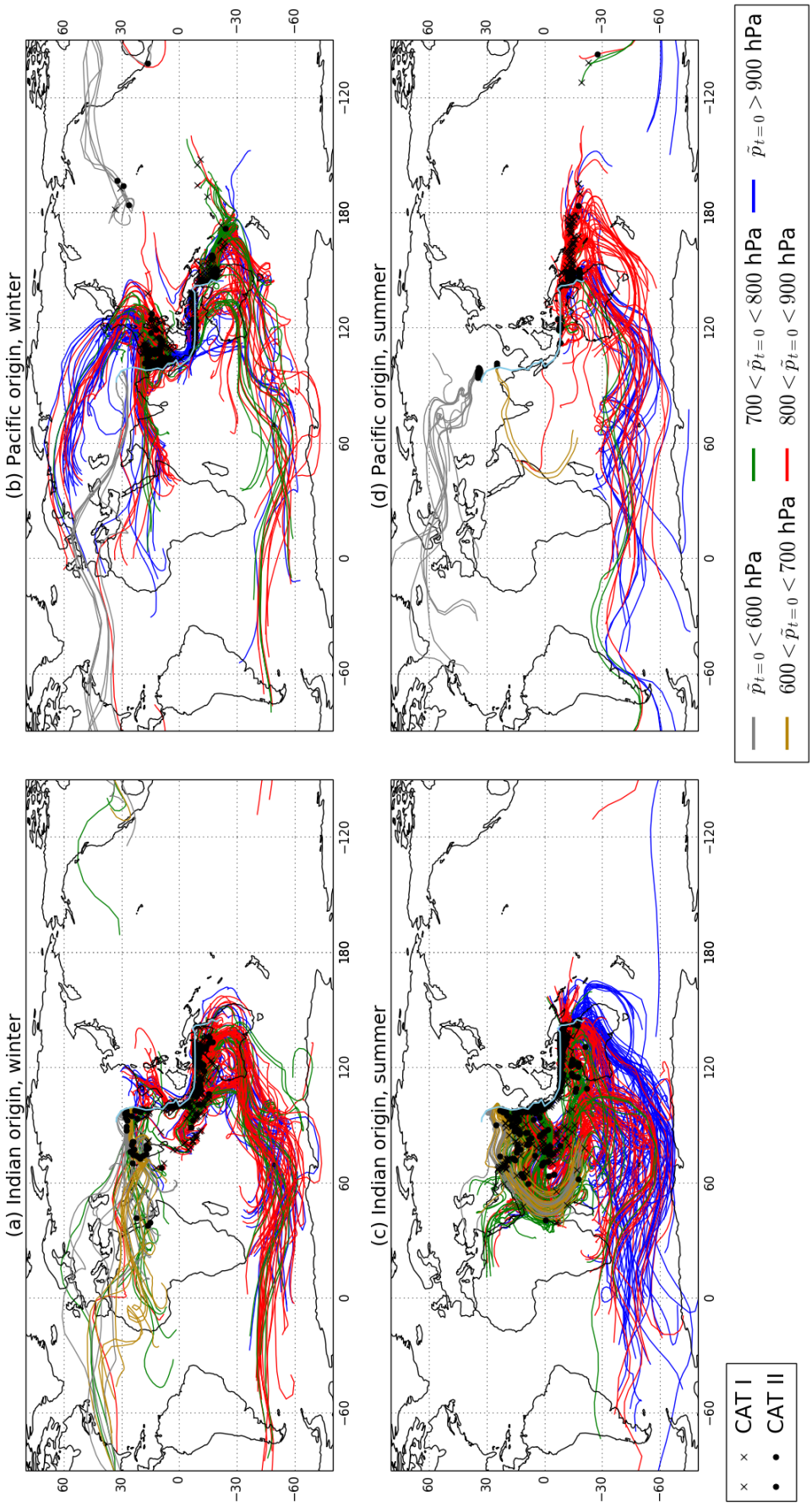

Figure 5.24: Trajectories released from the South-East Asian catchment boundary at 00 UTC on 11th January 2014 (a,b) and 00 UTC on 30th June 2014 (c,d). Panels (a) and (c) show trajectories with Indian origin and panels (d) and (d) show trajectories with Pacific origin. Trajectories are coloured by their pressure upon arrival at the catchment boundary ($\tilde{p}_{t=0}$). CAT I (crosses) and CAT II (dots) origin locations are also shown. The catchment boundary is shown in light blue.

Africa with flux-weighted densities in excess of 100×10^3 kg s^{-1} steradian^{-1} over the Caribbean Sea. The dominant dynamical process affecting the seasonal cycle of American $\overline{\mathbf{Q}} \cdot \hat{\mathbf{n}}_{Atl}$ is the Caribbean LLJ which is strongest in JJA due to the meridional sea level pressure gradient with the North Atlantic subtropical high (Wang, 2007). The AWP, which dominates the interannual variability of net American $\overline{\mathbf{Q}} \cdot \hat{\mathbf{n}}$ (section 4.4.1), does not appear to influence the seasonal cycle of $\overline{\mathbf{Q}} \cdot \hat{\mathbf{n}}_{Atl}$ as strongly as it peaks in September (Wang and Enfield, 2001) and is likely to inhibit moisture transport from the Atlantic across Central America due to anomalous low-level convergence associated with SST anomalies (Wang *et al.*, 2013).

Trajectory releases from the American catchment boundary for January and June are shown in Figure 5.26. The effect of the Caribbean LLJ is shown by the densely packed origins across the Caribbean Sea associated with low-level trajectories from the North Atlantic subtropical high or zonal mid-tropospheric flow across the tropical North Atlantic. Most of the trajectories associated with the Caribbean LLJ have origin in the Atlantic basin, but some

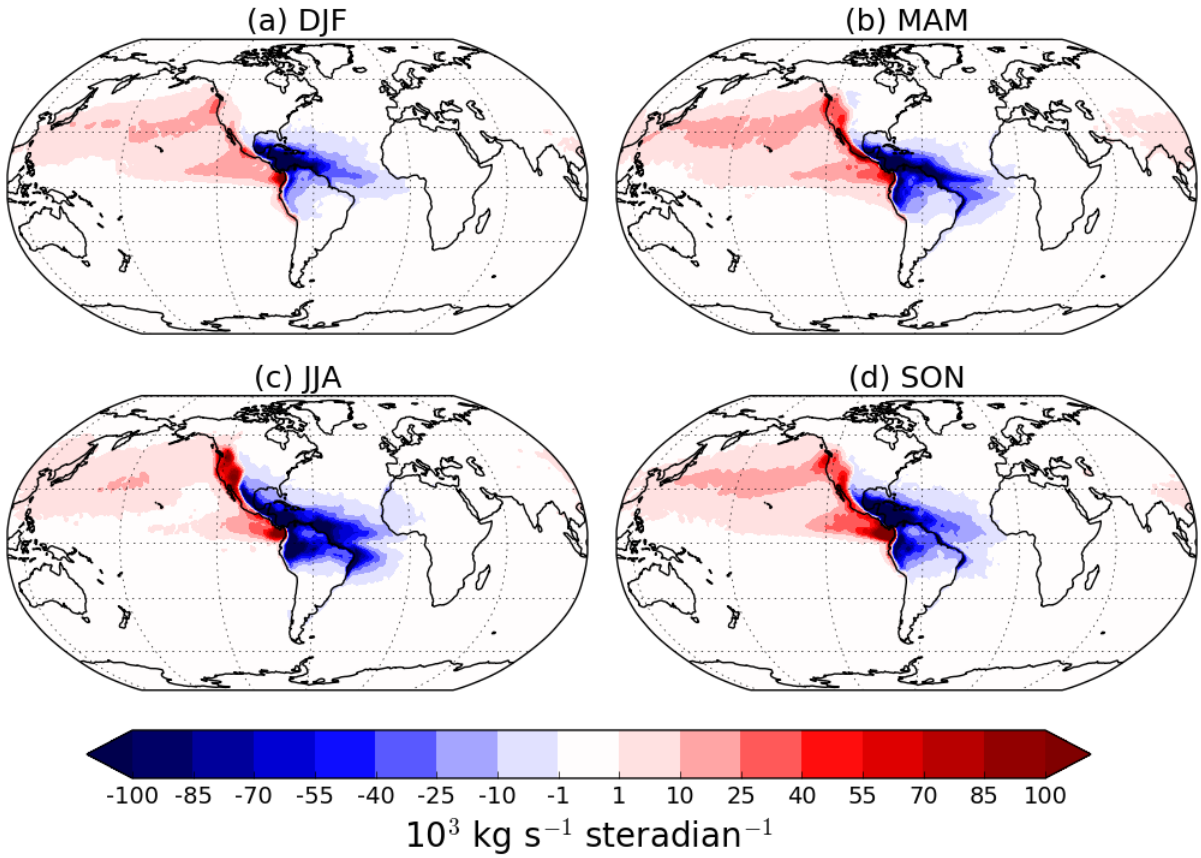

Figure 5.25: Flux-weighted density maps for the 2010-2014 climatological seasonal means of all trajectories with origin released from the Amerian catchment boundary. Red/positive contours indicate moisture flux which crosses the catchment boundary in a northward/eastward direction, and blue/negative contours indicate moisture flux which crosses the catchment boundary in a southward/westward direction.

cross Central America without making contact with the boundary layer or experiencing sufficient mixing until they are above the Pacific basin. Such trajectories undergo cyclonic curvature caused by surface convergence due to latent heat release from intense thunderstorms and pressure gradients from condensation from the Colombian rainforest (Poveda *et al.*, 2014), therefore contributing to eastward $\overline{\mathbf{Q}} \cdot \hat{\mathbf{n}}_{Pac}$ across the Andes and reducing Atlantic net evaporation. This extension of the Caribbean LLJ combines with the Choco LLJ at 5°N (Figure 5.26(d)) which, after crossing the equator, also undergoes cyclonic curvature, resulting in very heavy precipitation in the Colombian Andes (Poveda and Mesa, 2000).

The dominant dynamical processes influencing moisture fluxes associated with the $\overline{P-E}$ asymmetries are therefore the Asian Summer Monsoon and the Somali LLJ - both of which are associated with the continental geometry and topographic features of the Indian Ocean basin. In JJA the eastward moisture fluxes across India and the Bay of Bengal towards the South-East Asian catchment boundary dominate the annual mean South-East Asian net $\overline{\mathbf{Q}} \cdot \hat{\mathbf{n}}$ and therefore the atmospheric moisture budgets of the Indian and Pacific Ocean drainage basins (Figure 4.10). This results in the anomalies from $[\overline{qu}]$ discussed in section 4.3.3 that dominate the annual mean Pacific/Atlantic and Pacific/Indian $\overline{P-E}$ asymmetries. The Caribbean LLJ dominates the seasonal cycle of American $\overline{\mathbf{Q}} \cdot \hat{\mathbf{n}}_{Atl}$ and therefore plays an important role in the seasonal cycle of Atlantic $\overline{P-E}$, but it makes a far less significant contribution to net precipitation across the Pacific Ocean.

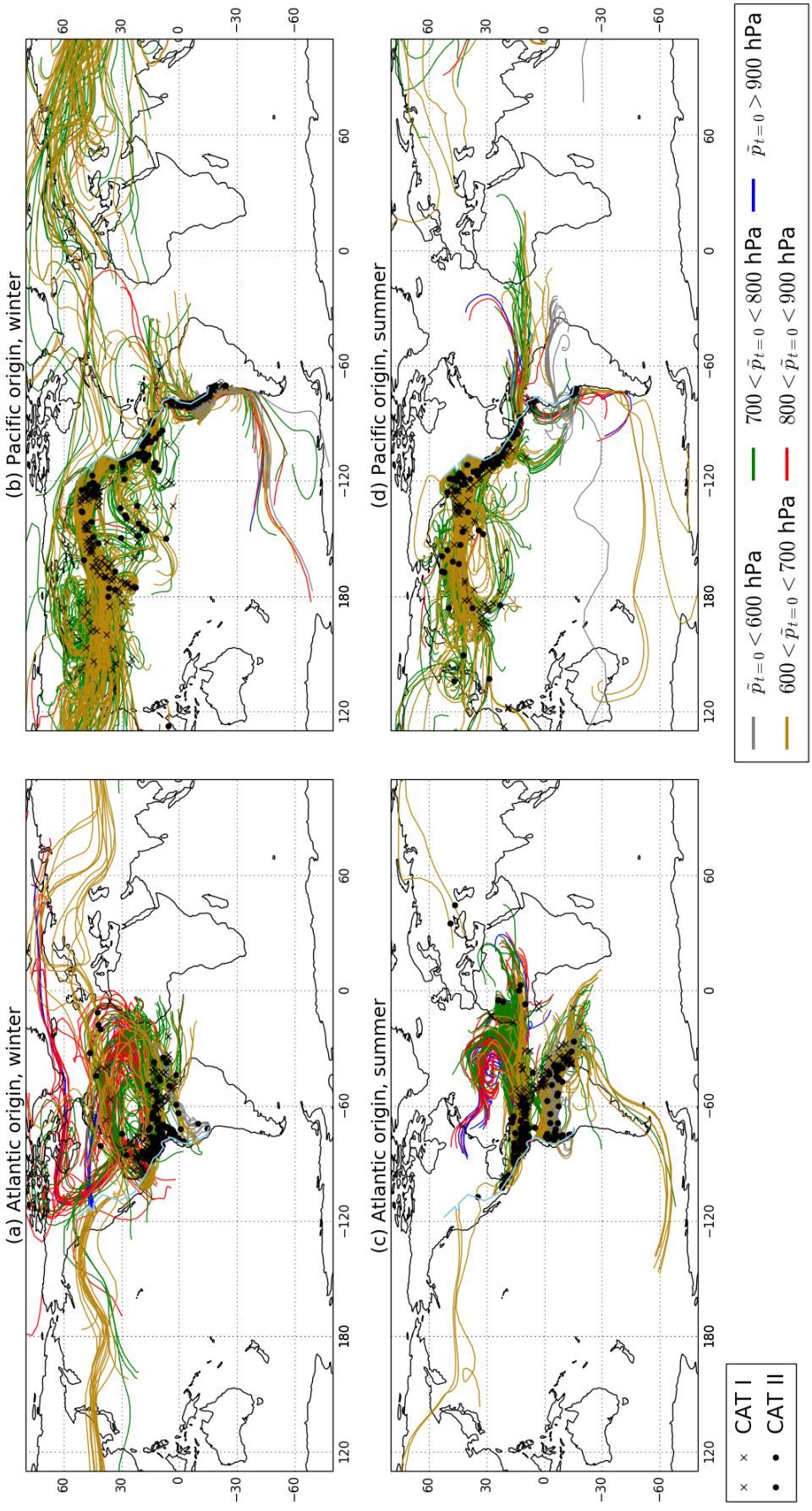

Figure 5.26: Trajectories released from the Americas catchment boundary at 00 UTC on 11th January 2014 (a,b) and 00 UTC on 30th June 2014 (c,d). Panels (a) and (c) show trajectories with Atlantic origin and panels (d) and (d) show trajectories with Pacific origin. Trajectories are coloured by their pressure upon arrival at the catchment boundary ($\tilde{p}_{t=0}$). CAT I (crosses) and CAT II (dots) origin locations are also shown. The catchment boundary is shown in light blue.

5.10 Summary

In this chapter an airmass trajectory model (Methven, 1997) with 14 day back trajectories released from the catchment boundaries surrounding each ocean drainage basin and the de Leeuw *et al.* (2017) method for assigning moisture origins were used to partition $\mathbf{Q} \cdot \hat{\mathbf{n}}$ into contributions from each ocean drainage basin with a view to understanding $\overline{P-E}$ asymmetries between the oceans. This was expected to build upon the Eulerian approach to understanding the $\overline{P-E}$ asymmmetries (chapter 4) and determine the main source regions for the moisture crossing each catchment boundary.

The key findings of this chapter are:

1. The highest moisture flux-weighted densities are found along or close to the catchment boundaries (Figures 5.12-5.16) and remote moisture sources are very low despite trajectory origins being found around the planet (Figure 5.7) indicating that trajectories which have distant origins have very low moisture content upon arrival at the catchment boundary.
2. Partitioning $\overline{\mathbf{Q}} \cdot \hat{\mathbf{n}}$ into contributions from origin drainage basins, the stratosphere and trajectories with no origin in 14 days shows that the $\overline{\mathbf{Q}} \cdot \hat{\mathbf{n}}_i$ from the drainage basins directly adjacent to each catchment boundary dominates $\overline{\mathbf{Q}} \cdot \hat{\mathbf{n}}$ (Figure 5.17). The moisture fluxes from trajectories with no assigned origin or stratospheric origin make small, negligible, contributions to $\overline{\mathbf{Q}} \cdot \hat{\mathbf{n}}$ despite often forming large percentages of the trajectory origins (Figure 5.11).
3. The Atlantic, Indian and Pacific drainage basins export (OUT) similar quantities of atmospheric moisture, slightly in excess of 1 Sv (Figure 5.18), with the Pacific importing (IN) almost the same quantity of moisture. The Atlantic and Indian basins, however, import only slightly over half of the moisture they import. Calculating each IN and OUT flux as fluxes per unit length (Table 5.1) shows that the atmosphere imports moisture more efficiently to the Pacific basin than it does to the Atlantic and Indian basins, with approximately equal levels of efficiency at exporting moisture for all three basins.
4. Northward $\overline{\mathbf{Q}} \cdot \hat{\mathbf{n}}_{Sou}$ per unit length along 35°S is weakest along the Atlantic sector of the Southern Ocean catchment boundary, which causes the strong net southward $\overline{\mathbf{Q}} \cdot \hat{\mathbf{n}}$ from Atlantic to Southern Oceans (section 4.3.1). Weak southward $\overline{\mathbf{Q}} \cdot \hat{\mathbf{n}}_{Ind}$ per unit length along the Indian sector of 35°S (compared to $\overline{\mathbf{Q}} \cdot \hat{\mathbf{n}}_{Atl}$ and $\overline{\mathbf{Q}} \cdot \hat{\mathbf{n}}_{Pac}$ for the respective sectors)

results in weak net southward $\overline{\mathbf{Q}} \cdot \hat{\mathbf{n}}$ from Indian to Southern Oceans (section 4.3.1). Both these results are due to the relative shapes of the subtropical highs and the fraction of the ocean basin occupied by the poleward part at 35°S (Figure 4.7).

5. Moisture transport from the Indian Ocean to the Pacific (primarily across South-East Asia) accounts for approximately 35% of Pacific IN flux and dominates Pacific $\overline{P-E}$ (Table 5.3). Trajectories with origin in the Indian Ocean are therefore the leading cause of net precipitation across the Pacific Ocean (Stohl and James, 2005) and dominate the $\overline{P-E}$ asymmetries.
6. Various LLJs are the prime mechanisms for importing atmospheric moisture from Atlantic-to-Pacific and Indian-to-Atlantic (Figure 5.19). However, American $\overline{\mathbf{Q}} \cdot \hat{\mathbf{n}}_{Atl}$ does not peak above Panama, indicating that the Isthmus of Panama is not the prime location for atmospheric import to the Pacific basin across Central America (Broecker, 1991; Leduc *et al.*, 2007).
7. The seasonal cycles of American, African and South-East Asian $\overline{\mathbf{Q}} \cdot \hat{\mathbf{n}}_i$ (Figure 5.21) show that the Asian Summer Monsoon and its association with the Somali LLJ dominate the $\overline{P-E}$ asymmetries by diverting moisture away from Africa in JJA into the westerlies across India and the Bay of Bengal towards the Pacific (Figure 5.24).

The findings from this chapter support the findings from the Eulerian analysis in chapters 3 and 4. By using trajectories it was possible to calculate the total moisture fluxes entering (IN) and leaving the basin (OUT) (section 5.8.2) - a disagnostic not available when simply calculating the moisture budgets from gridded fields. This diagnostic was consistent with Figure 3.5 where it was shown that the Pacific/Atlantic asymmetry is primarily caused by an asymmetry in area-averaged precipitation south of 30°N.

The Lagrangian diagnostic also explained the asymmetries in atmospheric moisture fluxes across 35°S (section 4.3.1). Net $\overline{\mathbf{Q}} \cdot \hat{\mathbf{n}}$ across the Atlantic sector is most efficient due to weak northward $\overline{\mathbf{Q}} \cdot \hat{\mathbf{n}}_{Sou}$ which in turn is due to the small fraction of the basin occupied by the equatorward part of the subtropical high at 35°S (Figure 4.7). Net $\overline{\mathbf{Q}} \cdot \hat{\mathbf{n}}$ across the Indian sector is weakest because of weak southward $\overline{\mathbf{Q}} \cdot \hat{\mathbf{n}}_{Ind}$, caused by very weak poleward $\overline{q}\,\overline{v}$ (Figure 4.7). This may be a result of the JJA dominance of the moisture flux field across the Indian Ocean where the Somali LLJ transports moisture across the equator and restricts the development of the poleward part of the subtropical high.

The Somali LLJ and Asian Summer Monsoon have been shown to play a key role in the $\overline{P-E}$ asymmetries. The seasonal cycles of $\overline{\mathbf{Q}}\cdot\hat{\mathbf{n}}_{Ind}$ (Figure 5.21) show a minimum in Indian-to-Atlantic transport across Africa and maximum in Indian-to-Pacific transport across South-East Asia. In JJA the Somali LLJ is fully developed and its westerly northern branch diverts trajectories away from Africa (Figure 5.24) towards the Asian Monsoon. The moisture fluxes associated with this were shown in chapter 4 to dominate the annual mean moisture budget asymmetries (Figure 4.10) and cause the zonally anomalous eastward moisture fluxes across South-East Asia (Figure 4.12). These results have therefore provided some quantatitive support for the conclusions of Emile-Geay *et al.* (2003) who linked the subpolar $\overline{P-E}$ asymmetries to moisture fluxes associated with the Asian Monsoon.

Topographic features and continental geometry are therefore a key part of the $\overline{P-E}$ asymmetries. The African topography has been shown to play a key role in the strength of the Somali LLJ (Rodwell and Hoskins, 1995; Wei and Bordoni, 2016) and the Asian Monsoon is often described in terms of a large scale sea breeze due to the different heat capacities of land and sea. The widths of the ocean basins (Schmitt *et al.*, 1989; Ferreira *et al.*, 2010) also affect the $\overline{q}\,\overline{v}$ patterns with the subtropical highs being particularly susceptible to different basin widths, thus affecting both poleward and equatorward moisture fluxes.

Chapter 6

Conclusions and Future Work

The atmospheric moisture budget asymmetry between the Atlantic and Pacific Oceans is a well documented feature of present-day climate (Broecker, 1991; Rahmstorf, 1996) where the Atlantic is a net evaporative ocean and the Pacific is close to moisture balance. The existence of this asymmetry has previously been framed as a consequence of enhanced Atlantic evaporation due to heat transport from the AMOC (Weijer *et al.*, 1999) with excess atmospheric moisture transported across Central America to the Pacific where it falls as precipitation (Broecker, 1991). In this thesis, the atmospheric moisture budget asymmetry is studied from both Eulerian and Lagrangian perspectives to understand the dominant moisture transports in setting this asymmetry. The Lagrangian approach also provides information regarding sources of moisture transported in the atmosphere between oceans which cannot be obtained from Eulerian approaches alone.

6.1 Dominant part of the moisture budget asymmetry

In chapter 3 seven published estimates (both atmospheric and oceanographic) of Atlantic, Pacific and Indian Ocean net freshwater flux (evaporation minus precipitation minus runoff, $E-P-R$) were compared with two additional estimates included from ERA-Interim vertically-integrated moisture flux divergence (div$\mathbf{Q}$) with Dai and Trenberth (2002) runoff and ECCOv4 ocean transports. The $E-P-R$ of each ocean are remarkably consistent across the estimates considering the different methods, input data and time periods used in calculating each estimate, as well as the different errors associated with each. When using the maximum latitudinal extents of the Atlantic and Pacific there is a difference of approximately 0.4 Sv between their

respective atmospheric moisture budgets (Figure 3.2).

To determine which part of the moisture budget asymmetry (evaporation, precipitation or runoff) is dominant, ERA-Interim E and P fields from the forecast model were used. Forecast model $E - P$ does not precisely balance div$\mathbf{Q}$ but this imbalance is only 0.08 mm day^{-1} for the Atlantic and Pacific Oceans (Table 3.2) - small enough for the E and P fields to be used to understand the moisture budget asymmetry. The time derivative term in the vertically-integrated moisture budget (equation (3.1)) is negligible in this case as it is orders of magnitude smaller than the divergence term over long time periods.

The difference (Pacific minus Atlantic) between area-averaged E, P and R in 10° latitude bands (Figure 3.5) shows that an asymmetry in E is only important in the midlatitudes/supbolar regions of the North Atlantic/Pacific where Atlantic E exceeds Pacific E by $\sim$20 cm yr^{-1}. This contrast is well known and thought to be caused by greater Atlantic SSTs due to enhanced northward heat transport in the AMOC (Warren, 1983; Emile-Geay *et al.*, 2003; Czaja, 2009), the relative widths of the oceans and the fraction of dry continental air affecting them (Schmitt *et al.*, 1989) and transient eddy moisture fluxes (Wills and Schneider, 2015). South of 20°N there is a larger asymmetry in area-averaged precipitation which is up to 100 cm yr^{-1} greater over the Pacific. This is likely a result of the relative widths of the oceans and the resulting stationary eddy patterns where ascending air leading to precipitation covers a larger fraction of the basin. Area-averaged R is only important in the tropical Atlantic where the mouths of the Amazon and Congo are located but the SSS asymmetry still exists in the tropics.

Further findings in chapter 3 are that the moisture budget asymmetry is steady both interannualy (error bars on ERA-Interim/ECCOv4 estimates in Figure 3.2) and in the annual cycle (Figure 3.6). Problems with the assimilation of rain-affected radiances in ERA-Interim caused precipitation to be underestimated over the oceans (Dee *et al.*, 2011) making it difficult to draw conclusions on the dominant part of $E - P$ in terms of interannual variability (Figure 3.12). Trends and variability in ERA-Interim precipitation are therefore unreliable but trends in evaporation of 3.4 mm yr^{-1} yr^{-1} and 2.0 mm yr^{-1} yr^{-1} for the Pacific and Atlantic respectively are consistent with other estimates (Yu and Weller, 2007; Iwasaki *et al.*, 2014) and may be physical.

6.2 Link between mean state and interannual variability of moisture fluxes and the moisture budget

As it was established in chapter 3 that precipitation dominates the moisture budget asymmetry it is clear that atmospheric moisture transport plays an important role. Therefore in chapter 4 the link between the moisture budgets of each ocean drainage basin (Atlantic, Indian, Pacific, Arctic, Southern) and atmospheric moisture transport are assessed from an Eulerian point of view.

A new estimate of the moisture fluxes normal to the catchment boundaries ($\overline{\mathbf{Q}} \cdot \hat{\mathbf{n}}$) is presented in Figure 4.2 (and simplified in Figure 6.1). This is an improvement on previous estimates (Rodriguez *et al.*, 2011; Levang and Schmitt, 2015; Singh *et al.*, 2016) with regards to the definition of the catchment boundaries (section 2.3) as $\overline{\mathbf{Q}} \cdot \hat{\mathbf{n}}$ is very sensitive to their placement. South-East Asian $\overline{\mathbf{Q}} \cdot \hat{\mathbf{n}}$ was particulalry sensitive to the placement of the catchment boundary and also to the dataset used as the coarse horizontal resolution of some renalyses (Rodriguez *et al.*, 2011) and climate models (Levang and Schmitt, 2015) resulted in westward $\overline{\mathbf{Q}} \cdot \hat{\mathbf{n}}$ rather than the eastward $\overline{\mathbf{Q}} \cdot \hat{\mathbf{n}}$ from ERA-Interim (Figure 4.2).

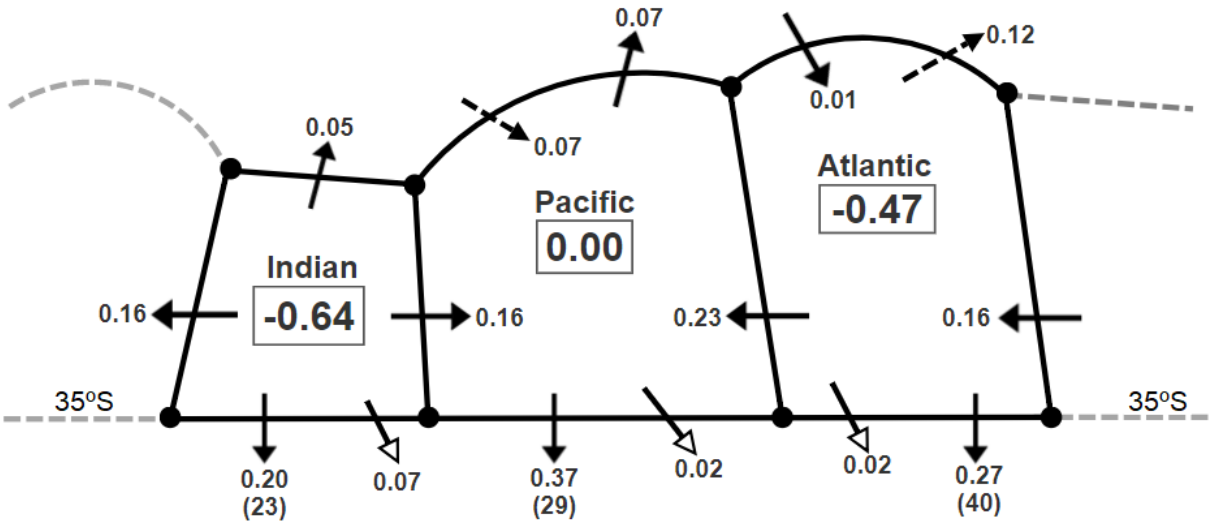

Figure 6.1: Simplified schematic of Figure 4.2 showing the vertically-integrated moisture fluxes across the catchment boundaries surrounding the Indian, Pacific and Atlantic Ocean drainage basins (arrows) and the basin-integrated $\overline{P-E}$ (boxes) calculated as the sum of the surrounding fluxes using equation (4.2). The arrows with dashed tails represent moisture flux across the Arctic catchment boundary to/from the Central Asian endorheic drainage basin, and the arrows with empty heads represent moisture flux across the land-only parts of the Southern Ocean catchment boundary. All values are in Sverdrups (1 Sv $\equiv 10^9$ kg s^{-1}) apart from the values in parenthesis which are the moisture fluxes per unit length across each sector of 35°S in kg s^{-1} m^{-1} from Table 4.1.

The annual mean Pacific/Atlantic precipitation minus evaporation ($\overline{P-E}$) asymmetry is dominated by the annual mean flow which imports 0.46 Sv into the Pacific basin but exports slightly in excess of 0.2 Sv from the Atlantic and Indian Oceans (Figure 4.8). Transient moisture fluxes, however, export moisture from all three basins with approximately double the quantity exported from the Pacific than the Atlantic and Indian basins. Furthermore, the $\overline{P-E}$ asymmetry is dominated by the June-July-August (JJA) $\overline{\mathbf{Q}} \cdot \hat{\mathbf{n}}$ and $\overline{P-E}$ where the Pacific becomes strongly net precipitative (0.55 Sv) and the Atlantic reaches its peak net evaporation (-0.63 Sv) due to strong eastward moisture fluxes across South-East Asia and peak American $\overline{\mathbf{Q}} \cdot \hat{\mathbf{n}}$ (Figure 4.10).

Despite having very different $\overline{P-E}$ the Atlantic and Pacific have similar latitudinal extents, with an ITCZ, two subtropical regions and one subpolar region. Such a basin would be expected to have net evaporation due to the missing region of moisture flux convergence in the southern hemisphere (Figure 4.11). Therefore if the atmospheric circulations above the Atlantic and Pacific are similar they would have similar moisture fluxes per unit length across the lateral (east and west) boundaries and across the boundaries seperating them from the two polar basins. This is the case for transient moisture fluxes across 35°S (Table 4.1) and American $\overline{\mathbf{Q}} \cdot \hat{\mathbf{n}}$ which approximately matches the integral of the zonal mean zonal moisture flux ($[\overline{qu}]$) between corresponding latitudes (Figure 4.12). However, African $\overline{\mathbf{Q}} \cdot \hat{\mathbf{n}}$ is weaker than would be expected from the zonal mean and South-East Asian $\overline{\mathbf{Q}} \cdot \hat{\mathbf{n}}$ is of opposite sign to the zonal mean between corresponding latitudes. Replacing the ERA-Interim $\overline{\mathbf{Q}} \cdot \hat{\mathbf{n}}$ on the American, African and South-East Asian catchment boundaries with $[\overline{qu}]$ between the corresponding latitudes (Figure 4.13) confirms that deviations from $[\overline{qu}]$ dominate the moisture budget asymmetries. If $\overline{\mathbf{Q}} \cdot \hat{\mathbf{n}}$ on the American, African and South-East Asian catchment boundaries matched $[\overline{qu}]$ then the Pacific would be the most evaporative basin per unit area and the Indian the least (Table 4.2). These results suggest that an asymmetry between the Pacific and Indian Oceans should be considered along with the Pacific/Atlantic asymmetry.

The interannual variability of each $\mathbf{Q} \cdot \hat{\mathbf{n}}$ and $P-E$ was also investigated in chapter 4. These results also indicate that South-East Asian $\mathbf{Q} \cdot \hat{\mathbf{n}}$ is the most important part of the moisture budget contrasts between the Pacific Ocean and the Atlantic/Indian Oceans as the correlations with Pacific and Indian $P-E$ are the strongest (Table 4.3). Most of the variability in South-East Asian $\mathbf{Q} \cdot \hat{\mathbf{n}}$ is related to ENSO where $\mathbf{Q} \cdot \hat{\mathbf{n}}$ reduces during the warm (El Niño) phase as the ascending branch of the Walker Circulation shifts east and the Somali LLJ weakens (Halpern

and Woiceshyn, 2001), thus reducing Pacific $P-E$ and increasing Indian $P-E$. Americas $\mathbf{Q}\cdot\hat{\mathbf{n}}$ has a weaker correlation with Pacific $P-E$ (although still fairly strong) but its correlation with Atlantic $P-E$ is the strongest surrounding the Atlantic.

It is not possible to find a statistical relationship between the interannual variability of SSS and $\mathbf{Q}\cdot\hat{\mathbf{n}}$ or $P-E$ as the mixing timescale for salinity is about 50 years (Zika *et al.*, 2015; Ferreira *et al.*, 2018). There are other processes affecting SSS which have a stronger influence than freshwater fluxes Yu (2011) but the imprint of a changing hydrological cycle can be seen in SSS on decadal timescales (Durack and Wijffels, 2010; Skliris *et al.*, 2014).

6.3 Dominant partitioned moisture fluxes in the moisture budget asymmetry

In chapter 5 an airmass trajectory model (Methven, 1997) is used to parition $\mathbf{Q}\cdot\hat{\mathbf{n}}$ into contributions from trajectories with origin in each of the five ocean drainage basins. The de Leeuw *et al.* (2017) method for assigning moisture origins based on mixing is used: last exit from the boundary layer, well mixed across the boundary layer to the surface (CAT I), and partial mixing in clouds, well mixed in equivalent potential temperature (CAT II).

The highest densities of trajectory origins are found close to the catchment boundaries as many trajectories are either released inside the boundary layer or experience mixing shortly before arriving at the catchment boundary (Figures 5.7-5.9). As a result the greatest flux-weighted densities occur close to the catchment boundaries (Figures 5.12-5.16).

Trajectories released from the American, African and South-East Asian catchment boundaries tend to have origin in the two neighbouring drainage basins and total $\overline{\mathbf{Q}}\cdot\hat{\mathbf{n}}$ is mostly composed of two neighbouring annual mean partitioned moisture fluxes ($\overline{\mathbf{Q}}\cdot\hat{\mathbf{n}}_i$) (Figure 5.17). American and African total $\overline{\mathbf{Q}}\cdot\hat{\mathbf{n}}$ are dominated by westward moisture fluxes in the tropics with Atlantic and Indian origin respectively with African $\overline{\mathbf{Q}}\cdot\hat{\mathbf{n}}_{Ind}$ about half the strength of American $\overline{\mathbf{Q}}\cdot\hat{\mathbf{n}}_{Atl}$. Net Atlantic-to-Pacific atmospheric moisture transport across the Americas is therefore dominated by westward moisture transport with Atlantic origin as assumed by Broecker (1991) and Leduc *et al.* (2007).

Unlike American and African $\overline{\mathbf{Q}}\cdot\hat{\mathbf{n}}$, South-East Asian $\overline{\mathbf{Q}}\cdot\hat{\mathbf{n}}$ is eastward and dominated by $\overline{\mathbf{Q}}\cdot\hat{\mathbf{n}}_{Ind}$ of 0.4 Sv. The westward $\overline{\mathbf{Q}}\cdot\hat{\mathbf{n}}_{Pac}$ is of similar strength to the westward $\overline{\mathbf{Q}}\cdot\hat{\mathbf{n}}_i$ across the other catchment boundaries so the large eastward $\overline{\mathbf{Q}}\cdot\hat{\mathbf{n}}_{Ind}$ - which is 3-4 times stronger than the other eastward $\overline{\mathbf{Q}}\cdot\hat{\mathbf{n}}_i$ - causes the deviation from $[\overline{qu}]$ discussed in chapter 4. This results

in greater $\overline{\mathbf{Q}} \cdot \hat{\mathbf{n}}$ per unit length entering the Pacific across the entire catchment boundary while the fluxes per unit length leaving the Atlantic, Indian and Pacific drainage basins are similar (Table 5.1). This is consistent with the results from chapter 3 where area-averaged evaporation rates are similar between basins but the Pacific has stronger area-averaged precipitation.

The Pacific/Atlantic and Pacific/Indian $\overline{P-E}$ asymmetries are caused by stronger atmospheric moisture import per unit length across the perimeter of the Pacific drainage basin (Table 5.1). This is mostly a result of the contribution of trajectories with Indian Ocean origin towards the Pacific moisture budget, associated with 0.43 Sv net precipitation across the Pacific Ocean (Table 5.3) which accounts for 38% of the moisture flux imported across the perimiter of the Pacific basin, a similar result to Stohl and James (2005). The strong Indian-to-Pacific moisture export compensates for the weak southward export across the Indian Ocean sector of 35°S (Table 5.2). Contrasting partitioned moisture fluxes per unit length across 35°S are direct consequences of contrasting $\overline{q}\,\overline{v}$ patterns (Figure 4.7) where the widths of the basins affect the relative fractions of 35°S occupied by the poleward and equatorward parts of the subtropical highs.

6.4 Dynamical processes affecting the moisture budget asymmetry

To understand the key dynamical processes which transport moisture in the atmosphere both Eulerian analysis in chapter 4 and Lagrangian analysis in chapter 5 were used. By partitioning total $\overline{\mathbf{Q}} \cdot \hat{\mathbf{n}}$ into its contributing $\overline{\mathbf{Q}} \cdot \hat{\mathbf{n}}_i$ the results from the Lagrangian analysis support the conclusions from the Eulerian analysis and provided a more detailed understanding of the key processes. The use of trajectories in chapter 5 builds on the Eulerian understanding of the key dynamical processes influencing the $\overline{P-E}$ asymmetries from chapter 4. Trajectories provide information regarding the history of an air parcel's thermodynamic properties and location, as well as representing vertical motion which is not possible from a static budget (Figure 4.2). The paths of the back trajectories (Figures 5.24 and 5.26) show distinctive features which highlight key dynamical processes.

In chapter 4 the temporal variation of the $\overline{P-E}$ asymmetries was analyzed from an Eulerian perspective. A Reynolds decomposition of $\overline{\mathbf{Q}} \cdot \hat{\mathbf{n}}$ and $\overline{P-E}$ (section 4.2.2) showed that the annual mean asymmetries are dominated by the annual mean flow which is associated with 0.46 Sv net precipitation across the Pacific but 0.25 Sv and 0.39 Sv net evaporation from the Atlantic and Indian basins respectively (Figure 4.8). Transient processes on short timescales are

less important and export moisture from each basin, particularly across 35°S where the transient moisture fluxes per unit length are similar for each sector (Table 4.1). The seasonal cycles of $\overline{\mathbf{Q}} \cdot \hat{\mathbf{n}}$ and $\overline{P-E}$ (Figure 4.10) show that the $\overline{P-E}$ asymmetries are dominated by JJA when Pacific net precipitation (0.55 Sv), Atlantic net evaporation (0.63 Sv) and Indian net evaporation (0.97 Sv) all peak. The largest change in $\overline{\mathbf{Q}} \cdot \hat{\mathbf{n}}$ is on the South-East Asian catchment boundary which changes sign throughout the year with a 0.59 Sv eastward moisture flux in JJA during the Asian Summer Monsoon hinting at its role in the $\overline{P-E}$ asymmetries.

The interannual variability of the $\overline{P-E}$ asymmetries were also discussed in chapter 4. The interannual variability of moisture fluxes across South-East Asia dominates the moisture budgets of the Pacific and Indian Oceans (section 4.4.1) with interannual fluctuations of up to 0.2 Sv in $\mathbf{Q} \cdot \hat{\mathbf{n}}$ (Figure 4.15). This variability is associated with El Niño-Southern Oscillation (ENSO). During the warm phase (El Niño) the Somali Low-Level Jet (LLJ) weakens thus reducing the eastward moisture transport across India towards the Pacific.

The impact of the Asian Monsoon in JJA dominates South-East Asian $\overline{\mathbf{Q}} \cdot \hat{\mathbf{n}}$ and $P-E$ across the Indian and Pacific Oceans. The Asian Monsoon therefore dominates the $\overline{P-E}$ asymmetries and provides some quantitive support for the conclusions drawn by Emile-Geay *et al.* (2003). Their study concluded that large scale low-level winds associated with the Asian Monsoon in JJA act to transport moisture to the subpolar North Pacific and therefore enhance the $P-E$ contrast. However, Emile-Geay *et al.* (2003) did not quantify the effect of the Asian Monsoon on the subpolar $P-E$ contrast or investigate moisture origins. Figure 6.2 shows that the asymmetry in area-averaged precipitation in JJA is not as pronounced as suggested by Emile-Geay *et al.* (2003) so the impact of the Asian Monsoon on subpolar $P-E$ appears to be somewhat limited. Instead it would appear that the contrast in tropical area-averaged precipitation (highlighted in chapter 3) is caused by the Asian Monsoon as this contrast and the overall moisture budget contrast peak in JJA (10-20°N, Figure 6.2) when both South-East Asian and American $\overline{\mathbf{Q}} \cdot \hat{\mathbf{n}}$ reach their peak strengths (Figure 4.10).

It was shown that the Somali LLJ is a key feature in the seasonal cycles of South-East Asian and African $\overline{\mathbf{Q}} \cdot \hat{\mathbf{n}}$, affecting $P-E$ of the Indian, Pacific and Atlantic Oceans. It reaches peak intensity in JJA and curves anti-cyclonically after crossing the equator thus diverting moisture away from Africa resulting in minima in $\overline{\mathbf{Q}} \cdot \hat{\mathbf{n}}_{Ind}$ on the African catchment boundary (Figure 5.21(b)) and transporting moisture towards the South-East Asian catchment boundary. The existence of the Somali LLJ and its role in the Asian Monsoon are crucial aspects of the $\overline{P-E}$

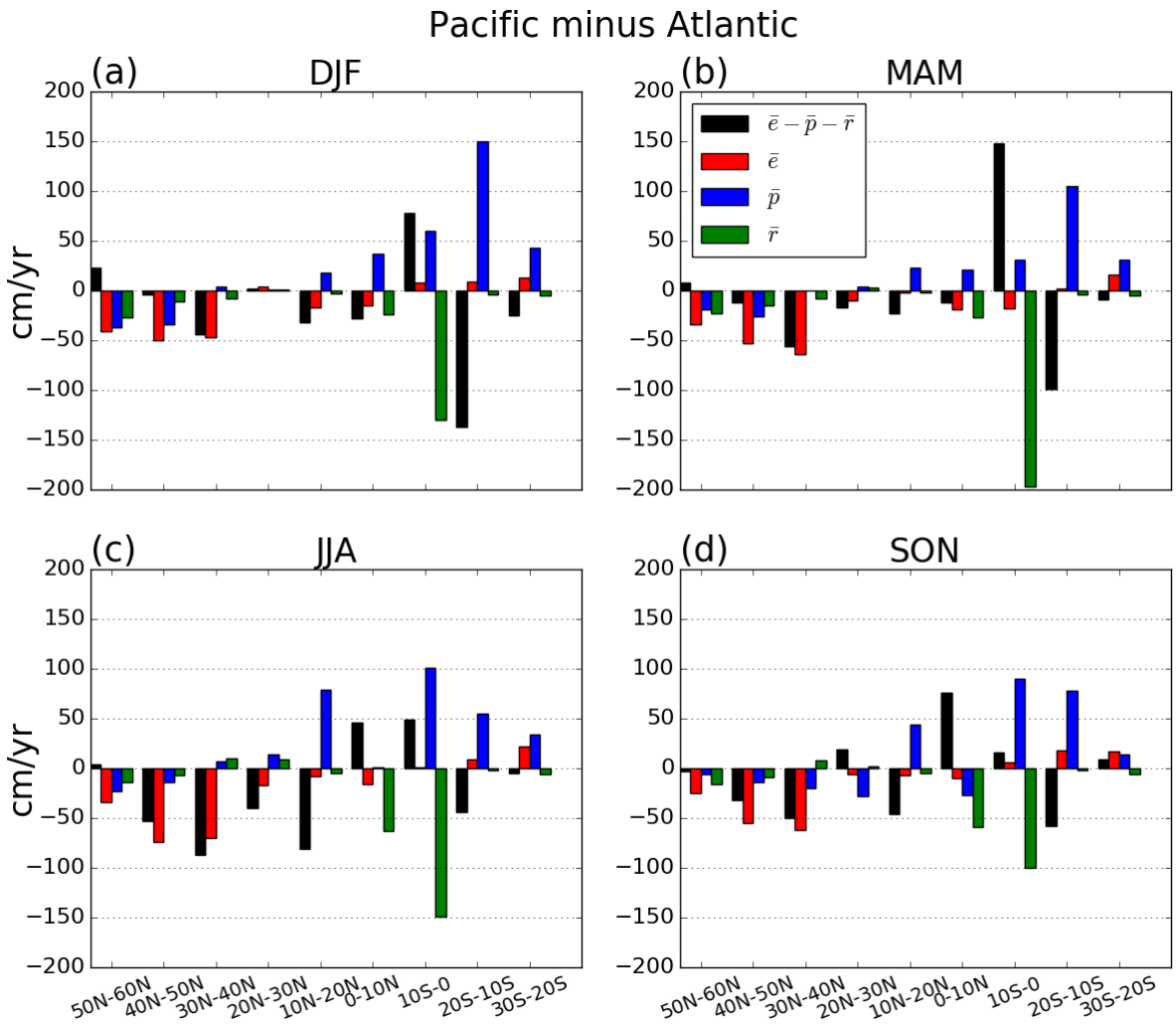

Figure 6.2: Differences between area-averaged climatological (1979-2014) mean (a) December-January-February (DJF), (b) March-April-May (MAM), (c) June-July-August (JJA) and (d) September-October-November (SON) ERA-Interim Pacific and Atlantic surface water fluxes in 10° latitude bands scaled by area with Dai and Trenberth (2002) runoff divided into the same 10° latitude bands.

asymmetries.

Peaks in $\overline{\mathbf{Q}} \cdot \hat{\mathbf{n}}$ along the American catchment boundary are caused by gap winds in three major valleys in the Central American mountains. These are linked to the trade winds and Caribbean LLJ which peak in DJF and JJA respectively, with peak $\overline{\mathbf{Q}} \cdot \hat{\mathbf{n}}_{Atl}$ in JJA (Figure 5.21(a)). This work has shown that the major peak in American $\overline{\mathbf{Q}} \cdot \hat{\mathbf{n}}$ occurs above Lake Nicaragua in the Papagayo jet rather than above Panama as suggested with little evidence by previous studies (Dietrich, 1963; Weyl, 1968; Broecker, 1991). It therefore appears to be incorrect to focus on the Isthmus of Panama when investigating Atlantic/Pacific asymmetries in moisture budget, salinity and overturning.

6.5 Future Work

This work has answered some key questions relating to the $\overline{P-E}$ asymmetries between the Pacific and Atlantic/Indian Oceans. These findings have raised further questions which are discussed below with regards to how they may be answered.

6.5.1 Modeling studies

The Atlantic/Pacific asymmetries in $\overline{P-E}$, SSS and overturning have been studied using models by modifying orography (Schmittner *et al.*, 2011; Sinha *et al.*, 2012), the location of deep convection (Ferreira *et al.*, 2010) and the $\overline{P-E}$ fields (Huisman *et al.*, 2012). However, some of these studies are highlighly idealized (Ferreira *et al.*, 2010) and tend to focus on moisture transport across the Americas (Schmittner *et al.*, 2011; Sinha *et al.*, 2012) with the anomalous eastward $\overline{\mathbf{Q}} \cdot \hat{\mathbf{n}}$ across South-East Asia so far ignored in such modeling studies. Possible ways to further study the role of South-East Asian $\overline{\mathbf{Q}} \cdot \hat{\mathbf{n}}$ are:

1. Use the values of $\overline{\mathbf{Q}} \cdot \hat{\mathbf{n}}$ and $\overline{P-E}$ from Figure 4.2 to force an ocean-only model and compare the SSS field and overturning state to a model run where the direction of South-East Asian $\overline{\mathbf{Q}} \cdot \hat{\mathbf{n}}$ is reversed so Pacifc $\overline{P-E}$ is negative and Indian $\overline{P-E}$ is less negative. The idealized American, African and South-East Asian $\overline{\mathbf{Q}} \cdot \hat{\mathbf{n}}$ matching $[\overline{qu}]$ could also be used to see how the SSS field and overturning circulation respond.
2. The work by Schmittner *et al.* (2011) and Sinha *et al.* (2012) could be taken further by investigating the effect of flattening and increasing Asian orography (Himalayas/Mongolia) on Pacific SSS and overturning. It would also be very interesting to see how the findings of Wei and Bordoni (2016) could compliment the findings of Schmittner *et al.* (2011) and Sinha *et al.* (2012).
3. As the representation of the Maritime Continent appears to be very important when calculating $\overline{P-E}$ for the Indian and Pacific Oceans, and South-East Asian $\overline{\mathbf{Q}} \cdot \hat{\mathbf{n}}$ has much stronger influence on Pacific $\overline{P-E}$ than American $\overline{\mathbf{Q}} \cdot \hat{\mathbf{n}}$, future modeling studies should focus on this region. For example, an understanding of how the freshwater and salt budgets are affected when the ocean transport (Indonesian Throughflow) is blocked would be useful. Kajtar *et al.* (2015) found that the Pacific retains ENSO-like variability in such experiments but the SST anomalies associated with ENSO shifted eastwards, but inter-basin interactions were still present which highlights the importance of the "atmospheric

bridge" across the Maritime Continent. To further investigate this experiments with increasing orography on the Maritime Continent may provide more information as to the influence of this atmospheric bridge on the oceans' freshwater salt budgets and the ocean circulation.

6.5.2 Subpolar Atlantic/Pacific evaporation contrast

Figure 3.5 showed that area-averaged evaporation over the Atlantic is greater than over the Pacific north of 30°N. This is a well known contrast and has been attributed to higher Atlantic SSTs due to the AMOC (Warren, 1983; Czaja, 2009) and the relative widths of the basins (Schmitt *et al.*, 1989). With two potentially conflicting explainations for the subpolar evaporation contrast it would be interesting to investigate this contrast further by using the ECMWF evaporation bulk formula (ECMWF, 2015):

$$E_i = \rho_a |U_{\mathrm{L}}| C_{\mathrm{H}} [q_{\mathrm{L}} - q_{\mathrm{sat}}(T_{\mathrm{sk}})], \tag{6.1}$$

where ρ_a is air density (kg m^{-3}), $|U_{\mathrm{L}}|$ is wind speed at the lowest atmospheric model level (m s^{-1}), C_{H} is the turbulent exchange coefficient, q_{L} specific humidty at lowest atmospheric model level (kg kg^{-1}), q_{sat} is saturated specific humidity (kg kg^{-1}) and $T_{\mathrm{sk},i}$ ocean skin temperature (K). Figure 6.3 shows that the ERA-Interim evaporation field from the forecast model can be approximated using equation (6.1) and the three-hourly surface forecast parameters (both instantaneous and accumulated) with the Wu (1996) approximation of $C_{\mathrm{H},i}$. By using equation (6.1) it will be possible to find the relative contributions of SST, q_{L} and $|U_{\mathrm{L}}|$ to the overall contrast in area-averaged subpolar evaporation.

6.5.3 Trajectories

The use of trajectories in chapter 5 to understand the $\overline{P-E}$ asymmetry has provided information not available from the Eulerian diagnostics used in chapter 4 such as the moisture origins and the moisture fluxes leaving and entering each drainage basin, and also links the moisture fluxes to various dynamical processes. Some other potential avenues for further research are:

1. A study with trajectories released from more η levels in the lower troposphere would reduce the vertical subsampling problem described in section 5.4.1 which caused problems in calculating African $\mathbf{Q} \cdot \hat{\mathbf{n}}$ and therefore Atlantic and Indian Ocean $P - E$. Another

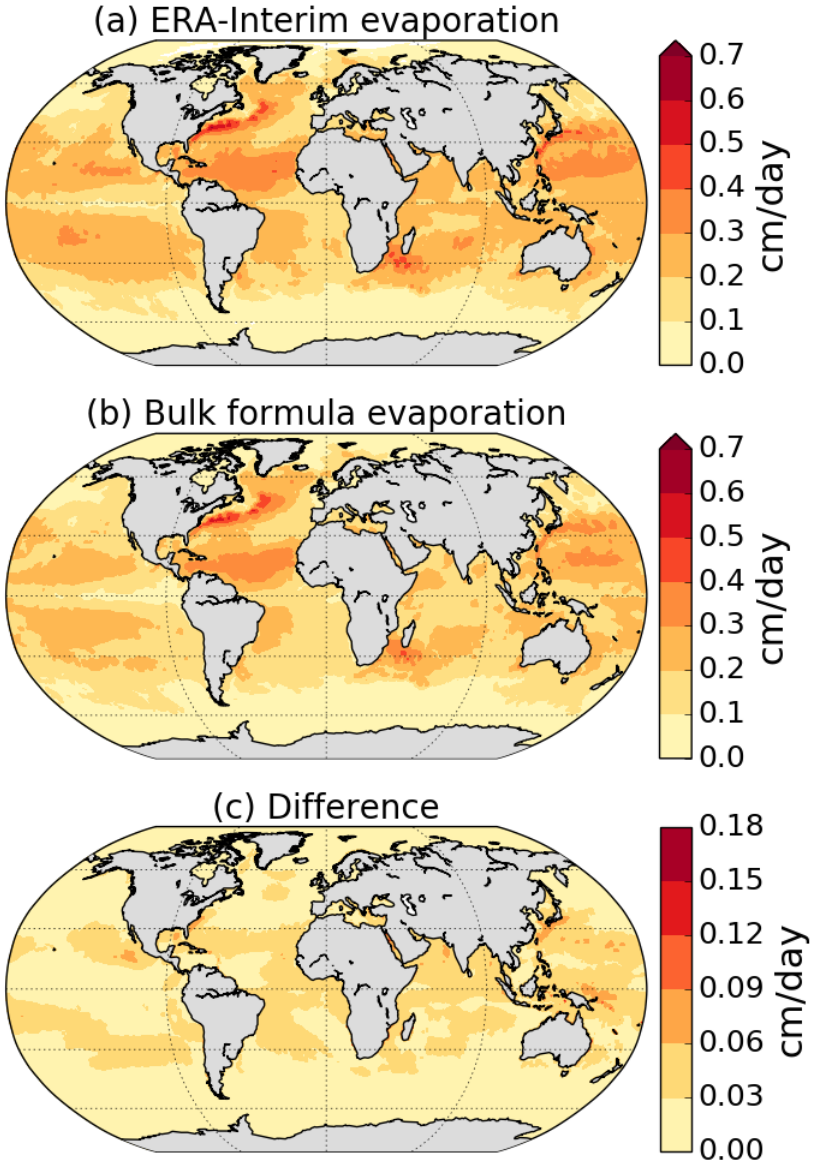

Figure 6.3: Global ERA-Interim evaporation field averaged over February 2011 from (a) the forecasr model and (b) equation (6.1) with (c) showing the difference between the two fields.

option would be to select vertical resolutions based on the vertical profiles of specific humidity along each catchment boundary. Either of these options would improve some of the results presented in chapter 5.

2. Using longer trajectories may reduce the proportions of trajectories with no assigned origin (Figure 5.11) and therefore the values of $\overline{\mathbf{Q}} \cdot \hat{\mathbf{n}}_{None}$ (Figure 5.17) which would lead to more accurate calculations of $\overline{P-E}$. Note that the ROTRAJ model has been used for trajectories as long as 27 days before (Cau *et al.*, 2007) and the use of the 4th order, 4 stage Runge-Kutta method for time integration means that the trajectory calculations are more accurate and more stable than other models with lower order methods (section 2.2.3).
3. The precipitation origins across the Pacific Ocean could be investigated using back tra-

jectories similar to de Leeuw *et al.* (2017). This may provide supporting evidence for this work's conclusion that the Asian Monsoon causes the strong area-averaged tropical Pacific precipitation through a "local vs. remote" diagnostic.

6.5.4 Past/future climate

Much of the Paleoclimate literature on Atlantic/Pacific MOC asymmetries focuses on moisture transport across Central America (Leduc *et al.*, 2007; Prange *et al.*, 2010) with reduced transport across Central America associated with increased Pacific SSS and therefore greater chance of a PMOC developing. However, this thesis has shown that in present climate moisture transport across South-East Asia is the dominant part of the $\overline{P-E}$ asymmetries so an improved understanding of the Asian Monsoon, Indo-Pacific Walker Circulation and the Maritime Continent in past climates could lead to an improved understanding of potential PMOCs in past climates.

Singh *et al.* (2016) showed that in a warmer climate moisture transport across Central America is expected to increase due to increased transport distances. This results in an amplification of the Atlantic/Pacific $\overline{P-E}$ and SSS contrasts (Levang and Schmitt, 2015) consistent with the Held and Soden (2006) "wet get wetter, dry get drier" scenario. However, this still focuses on Central America rather than South-East Asia. Levang and Schmitt (2015) present CMIP5 historical and projected moisture transports across South-East Asia but, probably due to low resolution, these are of opposing sign to ERA-Interim. Although it would be very useful to look at projected changes in transport across South-East Asia with regards to potential PMOC, this is inhibited by the current limitations of climate models in this region but as models are improved this research may become possible.

6.6 Concluding Remarks

This thesis has addressed the atmospheric moisture budget asymmetry between the Atlantic and Pacific Oceans and its link to atmospheric moisture transport using both Eulerian and Lagrangian diagnostics. The following key conclusions are drawn:

1. The Pacific/Atlantic asymmetry is primarily a result of stronger precipitation across the Pacific, mainly in the tropics. Higher subpolar Atlantic evaporation compared to the subpolar Pacific is relevant but less significant to the basin-scale moisture budget asymmetry.

2. Atmospheric moisture fluxes across South-East Asia dominate the mean state and interannual variability of the Pacific/Atlantic asymmetry, not moisture fluxes across Central America. A Pacific/Indian asymmetry should therefore also be considered.
3. The Indian Ocean acts as a moisture source for the Pacific. Trajectories with origin in the Indian Ocean are associated with net precipitation across the Pacific.
4. The continental geometry of the ocean basins plays a role in setting and maintaining the asymmetries with the dynamics associated with the Asian Summer Monsoon dominating the interbasin contrasts.

Overall, it has been shown that the Indian Ocean basin plays a more significant role in the moisture budget asymmetries than previously thought. The continental geometry and topographic features of this basin may therefore play a significant role in the state of the Pacific/Atlantic sea surface salinity asymmetry, and the lack of deep water formation in the subpolar Pacific Ocean.

BIBLIOGRAPHY

Adler, R.F., Huffman, G.J., Chang, A., Ferraro, R., Xie, P.P., Janowiak, J., Rudolf, B., Schneider, U., Curtis, S., Bolvin, D., Gruber, A., Susskind, J., Arkin, P., and Nelkin, E. (2003). The version-2 global precipitation climatology project (GPCP) monthly precipitation project analysis (1979-present). *Journal of Hydrometeorology*, **4**, 1147–1167.

Allen, M.R. and Ingram, W.J. (2002). Constraints on future changes in climate and the hydrologic cycle. *Nature*, **419**, 224–232.

Baker, A.J., Sodemann, H., Baldini, J.U.L., Breitenbach, S.F.M., Johnson, K.R., van Hunen, J., and Pingzhong, Z. (2015). Seasonality of westerly moisture transport in the East Asian summer monsoon and its implications for interpreting precipitation δ^{18}O. *Journal of Geophysical Research: Atmospheres*, **120**, 5850–5862.

Bakker, P., Schmittner, A., Lenearts, J.T.M., Abe-Ouchi, A., Bi, D., van den Broeke, M.R., Chan, W.L., Hu, A., Beadling, L.R., Marsland, S.J., Mernild, S.H., Saenko, O.A., Swingedouw, D., Sullivan, A., and Yin, J. (2016). Fate of the Atlantic Meridional Overturning Circulation: Strong decline under continued warming and Greenland melting. *Geophysical Research Letters*, **43**, 12252–12260.

Baumgartner, A. and Reichel, E. (1975). *The World Water Balance*. Elsevier, Amsterdam.

Beal, L.M., de Ruijter, P.M., Biastoch, A., and Zahn, R. (2011). On the role of the Agulhas system in ocean circulation and climate. *Nature*, **472**, 429–436.

Berbery, E.H. (2001). Mesoscale Moisture Analysis of the North American Monsoon. *Journal of Climate*, **14**, 121–137.

Berrisford, P., Kållberg, P., Kobayashi, S., Dee, D., Uppala, S., Simmons, A.J., Poli, P., and Sato, H. (2011). Atmospheric conservation properties in ERA-Interim. *Quarterly Journal of the Royal Meteorological Society*, **137**, 1381–1399.

Bingham, F.M. and Lee, T. (2017). Space and time scales of sea surface salinity and freshwater forcing variability in the global ocean (60°S-60°N). *Journal of Geophysical Research: Oceans*, **122**, 2909–2922.

Bingham, F.M., Foltz, G.R., and McPhaden, M.J. (2012). Characteristics of the seasonal cycle of surface layer salinity in the global ocean. *Ocean Science*, **8**, 915–929.

Bolton, D. (1980). The Computation of Equivalent Potential Temperature. *Monthly Weather Review*, **108**, 1046–1053.

Bonner, W.D. (1968). Climatology of the Low Level Jet. *Monthly Weather Review*, **96**, 833–850.

Bordoni, S. and Schneider, T. (2008). Monsoons as eddy-mediated regime transitions of the tropical overturning circulation. *Nature Geoscience*, **1**, 515–519.

Boyer, T.P. and Levitus, S. (2002). Harmonic analysis of climatological sea surface salinity. *Journal of Geophysical Research: Oceans*, **107**. 8006.

Brayshaw, D.J., Hoskins, B., and Blackburn, M. (2009). The Basic Ingredients of the North Atlantic Storm Track. Part I: Land-Sea Contrast and Orography. *Journal of the Atmospheric Sciences*, **66**, 2539–2558.

Broecker, W.S. (1991). The Great Ocean Conveyor. *Oceanography*, **4**, 79–89.

Broecker, W.S. (1997). Thermohaline circulation, the achilles heel of our climate system: Will man-made co_2 upset the current balance? *Science*, **278**, 1582–1588.

Brown, P.J. and Kummerow, C.D. (2014). An Assessment of Atmospheric Water Budget Components over Tropical Oceans. *Journal of Climate*, **27**, 2054–2071.

Bryden, H.L., King, B.A., McCarthy, G.D., and McDonagh, E.L. (2014). Impact of a 30% reduction in Atlantic meridional overturning circulation during 2009-2010. *Ocean Science*, **10**, 683–691.

Buckley, M.W. and Marshall, J. (2016). Observations, inferences, and mechanisms of the Atlantic Meridional Overturning Circulation: A review. *Reviews of Geophysics*, **54**, 5–63.

Bureau of Meteorology (2015). *Australian Hydrological Geospatial Fabric (Geofabric) Product Guide*. Canberra. version 3.0.

Cain, M., Methven, J., and Highwood, E.J. (2012). Quantification of chemical and physical processes influencing ozone during long-range transport using a trajectory ensemble. *Atmospheric Chemistry and Physics*, **12**, 70157039.

Camberlin, P., Janicot, S., and Poccard, I. (2001). Seasonality and atmospheric dynamics of the teleconnection between African rainfall and tropical sea-surface temperature: Atlantic vs. ENSO. *International Journal of Climatology*, **21**, 973–1005.

Candela, J. (2001). Mediterranean Water and Global Circulation. In G. Siedler, J. Church, and J. Gould, editors, *Ocean Circulation and Climate*, pages 475–488. Academic Press, London.

Carton, J.A., Chepurin, G.A., and Chen, L. (2018). SODA3: a new ocean climate reanalysis. *submitted to Monthly Weather Review*.

Cau, P., Methven, J., and Hoskins, B. (2007). Origins of dry air in the tropics and subtropics. *Journal of Climate*, **20**, 2745–2759.

Chaudhari, H.S., Pokhrel, S., Saha, S.K., Dhakate, A., and Hazra, A. (2014). Improved depiction of Indian summer monsoon in latest high resolution NCEP climate forecast system reanalysis. *International Journal of Climatology*, **35**, 3102–3119.

Cheng, W., Chiang, J.C.H., and Zhang, D. (2013). Atlantic Meridional Overturning Circulation (AMOC) in CMIP5 Models: RCP and Historical Simulations. *Journal of Climate*, **26**, 7187–7197.

Clark, E.A., Sheffield, J., van Vleit, M.T.H., Nijssen, B., and Lettenmaier, D.P. (2015). Continental Runoff into the Oceans (1950-2008). *Journal of Hydrometeorology*, **16**, 1502–1520.

Clarke, A.J. (1988). Inertial wind path and sea surface temperature patterns near the Gulf of Tehuantepec and the Gulf of Papagayo. *Journal of Geophysical Research: Oceans*, **93**, 15491–15501.

Craig, P.M., Ferreira, D., and Methven, J. (2017). The contrast between Atlantic and Pacific surface water fluxes. *Tellus A*, **69**(1330454).

Czaja, A. (2009). Atmospheric Control on the Thermohaline Circulation. *Journal of Climate*, **39**, 234–247.

Dacre, H.F., Gray, S.L., and Belcher, S.E. (2007). A case study of boundary layer ventilation by convection and coastal processes. *Journal of Geophysical Research: Oceans*, **112**. D17106.

D'Addezio, J.M. and Bingham, F.M. (2014). A subtropical North Atlantic regional atmospheric moisture budget. *Journal of Geophysical Research: Oceans*, **119**(12), 8731–8748.

Dai, A. and Trenberth, K.E. (2002). Estimates of Freshwater Discharge from Continents: Latitudinal and Seasonal Variations. *Journal of Hydrometeorology*, **3**, 660–687.

Dai, A. and Trenberth, K.E. (2003). New Estimates of Continental Discharge and Oceanic Freshwater Transport. In *AMS Symposium on Observing and Understanding the Variability of Water in Weather and Climate*, Long Beach, CA.

de Leeuw, J. (2014). *On the origin of summer precipitation variability in the UK*. Ph.D. thesis, University of Reading.

de Leeuw, J., Methven, J., and Blackburn, M. (2015). Evaluation of ERA-Interim reanalysis precipitation products using England and Wales observations. *Quarterly Journal of the Royal Meteorological Society*, **141**, 798–806.

de Leeuw, J., Methven, J., and Blackburn, M. (2017). Physical Factors Influencing Regional Precipitation Variability Attributed Using an Airmass Trajectory Method. *Journal of Climate*, **30**, 7359–7378.

Dee, D.P., Uppala, S.M., Simmons, A.J., Berrisford, P., Poli, P., Kobayashi, S., Andrae, U., Balmaseda, M.A., Balsamo, G., Bauer, P., Bechtold, P., Beljaars, A.C.M., van de Berg, L., Bidlot, J., Bormann, N., Delsol, C., Dragani, R., Fuentes, M., Geer, A.J., Haimberger, L., Healy, S.B., Hersbach, H., Holm, E.V., Isaksen, L., Kållberg, P., Köhler, M., Matricardi, M., McNally, A.P., Monge-Sanz, B.M., Morcrette, J.-J., Park, B-.K., Peuby, C., de Rosnay, P., Tavolato, C., Thépaut, J.-N., and Vitart, F. (2011). The ERA-Interim Reanalysis: configuration and performance of the data assimilation system. *Quarterly Journal of the Royal Meteorological Society*, **137**, 553–597.

Delcroix, T., Henin, C., Porte, V., and Arkin, P. (1996). Precipitation and sea-surface salinity in the tropical Pacific Ocean. *Deep-Sea Research I: Oceanographic Research Papers*, **43**, 1123–1141.

Dietrich, G. (1963). *General Oceanography*. Interscience, London, 2nd edition. Translated from German by F. Ostapoff. Originally published in 1957.

Dufour, A., Zolina, O., and Gulev, S.G. (2016). Atmospheric Moisture Transport to the Arctic: Assessment of Reanalyses and Analysis of Transport Components. *Journal of Climate*, **29**, 5061–5081.

Dunning, C.M., Black, E.C.L., and Allan, R.P. (2016). The onset and cessation of seasonal rainfall over africa. *Journal of Geophysical Research: Atmospheres*, **121**, 11405–11424.

Durack, P.J. and Wijffels, S.E. (2010). Fifty-Year Trends in Global Ocean Salinities and Their Relationship to Broad-Scale Warming. *Journal of Climate*, **23**, 4342–4362.

Duran-Queseda, A.M., Gimeno, L., Amador, J.A., and Nieto, R. (2010). Moisture sources for Central America: Identification of moisture sources using a Lagrangian analysis technique. *Journal of Geophysical Research*, **115**(D05103).

Eckhardt, S., Stohl, A., Wernli, H., James, P., Forster, C., and Spichtinger, N. (2004). A 15-Year Climatology of Warm Conveyor Belts. *Journal of Climate*, **17**, 218–237.

ECMWF (2015). IFS documentation Cy41r1, Part IV: Physical Processes. Online (accessed 5th November 2016). https://www.ecmwf.int/en/elibrary/9211-part-iv-physical-processes.

Emile-Geay, J., Cane, M.A., Naik, N., Seager, R., Clement, A.C., and van Geen, A. (2003). Warren revisited: Atmospheric freshwater fluxes and "Why is no deep water formed in the North Pacific". *Journal of Geophysical Research: Oceans*, **108**. 3178.

Emmanuel, K.A. (1994). *Atmospheric Convection*. Oxford University Press, New York.

Fairall, C.W., Bradely, E.F., Hare, J.E., Grachev, A.A., and Edson, J.B. (2003). Bulk Parameterization of AirSea Fluxes: Updates and Verification for the COARE Algorithm. *Journal of Climate*, **16**, 571–591.

Fawole, O.G., Cai, X., Levine, J.G., Pinker, R.T., and MacKenzie, A.R. (2016). Detection of a gas flaring signature in the AERONET optical properties of aerosols at a tropical station in West Africa. *Journal of Geophysical Research: Atmospheres*, **121**, 14513–14524.

Ferreira, D., Marshall, J., and Campin, J.-M. (2010). Localization of Deep Water Formation: Role of Atmospheric Moisture Transport and Geometrical Constraints on Ocean Circulation. *Journal of Climate*, **23**, 1456–1476.

Ferreira, D., Cessi, P., Coxall, H., de Boer, A., Dijkstra, H.A., Drijfhout, S.S., Eldevik, T., Harnik, N., McManus, J.F., Marshall, D.P., Nilsson, J., Roquet, F., Schneider, T., and Wills, R.C. (2018). Atlantic-Pacific asymmetry in deep water formation. *Annual Reviews of Earth and Planetary Sciences*, **46**(1).

Fleming, Z.L., Monks, P.S., and Manning, A.J. (2012). Untangling the influence of air-mass history in interpreting observed atmospheric composition. *Atmospheric Research*, **104**, 1–39.

Forget, G., Campin, J.-M., Heimbach, P., Hill, C.N., Ponte, R.M., and Wunsch, C. (2015). ECCO version 4: an integrated framework for non-linear inverse modeling and global ocean state estimation. *Geoscientific Model Development*, **8**(10), 3071–3104.

Gadgil, S. (2003). The Indian Monsoon and its Variability. *Annual Reviews of Earth and Planetary Sciences*, **31**, 429–467.

Ganachaud, A. and Wunsch, C. (2003). Large-Scale Ocean Heat and Freshwater Transports during the World Ocean Circulation Experiment. *Journal of Climate*, **16**, 696–705.

Ganachaud, A., Wunsch, C., Marotzke, J., and Toole, J. (2000). Meridional overturning and large-scale circulation of the Indian Ocean. *Journal of Geophysical Research: Oceans*, **105**(C11), 26117–26134.

Giannini, A., Biasutti, M., Held, H.M., and Sobel, A.H. (2008). A global perspective on African climate. *Climatic Change*, **90**, 359–383.

Gimeno, L., Drumond, A., Nieto, R., Trigo, R.M., and Stohl, A. (2010). On the origin of continental precipitation. *Geophysical Research Letters*, **37**(L13804).

Gimeno, L., Dominguez, F., Nieto, R., Trigo, R., Drumond, A., Reason, C.J.C., Taschetto, A.S., Ramos, A.M., Kumar, R., and Marengo, J. (2016). Major Mechanisms of Atmospheric Moisture Transport and Their Role in Extreme Precipitation Events. *Annual Review of Environment and Resources*, **41**, 117–141.

Good, S.A., Martin, M.J., and Rayner, N.A. (2013). EN4: Quality controlled ocean temperature and salinity profiles and monthly objective analyses with uncertainty estimates. *Journal of Geophysical Research: Oceans*, **118**, 6704–6716.

Gordon, A.L., Giulivi, C.F., Busecke, J., and Bingham, F.M. (2015). Differences Among Subtropical Surface Salinity Patterns. *Oceanography*, **28**, 32–39.

Goswami, B.N. and Sengupta, D. (2003). A note on the deficiency of NCEP/NCAR reanalysis surface winds over the equatorial Indian Ocean. *Journal of Geophysical Research: Oceans*, **108**. 3124.

Griffiths, D.F. and Higham, D.J. (2010). *Numerical Methods for Ordinary Differential Equations: Initial Value Problems*. Springer, London.

Hahn, D.G. and Manabe, S. (1975). The Role of Mountains in the South Asian Monsoon Circulation. *Journal of the Atmospheric Sciences*, **32**, 1515–1541.

Håkansson, B., Alenius, P., and Brydsten, L. (1996). Physical Environment in the Gulf of Bothnia. *Ambio*, pages 5–12.

Halpern, D. and Woiceshyn, P.M. (2001). Somali Jet in the Arabian sea, El Niño, and India Rainfall. *Journal of Climate*, **14**, 434–441.

Hawcroft, M.K., Shaffrey, L.C., Hodges, K.I., and Dacre, H.F. (2012). How much Northern Hemisphere precipitation is associated with extratropical cyclones? *Geophysical Research Letters*, **39**(L24809).

Held, I.M. and Soden, B.J. (2006). Robust Responses of the Hydrological Cycle to Global Warming. *Journal of Climate*, **19**, 5686–1560.

Higgins, R.W., Yao, Y., Yarosh, E.S., Janowiak, J.E., and Mo, K.C. (1997). Influence of the Great Plains low-level jet on summertime precipitation and moisture transport over the central United States. *Journal of Climate*, **10**, 481–507.

Hodges, K.I. (1996). Spherical Nonparametric Estimators Applied to the UGAMP Model Integration for AMIP. *Monthly Weather Review*, **124**, 2914–2932.

Huffman, G.J., Adler, R.F., Bolvin, D.T., and Gu, G. (2009). Improving the global precipitation record: GPCP Version 2.1. *Geophysical Research Letters*, **36**. L17808.

Huffman, G.J., Bolvin, D.T., Nelkin, E.J., and Adler, R.F. (2015). GPCP Version 2.2 Combined Precipitation Data Set.

Huisman, S.E., Dijkstra, H.A., von der Heydt, A., and de Ruijter, W.P.M. (2009). Robustness of multiple equilibria in the global ocean circulation. *Geophysical Research Letters*, **36**(1). L01610.

Huisman, S.E., Dijkstra, H.A., von der Heydt, A.S., and de Ruijter, W.P.M. (2012). Does Net *E-P* Set a Preference for North Atlantic Sinking? *Journal of Physical Oceanography*, **42**, 1781–1792.

Iwasaki, S., Kubota, M., and Watabe, T. (2014). Assessment of various global freshwater flux products for the global ice-free oceans. *Remote Sensing of the Environment*, **140**, 549–561.

Jackson, L.C., Kahana, R., Graham, T., Ringer, M.A., Woolings, T., Mecking, T.V., and Wood, R.A. (2015). Global and European climate impacts of a slowdown of the AMOC in a high resolution GCM. *Climate Dynamics*, **45**, 3299–3316.

Kajtar, J.B., Santoso, A., England, M.H., and Cai, W. (2015). Indo-Pacific Climate Interactions in the Absence of an Indonesian Throughflow. *Journal of Climate*, **28**, 5017–5029.

Kamphuis, V., Huisman, S.E., and Dijkstra, H.A. (2011). The global ocean circulation on a retrograde rotating earth. *Climate of the Past*, **7**, 487–499.

Korhonen, K., Giannakaki, E., Mielonen, T., Pfüller, A., Laakso, L., Vakkari, V., Baars, H., Engelmann, R., Beukes, P., Van Zyl, P.G., Ramandh, A., Ntsangwane, L., Josipovic, M., Tiitta, P., Fourie, G., Ngwana, I., Chiloane, K., and Komppula, M. (2014). Atmospheric boundary layer top height in South Africa: measurements with lidar and radiosonde compared to three atmospheric models. *Atmospheric Chemistry and Physics*, **14**, 4263–4278.

Kraus, E.B. and Turner, J.S. (????). A one-dimensional model of the seasonal thermocline ii: The general theory and its consequences. *Tellus*.

Läderach, A. and Sodemann, H. (2016). A revised picture of the atmospheric moisture residence time. *Geophysical Research Letters*, **43**, 924–933.

Latif, M., Roeckner, E., Mikolajewicz, U., and Voss, R. (2000). Tropical Stabilization of the Thermohaline Circulation in a Greenhouse Warming Simulation. *Journal of Climate*, **13**, 1809–1813.

Leduc, G., Vidal, L., Tachikawa, K., Rostek, F., Sonzogni, C., Beaufort, L., and Bard, E. (2007). Moisture transport across Central America as a positive feedback on abrupt climatic changes. *Nature*, **445**, 908–911.

Lehner, B., Verdin, K., and Jarvis, A. (2008). New global hydrology derived from spaceborne elevation data. *Eos, Transactions*, **89**, 93–94.

Lehner, B., Verdin, K., and Jarvis, A. (2013). HydroSHEDS Technical Documentation. Technical Report 1.2, US Geological Survey and World Wildlife Fund.

Lèlè, M.I., Leslie, L.M., and Lamb, P.J. (2015). Analysis of Low-Level Atmospheric Moisture Transport Associated with the West African Monsoon. *Journal of Climate*, **28**, 4414–4430.

Levang, S.L. and Schmitt, R.W. (2015). Centennial Changes of the Global Water Cycle in CMIP5 Models. *Journal of Climate*, **28**, 6489–6502.

Liebmann, B., Bladé, I., Kiladis, G.N., Carvalho, L.M.V., Senay, G.B., Allured, D., Leroux, S., and Funk, C. (2012). Seasonality of African Precipitation from 1996 to 2009. *Journal of Climate*, **25**, 4304–4322.

Lohmann, G. (2003). Atmospheric and oceanic freshwater transport during weak Atlantic overturning circulation. *Tellus A*, **55**, 438–449.

Lyon, B. and DeWitt, D.G. (2012). A recent and abrupt decline in the East African long rains. *Geophysical Research Letters*, **39**(L02702).

Marengo, J.A., Soares, W.R., Saulo, C., and Nicolini, M. (2004). Climatology of the Low-Level Jet East of the Andes as Derived from the NCEP–NCAR Reanalyses: Characteristics and Temporal Variability. *Journal of Climate*, **17**, 2261–2280.

Marotzke, J. and Willebrand, J. (1991). Multiple Equilibria of the Global Thermohaline Circulation. *Journal of Physical Oceanography*, **21**, 1372–1385.

Marshall, J. and Schott, F. (1999). Open-ocean convection: Observations, theory and models. *Reviews of Geophysics*, **37**, 1–64.

Marsham, J.H., Hobby, M., Allen, C.J.T., Banks, J.R., Bart, M., Brooks, B.J., Cavazos-Guerra, C., Engelstaedter, S., Gascoyne, M., Lima, A.R., Martins, J.V., McQuaid, J.B., O'Leary, A., Ouchene, B., Ouladichir, A., Parker, D.J., Saci, A., Salah-Ferroudj, M., Todd, M.C., and Washington, R. (2013). Meteorology and dust in the central Sahara: Observations from Fennec supersite-1 during the June 2011 Intensive Observation Period. *Journal of Geophysical Research: Atmospheres*, **118**, 4069–4089.

Martínez-Alvarado, O., Baker, L.H., Gray, S.L., Methven, J., and Plant, R.S. (2014). Distinguishing the Cold Conveyor Belt and Sting Jet Airstreams in an Intense Extratropical Cyclone. *Monthly Weather Review*, **142**, 2571–2595.

Methven, J. (1997). Offline trajectories: Calculation and accuracy. Technical Report 44, U.K. Univ. Global Atmos. Modelling Prog., Dept. of Meteorol., Univ. of Reading, U.K.

Methven, J., Evans, M., Simmonds, P., and Spain, G. (2001). Estimating relationships between air mass origin and chemical composition. *Journal of Geophysical Research: Atmospheres*, **106**, 5005–5019.

Millero, F.J., Feistel, R., Wright, D.G., and McDougall, T.J. (2008). The composition of Standard Seawater and the definition of the Reference-Composition Salinity Scale. *Deep-Sea Research I*, **55**, 50–72.

National Geophysical Data Center (1993). *5-minute Gridded Global Relief Data (ETOPO5)*. National Geophysical Data Center, NOAA. doi:10.7289/V5D798BF [accessed 10/02/2015].

Natural Resources Canada (2009). Atlas of Canada 1,000,000 National Frameworks Data, Hydrology. Government of Canada; Natural Resources Canada; Earth Sciences Sector; Canada Centre for Mapping and Earth Observation.

Newell, R.E. and Evans, M.J. (2000). Seasonal changes in pollutant transport to the North Pacific: the relative importance of Asian and European sources. *Geophysical Research Letters*, **27**, 2509–2512.

Nicholson, S. (2016). The Turkana low-level jet: mean climatology and association with regional aridity. *International Journal of Climatology*, **36**, 2598–2614.

Nieto, R., Gimeno, L., Gallego, D., and Trigo, R. (2007). Contributions to the moisture budget of airmasses over Iceland. *Meteorologische Zeitschrift*, **16**, 37–44.

Nilsson, J., Langen, P.L., Ferreira, D., and Marshall, J. (2013). Ocean Basin Geometry and the Salinification of the Atlantic Ocean. *Journal of Climate*, **26**, 6163–6184.

Numaguti, A. (1999). Origin and recycling processes of precipitating water over the Eurasian continent: Experiments using an atmospheric general circulation model. *Journal of Geophysical Research: Atmospheres*, **104**, 1957–1972.

Oki, T. and Sud, Y.C. (1998). Design of Total Runoff Integrating Pathways (TRIP): A Global River Channel Network. *Earth Interactions*, **2**, 1–37.

Oort, A.H. (1983). Global Atmospheric Circulation Statistics 1958-1973. NOAA Professional Paper 14, NOAA.

Orlanski, I. (1998). Poleward Deflection of Storm Tracks. *Journal of the Atmospheric Sciences*, **55**, 2577–2602.

Peake, D.L., Dacre, H.F., Methven, J., and Coceal, O. (2014). Meteorological factors controlling low-level continental pollutant outflow across a coast. *Atmospheric Chemistry and Physics*, **14**, 13295–13312.

Pfahl, S., O'Gorman, P., and Singh, M.S. (2015). Extratropical Cyclones in Idealized Simulations of Changed Climates. *Journal of Climate*, **28**, 9373–9392.

Poveda, G. and Mesa, O.J. (2000). On the Existence of Lloró (the Rainiest Locality on Earth): Enhanced Ocean-Land-Atmosphere Interaction by a Low-Level Jet. *Geophysical Research Letters*, **27**, 1675–1678.

Poveda, G., Jaramillo, L., and Vallejo, L.F. (2014). Seasonal precipitation patterns along pathways of south american low-level jets and aerial rivers. *Water Resources Research*, **50**, 98–118.

Prange, M., Steph, S., Schulz, M., and Keigwin, L.D. (2010). Inferring moisture transport across Central America: Can modern analogs of climate variability help reconcile paleosalinity records? *Quaternary Science Reviews*, **29**, 1317–1321.

Press, W.H., Teukolsky, S.A., Vetterling, W.T., and Flannery, B.P. (2003). *Numerical Recipes: The Art of Scientific Computing*. Cambridge University Press, Cambridge, 3rd edition.

Rahmstorf, S. (1996). On the freshwater forcing and transport of the Atlantic thermohaline circulation. *Climate Dynamics*, **12**, 799–811.

Ren, L., Hackert, E., Arkin, P., and Busalacchi, A.J. (2014). Estimating the global oceanic net freshwater flux from Argo and comparing it with satellite-based freshwater flux products. *Journal of Geophysical Research: Oceans*, **119**, 7869–7881.

Richter, I. and Xie, S.-S. (2010). Moisture transport from the Atlantic to the Pacific basin and its response to North Atlantic cooling and global warming. *Climate Dynamics*, **35**, 551–566.

Riddle, E.E. and Cook, K.H. (2008). Abrupt rainfall transitions over the Greater Horn of Africa: Observations and regional model simulations. *Journal of Geophysical Research: Atmospheres*, **113**. D15109.

Rignot, E. and Mouginot, J. (2012). Ice flow in Greenland for the International Polar Year 2008-2009. *Geophysical Research Letters*, **39**(L11501).

Roberts, C.D., Waters, J., Peterson, K.A., Palmer, M.D., McCarthy, G.D., Frajka-Williams, E., Haines, K., Lea, D.J., Martin, M.J., Storkey, D., Blockley, E.W., and Zuo, H. (2013). Atmosphere drives recent interannual variability of the Atlantic meridional overturning circulation at 26.5°N. *Geophysical Research Letters*, **40**(19), 5164–5170.

Rodriguez, J.M., Johns, T.C., Thorpe, R.B., and Wiltshire, A. (2011). Using moisture conservation to evaluate oceanic surface freshwater fluxes in climate models. *Climate Dynamics*, **37**, 205–219.

Rodwell, M.J. and Hoskins, B.J. (1995). A Model of the Asian Summer Monsoon Part II: Cross-Equatorial Flow and PV Behavior. *Journal of the Atmospheric Sciences*, **9**, 1341–1356.

Saenko, O.A., Gregory, J.M., Weaver, A.J., and Eby, M. (2002). Distinguishing the Influence of Heat, Freshwater, and Momentum Fluxes on Ocean Circulation and Climate. *Journal of Climate*, **15**, 3686–3697.

Saji, N.H., Goswami, B.N., Vinayachandran, P.N., and Yamagata, T. (1999). A dipole mode in the tropical Indian Ocean. *Nature*, **401**, 360–363.

Saulière, J., Brayshaw, S.J., Hoskins, B., and Blackburn, M. (2012). Further Investigation of the Impact of Idealized Continents and SST Distributions on the Northern Hemisphere Storm Tracks. *Journal of the Atmospheric Sciences*, **69**, 840–856.

Schanze, J.J., Schmitt, R.W., and Yu, L.L. (2010). The global oceanic freshwater cycle: A state-of-the-art quantification. *Journal of Marine Research*, **68**, 569–595.

Schiemann, R., Demory, M.-E., Mizielinski, M.S., Roberts, M.J., Shaffrey, L.C., Strachan, L.C., and Vidale, P.L. (2014). The sensitivity of the tropical circulation and Maritime Continent precipitation to climate model resolution. *Climate Dynamics*, **42**, 2455–2468.

Schmitt, R.W. (2008). Salinity and the Global Water Cycle. *Oceanography*, **21**, 12–19.

Schmitt, R.W., Bogden, P.S., and Dorman, C.E. (1989). Evaporation Minus Precipitation and Density Fluxes for the North Atlantic. *Journal of Physical Oceanography*, **19**, 1208–1221.

Schmittner, A., Silva, T.A.M., Fraedrich, K., Kirk, E., and E., Lunkeit (2011). Effects of Mountains and Ice Sheets on Global Ocean Circulation. *Journal of Climate*, **24**, 2814–2829.

Seager, R. and Henderson, N. (2013). Diagnostic Computation of Moisture Budgets in the ERA-Interim Reanalysis with Reference to Analysis of CMIP-Archived Atmospheric Model Data. *Journal of Climate*, **26**, 7876–7901.

Seager, R., Battisti, D.S., Yin, J., Gordon, N., Naik, N., Cement, A.C., and Cane, M.A. (2002). Is the Gulf Stream responsible for Europes mild winters? *Quarterly Journal of the Royal Meteorological Society*, **128**, 2563–2586.

Shoshiro, M., Kuwano-Yoshida, A., Nobumasa, K., Xie, S.-P., and Small, R.J. (2008). Influence of the Gulf Stream on the troposphere. *Nature*, **452**, 206–210.

Silverman, B.W. (1986). *Density Estimation for Statistics and Data Analysis*. Chapman and Hall, London.

Simmons, A.J. and Burridge, D.M. (1981). An energy and angular-momentum conserving vertical finite-difference scheme and hybrid vertical coordinates. *Monthly Weather Review*, **109**, 758–766.

Singh, A., Delcroix, T., and Cravatte, S. (2011). Contrasting the flavors of El Niño-Southern Oscillation using sea surface salinity observations. *Journal of Geophysical Research: Oceans*, **116**(C6). C06016.

Singh, H.K.A., Donohoe, A., Bitz, C.M., Nusbaumer, J., and Noone, D.C. (2016). Greater Moisture Transport Distances with Warming Amplify Interbasin Salinity Contrasts. *Geophysical Research Letters*, **43**, 8677–8684.

Sinha, B., Blaker, A.T., Hirschi, J.-M., Bonham, S., Brand, M., Josey, S., Smith, R.S., and Marotzke, J. (2012). Mountain ranges favour vigorous Atlantic meridional overturning. *Geophysical Research Letters*, **39**. L02705.

Skliris, N., Marsh, R., Josey, S.A., Good, S.A., Liu, C., and Allan, R.P. (2014). Salinity changes in the World Ocean since 1950 in relation to changing surface freshwater fluxes. *Climate Dynamics*, **43**, 709–736.

Sodemann, H., Schwierz, C., and Wernli, H. (2008). Interannual variability of Greenland winter precipitation sources Lagrangian moisture diagnostic and North Atlantic Oscillation influence. *Geophysical Research Letters*, **113**. D03107.

Steenburgh, W.J., Schultz, D.M., and Colle, B.A. (1998). The Structure and Evolution of Gap Outflow over the Gulf of Tehuantepec, Mexico. *Monthly Weather Review*, **126**, 2673–2691.

Stein, A.F., Draxler, R.R., Rolph, G.D, Stunder, B.J.B., and Cohen, M.D. (2015). NOAAs HYSPLIT Atmospheric Transport and Dispersion Modeling System. *Bulletin of the American Meteorological Society*, **96**, 2059–2077.

Stephens, G.L. and Ellis, T.D. (2008). Controls of Global-Mean Precipitation Increases in Global Warming GCM Experiments. *Journal of Climate*, **21**, 6141–6155.

Stohl, A (1998). Computation, Accuracy and Applications of Trajectories - A Review and Bibliography. *Atmospheric Environment*, **32**, 947–966.

Stohl, A. and James, P. (2005). A Lagrangian Analysis of the Atmospheric Branch of the Global Water Cycle. Part II: Moisture Transports between Earth's Ocean Basins and River Catchments. *Journal of Hydrometeorology*, **6**, 961–984.

Stommel, H. (1961). Thermohaline Convection with Two Stable Regimes of Flow. *Tellus*, **13**, 224–230.

Su, T. and Feng, G.L. (2015). Spatial-temporal variation characteristics of global evaporation revealed by eight reanalyses. *Science China: Earth Sciences*, **58**, 255–269.

Talley, L.D. (1991). An Okhotsk Sea water anomaly: implications for ventilation in the North Pacific. *Deep-Sea Research*, **38**, S171–S190.

Talley, LD (1993). Distribution and Formation of North Pacific Intermediate Water. *Journal of Physical Oceanography*, **23**, 517–537.

Talley, L.D. (2003). Shallow, Intermediate, and Deep Overturning Components of the Global Heat Budget. *Journal of Physical Oceanography*, **33**, 530–560.

Talley, L.D. (2008). Freshwater transport estimates and the global overturning circulation:Shallow, deep and throughflow components. *Progress in Oceanography*, **78**, 257–303.

Talley, L.D. (2013). Closure of the Global Overturning Circulation Through the Indian, Pacific, and Southern oceans: Schematics and Transports. *Oceanography*, **26**, 80–97.

Talley, L.D., Pickard, G.L., Emery, W.J., and Swift, J.H. (2011). *Descriptive Physical Oceanography: An Introduction*. Elsevier, London, 6th edition.

Tchilibou, M., Delcroix, T., Alory, G., Arnault, S., and Reverdin, G. (2015). Variations of the tropical Atlantic and Pacific SSS minimum zones and their relations to the ITCZ and SPCZ rain bands (1979-2009). *Journal of Geophysical Research: Oceans*, **120**, 5090–5100.

Trenberth, K.E. (1998). Atmospheric Moisture Residence Times and Cycling: Implications for Rainfall Rates and Climate Change. *Climatic Change*, **39**, 667–694.

Trenberth, K.E. and Caron, J.M. (2001). Estimates of Meridional Atmosphere and Ocean Heat Transports. *Journal of Climate*, **14**, 3433–3443.

Trenberth, K.E., Smith, L., Qian, T., Dai, A., and Fasullo, J. (2007). Estimates of the Global Water Budget and Its Annual Cycle Using Observational and Model Data. *Journal of Hydrometeorology*, **8**, 758–769.

Trenberth, K.E., Fasullo, J.T., and Mackaro, J. (2011). Atmospheric Moisture Transports from Ocean to Land and Global Energy Flows in Reanalyses. *Journal of Climate*, **24**, 4907–4924.

Valdivieso, M., Haines, K., Zuo, H., and Lea, D. (2014). Freshwater and heat transports from global ocean synthesis. *Journal of Geophysical Research*, **119**, 394–409.

van der Ent, R.J. and Savenije, H.H.G. (2013). Oceanic sources of continental precipitation and the correlation with sea surface temperature. *Water Resources Research*, **49**, 3993–4004.

van der Ent, R.J. and Tuinenburg, O.A. (2017). The residence time of water in the atmosphere revisited. *Hydrology and Earth System Sciences*, **21**, 779–790.

Vinogradova, N.T. and Ponte, R.M. (2013). Clarifying the link between surface salinity and freshwater fluxes on monthly to interannual time scales. *Journal of Geophysical Research: Oceans*, **118**, 3190–3201.

Viste, E. and Sorteberg, A. (2011). Moisture transport into the Ethiopian highlands. *International Journal of Climatology*, **33**, 249–263.

Wang, C. (2007). Variability of the Caribbean low-level jet and its relations to climate. *Climate Dynamics*, **29**, 411–422.

Wang, C. and Enfield, D.B. (2001). The tropical Western Hemisphere warm pool. *Geophysical Research Letters*, **28**, 1635–1638.

Wang, C., Zhang, L., and Lee, S.-K. (2013). Response of Freshwater Flux and Sea Surface Salinity to Variability of the Atlantic Warm Pool. *Journal of Climate*, **26**, 1249–1267.

Warren, B.A. (1983). Why is no deep water formed in the North Pacific? *Journal of Marine Research*, **41**, 327–347.

Weaver, A.J., Bitz, C.M., Fanning, A.F., and Holland, M.M. (1999). Thermohaline Circulation: High-Latitude Phenomena and the Difference Between the Pacific and Atlantic. *Annual Review of Earth and Planetary Sciences*, **27**, 231–285.

Wei, H.-H. and Bordoni, S. (2016). On the Role of the African Topography in the South Asian Monsoon. *Journal of the Atmospheric Sciences*, **73**, 3197–3212.

Weijer, W., de Ruijter, W.P.M., Dijkstra, H.A., and van Leeuwen, P.J. (1999). Impact of Interbasin Exchange on the Atlantic Overturning Circulation. *Journal of Physical Oceanography*, **29**, 2266–2284.

Weyl, P.K. (1968). *The role of the oceans in climate change: A theory of the ice ages*, volume 8 of *Meteorological Monographs*, pages 37–62. American Meteorological Society.

White, R.H., Battisti, D.S., and Roe, G.H. (2017). Mongolian Mountains Matter Most: Impacts of the Latitude and Height of Asian Orography on Pacific Wintertime Atmospheric Circulation. *Journal of Climate*, **30**, 4065–4082.

Whyte, F., Taylor, M.A., Stephenson, T.S., and Campbell, J.D. (2008). Features of the Caribbean low level jet. *International Journal of Climatology*, **28**, 199–128.

Wijffels, SE (2001). Ocean Transport of Fresh Water. In G. Siedler, J. Church, and J. Gould, editors, *Ocean Circulation and Climate*, pages 475–488. Academic Press, London.

Wijffels, S.E., Schmitt, R.W., Bryden, H.L., and Stigebrandt, A. (1992). Transport of Freshwater by the Oceans. *Journal of Physical Oceanography*, **22**, 155–162.

Wilcox, L.J., Shine, K.P., and Hoskins, B.J. (2012). Radiative forcing due to aviation water vapour emissions. *Atmospheric Environment*, **63**, 1–13.

Wills, R.C. and Schneider, T. (2015). Stationary eddies and the zonal asymmetry of net precipitation and ocean freshwater forcing. *Journal of Climate*, **28**, 5115–5133.

Wu, J. (1996). Moisture-transfer coefficient for climate models. *Boundary-Layer Meteorology*, **77**, 401–407.

Wunsch, C. (2002). What is the Thermohaline Circulation? *Science*, **298**, 1179–1180.

Würsch, M. and Sprenger, M. (2015). Swiss and Austrian Foehn revisited: A Lagrangian-based analysis. *Meteorologische Zeitschrift*, **24**, 225–242.

Xu, H., Xie, S.-S., Wang, Y., and Small, R.J. (2005). Effects of Central American Mountains on on the Eastern Pacific Winter ITCZ and Moisture Transport. *Journal of Climate*, **18**, 3856–3873.

Yu, L. (2007). Global Variations in Oceanic Evaporation (1958-2005): The Role of the Changing Wind Speed. *Journal of Climate*, **20**, 5376–5390.

Yu, L. (2011). A global relationship between the ocean water cycle and near-surface salinity. *Journal of Geophysical Research: Oceans*, **116**(C10025).

Yu, L. and Weller, R.A. (2007). Objectively Analyzed Air-Sea Heat Fluxes for the Global Ice-Free Oceans (1981-2005). *Bulletin of the American Meteorological Society*, **88**, 527–539.

Yu, L., Jin, X., Josey, S.A., Lee, T., Kumar, A., Wen, C., and Xue, Y. (2017). The Global Ocean Water Cycle in Atmospheric Reanalysis, Satellite, and Ocean Salinity. *Journal of Climate*, **30**, 3829–3852.

Zaucker, F. and Broecker, W.S. (1992). The Influence of Atmospheric Moisture Transport on the Fresh Water Balance of the Atlantic Drainage Basin: General Circulation Model Simulations and Observations. *Journal of Geophysical Research*, **97**, 2765–2773.

Zaucker, F., Stocker, T.F., and Broecker, W.S. (1994). Atmospheric freshwater fluxes and their effect on the global thermohaline circulation. *Journal of Geophysical Research*, **99**, 12433–12457.

Zhang, L., Wu, L., and Gan, B. (2013). Modes and Mechanisms of Global Water Vapor Variability over the Twentieth Century. *Journal of Climate*, **26**, 5578–5593.

Zika, J.D., Skliris, N., Nurser, A.J.G., Josey, S.A., Mudryk, L., Laliberté, F., and Marsh, R. (2015). Maintenance and Broadening of the Oceans Salinity Distribution by the Water Cycle. *Journal of Climate*, **28**, 9550–9560.

Zweng, M.M., Reagan, J.R., Antonov, J.I., Locarnini, R.A., Mishonov, A.V., Boyer, T.P., Garcia, H.E., Baranova, O.K., Johnson, D.R., Seidov, D., and Biddle, M.M. (2013). Salinity. In S. Levitus and A. Mishonov, editors, *World Ocean Atlas 2013*, volume 2. NOAA Atlas NESDIS 74.